ISSN 2525-2461

Vietnam Journal of Science, Technology and Engineering

JUNE 2019 • VOL.61 NUMBER 2

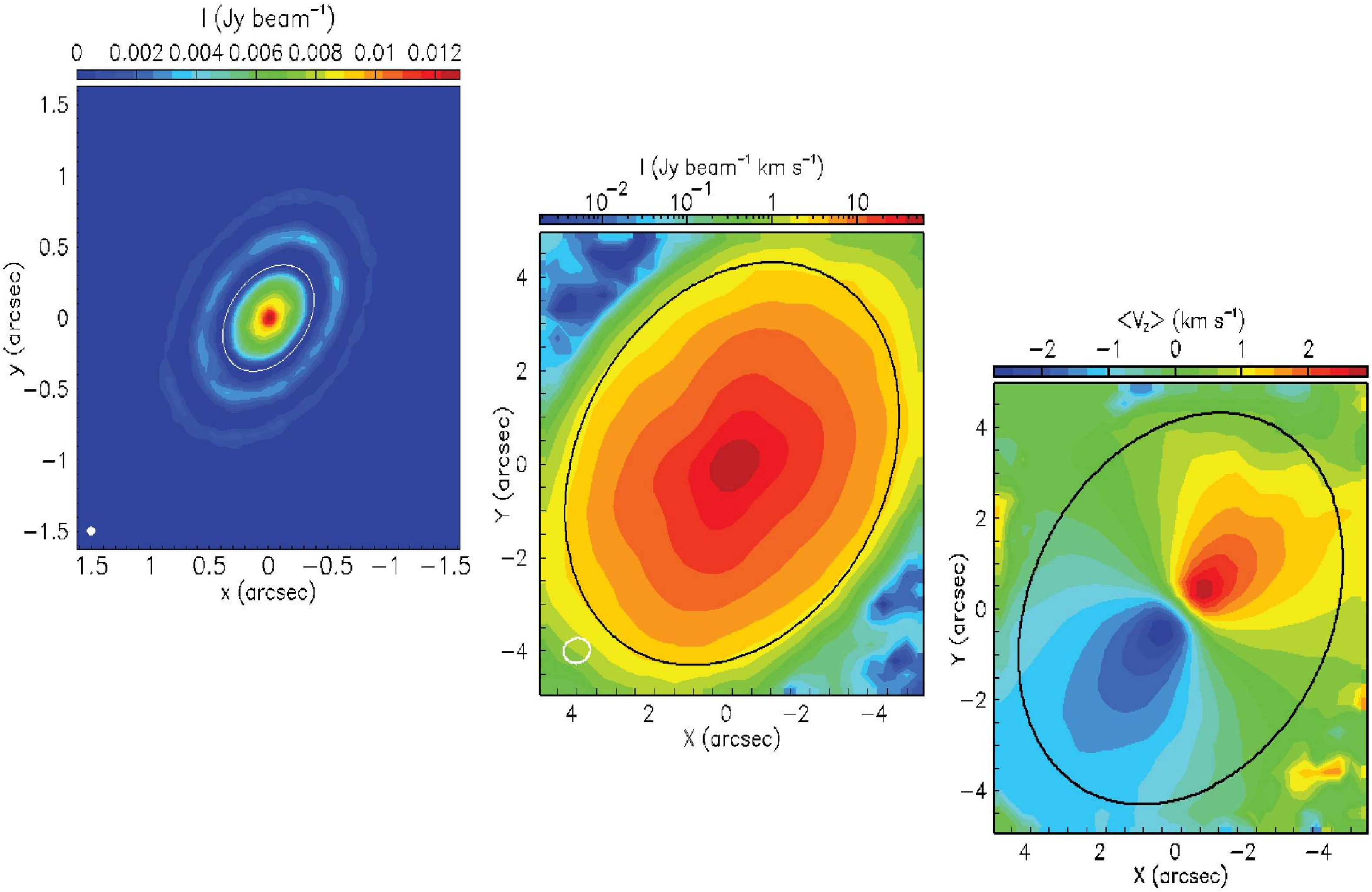

The protoplanetary disc HD 163296 as observed by ALMA

Vietnam Journal of Science, Technology and Engineering (VJSTE) **is a quarterly double-blind peer-reviewed academic journal. VJSTE publishes research articles and review articles in all areas of science, technology and engineering with the focus on the life sciences and environmental sciences including the following topics:**

- Agriculture
- Medicine
- Pharmacology
- Biology
- Biotechnology
- Ecology
- Climatology.

CLASSIFICATION SCHEME

1. Mathematics and Computer Science
   1.1. Mathematics
   1.2. Computer Science
   1.3. Computational Science

2. Physical Sciences
   2.1. Physics
   2.2. Chemistry
   2.3. Engineering

3. Life Sciences
   3.1. Agriculture
   3.2. Medicine
   3.3. Pharmacology
   3.4. Biology
   3.5. Biotechnology

4. Geosciences
   4.1. Geography
   4.2. Geology
   4.3. Geophysics
   4.4. Oceanography

5. Environmental Sciences
   5.1. Ecology
   5.2. Climatology

CONTENTS

JUNE 2019 • VOL.61 NUMBER 2

25

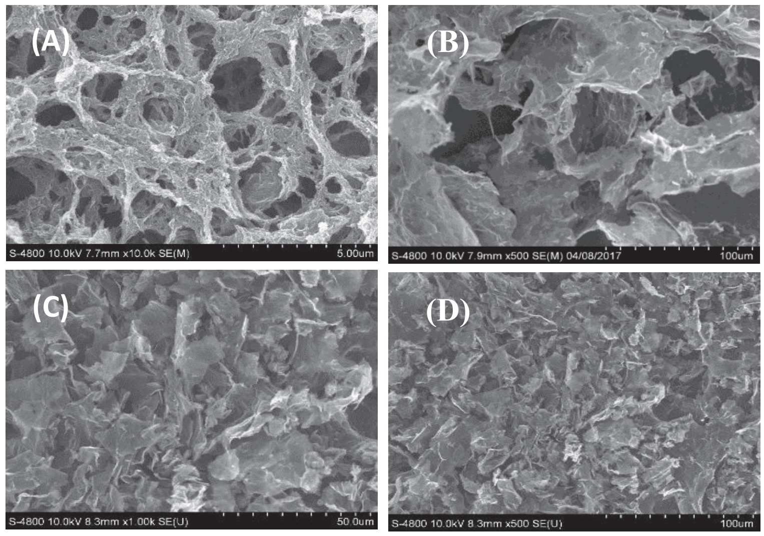

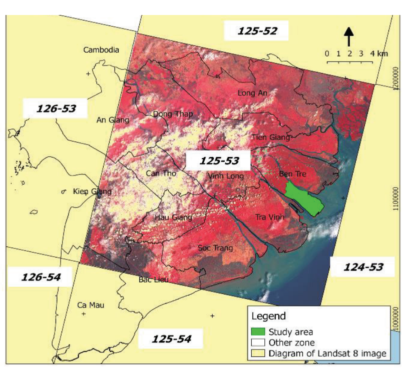

37

CONTENTS

JUNE 2019 • VOL.61 NUMBER 2

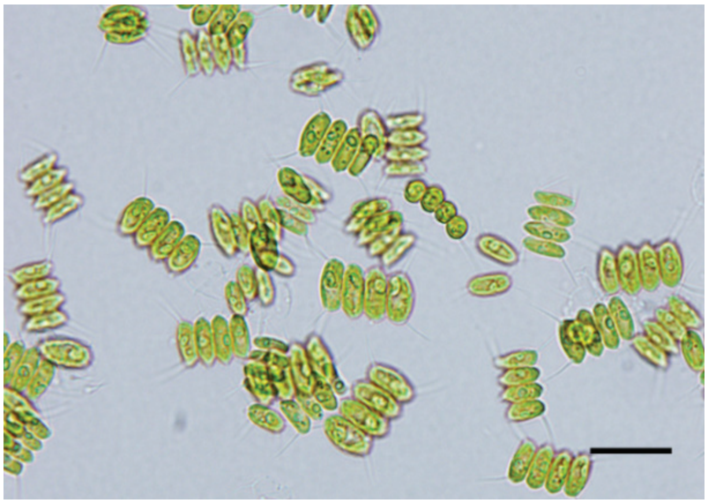

66

92

Doi: 10.31276/VJSTE.61(2).03-16

The protoplanetary disc HD 163296 as observed by ALMA

P.N. Diep*, D.T. Hoai, N.B. Ngoc, P.T. Nhung, N.T. Phuong, T.T. Thai, and P. Tuan-Anh

Department of Astrophysics, Vietnam National Space Center, Vietnam Academy of Science and Technology

Received 25 February 2019; accepted 3 April 2019

Abstract:

HD 163296 is one of the few protoplanetary discs displaying rings in the dust component. The present work uses ALMA observations of the 0.9 mm continuum emission, which have significantly better spatial resolution (~8 au) than previously available, to provide new insight into the morphology of the dust disc and its double ring structure. The disc is shown to be thin, and its position angle and inclination with respect to the sky plane are accurately measured as are the locations and shapes that characterise the observed ring-gap structure. Significant modulation of the intensity of the outer ring emission is revealed and discussed. In addition, earlier ALMA observations of the emission of three molecular lines, CO(2-1), $C^{18}O$(2-1), and DCO^+(3-2) with a resolution of ~70 au are used to demonstrate the Keplerian motion of the gas, which is found to be consistent with a central mass of 2.3 solar masses. An upper limit of ~9% of the rotation velocity is placed on the in-fall velocity. The beam size is shown to give the dominant contribution to the line widths, accounting for both their absolute values and their dependence on the distance to the central star.

Keywords: **planetary systems, protoplanetary discs, submillimetre astronomy.**

Classification number: **2.1**

Introduction

The study of ring-like structures observed in the dust emission of protoplanetary discs is expected to shed light on the mechanisms governing the formation of planets. Only two such discs were known before the discovery of the ring-gap structure of the HD 163296 disc [1]: TW Hya [2] and HL Tau [3]. Although still being debated, such ring-gap structure is thought to be associated with the presence of newly formed giant planets [4]. It is, therefore, important to identify effects that differentiate planet formation from other gap-opening mechanisms, such as aggregation of solids in low turbulence regions [5] and changes in dust opacity at the frost line of volatile elements [6, 7]. Keplerian shear resulting from the radial velocity gradient can cause turbulence, which, at a certain distance from the star, can lead to the formation of a gap similar to those carved by planets. A difference between this and planet formation is that a planet sucks up all the material (both gas and dust) around it, whereas turbulence removes the dust but not the gas.

HD 163296, the third system known to host multiple rings in dust emission at millimetre wavelength, is a Herbig Ae star of intermediate mass (2.3 solar masses). It is about 4 million years old and is located at a distance of 122 pc from Earth [8]. The gas disc is in Keplerian motion and has a radius of about 550 au, and the millimetre continuum emission from solid particles is confined to within 250 au of the star [9, 10].

Both gas and dust emissions from HD 163296 have been observed by ALMA. According to the analysis of Isella, et al. [1], the 1.3 mm continuum emission observed with a spatial resolution of 25 au reveals three concentric gap-ring pairs, with the dust-depleted gaps located at ~54, ~100, and 160 au from the central star. The gas morphology displayed by CO(2-1), ^{13}CO(2-1), and $C^{18}O$(2-1) emissions shows no clear evidence for ring-gap modulation, although small deviations from a smooth radial dependence have

*Corresponding author: Email: pndiep@vnsc.org.vn

been observed with the same resolution of ~25 au. Isella, et al. [1] interpret these as the result of a gas deficit restricted to the outer dust gaps but absent from the inner gap. They suggest that the outer gaps, at radial distances of 100 au and 160 au, are created by planets, probably about the mass of Saturn, but that the inner gap is due to gas turbulence or other physical phenomena within the disc. However, they do not exclude other possible interpretations. They evaluate the orbital radius and mass of the hypothetical planets from the location and shape of the dust gaps. The present study aims to provide additional information about this very interesting protoplanetary system.

Continuum emission

Observations

The continuum data used in the present study were collected on August 15th, 2017 and were reduced by the ALMA staff. The beam size is 0.069×0.061 arcsec^2 (FWHM) with a position angle of -88.8^o, three times smaller than was found in earlier observations [1]. The data have been corrected for the proper motion of the source, (-7.61, -39.42) mas yr^{-1}, which implies that the source has moved (-0.14, -0.70) arcsec to the south-west direction from its position in J2000. The continuum, observed at 330.588 GHz (~0.9 mm wavelength), displays a well-behaved Gaussian noise with a standard deviation of 0.26 mJy beam^{-1}. In what follows, unless otherwise stated, we apply a 3-σ cut to the data.

Sky plane morphology

Figure 1 (left) shows the map of the continuum intensity. The abscissa x and ordinate y measure offsets in arcsec from the central star with x pointing east and y pointing north. The middle and right panels show the projections of intensity on the x and y axes. The dust continuum emission is found to display central symmetry and to extend up to ~±1 arcsec on the sky plane.

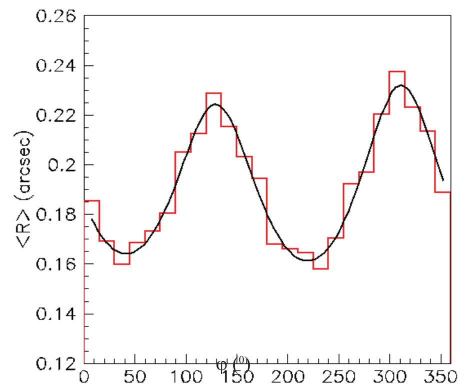

Fig. 2. Dependence of $<R>$ on position angle φ.

Figure 2 displays the dependence on φ of the mean value of the projected distance to the central star, $<R>$, where $\varphi=90^o-tan^{-1}(y/x)$ is the position angle measured counter-clockwise from north, and $R=\sqrt{(x^2+y^2)}$. $<R>$ is calculated using intensity as weight over the region contained inside the white ellipse shown in Fig. 1 (left), defined as having a semi-major axis of 0.44 arcsec, a semi-minor axis of 0.31 arcsec, and a position angle of the major axis of 138^o. It is small enough to avoid contribution of the bright ring at larger distance from the star and large enough not to introduce any bias in the evaluation of the geometry parameters of the disc. A fit to an ellipse of the dependence of $<R>$ on φ gives position angle of the major axis φ_0, semi-major axis a, and semi-minor axis b of 130^o, 0.23 arcsec, and 0.16 arcsec, respectively. When interpreted as a thin and flat circular disc inclined by an angle θ with respect to the plane of the sky,

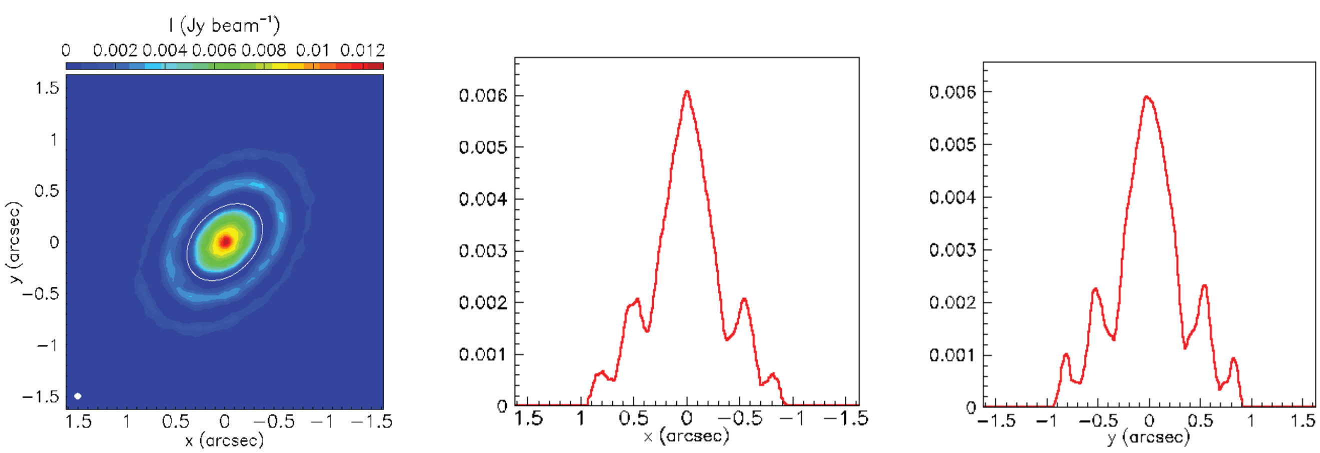

Fig. 1. Left: sky map of the continuum intensity. The white ellipse shows the region used to characterise the geometry of the disc. The beam is shown in the lower left corner of the map. Centre and right: projections on the x and y axes integrated over y and x respectively (in units of Jy beam^{-1} arcsec).

$\theta = \cos^{-1}(b/a) = 44^0$. Isella, et al. [1] quote values of 132^0 for φ_0 and 42^0 for θ, which are, respectively, 2^0 larger and 2^0 smaller than the present evaluations. This indicates good agreement since systematic uncertainties are expected to be at that level.

De-projected morphology

Figure 3 (top left) shows the de-projected intensity map in the disc plane. What is meant here by de-projection is a simple transformation from (x,y) coordinates to (x',y') coordinates, which is defined as follows:

$x' = x\cos 40^0 - y\sin 40^0$

$y' = (x\sin 40^0 + y\cos 40^0)/\cos 44^0$

Such a transformation would be accurate if the disc was perfectly flat and thin. In the disc plane, we define position angle φ' and radial distance r' from x' and y' in the same way as φ and R were defined from x and y: $\varphi' = 90^o - \tan^{-1}(y'/x')$ and $r' = \sqrt{(x'^2 + y'^2)}$.

Figure 3 (top right) shows the dependence on φ' of the intensity averaged over $r' < 1.31$ arcsec. It displays small fluctuations having a standard deviation of only 7% of the mean value (1.1 mJy beam^{-1}). Fig. 3 (bottom left) displays the dependence on r' of the intensity averaged over φ'. Compared with the results of Isella, et al. [1], the improved resolution produces much deeper gaps between the rings but provides no evidence for a third gap at $r' \sim 1.31$ arcsec. This is confirmed in Fig. 4 where the 3-σ cut has been lifted. Gaussian fits to the gaps and rings give values of the mean radius and standard deviation. These are listed in Table 1 and are in excellent agreement with the mean radii of the gaps quoted by Isella, et al. [1] as 0.44 arcsec and 0.81 arcsec, respectively.

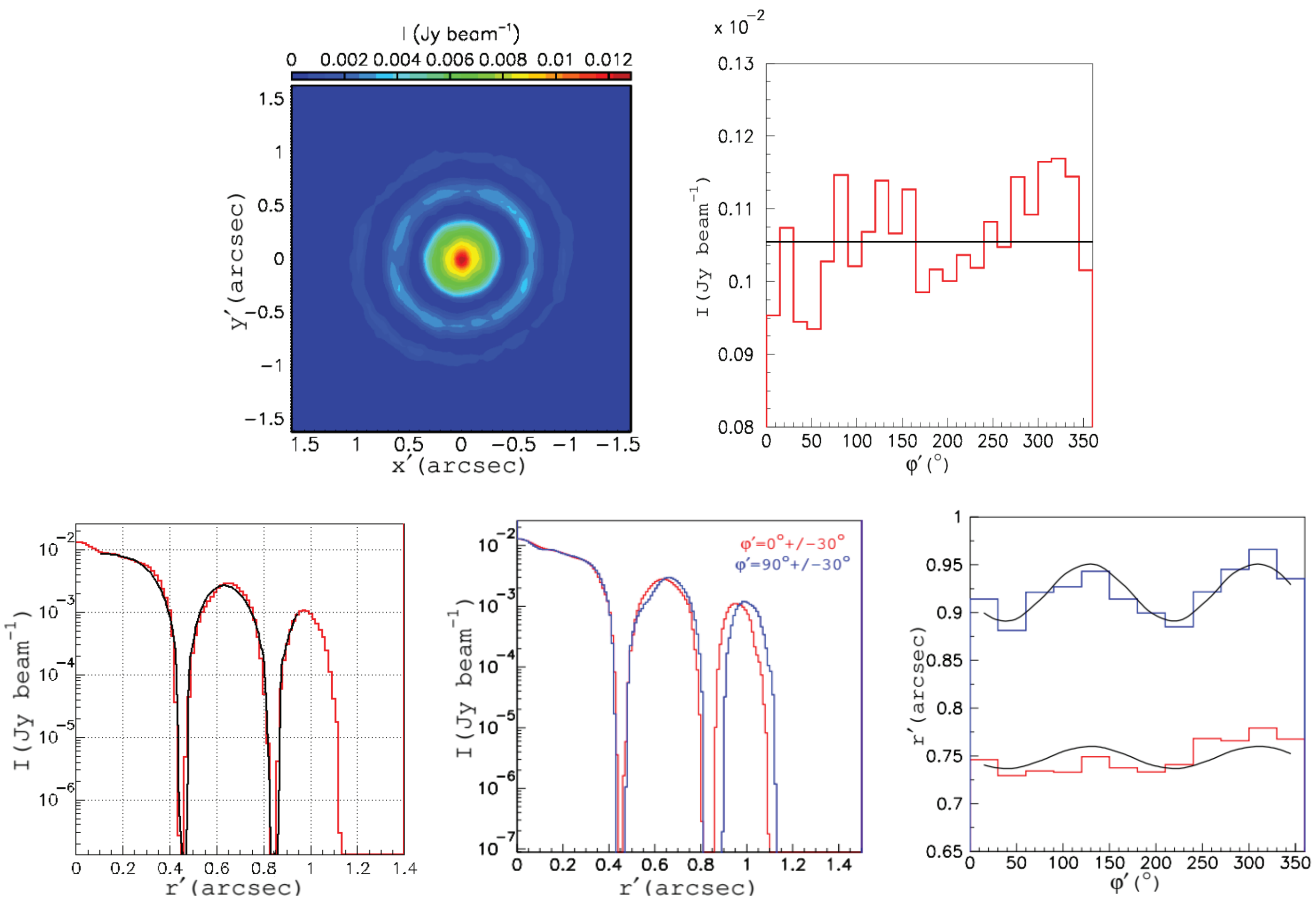

Fig. 3. Top left: intensity map de-projected in the disc plane (x', y'). Top right: dependence on position angle φ' measured in the disc plane of the intensity averaged over r'<1.31 arcsec; note the off-set scale of ordinate. Bottom left: dependence on r' measured in the disc plane of the intensity averaged over φ'; the black curves are Gaussian fits to the gaps. Bottom centre: this is the same as the graph on the lower left for position angles φ' less than 30^0 away from the minor axis (red) and less than 30^0 away from the major axis (blue). Bottom right: dependence on φ' of the radius of the inner (red) and outer (blue) edges of the outer gap; the curves are fits of the form $r' = r'_0 + k\cos 2(\varphi' - \varphi'_0)$.

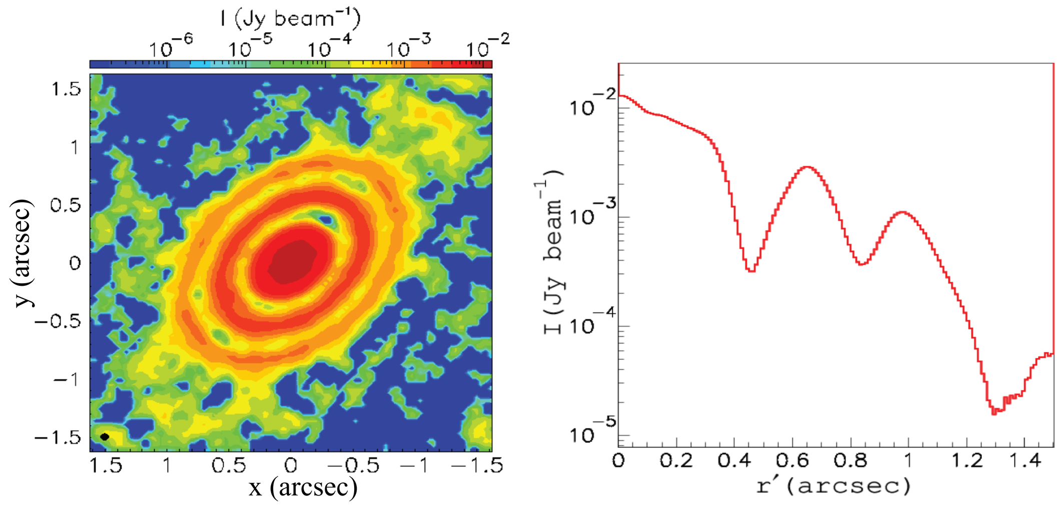

Fig. 4. Continuum intensity without application of the 3-σ cut. Left: map on the sky plane. Right: dependence on r' (averaged on φ').

Table 1. Parameters defining the gap-ring structure of the dust disc.

Distance from central star (arcsec), Gaussian fits to rings and gaps							
Inner ring		*Outer ring*		*Inner gap*		*Outer gap*	
Mean	rms	Mean	rms	Mean	rms	Mean	rms
0.65	0.07	0.98	0.05	0.44	0.11	0.82	0.13
De-projection (see text)							
Disc		*Outer gap (inner edge)*			*Outer gap (outer edge)*		
PA	θ	r'_0	θ		r'_0	θ	
40^0	44^0	0.75	44^0		0.92	46^0	

If the disc was thick, the edges of the gaps would be smeared along the y' axis but not along the x' axis, typically by a quantity at the scale of the disc thickness. Indeed, the standard deviations of the gap Gaussians ~0.12 arcsec are upper limits to such smearing. To check this, we compare in Fig. 3 (bottom centre) the radial distribution of the de-projected intensity in two 60^0 wide wedges bracketing the minor and major axes, defined as $|\sin\varphi'|<1/2$ and $|\cos\varphi'|<1/2$, respectively. The absence of a significant difference for the inner gap shows that the thickness of the dust disc cannot significantly exceed 10 au at r'~80 au. However, the outer gap, while showing no significant φ' dependence of the smearing of its edges, shows a clear dependence on φ' of both gap width and position. This is further illustrated in Fig. 3 (bottom right), which displays the dependence on φ' of the position of the edges of the outer gap; the outer edge displays significant deviation from a circle. A fit to an ellipse of the form $r'=r'_0+k\cos2(\varphi'-\varphi'_0)$ would suggest an inclination angle ($\theta=44^o-k/r'_0$) of 46^0, differing slightly from that of the disc plane. However, it might also be that the assumption that the disc is thin and flat, which was used to evaluate the inclination, does not apply to the outer ring, in which case the deviation from a circle could be associated with a dependence on φ' of the intensity or, more generally, of the morphology of the outer ring. Indeed, the dependence on φ' of the intensity, averaged over $0.44<r'<0.82$ arcsec for the inner ring and over $0.82<r'<1.31$ arcsec for the outer ring, which is illustrated in Fig. 5, shows that while the inner disc displays small fluctuations of only ~3%, the outer ring displays much larger fluctuations of ~31%. Therefore, it is unjustified to interpret the fluctuations of the mean radius of the outer disc as resulting from a different inclination of its plane.

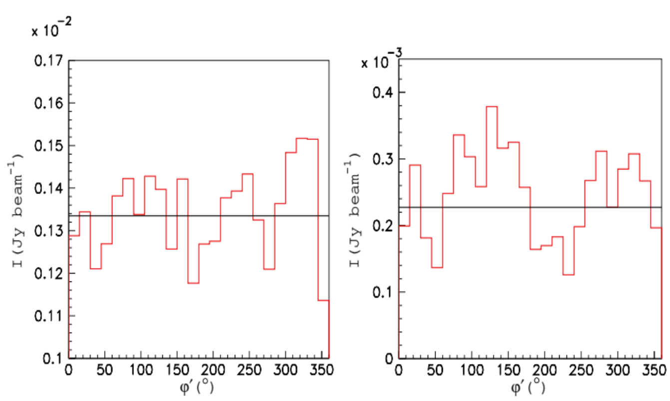

Fig. 5. Dependence on φ' of the average intensity measured in the inner ring (0.44<r'<0.82 arcsec, left panel) and in the outer ring (0.82<r'<1.31 arcsec, right panel). Note the different scales of ordinate.

Line emissions

Observations

To study the gas present in the HD 163296 disc, we use ALMA archival observations made on June 4th, 2014 for project 2013.1.00366.S. Their spatial resolution, ~0.7 arcsec (85 au), is the best currently available, since the data used by Isella, et al. [1], with a spatial resolution of 25 au, are inaccessible to the public. Three line emissions, CO(2-1), $C^{18}O$(2-1), and DCO^+(3-2), were observed in Cycle 2 of ALMA operation with spectral resolution of 0.04 km s^{-1}. The data were reduced by the ALMA staff into datacubes consisting of 300×300 pixels, each measuring 0.1×0.1 $arcsec^2$ with 800 bins of velocity, each 0.04 km s^{-1} wide. Table 2 below lists the main parameters of relevance. The noise distribution is well-behaved in each of the three lines. In what follows, unless otherwise stated, we apply a 3-σ cut to each datacube element, as was done for the study of continuum emission.

Table 2. Information of relevance to the line emissions.

Line	CO(2-1)	$C^{18}O$(2-1)	DCO^+(3-2)
Beam Size ($arcsec^2$)	0.69×0.53	0.70×0.55	0.70×0.57
Beam Position Angle	-80.9^0	-80.3^0	-79.4^0
Noise (σ, mJy $beam^{-1}$)	5.6	3.6	3.0
Right Ascension (J2000)	17h 56m 21.2 s		
Declination (J2000)	-21^0 57' 22"		
Systemic Velocity	5.80 km s^{-1}		
Pixel Size	0.1×0.1 $arcsec^2$		
Velocity Bin Size	0.04 km s^{-1}		

Main features

In what follows, we normally limit the analysis to ellipses where the signal is well above noise. These ellipses have semi-major and minor axes of (a, b)=(4.8, 3.8) arcsec, (3.5, 2.4) arcsec and (3.3, 2.4) arcsec for CO(2-1), $C^{18}O$(2-1), and DCO^+(3-2), respectively, with a common position angle of 135^o. Fig. 6 displays the Doppler velocity spectra of CO(2-1), $C^{18}O$(2-1), and DCO^+(3-2) emissions integrated over these ellipses. They are symmetric about the systemic velocity of 5.80 km s^{-1} taken as origin. We limit the present analysis to Doppler velocities not exceeding 6 km s^{-1} in absolute value.

Figure 7 displays sky maps of the integrated intensity and of the mean value and standard deviation of the Doppler velocity spectra. The mean Doppler velocity is seen to display a characteristic rotation pattern about the disc axis while the rms deviation from the mean is nearly isotropic. As was observed earlier by Isella, et al. [1] the intensity maps show no sign of a ring-gap structure, but their common orientation and aspect ratio are, at least qualitatively, the same as observed in continuum emission. Accordingly, in what follows, we use the same disc plane coordinates (x',y') as we used in the study of continuum emission. However, as the gas disc is expected to be significantly thicker than the dust disc, the thin disc hypothesis is no longer valid and the transformation of coordinates from (x,y) to (x',y') should no longer be strictly identified with de-projection as the disc thickness may cause significant smearing along the y' axis.

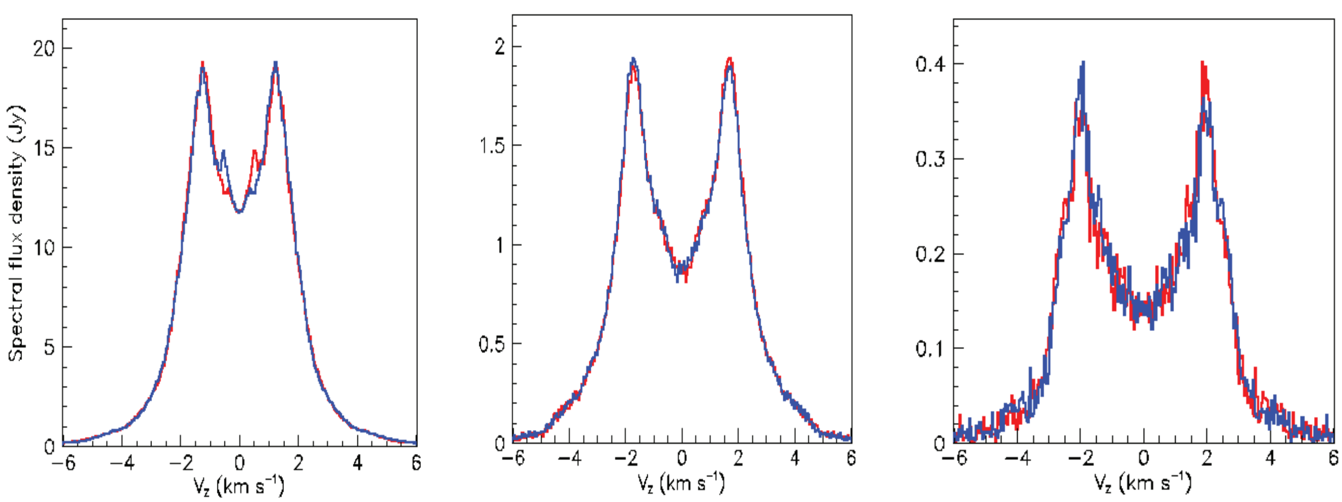

Fig. 6. From left to right: integrated spectra of CO(2-1), $C^{18}O$(2-1), and DCO^+(3-2) emissions integrated over the ellipses shown in Fig. 7. The blue histograms display spectra obtained by mirror symmetry about the origin.

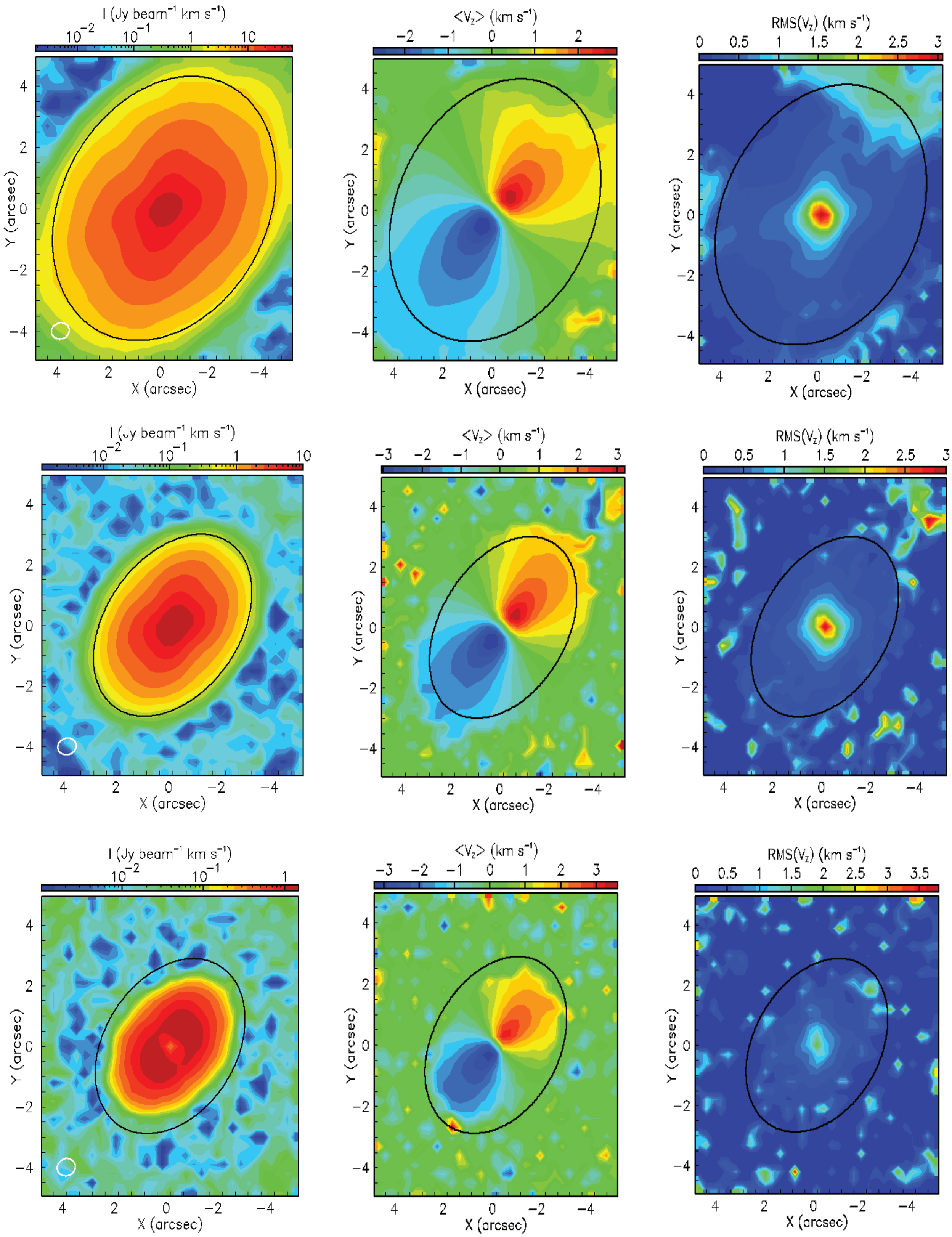

Fig. 7. Sky maps of velocity integrated intensity (left), of $\langle V_z \rangle$ (centre) and of Rms(V_z) (right) for CO(2-1) (top panels), $C^{18}O$(2-1) (centre panels), and DCO^+(3-2) (bottom panels) emissions. Ellipses indicate the regions of the sky plane generally retained in the analysis.

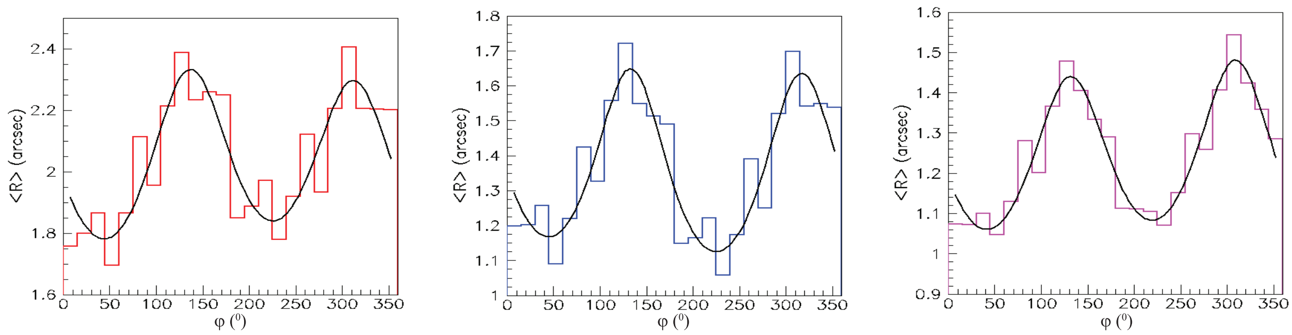

Fig. 8. Dependence on φ of <R> for CO (left), C^{18}O (centre), and DCO^{+} (right). The black curves are fits to ellipses (see text).

Repeating for the C^{18}O and DCO^{+} lines the same geometry analysis that was performed for the continuum, we obtain semi-minor axes of 1.15 and 1.07 arcsec and semi-major axes of 1.64 and 1.46 arcsec, respectively. These correspond to inclinations with respect to the sky plane of 45^0 and 43^0, respectively (see Fig. 8), which is in excellent agreement with the continuum results. Similar but less accurate results are obtained for the optically thick CO(2-1) emission (39^0).

The position angles φ_0 are best measured from the maps of the mean Doppler velocity, which maximise the asymmetry between the blue-shifted and red-shifted components. The position angle obtained this way is 135^0 for each of the three lines, which is close to the continuum value of 130^0.

Gas morphology

Figure 9 shows maps of the de-projected intensity in the central region (both $|x'|$ and $|y'|$ smaller than 2 arcsec) and their projections on the x' and y' axes. The similarity between the x' and y' projections illustrates the validity of describing them in terms of inclined circular discs with nearly identical values of φ_0 and θ. To a good approximation, they are both centred and symmetrical with respect to the origin, and the emission extends up to a distance from the central star of ~5.0 arcsec for CO(2-1), ~3.5 arcsec for C18O(2-1), and ~3.0 arcsec for DCO+(3-2).

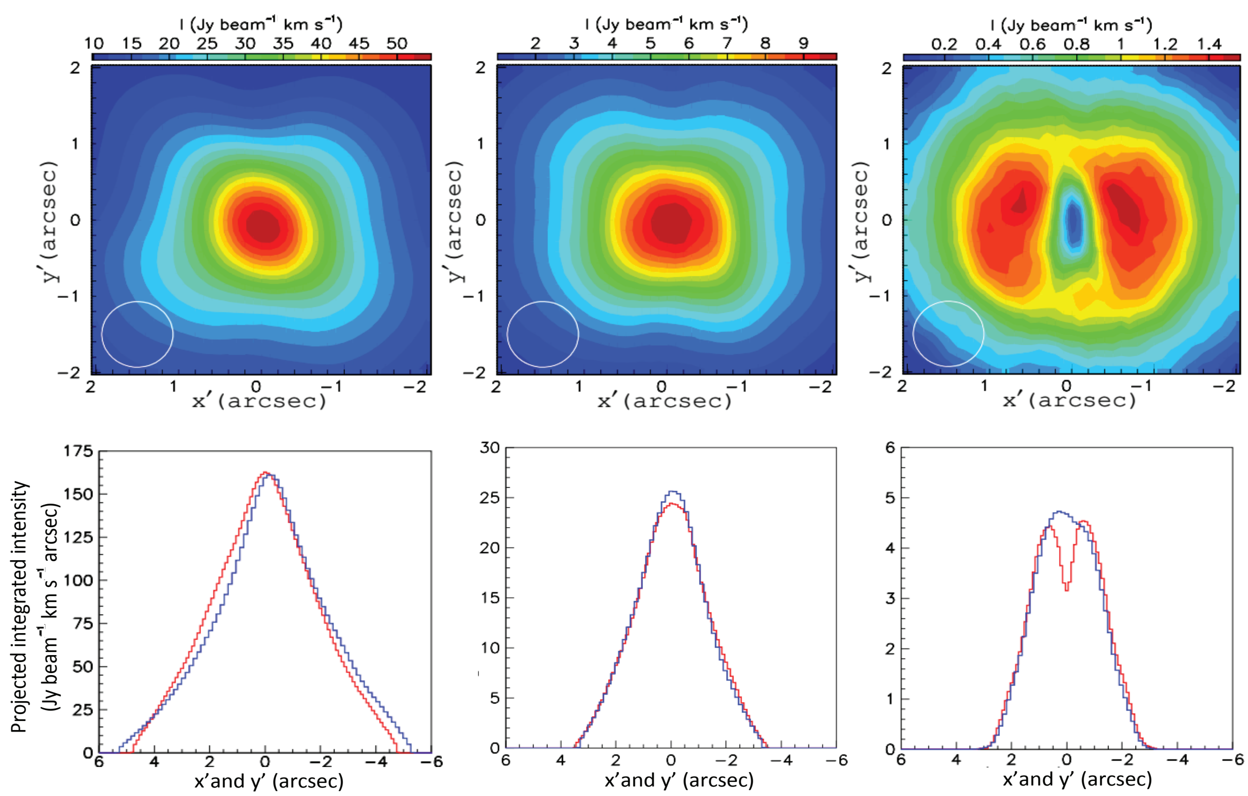

Fig. 9. De-projected intensity of, from left to right: CO(2-1), C^{18}O(2-1), and DCO^{+}(3-2) emissions. The top panels show the maps (y' vs x') and the bottom panels their projections (Jy beam^{-1} km s^{-1}) on the x' (red) and y' (blue) axes.

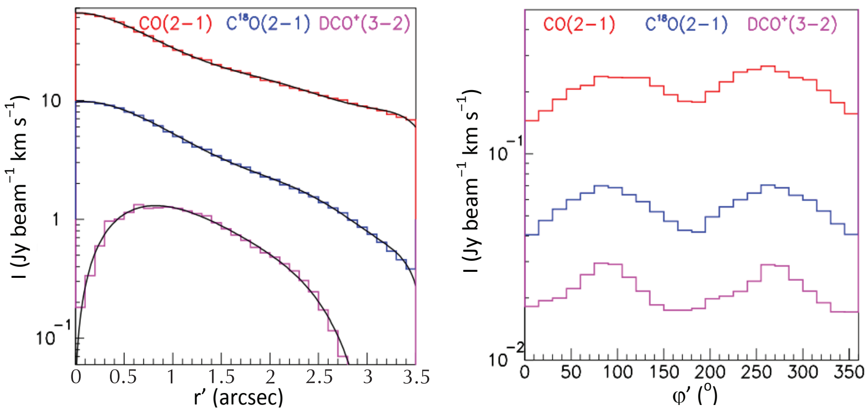

Fig. 10. Dependence of the intensity on *r′* (left) and *φ′* (right, averaged over 0.5<*r′*<2 arcsec). Red is for CO(2-1), blue for C^{18}O(2-1), and magenta for DCO$^+$(3-2).

Figure 10 (left) shows the dependence of intensity on *r'* averaged over *φ*'. It displays decrement factors evaluated in the interval 1<*r'*<2 arcsec of ~1.9 arcsec^{-1} for CO(2-1), ~2.3 arcsec^{-1} for C^{18}O(2-1), and ~2.7 arcsec^{-1} for DCO$^+$(3-2) emissions, the latter dropping to small values near the star. As remarked by Isella, et al. [1], who observed a similar drop and noted that the DCO$^+$(3-2) and continuum intensities are similar at small distances from the star, an excessive continuum subtraction would wrongly cause a significant decrease of the line emission. However, the effect is too important to be an artefact of continuum subtraction. While both continuum subtraction and beam convolution contribute important uncertainties to the detailed morphology of the observed depression, its reality is not in doubt. Fig. 10 (right) displays the dependence on *φ'* of the intensity averaged over 0.5<*r'*<2.0 arcsec, which corresponds to the dust rings. Significant modulations are observed and are similar for the three lines, which is reminiscent of what was observed for the outer dust ring (Fig. 5 right). We emphasise that these modulations are unrelated to the disc inclination (we are dealing here with average intensity and not with average radius) but rather are associated with real intensity modulations in the disc plane.

The maps of the mean Doppler velocity in the disc plane are shown in Fig. 11. In contrast to the intensity, the Doppler velocity shows remarkably similar behaviour for each of the three lines (see next section).

Finally, to reveal the finer structure of the gas morphology, Fig. 12 shows the difference between the measured intensity and its mean value at the corresponding disc radius averaged over position angle. Fluctuations are observed at the ~10% level. As CO(2-1) emission is optically thick and the two other lines optically thin, these fluctuations probe the disc at different depths and indeed display different structures: a north-south bipolar asymmetry for CO emission corresponding to the disc surface and a north-south/east-west quadripolar asymmetry for C^{18}O(2-1) and DCO$^+$(3-2) probing the whole disc thickness.

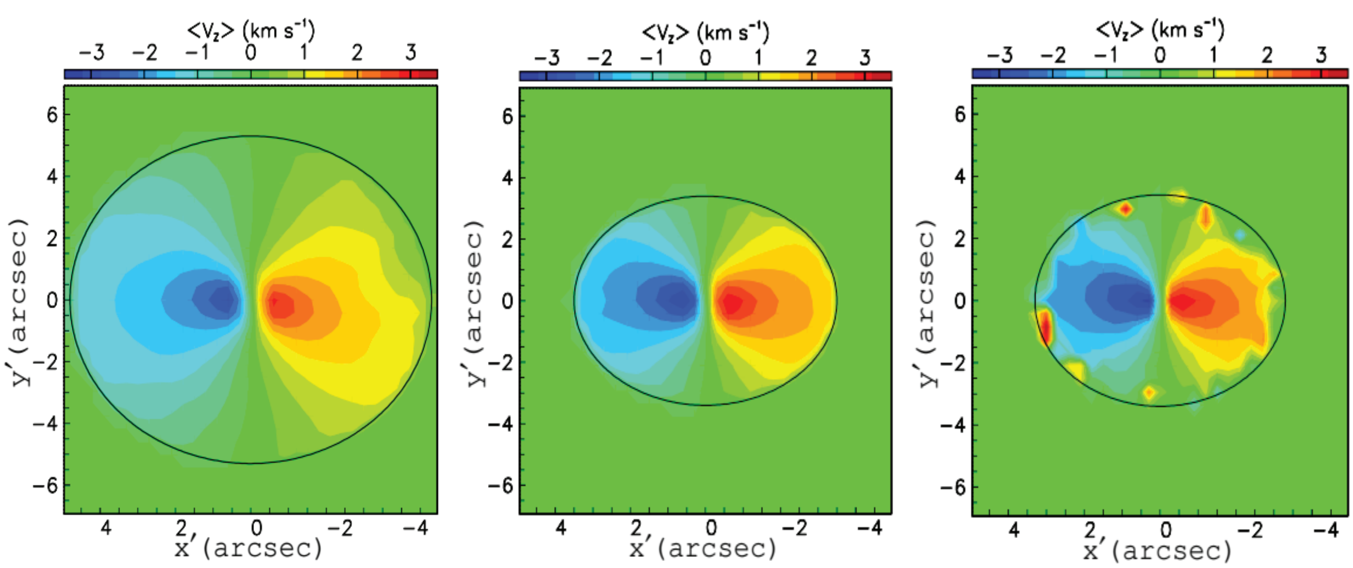

Fig. 11. Disc plane maps of <V_z> for CO(2-1) (left), C^{18}O(2-1) (centre), and DCO$^+$(3-2) (right). Ellipses surround the regions where data are retained for the analysis.

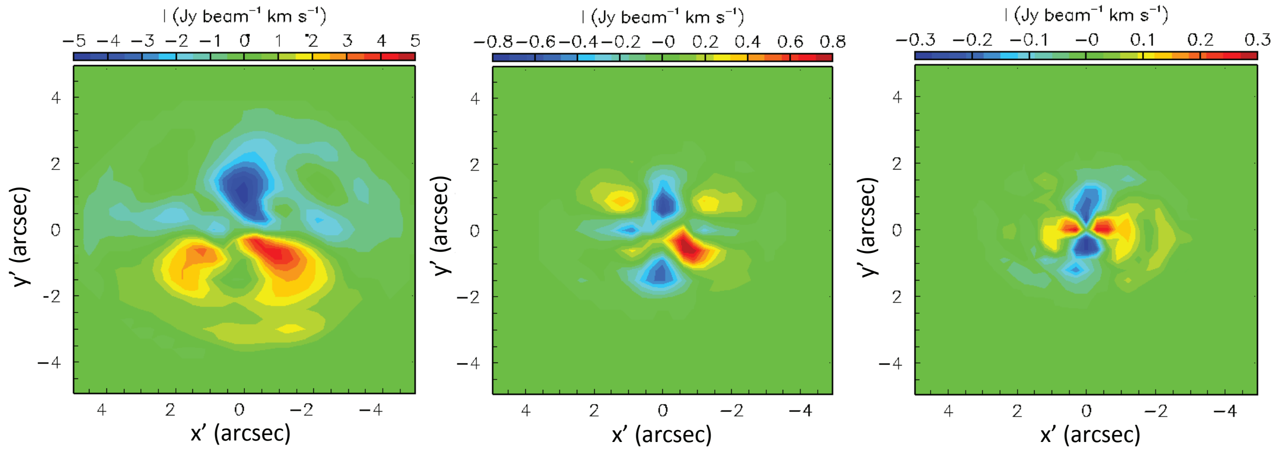

Fig. 12. Intensity maps in the disc plane showing the difference between the measured intensity and its average at the same radius for each of CO(2-1) (left), C^{18}O(2-1) (centre), and DCO$^+$(3-2) (right).

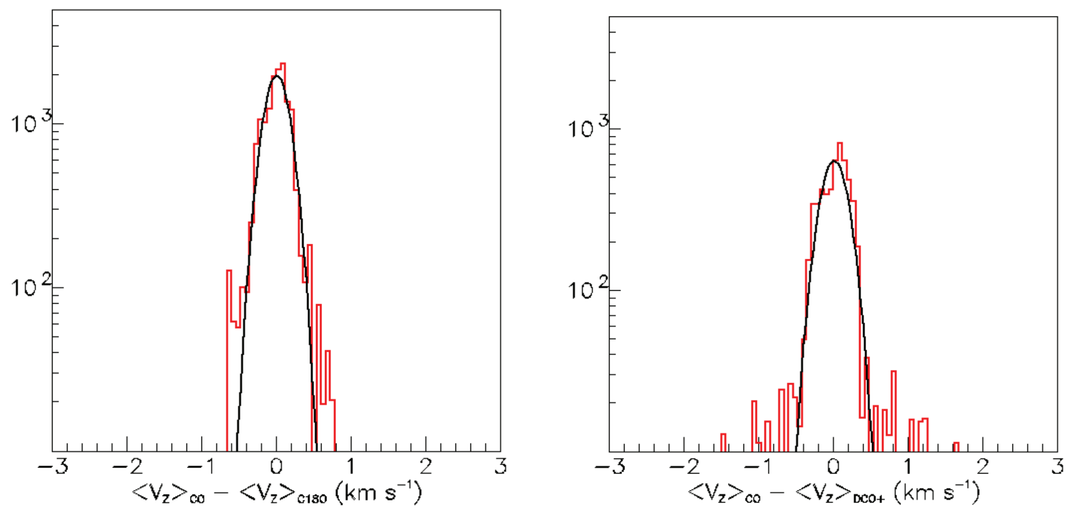

Fig. 13. Distribution of the differences $<V_z>_{CO}$ -$<V_z>_{C18O}$ (left) and $<V_z>_{CO}$-$<V_z>_{DCO+}$ (right) measured in the same pixel. Each pixel contribution is weighted by the geometrical mean $(I_1I_2)^{1/2}$ of the velocity integrated intensities I_1 and I_2 measured in the pixel for each of the two lines. The black curves show Gaussian fits to the peaks with σ's of 0.16 and 0.18 km s^{-1} and mean values of 0.004 and 0.010 km s^{-1}, respectively.

Gas kinematics

As remarked in the preceding section, the three line emissions display nearly identical kinematics. This is illustrated in Fig. 13, which displays the distributions of the difference between the mean Doppler velocity measured in a given pixel for CO(2-1) and that measured in the same pixel for C^{18}O(2-1) (left) and DCO$^+$(3-2) (right). The mean values are 0.01 and 0.03 km s^{-1} and the standard deviations 0.30 and 0.37 km s^{-1}, respectively.

In each datacube element, the Doppler velocity can be expressed as a function of rotation velocity, V_{rot}, and in-fall velocity, V_{fall}, as follows (Fig. 14):

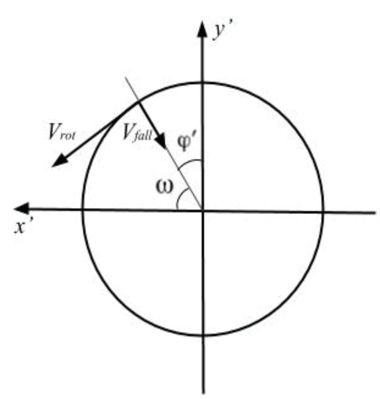

Fig. 14. Velocity and trajectory of gas molecules in the disc plane.

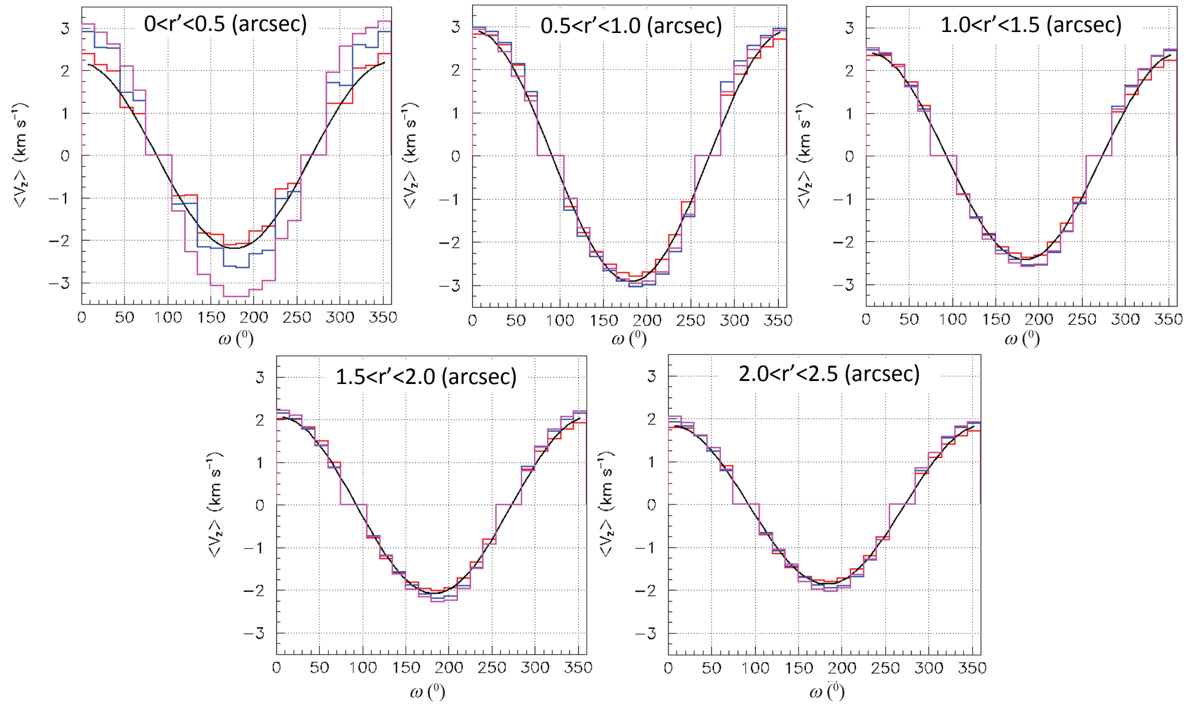

Fig. 15. Dependence on ω=90⁰-φ' of $<V_z>$ for five intervals of r' (see Table 3). The black curves are fits of the form $V_0 sin\theta sin(\varphi'-\varphi'_0)$ to the CO(2-1) distributions. Red is for CO(2-1), blue for $C^{18}O$(2-1), and magenta for DCO^+(3-2).

$$V_z = sin\theta(V_{rot} sin\varphi' - V_{fall} cos\varphi') = V_0 sin\theta sin(\varphi' - \varphi'_0)$$

with $V_{rot}=V_0 cos\varphi'_0$ and $V_{fall}=V_0 sin\varphi'_0$

namely $V_0=(V_{rot}^2+V_{fall}^2)^{½}$ and $\varphi'_0=tan^{-1}(V_{fall}/V_{rot})$.

Figure 15 shows the dependence of $<V_z>$ on φ' averaged over five different intervals of r' for each of the three lines separately. A fit of the form $<V_z>=V_0 sin\theta sin(\varphi'-\varphi'_0)$ is made to the CO(2-1) data in each interval of r' separately. The small values obtained for φ'_0 show the dominance of rotation over in-fall. We estimate that the measured distributions can accommodate a maximal phase shift of ~5° with respect to pure rotation, implying an upper limit of ~9% on the ratio between in-fall and rotation velocities. The results are summarised in Table 3.

Table 3. Parameters describing the gas kinematics.

	CO(2-1)				
r' interval	<0.5"	0.5"-1.0"	1.0"-1.5"	1.5"-2"	>2.0"
V_0(km s^{-1})	3.2	4.3	3.6	3.0	0.9
φ'_0	1.3⁰	-0.5⁰	-2.4⁰	-2.5⁰	-2.9⁰
	CO(2-1)	**$C^{18}O$(2-1)**		**DCO^+(3-2)**	
r' interval	0.8"-3.5"	0.8"-3.5"		0.8"-3.0"	
V^*_0	4.1	4.4		4.2	
n	0.46	0.49		0.40	

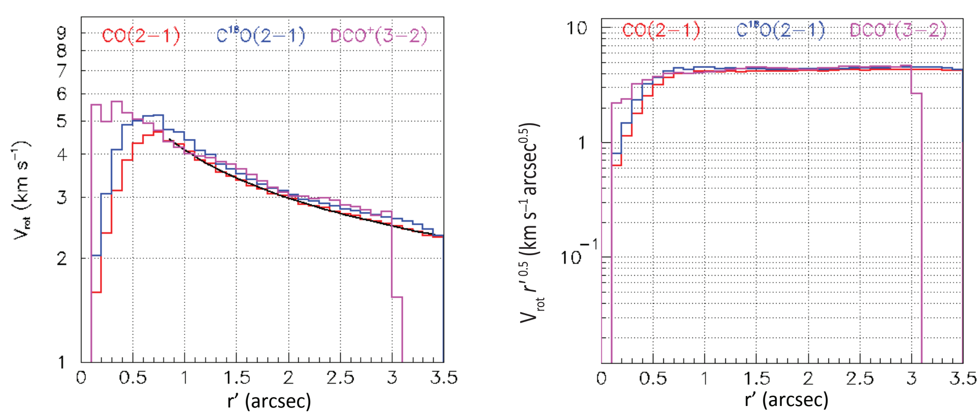

Fig. 16. Dependence on r' of V_{rot} (left) and of $V_{rot}r'^{0.5}$ (right). Red is for CO(2-1), blue for $C^{18}O$(2-1), and magenta for DCO^+(3-2).

Within the limits of a thin and flat disc and neglecting a possible in-fall velocity, the rotation velocity can be calculated for each data-cube element as $V_{rot}=V_z(\sin\theta\sin\varphi')^{-1}$ as long as $\sin\varphi'$ is not too small (in practice we require $|\sin\varphi'|>\sin15^o$). Fig. 16 (left) shows the dependence on r' of V_{rot} calculated in this manner. Fits of the form $V_{rot}=V^*_0 r'^{-n}$ yield the results listed in Table 3, providing evidence for approximate Keplerian motion. Clearer evidence is displayed in Fig. 16 (right) showing the dependence on r' of the Kepler factor $V_{rot}r'^{0.5}$, which is constant for Keplerian rotation. It is indeed observed to be constant down to r'~0.8 arcsec with a value of ~4 km s^{-1} arcsec^{½}, in good agreement with the expectation of 3.9 km s^{-1} arcsec^{½} corresponding to a central mass of 2.3 solar masses.

Line widths

Figure 17 (left) shows the distributions of the difference between the Doppler velocity and its mean calculated in the same pixel, $\Delta V_z=V_Z-<V_Z>$, for each line separately (we recall that we require $|V_Z|$ not to exceed 6 km s^{-1}). Gaussian fits to the central peaks (black curves) give standard deviations of 0.39, 0.32, and 0.31 km s^{-1} for CO(2-1), C^{18}O(2-1), and DCO$^+$(3-2), respectively. The dependence on r' and φ' of $Rms(V_z)$ (averaged over φ' and r', respectively) is shown in Figs. 17 (right) and 18, the latter separately in the five intervals of r'. They display similar shapes for each of the three lines but different amplitudes, significantly larger for CO than for the two other emissions. Apart from beam convolution effects, the velocity dispersion is a combination of 1) instrumental resolution; 2) the range of velocities covered in each pixel because of disc thickness, disc inclination and Keplerian shear; 3) thermal broadening, having a standard deviation $\sigma_v=(2kT/\mu)^{½}$ where k is Boltzmann constant, T the gas temperature and $\mu=28m_H$, $30m_H$, and $30m_H$ for CO, C^{18}O, and DCO$^+$, respectively; and 4) turbulence. All of these are expected to be significantly smaller than measured, never exceeding 0.1 km s^{-1} for $r'>1$ arcsec. However, beam convolution, with FWHM values nearing 0.7 arcsec, seven times larger than the pixel size, is expected to dominate the line width. To evaluate its effect, we assume that the disc is thin and flat, that the orbits are circular, and that other contributions to the line width can be neglected. Moreover, we assume pure Keplerian motion with $V_{rot}r'^{½}$=3.9 km s^{-1} arcsec^{½}, we use the r' dependence of the intensity displayed in Fig. 10 (left), and we neglect its dependence on φ'. A same 3-σ cut is applied to the model as to the data.

The results are compared with observations in Figs. 19, 20, and 21. The agreement is excellent considering the simplicity of the model. The apparent departure from Keplerian motion observed at distances from the star smaller than 0.8 arcsec is found to be largely due to beam convolution. The line width is reasonably well-reproduced by the model down to r'~0.5 arcsec, where temperature and turbulence effects are likely to be more important. Above this distance, effects other than beam convolution do not significantly contribute to the line width.

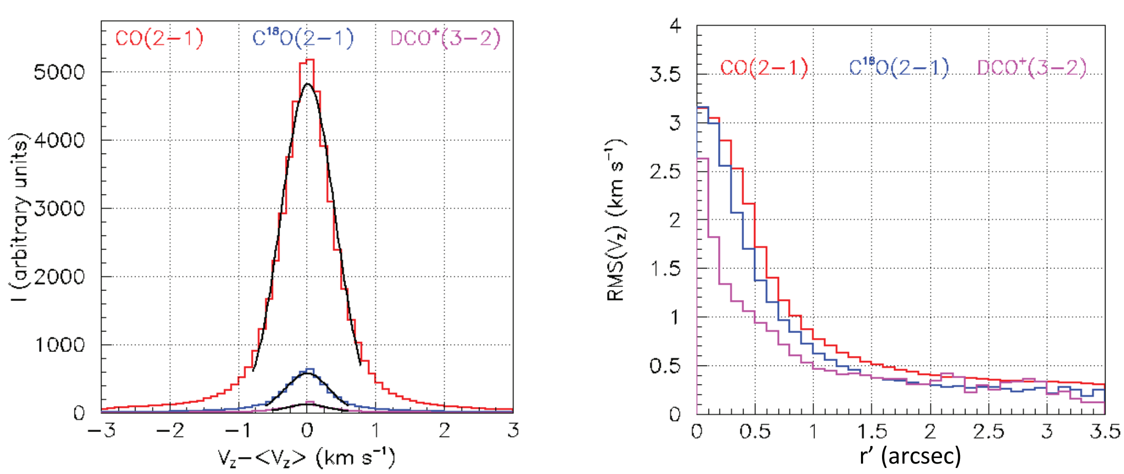

Fig. 17. Left: distribution of V_Z-<V_Z> in each pixel and for each line separately. Right: dependence on r' of Rms(V_Z). Red is for CO(2-1), blue for C^{18}O(2-1), and magenta for DCO$^+$(3-2).

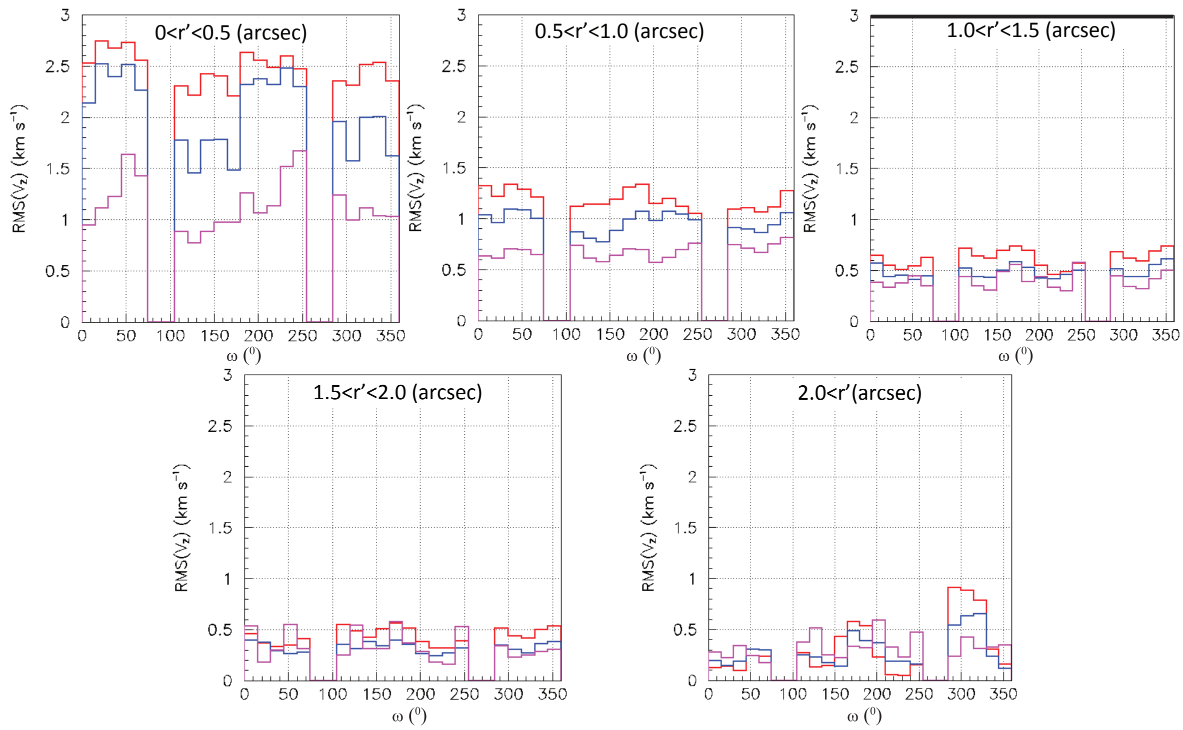

Fig. 18. Dependence on ω=90°-φ' of Rms(V_z). Red is for CO(2-1), blue for $C^{18}O$(2-1), and magenta for DCO^+(3-2).

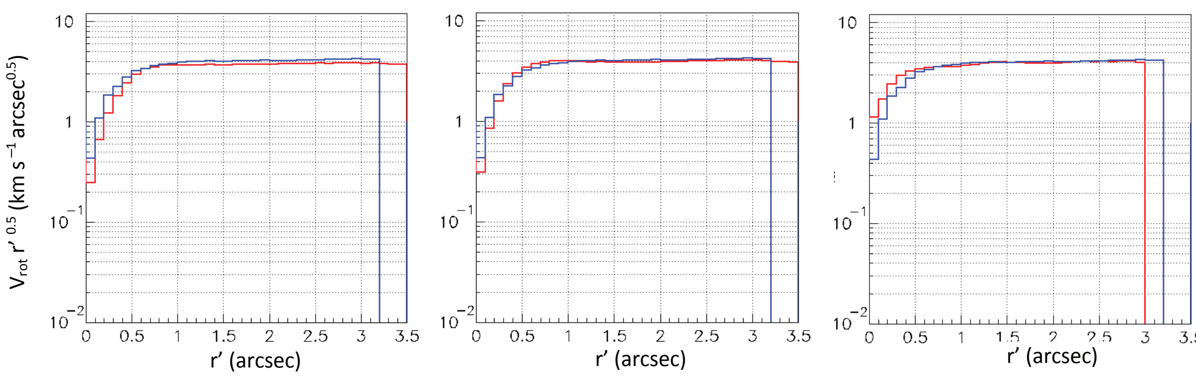

Fig. 19. From left to right: radial dependence of the Kepler factor $V_{rot}r'^{0.5}$ as observed (red) and predicted by the model (blue) for CO(2-1), $C^{18}O$(2-1), and DCO^+(3-2), respectively.

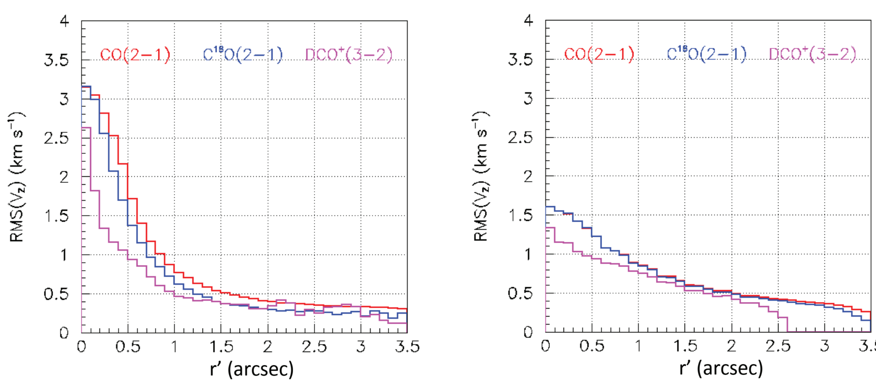

Fig. 20. Radial dependence of Rms(V_z) as observed (left) and predicted by the model (right). Red is for CO(2-1), blue for $C^{18}O$(2-1), and magenta for DCO^+(3-2).

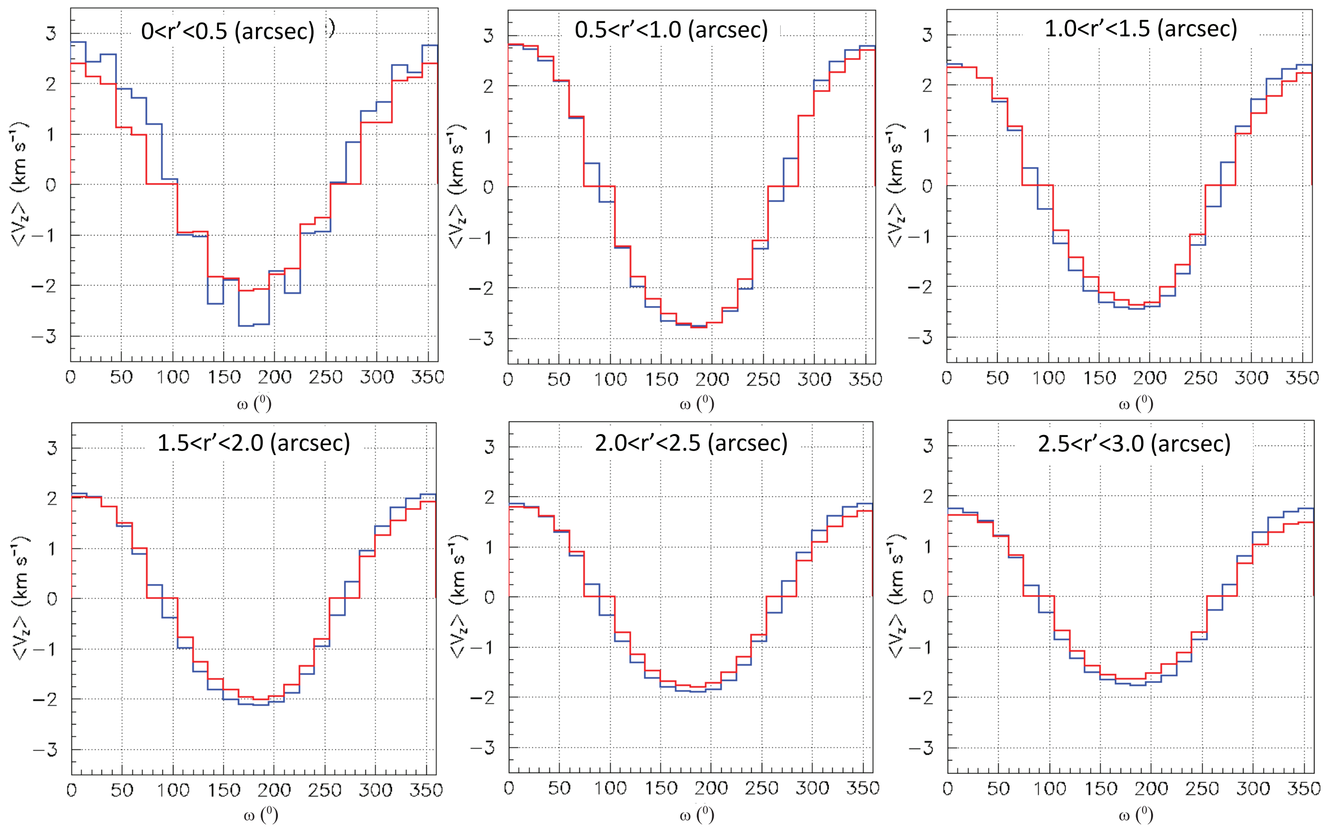

Fig. 21. Dependence of <V_z> (km s^{-1}) on ω=90º-φ' for six intervals of r', 0.5 arcsec wide and covering between 0 and 3 arcsec. Red is for the observations and blue for the model.

Summary and conclusions

Using ALMA observations of the continuum emission at 0.9 mm wavelength and of molecular line emissions from CO(2-1), C^{18}O(2-1), and DCO$^+$(3-2), the morphology of the dust and gas disc of HD 163296 has been explored; the position and inclination with respect to the sky plane have been accurately measured and found to be identical for gas and dust. The ring-gap structure of the dust disc has been described with better precision than previously achieved [1], and no evidence has been found for a third gap at a distance of ~1.31 arcsec from the star, as claimed by Isella, et al. [1]. The outer gap and ring have been shown to display a significant modulation of their morphology and intensity. The disc thickness at ~80 au has been shown to be smaller than 10 au.

Small intensity fluctuations in the three line emissions CO(2-1), C^{18}O(2-1), and DCO$^+$(3-2) have been revealed and precisely located and measured; they explore different regions across the disc thickness and display clearly different structures. In the region of the dust rings in particular, modulations of the intensity reminiscent of those displayed by the outer dust disc have been observed.

The three line emissions display remarkably similar kinematics dominated by Keplerian rotation. An upper limit of 9% of the rotation velocity has been placed on a possible in-fall velocity. A Keplerian factor of 4.0 km s^{-1} arcsec^{½} has been measured, consistent with the expectation of 3.9 km s^{-1} arcsec^{½} corresponding to a central mass of 2.3 solar masses. Apparent departure from Keplerian motion at distances from the star smaller than ~0.8 arcsec has been shown to be essentially due to beam size (~0.7 arcsec FWHM). The observed line widths have been shown to be dominated by beam size effects over most of the radial range. A simple model accounting for the effect of beam convolution has been shown to very well reproduce the observations.

Recently, several new protoplanetary discs displaying a ring-gap structure have been discovered and imaged with high resolution by ALMA (for a review, see Reference [11]). The complexity of their morphology, which includes spirals and clumps in addition to rings, has come as a surprise. This has triggered a surge of studies aimed at interpreting the gap-forming mechanism, usually in terms of planet formation (see for example Reference [12]). The present work has shown that the case of HD 163296 is particularly well-suited to give important contributions to this domain of stellar physics. The present data, which give evidence for strong radial depletion of the dust disc with no significant counterpart observed in the gas disc, do not strongly support the presence of planets in formation. However, higher resolution observations of the molecular line emissions should shed better light on this issue.

ACKNOWLEDGEMENTS

We thank Nguyen Xuan Que for contributing to this work in its earlier phase and Prof. P. Darriulat for guidance and advice. This paper makes use of data from the ALMA projects ADS/JAO.ALMA#2013.1.00601.S and ADS/JAO.ALMA#2013.1.00366.S. ALMA is a partnership of ESO (representing its member states), NSF (USA), and NINS (Japan), together with NRC (Canada), NSC, ASIAA (Taiwan), and KASI (Republic of Korea), in cooperation with the Republic of Chile. The ALMA Observatory is operated by ESO, AUI/NRAO, and NAOJ. We thank the ALMA staff for the reduction of the data and for their help with understanding the origin of a spurious emission in the CO(2-1) data at Doppler velocities well above the line emission. This research has made use of the SIMBAD database, operated at CDS, Strasbourg, France, and of the NASA ADS Abstract Services. The study is funded by the Vietnam National Foundation for Science and Technology Development (NAFOSTED) (No. 103.99-2016.50). We acknowledge support from the World Laboratory, Rencontres du Viet Nam, the Odon Vallet fellowships, the Vietnam National Space Center, the Graduate University of Science and Technology, and the Vietnam Academy of Science and Technology.

The authors declare that there is no conflict of interest regarding the publication of this article.

REFERENCES

[1] A. Isella, et al. (2016), "Ringed structures of the HD 163296 protoplanetary disk revealed by ALMA", *Phys. Rev. Lett.*, **117**, 251101, Doi: 10.1103/PhysRevLett.117.251101.

[2] S.M. Andrews, D.J. Wilner, Z. Zhu, et al. (2016), "Ringed substructure and a gap at 1 au in the nearest protoplanetary disk", *Astrophys. J. Lett.*, **820**, L40, Doi:10.3847/2041-8205/820/2/L40.

[3] ALMA Partnership, C.L. Brogan, et al. (2015), "The 2014 ALMA Long Baseline Campaign: First Results from High Angular Resolution Observations toward the HL Tau Region", *Astrophys. J. Lett.*, **808**, L3, Doi: 10.1088/2041-8205/808/1/L3.

[4] G. Bryden, X. Chen, D.N.C. Lin, et al. (1999), "Tidally induced gap formation in protostellar disks: gap clearing and suppression of protoplanetary growth", *Astrophys. J.*, **514**, pp.344-367.

[5] P. Barge and J. Sommeria (1995), "Did planet formation begin inside persistent gaseous vortices?", *Astron. Astrophys.*, **295**, L1, arXiv:astro-ph/9501050.

[6] K. Zhang, G.A. Blake, and E.A. Bergin (2015), "Evidence of fast pebble growth near condensation fronts in the HL Tau protoplanetary disk", *Astrophys. J. Lett.*, **806**, L7, Doi:10.1088/2041-8205/806/1/L7.

[7] S. Okuzumi, M. Momose, S. Sirono, H. Kobayashi, et al. (2016), "Sintering-induced dust ring formation in protoplanetary disks: application to the HL Tau disk", *Astrophys. J.*, **821**, Doi:10.3847/0004-637X/821/2/82.

[8] M.E. van den Ancker, P.S. The, H.R.E. Tjin A. Djie, et al. (1997), "Hipparcos data on Herbig Ae/Be stars: an evolutionary scenario", *Astron. Astrophys.*, **324**, pp.L33-L36.

[9] A. Isella, L. Testi, A. Natta, et al. (2007), "Millimeter imaging of HD 163296: probing the disk structure and kinematics", *Astron. Astrophys.*, **469**, pp.213-222.

[10] I. de Gregorio-Monsalvo, et al. (2013), "Unveiling the gas and dust disk structure in HD 163296 using ALMA observations", *Astron. Astrophys.*, **557**, A133, Doi: 0.1051/0004-6361/201321603.

[11] S.M. Andrews, J. Huang, L.M. Pérez, A. Isella, et al. (2018), "ALMA observations of the epoch of planet formation", *The Messenger*, **174**, pp.19-23 and "The disk substructures at high angular resolution project (DSHARP). I. Motivation, sample, calibration, and overview", *The Astrophysical Journal Letters*, **869(2)**, L41.

[12] R. Dong, S. Li, E. Chiang, and H. Li (2017), *The Astrophysical Journal*, **843(2)**, 127D.

On the melting of interstitial alloys FeH, FeSi and FeC with a body-centred cubic structure under pressure

Nguyen Quang Hoc[1], Nguyen Thi Hoa[2], Tran Dinh Cuong[1*], Dang Quoc Thang[1]

[1]Hanoi National University of Education, Vietnam
[2]University of Transport and Communications, Hanoi, Vietnam

Received 18 October 2018; accepted 21 December 2018

Abstract:

Taking the model of interstitial alloy *AB* with a body-centred cubic structure and the condition of absolute stability for the crystalline state, we derive analytic expression for the temperature of the limit of absolute stability for the crystalline state, the melting temperature, and the equation for the melting curve of this alloy using the statistical moment method. The results allow us to determine the melting temperature of alloy *AB* under pressure as well as at zero pressure. In limit cases, we obtain the melting theory of main metal *A* with a body-centred cubic structure. The theoretical results are numerically applied for alloys FeH, FeSi and FeC using different potentials.

Keywords: **absolute stability of the crystalline state, interstitial alloy, statistical moment method.**

Classification number: **2.1**

Introduction

Alloys in general, and interstitial alloys in particular, are widely used in material technology and science. Therefore, they are of particular interest to many researchers.

The melting temperature (MT) of materials under pressure is a crucial problem in solid state physics and material science [1, 2]. The MT of crystal is usually is the Simon experimental equation:

$$\frac{P_m - P_0}{a} = (T_m - T_0)^c - 1 \tag{1.1}$$

where T_m is the MT, P_m is the melting pressure, a and c are constants, P_0 and T_0 are the pressure and the temperature, respectively, of the triple point on the phase diagram.

Normally, when the value of P_0 is small, we can write equation (1.1) in the form:

$$\frac{P_m}{a} = (T_m - T_0)^c - 1 \tag{1.2}$$

However, equation (1.2) cannot describe the melting of crystal at high pressures. Kumari, et al. [3] have introduced the following phenomenological equation:

$$\frac{\Delta T_m}{\left[T_0(P_m - P_0)\right]} = A + B\left(P_m - P_0\right) \tag{1.3}$$

where T_m and T_0 are the MT at pressures P_m and P_0, respectively, $\Delta T_m = T_m - T_0$, and A and B are constants. Equation (1.3) allows us to determine the MT of crystal at high pressures.

Theoretically, it is necessary to use the solid-liquid equilibrium to determine the MT of crystal. However, this does not allow us to explicitly express the MT. According to some researchers, the temperature corresponding to the absolute stability limit for crystalline state at a certain pressure (T_s) is close to the MT at the same pressure. Therefore, according to the authors of [4], the melting curve of crystal coincides with the curve representing the absolute stability limit for the crystalline state. Accordingly, the self-consistent phonon-field method and the one-particle distribution function are used to investigate the MT. However, the results are not consistent with experiments. This has led some scientists to conclude that the MT can

*Corresponding author: Email: trcuong1997@gmail.com.

never be found using the stability limit for the solid phase. Other researchers have used the correlation effect to calculate the temperature of the absolute stability limit for the crystalline state. Although the results of this are more exact, they are limited at low pressures.

In support of the statistical moment method (SMM), N. Tang and V.V. Hung [4, 5] show that we can, in fact, determine the MT using the solid phase of crystal. First, they determine the absolute stability temperature (T_s) at different pressures using the SMM and then carry out the regulation in order to find T_m from T_s. The results of the SMM correspond better with experiments than those of other methods.

The research content

Analytical results

In the model of the interstitial alloy *AB*, which has a body-centred cubic (BCC) structure, the large atoms *A* are in the peaks and the centre of the cube, and the smaller interstitial atoms *B* are in the centres of the cube faces. In [6-11], we derived the analytic expressions for the nearest neighbour distance, the cohesive energy and the alloy parameters for atoms *B, A,* and A_1 (the main atom *A* which is closest to atom *B*) and A_2 (the main atom *A* which is second closest to atom *B*).

The equations representing the state of the BCC interstitial alloy *AB* at temperature *T* and at zero temperature, respectively, are as follows:

$$Pv = -a_X\left[\frac{1}{6}\frac{\partial u_{0X}}{\partial a_X} + \theta xcthx\frac{1}{2k_X}\frac{\partial k_X}{\partial a_X}\right] \quad (2.1)$$

$$Pv = -a_X\left[\frac{1}{6}\frac{\partial u_{0X}}{\partial a_X} + \frac{\hbar\omega_0}{4k_X}\frac{\partial k_X}{\partial a_X}\right] \quad (2.2)$$

From equation (2.2), we can calculate the nearest neighbour distance a_x $(P, 0)$ $(X = B, A, A_1, A_2)$ and then the parameters k_x $(P, 0)$, γ_{1x} $(P, 0)$, γ_{2x} $(P, 0)$, and γ_x $(P, 0)$. The displacement of atoms from the equilibrium position is determined as in [6, 7]. From that, we can calculate the nearest neighbour distance a_x (P, T) as follows:

$$a_B(P,T) = a_B(P,0) + y_{A_1}(P,T),\ a_A(P,T) = a_A(P,0) + y_A(P,T) \quad (2.3)$$
$$a_{A_1}(P,T) \approx a_B(P,T),\ a_{A_2}(P,T) = a_{A_2}(P,0) + y_B(P,T)$$

The approximate mean nearest neighbour distance between two atoms in the interstitial alloy *AB* is determined by:

$$a_{AB}(P,T) = a_{AB}(P,0) + y_{AB}(P,T)$$
$$a_{AB}(P,0) = (1-c_B)a_A(P,0) + c_B a'_A(P,0),\ a'_A(P,0) = \sqrt{3}a_B(P,0)$$
$$y_{AB}(P,T) = (1-7c_B)y_A(P,T) + c_B y_B(P,T) + 2c_B y_{A_1}(P,T) + 4c_B y_{A_2}(P,T) \quad (2.4)$$

The free energy of interstitial alloy *AB* with concentration condition $c_B << c_A$ has the form [6-11]:

$$\psi_{AB} = (1-7c_B)\psi_A + c_B\psi_B + 2c_B\psi_{A_1} + 4c_B\psi_{A_2} - TS_c$$
$$\psi_X \approx U_{0X} + \psi_{0X} + 3N\left\{\frac{\theta^2}{k_X^2}\left[\gamma_{2X}X_X^2 - \frac{2\gamma_{1X}}{3}\left(1+\frac{X_X}{2}\right)\right] + \right.$$
$$\left.\frac{2\theta^3}{k_X^4}\left[\frac{4}{3}\gamma_{2X}^2 X_X\left(1+\frac{X_X}{2}\right) - 2\left(\gamma_{1X}^2 + 2\gamma_{1X}\gamma_{2X}\right)\left(1+\frac{X_X}{2}\right)(1+X_X)\right]\right\}$$

$$U_{0X} = \frac{N}{2}u_{0X},\ \psi_{0X} = 3N\theta\left[x_X + \ln(1-e^{-2x_X})\right],\ X_X \equiv x_X\coth x_X \quad (2.5)$$

where ψ_A is the free ener.gy of atom *A* in the pure metal *A*, ψ_B is the free energy of atom *B* in the interstitial alloy *AB*, ψ_{A_1} and ψ_{A_2} are the free energy values of atoms A_1 and A_2, respectively, and S_c is the configuration entropy of the interstitial alloy *AB*.

The pressure is calculated as follows:

$$P = -\left(\frac{\partial\psi_{AB}}{\partial V_{AB}}\right)_T = -\frac{a_{AB}}{3V_{AB}}\left(\frac{\partial\psi}{\partial a_{AB}}\right)_T \quad (2.6)$$

Setting

$$\gamma_G^T = -\frac{a_{AB}}{6}\left[\frac{1}{k_A}\frac{\partial k_A}{\partial a_A}(1-7c_B)x_A\coth x_A + \frac{1}{k_B}\frac{\partial k_B}{\partial a_B}c_B x_B\coth x_B + \right.$$
$$\left.\frac{1}{k_{A_1}}\frac{\partial k_{A_1}}{\partial a_{A_1}}2c_B x_{A_1}\coth x_{A_1} + \frac{1}{k_{A_2}}\frac{\partial k_{A_2}}{\partial a_{A_2}}4c_B x_{A_2}\coth x_{A_2}\right] \quad (2.7)$$

where, γ_G^T is the Grüneisen parameter of alloy *AB*. Then,

$$P = -\frac{a_{AB}}{6V_{AB}}\left[(1-7c_B)\frac{\partial U_{0A}}{\partial a_A} + c_B\frac{\partial U_{0B}}{\partial a_B} + 2c_B\frac{\partial U_{0A_1}}{\partial a_{A_1}} + 4c_B\frac{\partial U_{0A_2}}{\partial a_{A_2}}\right] + \frac{3\gamma_G^T\theta}{V_{AB}} \quad (2.8)$$

From the condition of absolute stability limit

$$\left(\frac{\partial P}{\partial V_{AB}}\right)_T = 0 \ \text{ or } \ \left(\frac{\partial}{\partial \ _{AB}}\right) \quad (2.9)$$

we can derive the absolute stability temperature for the crystalline state in the form:

$$T_s = \frac{TS_1}{MS_1},\ TS_1 = 2PV_{AB} + \frac{a_{AB}^2}{6}\left[(1-7c_B)\frac{\partial^2 U_{0A}}{\partial a_A^2} + c_B\frac{\partial^2 U_{0B}}{\partial a_B^2} + 2c_B\frac{\partial^2 U_{0A_1}}{\partial a_{A_1}^2} + 4c_B\frac{\partial^2 U_{0A_2}}{\partial a_{A_2}^2}\right] -$$

$$(1-7c_B)\left[\frac{a_{AB}}{2k_A}\left(\frac{\partial k_A}{\partial a_A}\right)^2 - a_{AB}\frac{\partial^2 k_A}{\partial a_A^2}\right]\frac{\hbar\omega_A a_{AB}}{4k_A} - c_B\left[\frac{a_{AB}}{2k_B}\left(\frac{\partial k_B}{\partial a_B}\right)^2 - a_{AB}\frac{\partial^2 k_B}{\partial a_B^2}\right]\frac{\hbar\omega_B a_{AB}}{4k_B} -$$

$$2c_B\left[\frac{a_{AB}}{2k_{A_1}}\left(\frac{\partial k_{A_1}}{\partial a_{A_1}}\right)^2 - a_{AB}\frac{\partial^2 k_{A_1}}{\partial a_{A_1}^2}\right]\frac{\hbar\omega_{A_1} a_{AB}}{4k_{A_1}} - 4c_B\left[\frac{a_{AB}}{2k_{A_2}}\left(\frac{\partial k_{A_2}}{\partial a_{A_2}}\right)^2 - a_{AB}\frac{\partial^2 k_{A_2}}{\partial a_{A_2}^2}\right]\frac{\hbar\omega_{A_2} a_{AB}}{4k_{A_2}}$$

$$MS_1 = (1-7c_B)\frac{a_{AB}^2 k_{Bo}}{4k_A^2}\left(\frac{\partial k_A}{\partial a_A}\right)^2 + c_B\frac{a_{AB}^2 k_{Bo}}{4k_B^2}\left(\frac{\partial k_B}{\partial a_B}\right)^2 + 2c_B\frac{a_{AB}^2 k_{Bo}}{4k_{A_1}^2}\left(\frac{\partial k_{A_1}}{\partial a_{A_1}}\right)^2 + 4c_B\frac{a_{AB}^2 k_{Bo}}{4k_{A_2}^2}\left(\frac{\partial k_{A_2}}{\partial a_{A_2}}\right)^2 \quad (2.10)$$

In the case of zero pressure,

$$T_s = \frac{TS_2}{MS_2}, TS_2 = \frac{a_{AB}^2}{6}\left[(1-7c_B)\frac{\partial^2 U_{0A}}{\partial a_A^2} + c_B\frac{\partial^2 U_{0B}}{\partial a_B^2} + 2c_B\frac{\partial^2 U_{0A_1}}{\partial a_{A_1}^2} + 4c_B\frac{\partial^2 U_{0A_2}}{\partial a_{A_2}^2}\right] -$$

$$(1-7c_B)\left[\frac{a_{AB}}{2k_A}\left(\frac{\partial k_A}{\partial a_A}\right)^2 - a_{AB}\frac{\partial^2 k_A}{\partial a_A^2}\right]\frac{\hbar\omega_A a_{AB}}{4k_A} - c_B\left[\frac{a_{AB}}{2k_B}\left(\frac{\partial k_B}{\partial a_B}\right)^2 - a_{AB}\frac{\partial^2 k_B}{\partial a_B^2}\right]\frac{\hbar\omega_B a_{AB}}{4k_B} -$$

$$2c_B\left[\frac{a_{AB}}{2k_{A_1}}\left(\frac{\partial k_{A_1}}{\partial a_{A_1}}\right)^2 - a_{AB}\frac{\partial^2 k_{A_1}}{\partial a_{A_1}^2}\right]\frac{\hbar\omega_{A_1} a_{AB}}{4k_{A_1}} - 4c_B\left[\frac{a_{AB}}{2k_{A_2}}\left(\frac{\partial k_{A_2}}{\partial a_{A_2}}\right)^2 - a_{AB}\frac{\partial^2 k_{A_2}}{\partial a_{A_2}^2}\right]\frac{\hbar\omega_{A_2} a_{AB}}{4k_{A_2}}$$

$$MS_2 = (1-7c_B)\frac{a_{AB}^2 k_{Bo}}{4k_A^2}\left(\frac{\partial k_A}{\partial a_A}\right)^2 + c_B\frac{a_{AB}^2 k_{Bo}}{4k_B^2}\left(\frac{\partial k_B}{\partial a_B}\right)^2 + 2c_B\frac{a_{AB}^2 k_{Bo}}{4k_{A_1}^2}\left(\frac{\partial k_{A_1}}{\partial a_{A_1}}\right)^2 + 4c_B\frac{a_{AB}^2 k_{Bo}}{4k_{A_2}^2}\left(\frac{\partial k_{A_2}}{\partial a_{A_2}}\right)^2 \quad (2.11)$$

Because the curve of the absolute stability limit for the crystalline state is close to the MS of crystal, the temperature (T_s) is usually high and $x_X \coth x_X \approx 1$ at T_s. Therefore,

$$\frac{1}{(1-7c_B)\frac{a_{AB}^2 k_{Bo}}{4k_A^2}\left(\frac{\partial k_A}{\partial a_A}\right)^2 + c_B\frac{a_{AB}^2 k_{Bo}}{4k_B^2}\left(\frac{\partial k_B}{\partial a_B}\right)^2 + 2c_B\frac{a_{AB}^2 k_{Bo}}{4k_{A_1}^2}\left(\frac{\partial k_{A_1}}{\partial a_{A_1}}\right)^2 + 4c_B\frac{a_{AB}^2 k_{Bo}}{4k_{A_2}^2}\left(\frac{\partial k_{A_2}}{\partial a_{A_2}}\right)^2} \times$$

$$\left\{2PV_{AB} + \frac{a_{AB}^2}{6}\left[(1-7c_B)\frac{\partial^2 U_{0A}}{\partial a_A^2} + c_B\frac{\partial^2 U_{0B}}{\partial a_B^2} + 2c_B\frac{\partial^2 U_{0A_1}}{\partial a_{A_1}^2} + 4c_B\frac{\partial^2 U_{0A_2}}{\partial a_{A_2}^2}\right] -\right.$$

$$(1-7c_B)\left[\frac{a_{AB}}{2k_A}\left(\frac{\partial k_A}{\partial a_A}\right)^2 - a_{AB}\frac{\partial^2 k_A}{\partial a_A^2}\right]\frac{\hbar\omega_A a_{AB}}{4k_A} - c_B\left[\frac{a_{AB}}{2k_B}\left(\frac{\partial k_B}{\partial a_B}\right)^2 - a_{AB}\frac{\partial^2 k_B}{\partial a_B^2}\right]\frac{\hbar\omega_B a_{AB}}{4k_B} -$$

$$\left.2c_B\left[\frac{a_{AB}}{2k_{A_1}}\left(\frac{\partial k_{A_1}}{\partial a_{A_1}}\right)^2 - a_{AB}\frac{\partial^2 k_{A_1}}{\partial a_{A_1}^2}\right]\frac{\hbar\omega_{A_1} a_{AB}}{4k_{A_1}} - 4c_B\left[\frac{a_{AB}}{2k_{A_2}}\left(\frac{\partial k_{A_2}}{\partial a_{A_2}}\right)^2 - a_{AB}\frac{\partial^2 k_{A_2}}{\partial a_{A_2}^2}\right]\frac{\hbar\omega_{A_2} a_{AB}}{4k_{A_2}}\right\} +$$

$$\frac{2V_{AB}}{k_{Bo}a_{AB}\left[\frac{1}{k_A}\frac{\partial k_A}{\partial a_A}(1-7c_B) + \frac{1}{k_B}\frac{\partial k_B}{\partial a_B}c_B + \frac{1}{k_{A_1}}\frac{\partial k_{A_1}}{\partial a_{A_1}}2c_B + \frac{1}{k_{A_2}}\frac{\partial k_{A_2}}{\partial a_{A_2}}4c_B\right]} \times$$

$$\left\{P + \frac{a_{AB}}{6V_{AB}}\left[(1-7c_B)\frac{\partial U_{0A}}{\partial a_A} + c_B\frac{\partial U_{0B}}{\partial a_B} + 2c_B\frac{\partial U_{0A_1}}{\partial a_{A_1}} + 4c_B\frac{\partial U_{0A_2}}{\partial a_{A_2}}\right]\right\} = 0 \quad (2.12)$$

This is the equation for the curve of the absolute stability limit for the crystalline state. Therefore, the pressure is a function of the mean nearest neighbour distance:

$$P = P(a_{AB}) \quad (2.13)$$

Temperature $T_s(0)$ at zero pressure has the form:

$$T_s(0) = \frac{a_{AB}}{18\gamma_G^T k_{Bo}}\left[(1-7c_B)\frac{\partial U_{0A}}{\partial a_A} + c_B\frac{\partial U_{0B}}{\partial a_B} + 2c_B\frac{\partial U_{0A_1}}{\partial a_{A_1}} + 4c_B\frac{\partial U_{0A_2}}{\partial a_{A_2}}\right] \quad (2.14)$$

where the parameters a_{AB}, $\frac{\partial U_{0X}}{\partial a_X}$, γ_G^T are determined at $T_s(0)$. Temperature T_s at pressure P has the form:

$$T_s \approx T_s(0) + \frac{V_{AB}P}{3k_{Bo}\left(\gamma_G^T\right)^2}\left(\frac{\partial \gamma_G^T}{\partial T}\right)_{a_{AB}} T_s \quad (2.15)$$

where k_{Bo} is the Boltzmann constant, $V_{AB}, \gamma_G^T, \partial\gamma_G^T/\partial T$ are determined at T_s, and T_m is approximately the same as T_s. In order to solve equation (2.15), we can use the approximate iteration method. In the first approximate iteration,

$$T_{s1} \approx T_s(0) + \frac{V_{AB}(T_s(0))P}{3k_{Bo}\gamma_G(T_s(0))} \quad (2.16)$$

where $T_s(0)$ is the temperature of the absolute stability limit for the crystalline state at pressure P. Inserting T_{s1} into equation (2.15), we obtain a better approximate value (T_{s2}) for T_s at pressure P in the second approximate iteration:

$$T_{s2} \approx T_s(0) + \frac{V_{AB}(T_{s1})P}{3k_{Bo}\gamma_G(T_{s1})} - \frac{V_{AB}(T_{s1})P}{3k_{Bo}\gamma_G^2(T_{s1})}\left(\frac{\partial \gamma_G^T}{\partial T}\right)_{a_{AB}} T_{s1} \quad (2.17)$$

Analogously, we can obtain better approximate values for T_s at pressure P in the third, fourth, and subsequent approximate iterations. These approximations are applied at low pressures.

In the case of high pressure, the MT of the alloy at pressure P is calculated by:

$$T_m(P) = \frac{T_m(0)B_0^{\frac{1}{B_0'}}}{G(0)} \cdot \frac{G(P)}{(B_0 + B_0'P)^{\frac{1}{B_0'}}} \quad (2.18)$$

where $T_m(P)$ and $T_m(0)$ are the MT at pressure P and zero pressure, respectively, $G(P)$ and $G(0)$ are the shear modulus at pressure P and zero pressure, respectively,

B_0 is the isothermal elastic modulus at zero pressure, $B_0' = \left(\frac{dB_T}{dP}\right)_{P=0}$, and $B_T = B_T(P)$ is the isothermal elastic modulus at pressure P.

Numerical results for alloys FeH, FeSi and FeC

For alloys FeH, FeSi, and FeC, we use the Morse potential, the m - n potential, and the Finnis-Sinclair potential as follows:

$$\varphi(r) = D\left[e^{-2\alpha(r-r_0)} - 2e^{-\alpha(r-r_0)}\right] \quad (2.19)$$

$$\varphi(r) = \frac{D}{n-m}\left[m\left(\frac{r_0}{r}\right)^n - n\left(\frac{r_0}{r}\right)^m\right] \quad (2.20)$$

$$U = -A\sqrt{\sum_{i\neq j}\rho(r_{ij})} + \frac{1}{2}\sum_{i\neq j}\varphi(r_{ij})$$

$$\rho(r) = t_1(r-R_1)^2 + t_2(r-R_1)^3 \quad (r < R_1)$$

$$\varphi(r) = (r-R_2)^2(k_1 + k_2 r + k_3 r^2) \quad (r < R_2) \quad (2.21)$$

The Morse potential parameters for Fe-Fe and Fe-H are shown in Table 1, the m - n potential parameters for Fe-Si are presented in Table 2, and the Finnis-Sinclair potential parameters for Fe-C are shown in Table 3.

Table 1. The Morse potential parameters for Fe-Fe [12] **and Fe-H** [13].

Interaction	D(eV)	α (Å)$^{-1}$	r_0(Å)
Fe-Fe	0.42	1.40	2.85
Fe-H	0.32	1.34	1.73

Table 2. The m - n potential parameters for Fe-Si [14].

Interaction	m	n	D(eV)	r_0(Å)
Fe-Si	2.0	5.5	1.06	2.3845

Table 3. The Finnis-Sinclair potential parameters for Fe-C [15].

A (eV)	R_1 (Å)	t_1 (Å)$^{-2}$	t_2 (Å)$^{-3}$	R_2 (Å)	k_1 (eV(Å)$^{-2}$)	k_2 (eV(Å)$^{-3}$)	k_3 (eV(Å)$^{-4}$)
2.958787	2.545937	10.024001	1.638980	2.468801	8.972488	-4.086410	1.483233

Our numerical results for the MT of alloys FeH, FeSi and FeC are summarized in Tables 4-7 and described in Figs. 1-6.

Table 4. The MT (T_m) of metal Fe under pressure obtained from the SMM and the experimental data (EXPT) [16].

P (GPa)	1	2	3	4	5	6
T_m - SMM	1861.43	1911.07	1959.08	2005.61	2050.77	2094.69
T_m - EXPT	1873	1908	1943	1978	2013	2033

Note that the MT of Fe at P = 0 is taken from EXPT [17], the MT of FeH at P = 0 is taken from EXPT [18], and the MT of FeSi and FeC at P = 0 are taken from EXPT [19].

Table 5. The MT (T_m) of alloy FeH under pressure obtained from the SMM.

c_H (%)	P (GPa)	1	2	3	4	5	6	8	10
0	T_m (K)	1861.43	1911.07	1959.08	2005.61	2050.77	2094.69	2179.09	2259.44
1		1858.50	1905.28	1950.51	1994.31	2036.80	2078.08	2157.38	2232.78
2		1855.41	1899.17	1941.47	1982.40	2022.09	2060.64	2134.61	2204.87
3		1852.16	1892.77	1932.00	1969.95	2006.73	2042.42	2110.87	2175.82
4		1848.77	1886.11	1922.15	1957.00	1990.76	2023.50	2086.24	2145.70
5		1845.26	1879.20	1911.94	1943.59	1974.23	2003.93	2060.77	2114.58

Table 6. The MT (T_m) of alloy FeSi under pressure obtained from the SMM.

c_{Si} (%)	P (GPa)	1	2	3	4	5	6	8	10
0	T_m (K)	1861.43	1911.07	1959.08	2005.61	2050.77	2094.69	2179.09	2259.44
1		1838.56	1884.48	1928.86	1971.84	2013.54	2054.06	2131.86	2205.84
2		1821.81	1864.13	1905.00	1944.56	1982.90	2020.13	2091.57	2159.41
3		1805.02	1843.68	1881.01	1917.10	1952.07	1985.99	2051.02	2112.68
4		1788.18	1823.16	1856.90	1889.50	1921.06	1951.66	2010.23	2065.69
5		1771.30	1802.56	1832.68	1861.77	1889.89	1917.14	1969.22	2018.45

Table 7. The MT (T_m) of alloy FeC under pressure obtained from the SMM.

c_C (%)	P (GPa)	1	2	3	4	5	6	8	10
0	T_m (K)	1861.43	1911.07	1959.08	2005.61	2050.77	2094.69	2179.09	2259.44
1		1801.22	1845.45	1888.22	1929.66	1969.88	2008.96	2084.05	2155.50
2		1755.24	1794.55	1832.56	1869.38	1905.12	1939.84	2006.55	2069.98
3		1709.51	1744.12	1777.60	1810.03	1841.51	1872.09	1930.84	1986.69
4		1664.07	1694.29	1723.53	1751.85	1779.34	1806.04	1857.32	1906.07
5		1618.98	1645.12	1670.40	1694.91	1718.68	1741.78	1786.14	1828.29

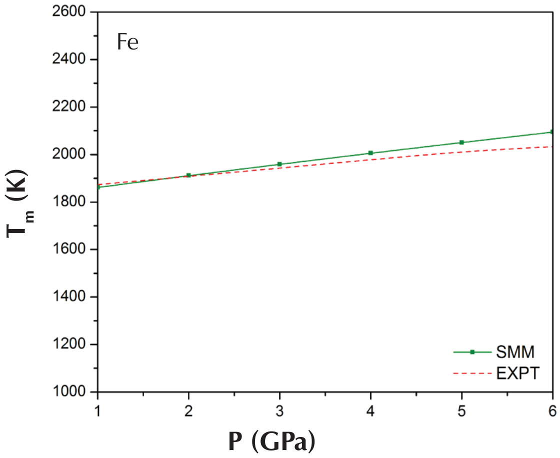

Fig. 1. T_m(P) of Fe obtained from the SMM and EXPT [16].

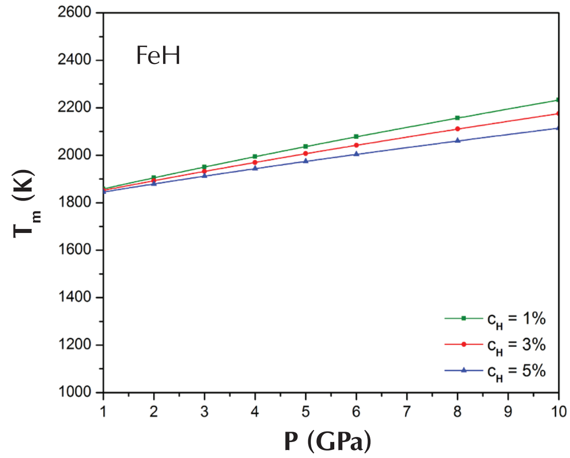

Fig. 2. T_m(P) of FeH obtained from the SMM.

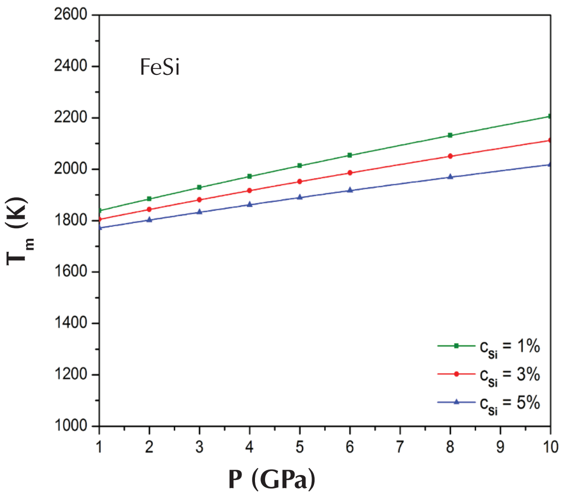

Fig. 3. T_m(P) of FeSi obtained from the SMM.

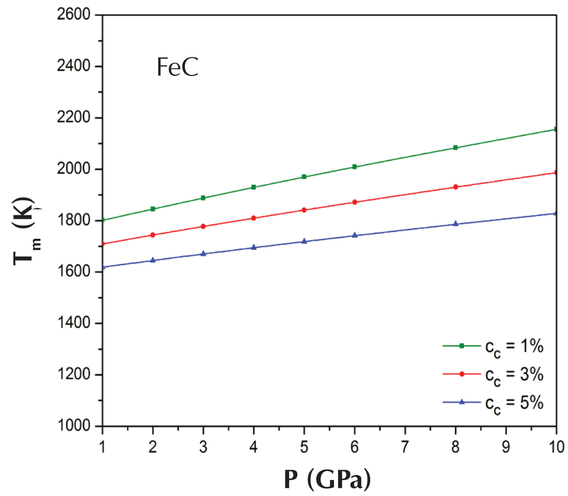

Fig. 4. T_m(P) of FeC obtained from the SMM.

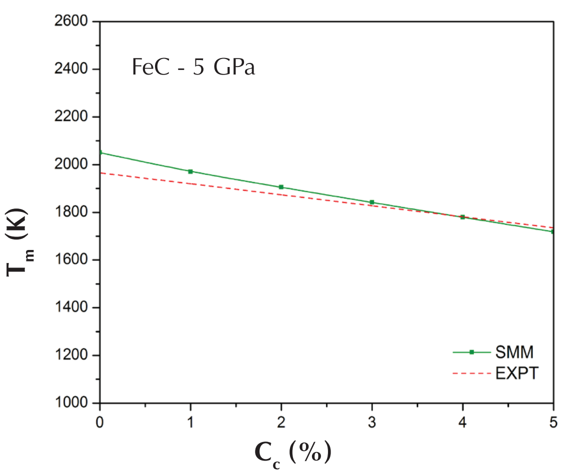

Fig. 5. $T_m(c_C)$ of FeC at 5 GPa obtained from the SMM and EXPT [20].

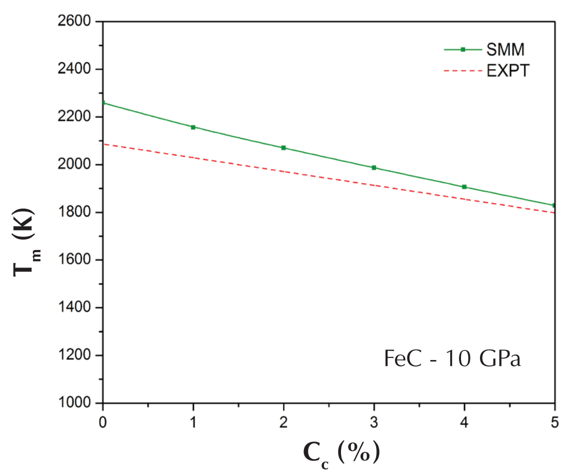

Fig. 6. $T_m(c_C)$ of FeC at 10 GPa obtained from the SMM and EXPT [20].

For the pure metal Fe, the SMM's results correspond well with experiments [16]. In the range of pressure from 0 to 6 GPa, the differences are lower than 3%. When pressure increases, the MT of Fe also increases.

For the interstitial alloys FeH, FeSi, and FeC with the same concentration of interstitial atoms, the MT also increases when pressure increases. For example, at $c_B = 5\%$, when the pressure (P) increases from 1 to 10 GPa, the MT (T_m) of FeH increases from 1845.26 to 2114.58 K, the MT (T_m) of FeSi increases from 1771.30 to 2018.45 K, and the MT (T_m) of FeC increases from 1618.98 to 1828.29 K.

At the same pressure, the MTs of alloys FeH, FeSi and FeC decrease when the concentration of interstitial atoms increases. For example, at P = 10 GPa when the concentration (c_B) increases from 0 to 5%, the MT (T_m) of FeH decreases from 2259.44 to 2114.58 K, the MT (T_m) of FeSi decreases from 2259.44 to 2018.45 K, and the MT (T_m) of FeC decreases from 2259.44 to 1828.29 K. When their the physical conditions are the same, the MT of FeC is lower than that of FeSi, the MT of FeSi is lower than that of FeH, and the MTs of the interstitial alloys FeH, FeSi and FeC are lower than the MT of Fe.

Figures 5 and 6 show that the MT (T_m) of FeC from the SMM corresponds well with EXPT [20]. The differences are lower than 4.3% at P = 5 GPa and lower than 8.3% at P = 10 GPa.

Conclusions

Using the SMM, we derive the analytic expressions for the temperature of the limit of absolute stability for the crystalline state, the MT, and the melting curve of the binary interstitial alloy at different pressures and concentrations of interstitial atoms. In limit cases, we obtain the melting theory of main metal A with a BCC structure. The theoretical results are numerically applied for alloys FeH, FeSi and FeC using the Morse potential, the m - n potential, and the Finnis-Sinclair potential.

The authors declare that there is no conflict of interest regarding the publication of this article.

REFERENCES

[1] A.B. Belonoshko, S.I. Simak, A.E. Kochetov, B. Johansson, L. Burakovsky and D.L. Preston (2004), "High-pressure melting of molybdenum", *Phys. Rev. Lett.,* **92(19)**, p.195701.

[2] L. Burakovsky, et al. (2000), "Analysis of dislocation mechanism for melting of elements: pressure dependence", *Journal of Applied Physics*, **88(11)**, p.6294.

[3] M. Kumari, K. Kumari, and N. Dass (1987), "On the melting law at high pressure", *Phys. Stat. Sol. (a)*, **99(1)**, pp.K23-K26.

[4] N. Tang and V.V. Hung (1998), "Investigation of the thermodynamic properties of anharmonic crystals by the momentum method. I. General results for face-centred cubic crystals", *Phys. Stat. Sol. (b),* **149(2)**, pp.511-519.

[5] V.V. Hung, K. Masuda-Jindo (2000), "Application of statistical moment method to thermodynamic properties of metals at high pressures", *J. Phys. Soc. Jpn.*, **69**, pp.2067-2075.

[6] N.Q. Hoc, D.Q. Vinh, B.D. Tinh, N.L. Phuong, T.T.C. Loan, T.T. Hue, D.T.T. Thuy (2015), "Thermodynamic properties of binary interstitial alloys with BCC structure: dependence on temperature and concentration of interstitial atoms", *HNUE Journal of Science: Mathematical and Physical Sciences*, **60(7)**, pp.146-155.

[7] N.Q. Hoc, D.Q. Vinh, N.T. Hang, N.T. Nguyet, L.X. Phuong, N.N. Hoa, N.T. Phuc, and T.T. Hien (2016), "Thermodynamic properties of a ternary interstitial alloy with BCC structure: dependence on temperature, concentration of substitution atoms and concentration of interstitial atoms", *HNUE Journal of Science: Mathematical and Physical Sciences*, **61(7)**, pp.65-74.

[8] N.Q. Hoc and N.D. Hien (2017), "Study on elastic deformation of interstitial alloy AB with BCC structure under pressure", *Proceedings of the 10th National Conference on Solid State Physics and Material Science* (*SPMS*), pp.911-914.

[9] N.Q. Hoc, N.T. Hoa, D.Q. Vinh (2017), "Study on the melting temperature of substitution alloy AB with interstitial atom C and BCC structure under pressure", *Journal of Science of Hanoi Pedagogical University No.2*, **50**, pp.130-143.

[10] N.Q. Hoc and N.D. Hien (2018), "Study on elastic deformation of substitution alloy AB with interstitrial atom C and BCC structure under pressure", *Journal of Physics: Conf. Series,* **1034(1)**, 012005.

[11] N.Q. Hoc, B.D. Tinh, D.Q. Vinh (2018), "Study on the melting of interstitial alloy AB with FCC structure under pressure", *Physics and Astronomy International Journal*, **2(3)**, pp.231-235.

[12] N.V. Hung, T.T. Hue, N.B. Duc (2015), "Calculation of morse potential parameters of bcc crystals and applications to anharmonic interatomic effective potentias, local force constant", *VNU Journal of Science: Mathematics - Physics*, **31(3)**, pp.23-30.

[13] J. Bardeen and C. Herring (1951), *Atom movements*, Ed. J.H. Hollomon, p.260.

[14] M.N. Magomedov (1987), "Calculation of the debye temperature and the gruneisen-parameter", *J. Fiz. Khimic*, **61(4)**, pp.1003-1009.

[15] T.L. Timothy, J.F. Clemens, Xi Lin, D.G. Julian, Y. Sidney, J.V.V. Krystyn (2007), "Many-body potential for point defect clusters in Fe-C alloys", *Phys. Rev. Lett.*, **98(21)**, 215501.

[16] A.F. Guillermet & P. Gustafson (1984), "An assessment of the thermodynamic properties and the (p, T) phase diagram of iron", *High Temp.-High Press.*, **16(6)**, pp.591-610.

[17] E. Yu Tonkov, E.G. Ponyatovsky (2005), *Phase transformations of elements under high pressure*, CRC Press.

[18] A. San-Martin, F.D. Manchester (1990), "The Fe-H (iron-hydrogen) system", *Bulletin of Alloy Phase Diagrams*, **11(2)**, pp.173-184.

[19] H. Okamoto (2000), *Desk handbook: phase diagrams for binary alloys*, ASM International.

[20] O.T. Lord, M.J. Walter, R. Dasgupta, D. Walker, S.M. Clark (2009), "Melting in the Fe–C system to 70 GPa", *Earth and Planetary Science Letters*, **284(1-2)**, pp.157-167.

Doi: 10.31276/VJSTE.61(2).23-28

Synthesis and application of graphene aerogel as an adsorbent for water treatment

Thi Lan Nguyen[1], Tri Tin Nguyen[1], Hoang Tu Tran[1], Minh Dat Nguyen[1], Huu Hieu Nguyen[1, 2*]

[1]*Key Laboratory of Chemical Engineering and Petroleum Processing*
[2]*Faculty of Chemical Engineering*
University of Technology - Vietnam National University, Ho Chi Minh city

Received 1 June 2018; accepted 1 August 2018

Abstract:

In this research, graphene aerogel (GA) was fabricated by chemical reduction method, in which ethylenediamine (EDA) was used as a reducing and functionalising agent. The characterisation of GA was studied by density, field-emission scanning electron microscope, Brunauer-Emmett-Teller (BET) specific surface area, Fourier transform infrared spectroscopy, and X-ray diffraction. The results of the analysis showed that GA exhibits low density, ranging from 4-8 mg/cm^3, high porosity, and BET specific surface area changes from 176 to 1845 m^2/g. It was found that the suitable content of EDA on the synthesis of GA is 30 µl. The obtained GA was used as an adsorbent for removal of oils and methylene blue (MB) from aqueous solutions. The maximum adsorption capacities of GA for lubricant and crude oils are 160 g/g and 110 g/g respectively. The effecting factors including pH, contact time, and initial concentrations on the adsorption capacity of GA for MB were investigated. The adsorption process of MB onto GA followed the *pseudo-second-order* kinetic and well-fitted to Langmuir isotherm model. The maximum adsorption capacity for MB from linear Langmuir model was calculated to be 212.76 mg/g at pH 7. Accordingly, GA could be used as a potential adsorbent for removal of oils and MB from water.

Keywords: **chemical reduction, crude oil, graphene aerogel, lubricant oil, methylene blue.**

Classification number: **2.2.**

Introduction

Water, an important resource in nature, has significant impacts on the living conditions of creatures on the earth. However, rapid industrialisation and urbanisation have resulted in water pollution. The pollutants, such as metal ions, oils, organic dyes, etc., are released into the environment, which cause serious problems for the environment, humans, and other organisms. Many methods have been developed, such as adsorption, chemical oxidation, electrochemical, biological, membrane separation, ion exchange, etc. for removal of toxic contaminants from water. Adsorption is one of widely used procedure for removal of pollution from water. The traditional absorbent materials showed low adsorption capacity and faced difficulty in separating pollutants like activated carbon, zeolite, natural clays, agricultural waste, biomass, polymeric, etc. [1, 2].

Recently, graphene (Ge), a single atomic layer graphite, has attracted great interest among scientists. Ge has unique properties such as chemical stability, excellent mechanical strength, high electrical and thermal conductivities and good optical and large specific surface area. Ge is used in many applications including catalyst, energy-storage and environmental. However, Ge nanosheets tend to aggregate and restack, leading to significant reduction of specific surface area and application ability [3, 4]. To solve this problem, three-dimensional (3D) graphene nanomaterials, especially graphene aerogel (GA), are being developed. GA has unique features like low weight, high porosity, large surface area and chemical stabilities. Based on these properties, GA materials have been considered as ideal adsorbents for water treatment.

Several methods have been applied to synthesise GA including 3D printing, cross-linking, hydrothermal reduction, organic functionality and template-directing method. However, these methods are difficult to control in synthesis conditions, the research process of 3D-

*Corresponding author: Email: nhhieubk@hcmut.edu.vn

GA is limited [5-8]. In recent years, chemical reduction method has developed benefits like simple, environmental friendly, reduction at low temperature (T<100^{0}C), and easy scalability, which is why it is commonly used to synthesise GA. The mild reduction agents such as acid ascorbic, sodium ascorbate, ammoniac, urea, ethylenediamine (EDA), etc. are widely used to synthesise GA. During the reduction process, Graphene oxide (GO) was changed to reduced graphene oxide (rGO) nanosheets, the electrostatic repulsion was decreased. As a result the performance of self-assembly of rGO was enhanced to form network structure [9, 10].

In this study, GA was synthesised by chemical reduction method using EDA as a reducing agent. Effect of EDA content on the synthesis of GA was studied. The structure and morphology of GA were characterised by calculating apparent density, field-emission scanning electron microscope (SEM), Brunauer-Emmett-Teller (BET) specific surface area, Fourier transform infrared spectroscopy (FTIR), and X-ray diffraction (XRD). The obtained GA was used as an adsorbent for removal of oils and methylene blue (MB) from water.

Materials and methods

Materials

Graphite powder with an average particle size of 20 µm and EDA solution (99%) was purchased from Sigma Aldrich, Germany. Potassium permanganate (99%), ethanol (99%) and hydrogen peroxide (30%) were obtained from VN Chemsol, Vietnam. Sulfuric acid (98%), phosphoric acid (85%), hydrochloric acid (36%) and MB (99%) were purchased from Xilong Chemical, China. Lubricant and crude oils were supplied from Petrolimex, Vietnam. Twice-distilled water was used in all experiments.

Synthesis of GA

GO was synthesised using the improved Hummers method as mentioned in our previous work [11]. In a typical process, GO was dispersed into water with concentration of 5 mg/ml. Then, different content of EDA was added to GO suspension. The mixture was heated at 90^{0}C for 6 hours to form graphene hydrogel (GH). Then, GH was immersed and exchanged in ethanol and deionized water for at least 5 times to remove extra EDA and other impurities. Finally, GH was sublimated at -60^{0}C for 48 hours to obtain GA. The sample with EDA content of 15, 30, 45 and 60 µl are labelled as GA15, GA30, GA45 and GA60.

Characterisation

The dimension of GA was measured by a caliper (VOREL-15240, Germany) to calculate the volume. The weight was determined by analytical balance (Sartoius CPA225D, Germany). The density of GA is its mass per unit volume, which was calculated using the following equation:

$$p = \frac{m}{V} \tag{1}$$

where p is the density (mg/cm^3), V is the volume (cm^3) and m is weight (mg) of GA.

The morphology of samples was studied using the FE-SEM images (S-4800, Hitachi, Japan). The surface area and pore volume of GA were determined by BET method with a Nova 1200e instrument (Quantachrome, USA). The void-space of GA was calculated from pore volume results. The porosity is a ratio of the void-space and bulk volume of material, which was obtained from equation (2).

$$\varepsilon = \frac{V_V}{V_T} 100\% \tag{2}$$

where Ɛ is the porosity (%); V_v and V_T are the pore volume and the bulk volume of materials (cm^3/g) respectively. FTIR spectra was recorded with an Alpha-E Brucker (Brucker Optik GmbH, Ettlingen, Germany) spectrometer ranging in wavenumber from 500 to 4000 cm^{-1} to study the functional groups on the surface of materials. XRD patterns were performed on an X-ray Diffusion instrument (D8 Advance, Brucker, Germany).

Oil adsorption

The adsorption capacity of GA for oil was determined with the help of the weight method. First, the GA sample was weighed (W_i) then put into crude or lubricant oils. After being fully adsorbed, the sample was taken out. After removing oil residue on the surface with filter papers, the sample was weighted (W_f). The oil adsorption performance was reflected by the saturated adsorption capacity per unit mass of the GA samples, which was showed by the following equation:

$$q_{oil} = \frac{W_f - W_i}{W_i} \tag{3}$$

where q_{oil} is the adsorption capacity for oil at saturated state. W_i and W_f are the initial and final weights (at adsorption saturation) of GA respectively [3, 12].

Methylene blue adsorption

The adsorption experiments were conducted to study adsorption behaviour and kinetics process of dyes adsorption. Batch experiments were performed by adding 20 mg of adsorbent into 20 ml of MB solution with constant shaking (100 rpm) at room temperature to study the effects of contact time (time: 0-1440 min, pH 6, C_o 200 mg/l), pH values (pH 3-10, C_o 200 mg/l, equilibrium time), and initial concentration (C_o 50-400 mg/l, equilibrium time, optimal pH). After adsorption equilibrium, the residual concentration of MB was measured by UV-Vis spectrophotometer (Dual FL, Horiba, Japan) at the wavelength of 664 nm. The adsorption capacity (q) was calculated using the following equation:

$$q = \frac{(C_0 - C_e)\,V}{m} \quad (4)$$

where C_0, C_e are the concentration of MB before and after the adsorption, V is the volume of MB solution (ml) and m is the weight of material (mg).

The *pseudo-first-order* and *pseudo-second-order* models were applied to study the adsorption kinetic. The equation of models are as follows:

$$ln(q_e - q_t) = lnq_e - k_1 t \quad (5)$$

$$\frac{t}{q_t} = \frac{1}{k_2 q_e^2} + \frac{1}{q_e} t \quad (6)$$

where q_e and q_t are the amounts of MB adsorbed on the surface of GA at equilibrium and at time t (mg/g) respectively; k_1 and k_2 are the *pseudo-first-order* and *pseudo-second-order* constant respectively.

In order to evaluate the adsorption capacity of adsorbent, the experiment data was analysed using the Langmuir and Freundlich isotherms models. The linear equation models were presented by the following equations:

$$\frac{C_e}{q_e} = \frac{C_e}{q_m} + \frac{1}{q_m k_l} \quad (7)$$

$$lnq_e = lnk_f + \frac{1}{n} lnC_e \quad (8)$$

where q_m is the maximum uptake capacity (mg/g), C_e is the concentration of MB solution at equilibrium (mg/l), and k_l is the Langmuir constant (l/mg); k_f and n are the Freundlich constants [2, 13].

Results and discussion

Characterisation

Density of GA: the 3D-structure of GH was formed by self-assembling of rGO through hydrogen bonds, π-π interactions, and Van der Waals forces [9, 14]. Then, the freeze drying process was conducted. After sublimation, the content of water in structure was removed but the morphology of GA still remained with very low density ranging from 4 to 8 mg/cm as shown in Table 1.

Table 1. Density of GA.

Sample	GA15	GA30	GA45	GA60
p (mg/cm^3)	6.37	4.57	6.76	7.95

SEM images: the porous structure of GA was studied as shown in Fig. 1. As can be seen, GA was described using a honeycomb-like 3D porous structure with the pore size ranging from 5-80 µm. Among that, the obtained GA30 had optimum pore size of the network, which is the highest, approximate a hundred micrometres. This pointed out that the partial over-lapping of coalescing of rGO nanosheets occurred due to partial restoration of sp^2 regions, π-π stacking, and cross-linking under the effect of EDA, leading to the formation of 3D-architecture [7, 15].

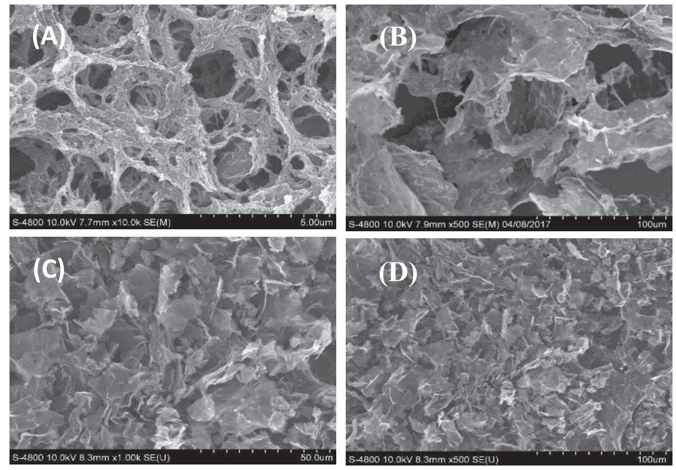

Fig. 1. SEM images of GA15 (A), GA30 (B), GA45 (C), and GA60 (D).

FTIR spectra: Fig. 2 shows the FTIR spectra of GO and GA. The characteristic peaks of GO appear at 1734, 1650, 1229 and 1055 cm^{-1} corresponding to C=O, C=C, C-O, and C-O-C groups respectively [3, 11]. For GO aqueous solution treated with EDA, the characteristic peaks of C=O, C-O groups were decreased, and the new peaks were 1550 and 1190 cm^{-1} relating to the vibration of N-H and C-N groups respectively. These results confirmed that the nucleophilic reaction between the epoxide group in rGO and the amine group in EDA resulted in crosslink between the rGO nanosheets to form porous framework [15, 16].

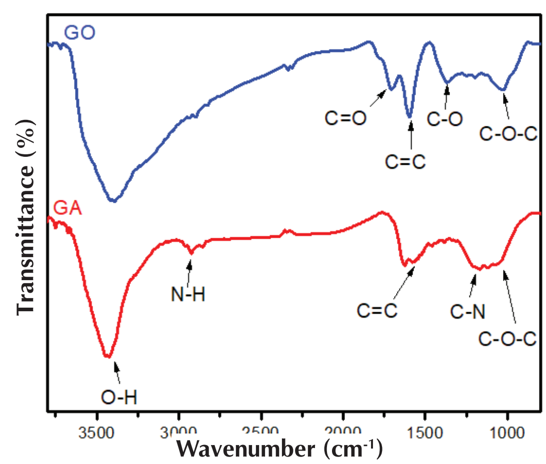

Fig. 2. FTIR spectra of GO and GA.

XRD patterns: the structural phases and interlayer spacing of GO and GA were studied by XRD as shown in Fig. 3. For GO, XRD pattern shows a sharp peak at 2θ = 10.6^0 with an interlayer spacing is 8.32 Å. This result indicated the formation of oxygen-containing groups on the surface of graphene nanosheets. For GA, a wide peak at 2θ = 23.65^0 appeared with an interlayer distance of 3.67 Å. The interlayer distance of GA is larger than that of graphite

(3.4 Å), which explains the fact that the oxygen-containing functional groups on GO surface were partially reduced and rGO self-assembled to form a 3D-architecture [15, 17, 18].

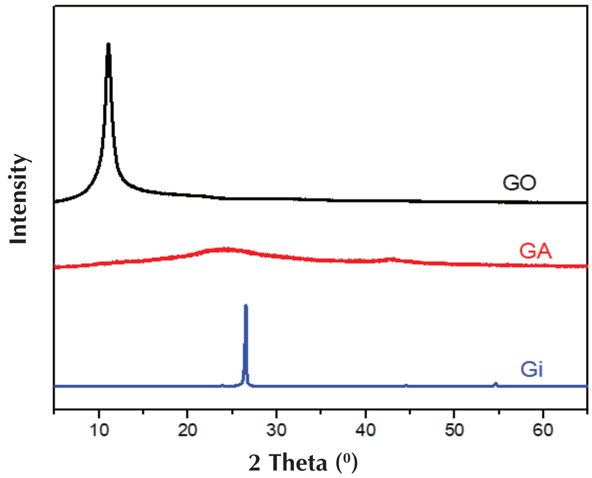

Fig. 3. XRD pattern of Gi, GO, and GA.

BET specific surface area: BET was used to calculate the specific surface area of GA, which is shown in Table 2. This result can be explained by the self-assembly process of rGO nanosheets to form interconnected structure with large pore volume, leading to an increase in the surface area of GA [19]. These BET results were in good agreement estimated from the SEM images. GA30 had the specific surface area of 1845 m^2/g and the porosity of 98.06% was the selected adsorbent for the following experimental adsorption.

Table 2. BET Specific surface area of GA.

Samples	GA15	GA30	GA45	GA60
Specific surface area (m^2/g)	576	1845	285	176

Oil adsorption

Due to their light weight, high porosity structure, large specific surface area and excellent hydrophobicity, GA was used as an absorbent material for oils. The adsorption efficiency of GA for lubricant and crude oils is shown in Table 3.

Table 3. The adsorption capacities of GA for oils.

Sample	GA
Lubricant oil (g/g)	160
Crude oil (g/g)	110

The adsorption capacity of GA for lubricant oil 160 g/g was larger than that for crude oil 110 g/g. The adsorption capacity depends on density of oil and it was found that the adsorption increases as per the density of the materials. The results were in agreement with previous study suggesting that GA has large pores and high surface area, resulting in higher oil adsorption capacity [16].

Effect of conditions on methylene blue adsorption

Contact time: the effect of contact time was carried out at initial concentrations of 200 mg/l as shown in Fig. 4. The adsorption was increased rapidly at 240 mins and the equilibrium was established after 480 mins. This suggests that the network structure of GA with large area and volume pores increased exposure and diffusion rate of MB for adsorption sites on surface of GA.

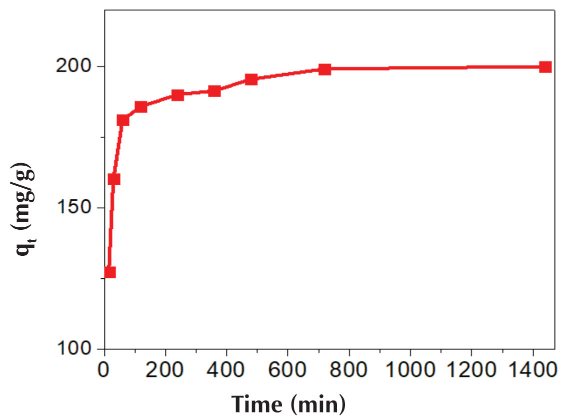

Fig. 4. Effect of contact time on the adsorption of MB on GA.

The correlation coefficient (R^2) from linear *pseudo-second-order* was closed to 1 (R^2 = 0.9999) as shown in Fig. 5. The adsorption process of MB into GA fitted well with the *pseudo-second-order* kinetic.

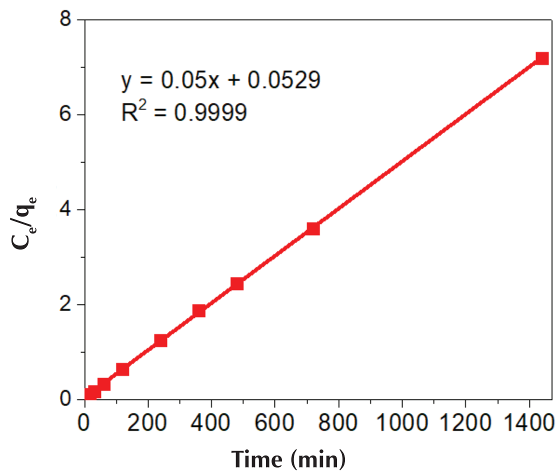

Fig. 5. The *pseudo-second-order* kinetic.

pH: Fig. 6 shows the effect of the initial pH on adsorption. The uptake capacity enhanced with the increase in pH value and reached the highest level at pH 7. The change of the capacity may be π-π stacking and electrostatic interactions between the functional groups on GA surface and MB [13, 18].

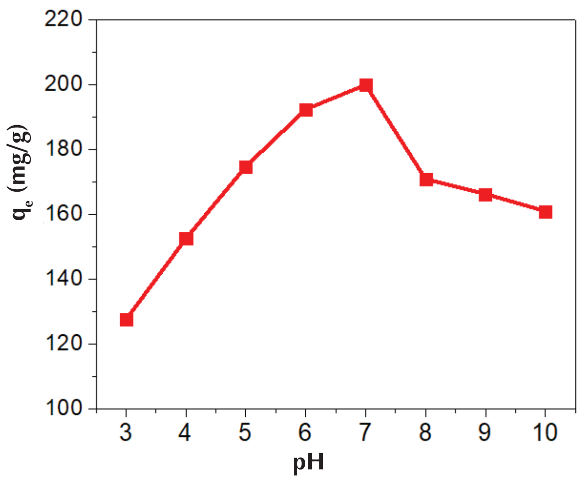

Fig. 6. Effect of pH on the adsorption of MB on GA.

Initial concentration: Fig. 7 shows the relationship between adsorption capacity and initial MB concentration. At low concentration (50-150 mg/l), the adsorption capacity was rapidly increased and at higher concentration (>150 mg/l) the adsorption capacity was slowly enhanced. This phenomenon proved that the adsorption was almost saturated.

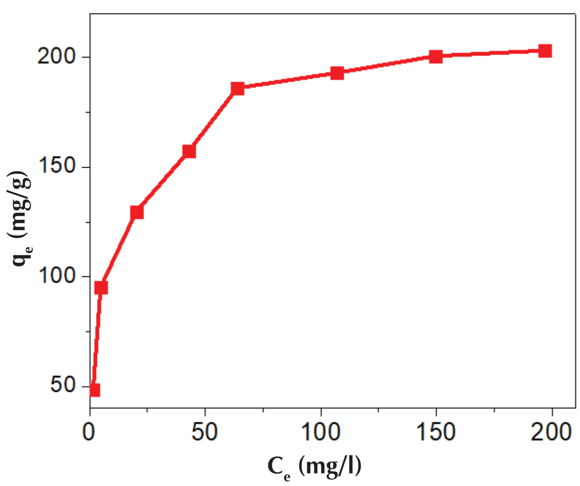

Fig. 7. Effect of initial concentration on the adsorption of MB on GA.

The correlation coefficient from Langmuir model (R^2 = 0.9979) was higher than that of Freundlich model (R^2 = 0.9408) (Fig. 8). The adsorption process for MB into GA was well-fitted to Langmuir isotherm model with the maximum adsorption capacity of 212.76 mg/g.

The maximum adsorption capacity of MB on GA compared with graphene-based materials is shown in Table 4. The results were higher compared to other materials, which indicated that the interconnected porous structure of GA increased the MB diffusion process, leading to enhancement of the adsorption capacity.

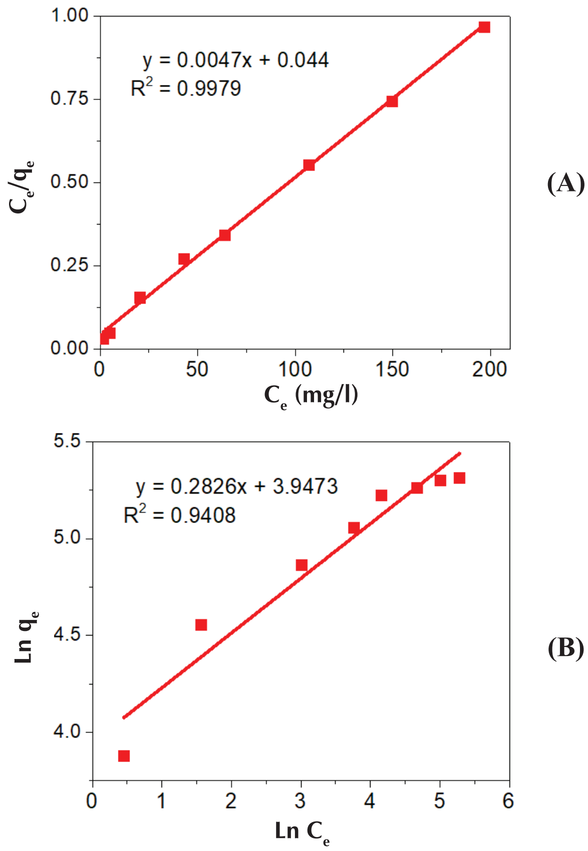

Fig. 8. Langmuir (A) and Freunlich (B) isotherm models for adsorption MB on GA.

Table 4. Maximum adsorption capacity (q_m) of various adsorbent.

Adsorbent	q_m (mg/g)	References
GA	212.76	Present work
Ge	100.0	[20]
TiO_2 (P25) - GH	87.63	[21]

Conclusions

In this study, GA was successfully synthesised by chemical reduction method. SEM images showed self-assembly of reduced GO to form porous 3D framework. FTIR, XRD and Raman results indicated that the oxygen-containing functional groups were partially reduced and GO was transformed into rGO. It was found that the suitable content of EDA for the synthesis of GA is 30 µl. GA had the maximum adsorption capacities for lubricant and crude oils, which were 160 g/g and 110 g/g respectively. The equilibrium time for adsorption of MB into the GA was 480 mins. The adsorption process of MB on GA fitted to the *pseudo-second-order* kinetic and Langmuir isotherm model with the maximum capacity of 212.76 mg/g at pH

7. Accordingly, GA could be considered as a promising adsorbent for removal of oils and MB from water.

ACKNOWLEDGEMENTS

The authors gratefully acknowledge the financial support from the Ho Chi Minh city Department of Science and Technology through the contract No. 234/2017/HD-SKHCN.

The authors declare that there is no conflict of interest regarding the publication of this article.

REFERENCES

[1] J. Huang and Z. Yan (2018), "Adsorption mechanism of oil by resilient graphene aerogels from oil-water emulsion", *Langmuir*, **34(5)**, pp.1890-1898.

[2] P.K. Malik (2004), "Dye removal from wastewater using activated carbon developed from sawdust: adsorption equilibrium and kinetics", *Journal of Hazardous Materials*, **113(1)**, pp.81-88.

[3] Y. Cheng, P. Xu, W. Zeng, C. Ling (2017), "Highly hydrophobic and ultralight graphene aerogel as high eficiency oil absorbent material", *Journal of Environmental Chemical Engineering*, **5(2)**, pp.1957-1963.

[4] T. Wu, M. Chen, L. Zhang, X. Xu, Y. Liu (2013), "Three-dimensional graphene-based aerogels prepared by a self-assembly process and its excellent catalytic and absorbing performance", *J. Mater. Chem. A*, **1**, pp.7612-7621.

[5] M.A. Worsley, T.T. Olson, J.R.I. Lee, T.M. Willey (2011), "High surface area, sp^2-cross-linked three-dimensional graphene monoliths", *J. Phys. Chem. Let.*, **8**, pp.921-925.

[6] Y. Xu, et al. (2010), "Self-assembled graphene hydrogel via a one step hydrothermal process", *ACS Nano*, **4**, pp.4324-4330.

[7] H. Sun, Z. Xu, C. Gao (2013), "Multifunctional, ultra-flweight, synergistically assembled carbon aerogels", *Adv. Mater.*, **25**, pp.2554-2560.

[8] G. Gorgolis, C. Galiotis (2017), "Graphene aerogels: a review", *2D Mater.*, **4**, p.032001.

[9] W. Chen and L. Yan (2011), "*In situ* self-assembly of mild chemical reduction graphene for three-dimensional architectures", *Nanoscale*, **3**, pp.3132-3137.

[10] K.X. Sheng, et al. (2011), "High-performance self-assembled graphene hydrogels prepared by chemical reduction of graphene oxide", *New Carbon Mater.*, **26**, pp.9-15.

[11] D.C. Marcano, D.V. Kosynkin, J.M. Berlin, A. Sinitskii, Z. Sun, A. Slesarev, Lawrence, B. Alemany, W. Lu, and J.M. Tour (2010), "Improved synthesis of graphene oxide", *ACS Nano*, **4(8)**, pp.4806-4814.

[12] C. Chi, H. Xu, K. Zhang, Y. Wang (2015), "3D hierarchical porous graphene aerogels for highly improved adsorption and recycled capacity", *Materials Science and Engineering B*, **194**, pp.62-67.

[13] P. Wang, M. Cao, C. Wang (2014), "Kinetics and thermodynamics of adsorption of methylene blue by a magnetic graphene-carbon nanotube composite", *Applied Surface Science*, **290**, pp.116-124.

[14] Yangsu Xie, Shen Xu, Zaoli Xu, Hongchao Wu, Cheng Deng (2016), "Interface-mediated extremely low thermal conductivity of graphene aerogel", *Carbon*, **98**, pp.381-390.

[15] X. Xu, H. Li, Q. Zhang, H. Hu (2015), "Self-sensing, ultralight and conductive 3D Graphene/iron oxide aerogel elastomer deformable in magnetic field", *ACS Nano*, **9(4)**, pp.3969-3977.

[16] Y.L. He, J.H. Li, J.B. Chen (2016), "The synergy reduction and self-assembly of graphene oxide via gamma-ray irradiation in an ethanediamine aqueous solution", *Nuclear Science and Techniques*, **27**, pp.61-69.

[17] J. Li, H. Meng, S. Xie, B. Zhang, L. Li (2014), "Ultra-light, compressible and fire-resistant graphene aerogel as the highly efficient and recyclable absorbent for organic liquids", *Journal of Materials Chemistry A*, **2**, pp.2934-2941.

[18] W. Si, X. Wu, J. Zhou, F. Guo, S. Zhuo (2013), "Reduced graphene oxide aerogel with high-rate supercapacitive performance in aqueous electrolytes", *Nanoscale Res. Lett.*, **8(1)**, pp.247.

[19] W. Wan, F. Zhang, S. Yu, R. Zhang (2016), "Hydrothermal formation of graphene aerogel for oil sorption: the role of reducing agent, reaction time and temperature", *New J. Chem.*, **40**, pp.3040-3046.

[20] T. Liu, Y. Li, Q. Du (2012), "Adsorption of methylene blue from aqueous solution by graphene", *Colloids and Surfaces B: Biointerfaces*, **90**, pp.197-203.

[21] C. Hou, et al. (2012), "P25-graphene hydrogels: room-temperature synthesis and application for removal of methylen blue from aqueous solution", *Journal of Hazardous Materials*, **206**, pp.229-235.

Doi: 10.31276/VJSTE.61(2).29-34

Treatment of benzene, toluene, and xylene by deep oxidation on CuO catalytic materials synthesised from red mud and rice husk ash

Thanh Tinh Nguyen[1], Phung Anh Nguyen[2], Thi Thuy Van Nguyen[2], Tri Nguyen[2], Ky Phuong Ha Huynh[1*]

[1]*Research Institute for Sustainable Energy, University of Technology, Vietnam National University, Ho Chi Minh city*

[2]*Institute of Chemical Technology, Vietnam Academy of Science and Technology*

Received 5 October 2018; accepted 10 January 2019

Abstract:

In this study, CuO-doped material fabricated from rice husk ash and red mud was modified by CeO_2 promoter and urea using the impregnation method. The obtained samples were investigated for catalytic degradation of aromatic derivatives (benzene, toluene, and *p*-xylene - BTX) at a temperature range of 275 to 450°C. This demonstrated that all samples were highly active in the BTX treatment. Several techniques, such as X-ray powder diffraction analysis (XRD), scanning electron microscopy (SEM), transmission electron microscopy (TEM), BET surface areas and pore parameters (N_2 physisorption), and hydrogen temperature programed reduction (H_2-TPR), were applied to analyse properties of obtained materials. The modification of CuO-doped catalytic material by both CeO_2 promoter and urea resulted in decreased particle size, increased CuO dispersion, and improved catalytic activity of the material. In relation to this material, the conversions of benzene, toluene, and p-xylene were 66.1%, 96.8%, and 96.8% respectively at 375°C.

Keywords: **benzene, CuO-doped catalytic material, toluene, treatment, xylene.**

Classification numbers: **2.2, 2.3**

Introduction

The emission of volatile organic compounds (VOCs) due to industrial manufacturing has caused many severe environmental problems, such as petrochemical smog, acid rain, ozone layer depletion, and climate change [1]. Aromatic compounds, particularly benzene, toluene, and xylene (BTX), are used as raw materials in the production of chemicals as well as ordinary solvents [2]. Therefore, emissions of these pollutants require strict monitoring. Deep oxidation is a potential method of treating VOCs at low concentrations [3]. This does not require additional fuel, which enables the reduced consumption of energy; this method can also be applied at a lower temperature (≤450°C) relative to thermal oxidation (700°C) [4]. The exploitation of catalysts for deep oxidation based on waste materials has recently sparked interest because it is an environmentally friendly process which can not only reduce costs but also save raw materials.

Red mud (RM) refers to the residual solid waste which remains after bauxite leaching by alkali in the aluminum industry. Its primary components include Fe_2O_3, Al_2O_3, SiO_2, CaO, and Na_2O [5, 6]. Since it offers advantages such as small particle size, high thermal stability, sintering resistance, and resistance to poisoning, substantial efforts have been directed toward utilising RM as an adsorbent as well as a catalyst for environmentally benign processes [6, 7]. However, the catalytic application of RM is limited due to its high alkalinity, primarily originating from Na and Ca, which can poison and reduce catalytic activity [8]. Rice husk ash (RHA), which is composed of SiO_2 (95%), was released through a reuse RHA process for energy purposes. One idea has been considered to investigate the synthesis of material with a partial zeolite structure (ZRM) through the

*Corresponding author: Email: hkpha@hcmut.edu.vn

combination of RHA and RM with the primary components of Fe_2O_3, Al_2O_3, SiO_2, CaO, and Na_2O at high pH. The alkalinity must be neutralised or acidified, which can reduce the cost of this synthesis process. In the research of Quyen, et. al. [6], material in nanoparticles with a partial zeolite structure (ZRM) was synthesised successfully by using the waste materials from red mud (RM) containing alumina and alkalis, or NaOH and rice husk ash (RHA). Relative to RM (23.59 m^2/g) or RHA (28.35 m^2/g), catalysts with partial zeolite structure have significantly higher specific surface area (70.76 m^2/g) [6].

Furthermore, CuO-CeO_2 catalysts supported on ZRM were prepared through the co-impregnation method. The modification of the CuO and ZRM catalyst by adding CeO_2 had reduced the size and increased the dispersive performance, and the synchronism of catalysts' nanoparticles significantly improved the catalytic activity in *p*-xylene oxidation at 275 to 400^{0}C. Sample 5 wt.% CuO and ZRM modified with 3 wt.% CeO_2 (denoted as CuCe) was optimal for *p*-xylene deep oxidation. Furthermore, CuO and ZRM catalyst was also prepared through a urea-nitrate combustion technique. It demonstrated that through this technique, active sites such as copper and iron oxides had enhanced dispersion on material surfaces with smaller particle size, which increased the activity of catalysts in *p*-xylene oxidation. Catalyst 5 wt.% CuO and ZRM synthesised with the urea and nitrate molar ratio of 2 was optimal (denoted as Cu(U)). Therefore, the combination of adding CeO_2 and using the urea-nitrate combustion technique is expected to improve properties of material, resulting in an enhanced catalytic performance in the BTX oxidation. In this research, 5 wt.% CuO/ZRM material modified with 3 wt.% CeO_2 was synthesised through a urea-nitrate combustion method with the urea-nitrate molar ratio of 2 (denoted as CuCe(U)). The obtained catalyst and the optimal catalysts in our previous research (i.e., Cu(U) and CuCe samples) were investigated through BTX oxidation.

Experimental

Catalyst synthesis and characterisation

The material with partial zeolite structure (ZRM) was synthesised from red mud and rice husk based on the process detailed in the research [6], which involved $Cu(NO_3)_2.3H_2O$ (Xilong, >99%), $Ce(NO_3)_3.6H_2O$ (Merck, >99%), urea (Xilong, >99%), and deionised water. Cu(U) and ZRM as well as CuCe and ZRM catalysts were synthesised based on the process detailed in our previous research [9]. Catalysts were obtained through the wet impregnation of the mixture solution of $Cu(NO_3)_2$, and $Ce(NO_3)_3$ and urea on ZRM. The loading content of CuO and CeO_2 was fixed at 5 wt.% and 3 wt.%, respectively, and a urea-nitrate molar ratio of 2. The obtained suspension was dried in air at 80, 100, and 120^{0}C for 2 hours at each temperature. Finally, the sample was calcined in air flow at 500^{0}C for 3 hours. This sample was denoted as CuCe(U) and ZRM. The characteristics of the as-synthesised materials were determined using the distinct techniques presented in our paper [9].

Catalytic activity

Before the activity was tested, all samples were activated at 450^{0}C for 4 hours in air flow with a velocity of 200 $ml.min^{-1}$. The catalytic measurement of the samples in deep oxidation of BTX (benzene, toluene and p-xylene) was performed in a micro-flow reactor under atmospheric pressure at a temperature range of 275 to 450^{0}C. The concentrations of BTX and O_2 in the stream were 0.34 and 10.5 mol%, respectively. The weight hourly space velocity (WHSV) was 12,000 $ml.h^{-1}.g^{-1}$, and the mass of catalyst was 1.0 g with a size range of 0.25 to 0.50 mm.

Gas mixtures in the input and output flow of the reactor were analysed using the Agilent 6890 Plus Gas Chromatograph (HP-USA) with FID detector, capillary column DB 624 (outer diameter of 0.32 mm; thickness of 0.25 μm and length of 30 m). The tests were conducted in triplicate to ensure the accuracy of the results.

Results and discussion

Physicochemical characteristics of materials

X-ray powder diffraction (XRD) patterns of the samples were displayed in Fig. 1, which indicates the main components of red mud and rice husk ash; the typical reflections of hematite (Fe_2O_3) can be observed at 2θ = 24.4, 29.8, 34.5, 36.1, 41.3, 54.4, 63.5, and 64.5^0. According to Huang, et al. [7], the peaks of A-type zeolite can be observed at 2θ = 24.4, 29.8, and 36.1^0. Additionally, according to Volanti, et al. [10], the typical reflections of CuO can be exhibited at 2θ = 36.1, 41.3, 49.9, and 54.4^0 in the XRD patterns. Therefore, it demonstrated that the XRD patterns of the samples appeared simultaneously with the primary components of the red mud (hematite), A-type zeolite, and CuO crystals, with the strongest intensity at 2θ = 34.5 and 36.1^0. No additional peaks of CeO_2 phase were observed in CuCe and CuCe(U) samples. It indicated that the CeO_2 species could barely be detected by means of the XRD technique, even with the CeO_2 loading up to 4 wt.%; the CeO_2 phase was well-dispersed on the material. Based on the XRD result at the highest peak with 2θ = 36.1^0, the average size of crystals in the samples was determined based on the Scherrer's equation. The average crystal sizes of Cu(U), CuCe, and CuCe(U) catalysts were determined as being 17.2, 15.7, and 14.5 nm, respectively. With CuCe and CuCe(U) samples, the CeO_2 species could barely be detected bythe XRD technique, which suggests that CeO_2 is well-dispersed.

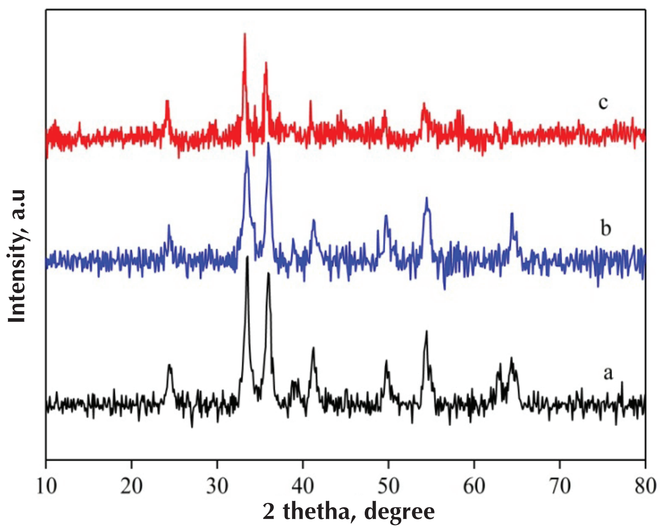

Fig. 1. XRD patterns of catalysts: a) Cu(U); b) CuCe; c) CuCe(U).

The SEM images illustrated that the catalysts reached high porosity with small nanoparticle size (illustrated in Fig. 2). The surface structure of all samples appeared to be more porous. Based on the TEM images of samples, one can deduce that the modification of CuO supported on ZRM by the CeO_2 promoter and the addition of urea in the solution of precursors resulted in reduced particle size and increased CuO dispersion on the material relative to the CuO and ZRM catalyst [9] (illustrated in Fig. 3).

Based on TEM images of samples from the ImageJ software, the nanosized distribution of the samples was depicted in Fig. 4. Base on the size distribution histogram, the nanoparticles on the catalysts had a size range smaller than 50 nm, and the average particle sizes of the Cu(U), CuCe, and CuCe(U) catalysts were determined as being 16.6, 15.4, and 14.7 nm, respectively. These results were consistent with those obatined from the XRD results (seen in Fig. 5), in which the CuCe(U) sample exhibited the smallest nanoparticles.

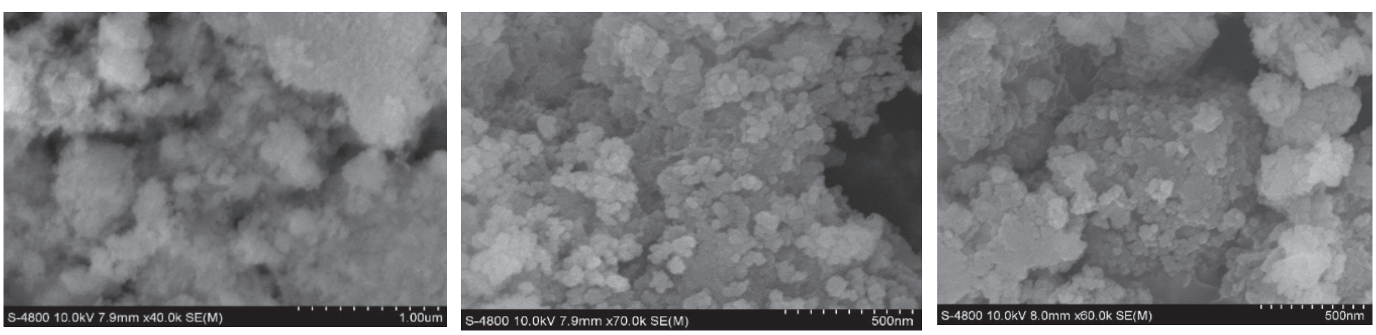

(A) Cu(U) **(B) CuCe** **(C) CuCe(U)**

Fig. 2. SEM images of catalysts.

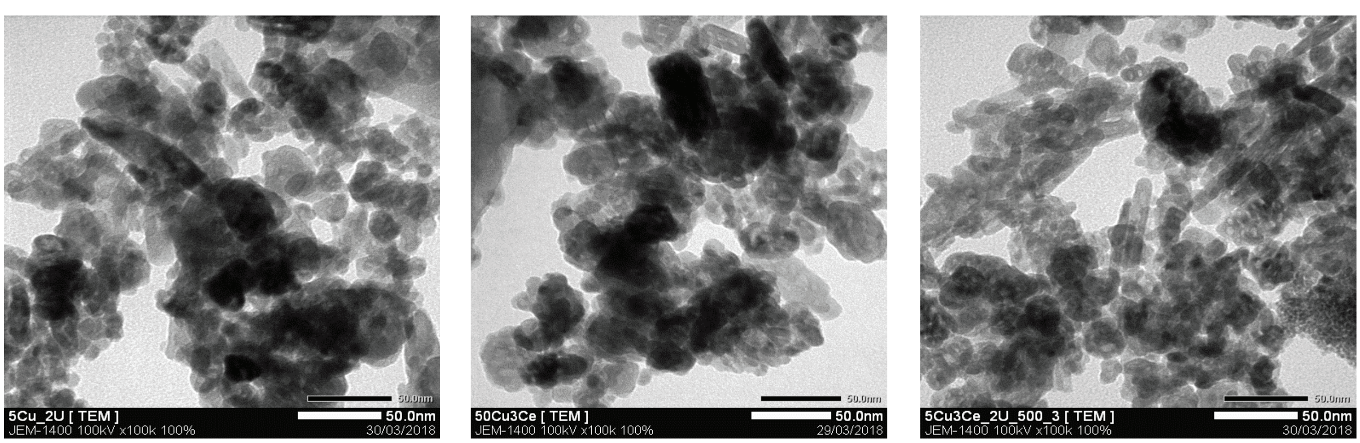

(A) Cu(U) **(B) CuCe** **(C) CuCe(U)**

Fig. 3. TEM images of catalysts.

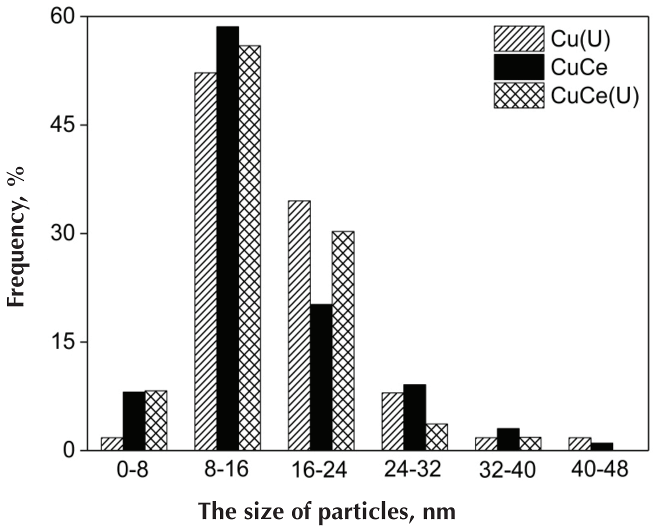

Fig. 4. Size distribution histogram of catalysts.

Comparisons of the BET specific surface area, average pore diameter, pore volume and particle size of the samples are illustrated in Fig. 5. The samples reached medium BET surface and porosity. Relative to CuCe and Cu(U), the CuCe(U) catalyst had a higher BET surface area (40 m^2/g) and a larger pore volume (0.027 m^3/g). The results demonstrated that the CuCe(U) sample exhibited higher porosity and smaller nanoparticles with higher reduction, which could result in an enhanced catalytic performance in BTX deep oxidation.

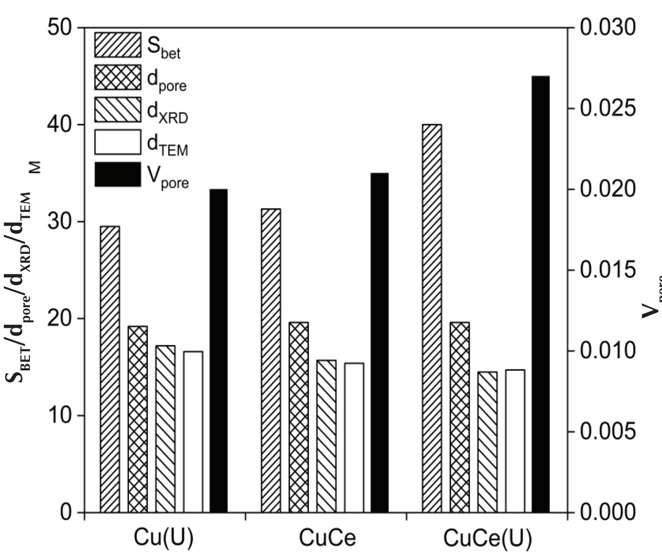

Fig. 5. Comparison of the BET surface (S_{BET}, m^2/g), average pore diameter (d_{pore}, Å), pore volume (V_{pore}, cm^3/g), and average diameter of particles based on the XRD results at 2θ = 36.1^0 (d_{XRD}, nm) and the TEM results (d_{TEM}, nm) of samples.

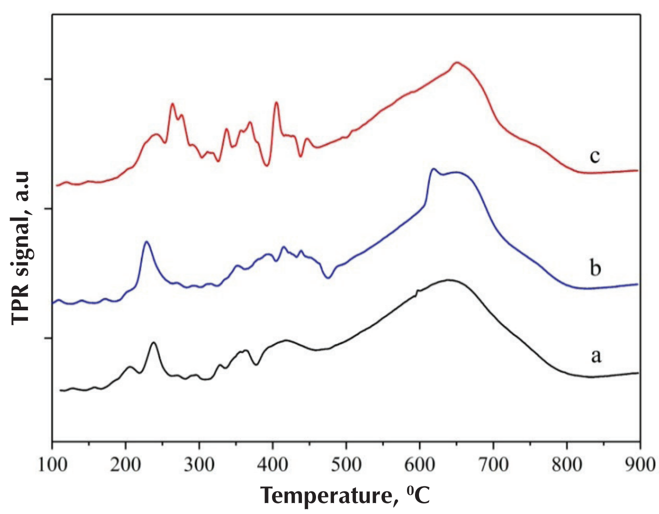

Fig. 6. TPR profiles of catalysts: (a) Cu(U); (b) CuCe; (c) CuCe(U).

The H_2-TPR patterns of samples are depicted in Fig. 6. The H_2-TPR profile of the CuCe sample displays three reduction peaks. The first peak at the temperature range of 200 to 300^{0}C resulted from the reduction of the bulk-like CuO phases [11]; the second peak with a low intensity at the temperature range of 300 to 450^{0}C was attributed to the reduction of Fe_2O_3 to Fe_3O_4; the third broad one at 450 to 850^{0}C with T_{max} = 700^{0}C could be ascribed to the reduction process from Fe_3O_4 to FeO or Fe [12]. On the CuCe and CuCe(U) samples, another peak at the range of 400 to 500^{0}C was regarded as a characteristic of CuO bound to CeO_2. Relative to previous studies [9], the materials shifted to the lower temperature range; therefore, this catalyst was reduced more easily. In the CuCe(U) sample, the peak was narrower than another. This proved that CuO, CeO_2, and Fe_2O_3 had enhanced dispersion with smaller particle sizes in this sample.

Performance of the materials in the BTX treatment

Figure 7 illustrates the catalytic activity of the materials in terms of BTX oxidation. The conversion of p-xylene on all catalysts was higher than that of both benzene and toluene. Evidently, the catalytic activity of all samples increased in the following order: benzene < toluene < *p*-xylene. This consequence confirmed that the catalytic activity for the treatment of aromatic compounds is highly reliant upon the ionisation potential of methyl derivatives, the strength of the weakest C\H bond in the structure, and the relative adsorption strength of model compounds. All

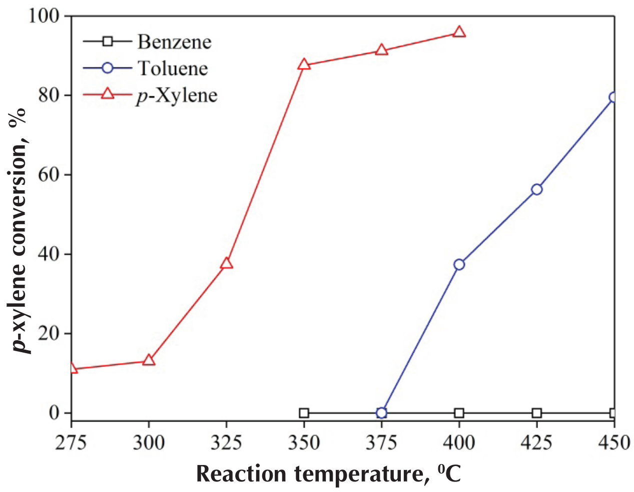

(A) Cu(U) catalyst

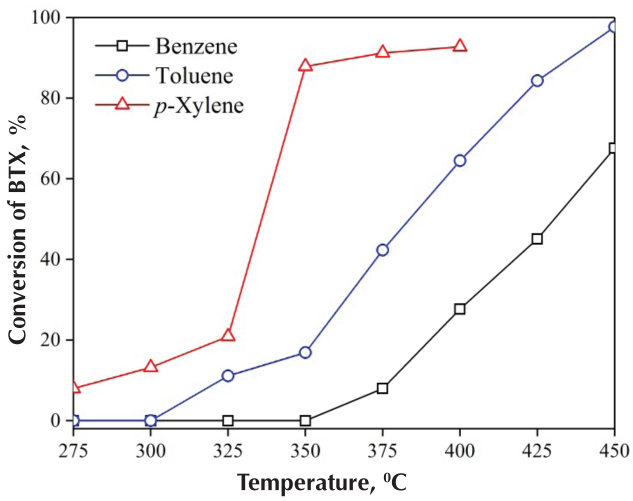

(B) CuCe catalyst

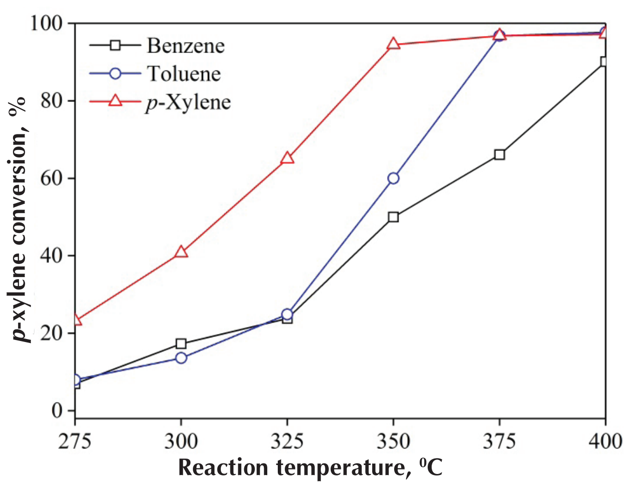

(C) CuCe(U) catalyst

Fig. 7. The catalytic activity of samples in deep oxidation of benzene, toluene, and *p*-xylene (V = 12,000 ml.h^{-1}.g^{-1}; m_{cat} = 1.0 gam; C_{BTX}= 0.34 mol%; C_{oxy} = 10.5 mol%).

catalysts exhibited low activity at reaction temperatures below 300°C. With further increasing reaction temperature, the catalysts became highly active performances, in which the complete conversion of *p*-xylene over all materials was obtained at the reaction temperature of 400°C; it achieved complete conversion of toluene at 450°C. This indicated that the highest BTX conversion was obtained by the CuCe(U) sample. It exhibited superior catalytic performance in terms of the conversions of *p*-xylene, toluene, and benzene, corresponding to 95, 60, and 55% at a reaction temperature of 350°C.

Therefore, the modification of CuO and ZRM by the combination of the CeO_2 promoter and addition of urea to the solution of precursors resulted in reduced particle size, increased CuO dispersion on the material surface, and enhanced catalytic activity of the material. This was demonstrated by the XRD, SEM, TEM, BET, and H_2-TPR results.

Conclusions

Three catalysts prepared through wetness impregnation or the combustion method towards BTX deep oxidation have been evaluated. All samples demonstrated the small nanoparticle size, the high dispersion of copper and the ceria species, and the strong support of metal interaction, which presented more Ce^{4+}/Ce^{3+} and/or Cu^{2+}/Cu^{+} redox couples and indicated a high redox ability. The material synthesised through the combination of the CeO_2 promoter and the addition of urea to the solution of the precursors - CuCe(U) sample exhibited the optimal catalytic performance in terms of BTX oxidation. The catalytic activity of materials in the oxidation of BTX compounds is significantly impacted by the strength of the weak C\H bond in the structure of each BTX.

ACKNOWLEDGEMENTS

The study was supported by Science and Technology Incubator Youth Program, managed by the Center for Science and Technology Development, Ho Chi Minh Communist Youth Union, the contract number is "09/2018/HD-KHCN-VU".

The authors declare that there is no conflict of interest regarding the publication of this article.

REFERENCES

[1] M.S. Kamal, S.A. Razzak, M.M. Hossain (2016), "Catalytic oxidation of volatile organic compounds (VOCs) - a review", *Atmospheric Environment*, **140**, pp.117-134.

[2] A.J. Schwanke, S.B. Pergher, L.F. Probst, R. Balzer (2017), "Gallium-containing mesoporous silica: supported catalysts with high catalytic activity for oxidation of benzene, toluene and o-xylene", *Journal of the Brazilian Chemical Society*, **28(1)**, pp.42-48.

[3] W.A. da Costa, C.R. Lima, F.G.S. da Silva Filho, M.S. de Oliveira, R.M. Cordeiro, R.N. de Carvalho Junior, M.C. Martelli, D.D.S.B. Brasil (2017), "Computer simulation of benzene, toluene and p-xylene adsorption onto activated carbon", *African Journal of Biotechnology*, **16(20)**, pp.1176-1181.

[4] H.S. Kim, T.W. Kim, H.L. Koh, S.H. Lee, B.R. Min (2005), "Complete benzene oxidation over Pt-Pd bimetal catalyst supported on γ-alumina: influence of Pt-Pd ratio on the catalytic activity", *Applied Catalysis A: General*, **280(2)**, pp.125-131.

[5] Y. Liu, R. Naidu, H. Ming (2011), "Red mud as an amendment for pollutants in solid and liquid phases", *Geoderma*, **163(1-2)**, pp.1-12.

[6] D.T.N. Quyen, L.C. Loc, H.K.P. Ha, D.T.H. Nga, N. Tri, N.T.T. Van (2017), "Synthesis of adsorbent with zeolite structure from red mud and rice husk ash and its properties", *AIP Conference Proceedings*, p.020034.

[7] A. Huang, Y. Lin, W. Yang (2004), "Synthesis and properties of A-type zeolite membranes by secondary growth method with vacuum seeding", *Journal of Membrane Science*, **245(1-2)**, pp.41-51.

[8] S. Ordóñez, H. Sastre, F.V. Díez (2001), "Characterisation and deactivation studies of sulfided red mud used as catalyst for the hydrodechlorination of tetrachloroethylene", *Applied Catalysis B: Environmental*, **29(4)**, pp.263-273.

[9] D.T.M. Hieu, T.Q. Thinh, N. Tri, N.T.T. Van, H.K.P. Ha (2018), "Fabrication of CuO-doped catalytic nanomaterial containing zeolite synthesized from red mud and rice husk ash for CO oxidation", *Adv. Nat. Sci.: Nanosci. Nanotechnol.*, **9**, p.025005 (7pp).

[10] D. Volanti, D. Keyson, L. Cavalcante, A.Z. Simões, M. Joya, E. Longo, J.A. Varela, P. Pizani, A. Souza (2008), "Synthesis and characterization of CuO flower-nanostructure processing by a domestic hydrothermal microwave", *Journal of Alloys and Compounds*, **459(1)**, pp.537-542.

[11] C.L. Luu, T. Nguyen, T.C. Hoang, M.N. Hoang, C.A. Ha (2015), "The role of carriers in properties and performance of Pt-CuO nanocatalysts in low temperature oxidation of CO and p-xylene", *Adv. Nat. Sci.: Nanosci. Nanotechnol.*, **6**, p.015011 (9pp).

[12] S. Sushil, V.S. Batra (2008), "Catalytic applications of red mud, an aluminium industry waste: a review", *Applied Catalysis B: Environmental*, **81(1)**, pp.64-77.

Doi: 10.31276/VJSTE.61(2).35-41

Determination of aquaculture distribution by using remote sensing technology in Thanh Phu district, Ben Tre province, Vietnam

Nguyen Thi Hong Diep[1*], Thitinat Korsem[2], Nguyen Trong Can[1], Walaiporn Phonphan[2], Vo Quang Minh[1]

[1]*College of Environment and Natural Resources, Can Tho University, Vietnam*
[2]*Faculty of Science and Technology, Suan Sunandha Rajabhat University, Thailand*

Received 18 July 2018; accepted 25 October 2018

Abstract:

Aquaculture is an important economic activity in the coastal zone of Vietnam. Thanh Phu is one the coastal districts in Ben Tre province that rears brackish aquaculture. In recent years, farmers could not grow shrimp because of salinity intrusion and market price fluctuation. This study aims to determine aquaculture and fallow aquaculture pond distribution by using the three indices of NDVI (Normalized Difference Vegetation Index), MNDWI (Modified Normalized Difference Water Index) and NDBaI (Modified Difference Bareness Index) on Landsat 8 imagery. The results reveal that remote sensing can support the detection of aquaculture and fallow ponds with a high accuracy of 77%. The total aquaculture area is approximately 13,093.65 ha, of which the total fallow area is 581.49 ha (roughly 4.44% of the total aquaculture area). Moreover, the fallow ponds are randomly distributed in all four ecological zones and mostly in the fourth ecological region (about 73.92%). In the fourth region, saline concentration in water is from 20 to 30‰, which directly influences cultured shrimp farms. The results also indicate the spatial distribution of aquaculture ponds and ineffective aquaculture locations using Landsat 8 imagery via index image analysis. The findings support the local management's decision making on further aquaculture planning.

Keywords: **aquaculture, Ben Tre province, ecological zone, fallow pond, satellite image indices.**

Classification number: **2.3**

Introduction

Ben Tre province is one of the coastal provinces located in the Lower Mekong River, Vietnam. Its major industry is agriculture, including orchard and rice crop cultivation and aquaculture. The famous products of Ben Tre province are made from coconuts. Two types of farming system are commonly adopted in the coastal areas, namely rice-shrimp rotation and shrimp farming [1]. These farming systems can generate higher income than mono-cropping or double rice cropping.

Changes in climate have adversely affected the coastal areas in recent years, causing sea level rise, increase in temperature and rainfall, drought, salinity intrusion, and spread of epidemic diseases in both rice and shrimp farms; consequently, aquaculture farming encountered a reduction in both production and income [2].

Remote sensing and geographical information system (GIS) are useful tools for detecting the spatial distribution of natural resources and aquaculture areas. This research applied remote sensing and GIS technologies to determine shrimp farming and ineffective shrimp pond. That refers to a pond where farming culture has ceased due loss of profit caused by the damage of shrimp diseases, thereby resulting in "a fallow pond". This study aims to identify aquaculture distribution and locate ineffective shrimp ponds. Its findings endeavour to support local decision making on the management of coastal aquaculture resources.

Materials and methodology

Study area

Thanh Phu is one of coastal districts located in the

*Corresponding author: Email: nthdiep@ctu.edu.vn

southeast of Ben Tre province. Its distance from the seashore is approximately 45 km, and its total area is roughly 411 km^2 (Fig. 1) [3]. Thanh Phu was established by an accretion of Ham Luong and Co Chien rivers several centuries ago. Its coastal land consists of paddy fields, sand dunes and mangrove forests. Thanh Phu district is considered as a developing core of the third economic region (i.e. salty region) [4]. The entire district land is affected by salinity intrusion that is suitable for brackish farming systems, including rice-shrimp rotation, extensive-intensive shrimp and clam exploitation on the coastal tidal mudflats [4, 5]. The brackish aquaculture is a principal agricultural product and plays an important role in the district economy [6].

Materials

Satellite imagery: Landsat 8 (OLI) images from 2015 to 2016 were collected from the U.S. Geological Survey website (http://earthexplorer.usgs.gov/). The Landsat 8 images have a medium resolution with 30 metres. Eight images were used, including four images each for the sunny and rainy seasons. The acquired period was focused on the two seasons to detect shrimp culture, rice-shrimp rotation system and fallow shrimp pond culture. Farmers in Thanh Phu district discontinued the cultivation of shrimp farms in the dry season of 2016 due to shrimp diseases, which reduced production.

GIS data: administrative and land use maps, natural river and canal maps and information about ecological zones in Thanh Phu district, Ben Tre province were obtained from the Ben Tre Department of Natural Resources and Environment (Ben Tre DNRE) and the Ben Tre Department of Agriculture and Rural Development (Ben Tre ARD).

Methods

Remote sensing methods:

A subset study area was identified to limit the scope of the research area. Besides, rivers and canals were also removed to reduce the confusion between rivers and aquaculture areas throughout the year.

Removing cloud from the imagery: Landsat 8 level 1 data products include a 16-bit quality assessment (QA) band containing integer values that represent bit-packed combinations of surface, atmosphere and sensor conditions in which bits 12-13 can be cirrus cloud and bits 14-15 are cloudy pixels. The reference values from 36,864 to 39,936 may be cloud, and the values from 53,248 to 61,440 are cloudy values [7]. We also used band 1 (coastal aerosol), band 9 (cirrus) and band 10 (thermal infrared, or TIR) to remove cloud. Thick cloud was detected by selecting a threshold on bands 9 and 10 (i.e. high values on band 9 and low values on band 10). Thin cloud was masked using bands 1, 9 and 10 using only the low values in both bands

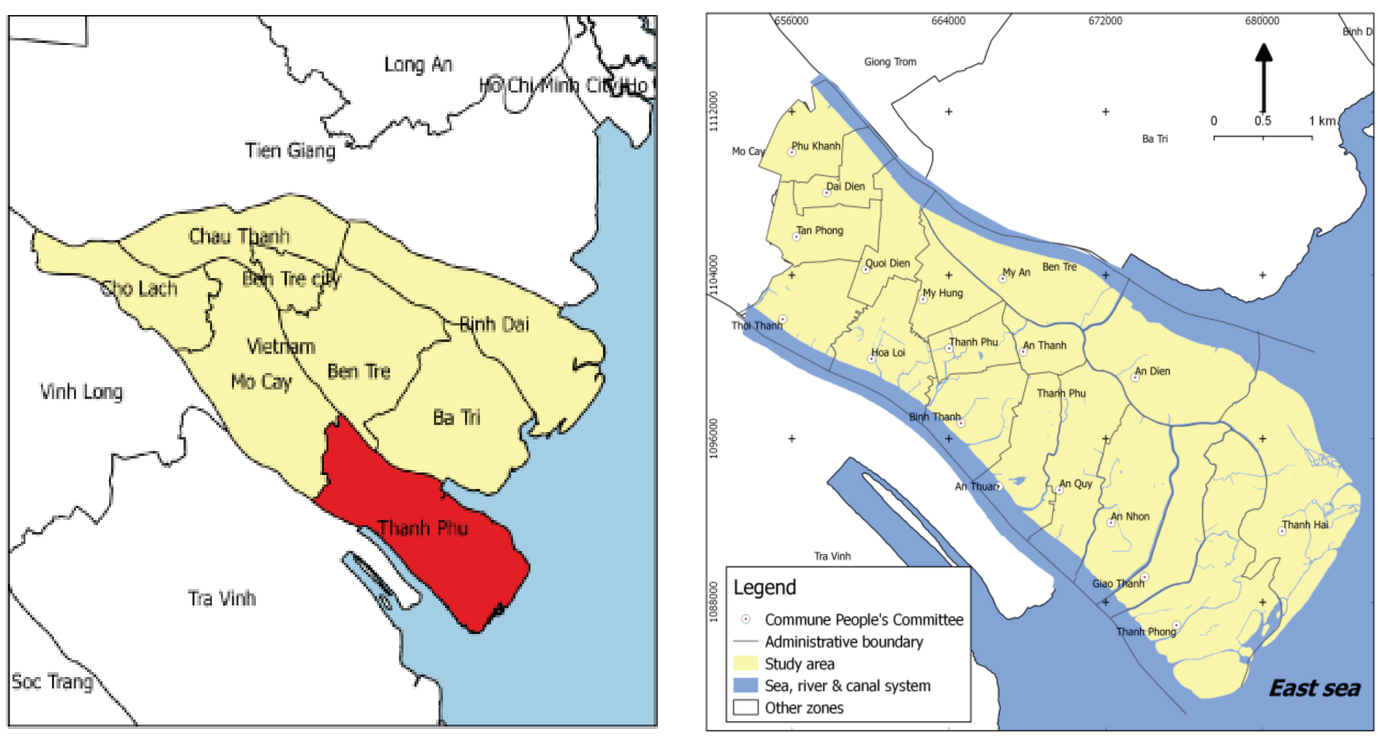

Fig. 1. Study site of Thanh Phu district.

9 and 10. Cloud is also normally brighter than the other objects, especially in the blue band, which is given a result in high pixel values on band 1 [8]. The cloudy values were used to create cloud mask in each image; cloud pixels were subsequently deleted by the cloud mask and filled values by multi-time images.

Creating spectral indices: the research applied three indices to extract information about vegetation, water and bare land from Landsat 8 imagery. The corresponding indices are normalized difference vegetation index (NDVI), modified normalized difference water index (MNDWI) and modified difference bareness index (NDBaI). These indices were calculated using Equations (1) to (3) (Table 1).

Table 1. Spectral index equations.

Index name	Equation	Reference	Equation number
NDVI	$\frac{NIR - Red}{NIR + Red}$	[9]	(1)
MNDWI	$\frac{Green - SWIR}{Green + SWIR}$	[10, 11]	(2)
NDBaI	$\frac{SWIR - TIRS}{SWIR + TIRS}$	[12, 13]	(3)

*Note: on the Landsat 8 (OLI) imagery, Red: visible spectrum band of red wavelength (band 4); Green: visible spectrum band of green wavelength (band 3); NIR: near-infrared radiation (band 5); SWIR: shortwave infrared (band 6); and TIR: thermal infrared (band 10).

Classification: the range of the index value is from -1 to 1. The threshold method of classification was applied to categorize the index images into three land cover types, namely aquaculture, vegetation and bare land. Positive values ranging from 0 to 1 were applied to classify water body and vegetation using NDVI and MNDWI indices; meanwhile, the beginning values of the NDBaI range were categorized for bare land.

Accuracy assessment:

The accuracy of class identification requires assessment. This research applied a confusion matrix (or error matrix) as the quantitative method of characterizing image classification accuracy. The overall accuracy (OA) of the classification is the sum of the pixels of diagonal elements by the total number of pixels (see Eq. (4)), where PCP are pixels correctly classified, and TP is the total pixels on the image classification [14].

$$OA = \frac{PCP}{TP} \quad (4)$$

Kappa coefficient is another accuracy indicator. It is a measure of how the classification results compare to the values assigned by chance. It can take values from 0 to 1. The random point tool was used to create 100 randomly ground truth points on the classified results that were collated with the aquaculture layer on the land use map.

GIS methods:

The land cover classifications from the eight index images were converted to vector file data. The same index data were overlaid by a union algorithm to synthesize all surface distributions. The results revealed the distribution of vegetation, aquaculture and bare land. The synthesized data were overlaid to detect land use/land cover (LULC) and aquaculture farming distribution.

Results

Satellite imagery data collection

The eight scenes of Landsat 8 were selected from 2015 (January, February, November and December) and 2016 (February, March, April and May). The images were located in path 125 and row 53; UTM 48 Northern and WGS-84 were used as the projection and reference ellipsoid, respectively (Fig. 2). One scene covers approximately 185×180 km and a 30-metre spatial resolution for the multispectral bands and a 15-metre spatial resolution for the panchromatic band. Landsat 8 Level 1 product includes 11 bands, QA band and metadata file.

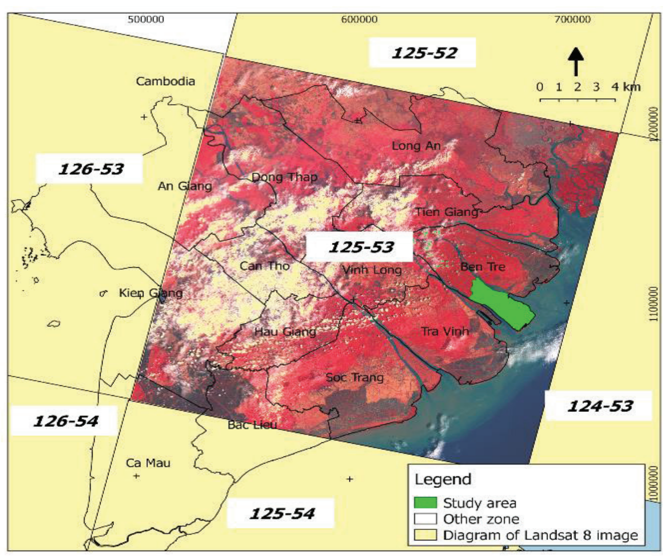

Fig. 2. Landsat image scene, with the study area highlighted in green.

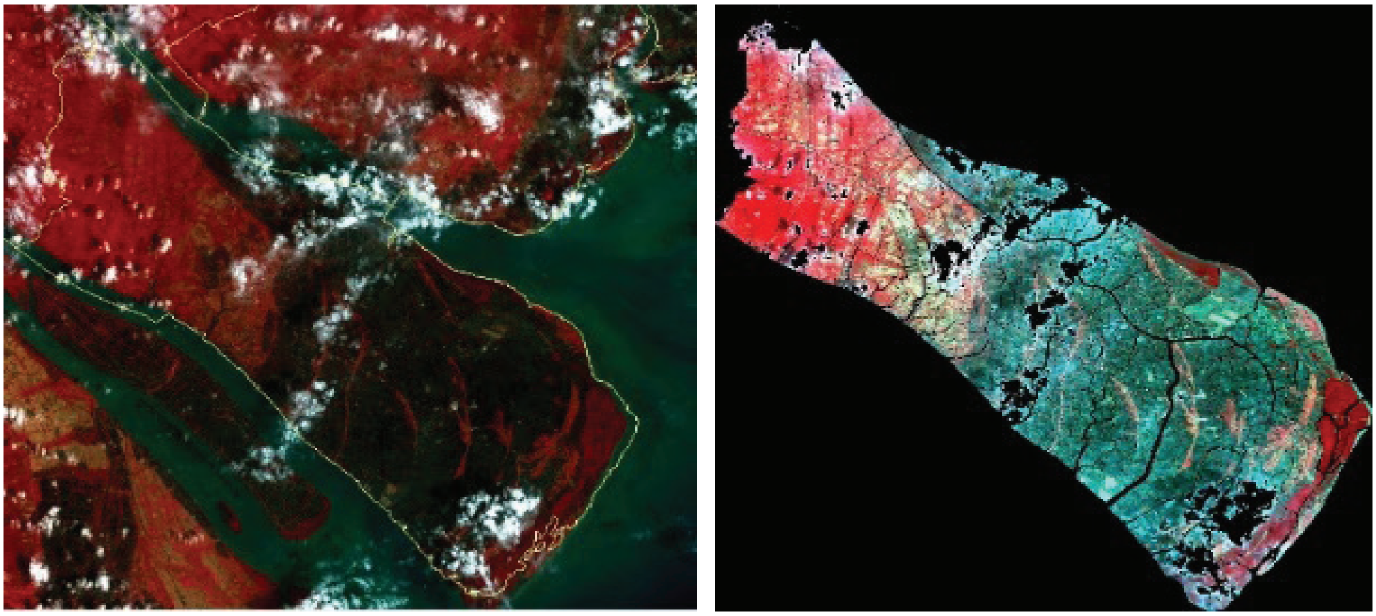

(A) (B)

Fig. 3. (A) Landsat 8 image, (B) subset study area with removed cloud.

Determining the study area and removing clouds

The Landsat images were affected by clouds (Fig. 3A) and included unrelated zones, rivers and cloud. The subset study area was removed cloud to limit the confusion between water surface and aquaculture area (Fig. 3B).

Land covers distribution

Figure 4A illustrates the vegetation that was detected by NDVI index with a range of value from 0.17 to 0.57. The vegetation area is approximately 18,972.72 ha, of which roughly 1,350 ha comprise freshwater plants in the northwest, including rice crops, orchards and annual plants. The plantation is near Mo Cay Nam boundary in the communes of Thoi Thanh, Hoa Loi and Tan Phong. The vegetation also includes a mangrove forest in the coastal area of Thanh Hai commune, and it measures 1,450 ha (Fig. 4A).

Water surfaces were determined by the MNDWI index from 0 to 0.33. The largest water surface area was contributed by the images in the sunny season, the main season for cultivating shrimp culture. The total area of water surfaces was roughly 20,885.85 ha, including extensive-intensive shrimp farming, rice-shrimp rotational cropping and wetland area. Water surface was distributed virtually

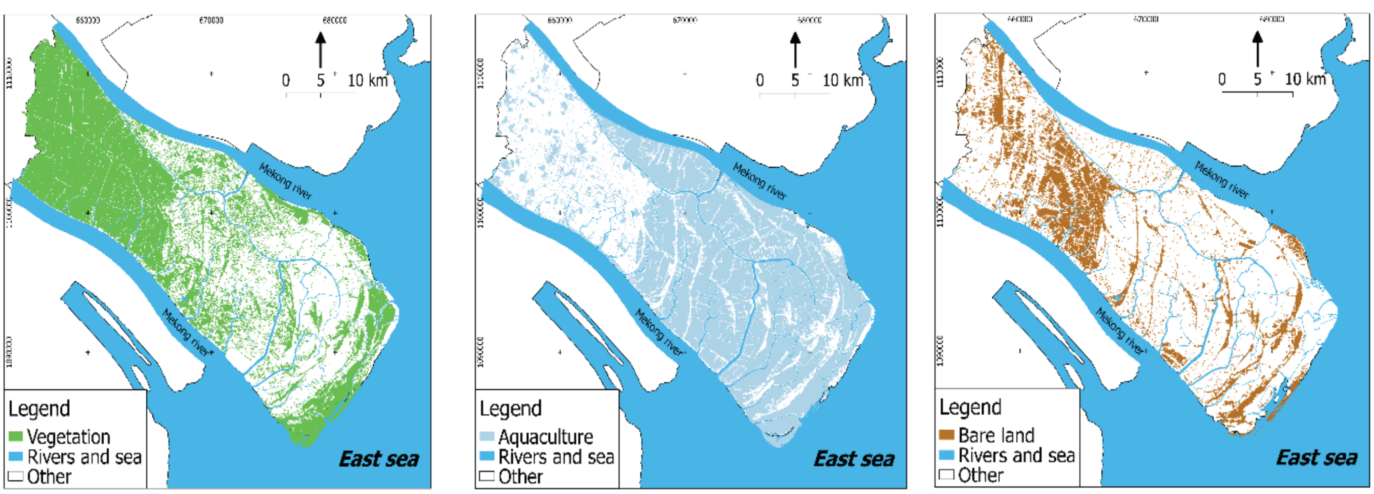

(A) Vegetation **(B) Water surfaces** **(C) Bare land**

Fig. 4. Land cover distribution of vegetation (A), water surfaces (B) and bare land (C) on the study site.

along the coastal villages such as Thuan Phong (3,300 ha), Thanh Hai (2,800 ha), An Dien (2,400 ha) and An Nhon (2,000 ha) (Fig. 4B).

Bare land was retrieved by the NDBaI index from -0.375 to -0.001. It covered about 7,414.21 ha and achieved the largest area in January, February and March after harvesting rice crops. Bare land was mainly located in My Hung, Thanh Phu and Hoa Loi communes (i.e. harvested paddy fields), and sandy dunes located along the seaside (Fig. 4C).

Aquaculture and fallow ponds

Land use/land cover is classified into six types, namely paddy field (i.e. mono and triple crops), sandy soil, residential area, rice-shrimp rotation farming, perennial plant (i.e. orchard and mangrove forest) and aquaculture. The aquaculture area was extracted from the LULC map. It is located in the southeast part (i.e. both in the central and coastal areas) of Thanh Phu district; its distribution is denser than in the coastal zones. The total aquaculture area of 13,093.65 ha consists of extensive-intensive shrimp farming.

The fallow area was also extracted by superimposing the water surface and bare land layers. A fallow shrimp pond assumed shrimp cultivation in 2015 and halted this activity in 2016. Thus, the fallow shrimp pond was detected when its attribute data had both water-surface and bare-land in 2015 and 2016, respectively. The total fallow aquaculture area was 581.49 ha, which accounted for 4.44% of the total aquaculture area. Generally, the fallow aquaculture ponds were distributed randomly in the study area, and their distribution was almost along the seashore (Fig. 5).

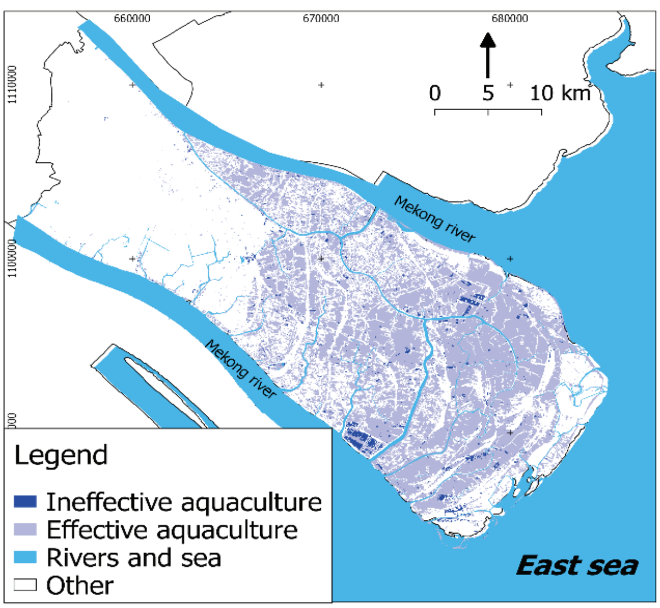

Fig. 5. Distribution map of aquaculture and fallow aquaculture ponds.

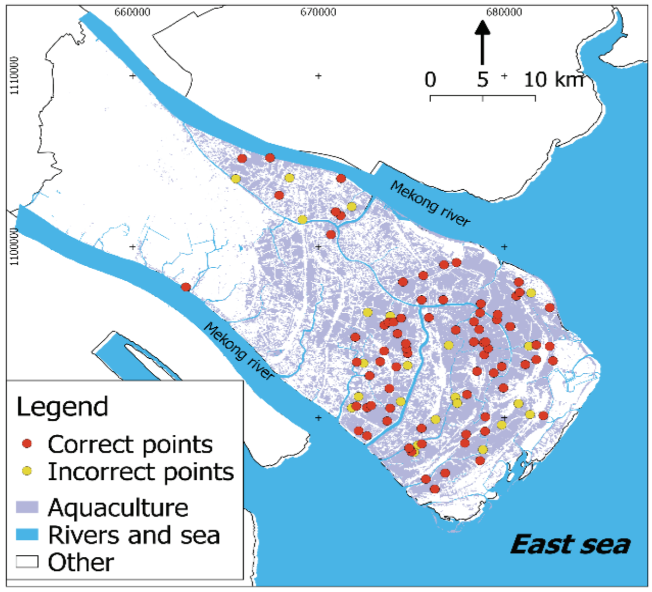

Fig. 6. Random points in the aquaculture area.

Accuracy assessment

Land use map utilized the aquaculture layer (Ben Tre DNRE, 2015) as truth data to assess the accuracy and collate the classified results and survey on 100 ground truth points. A total of 77/100 correct points (Fig. 6) demonstrated the overall accuracy achieved, with a high reliability of 77%.

Determining the fallow area in ecological regions

Thanh Phu district comprise four natural ecological regions. The detailed characteristics of each ecological region are presented in Table 2, highlighting the differences in saline concentration. Ecological region 1 has a freshwater ecosystem that is suitable for farming systems of rice crop, orchard, giant freshwater prawn and freshwater fish culture. The rest of the ecological regions (i.e. regions 2, 3, and 4) have a brackish water ecosystem that is appropriate for rice-shrimp rotation farming and shrimp cultivation such as extensive shrimp, intensive shrimp and shrimp-blood cockle combination.

Table 2. Ecological region in Thanh Phu district.

Region	ASSD (cm)	Salinity (°/$_{oo}$)	Flood level (cm)	Area (ha)
1	No (<50)	<4	0-40	3,211.6
2	No	4-10	0-20	8,210.3
3	No (>50)	10-20	0-40	6,993.0
4	No	20-30	0-40	17,171.6

*Note: ASSD: acid sulphate soil depth.
Source: Ben Tre Department of Agriculture and Rural Development, 2015.

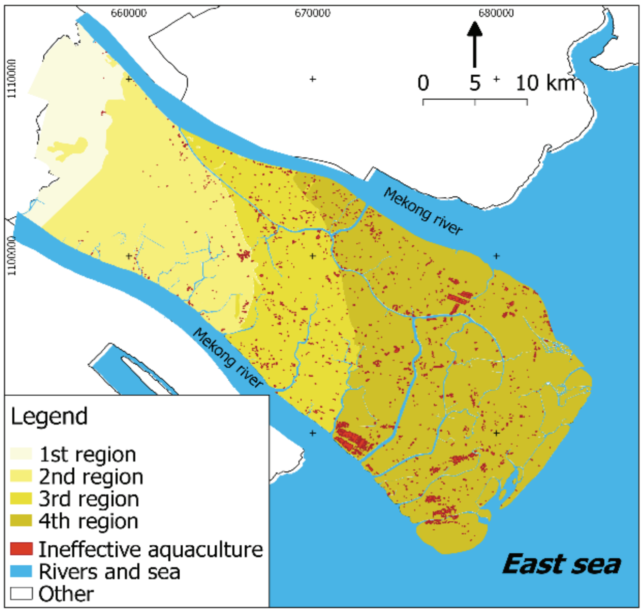

Fig. 7. Fallow ponds in each ecological zone.

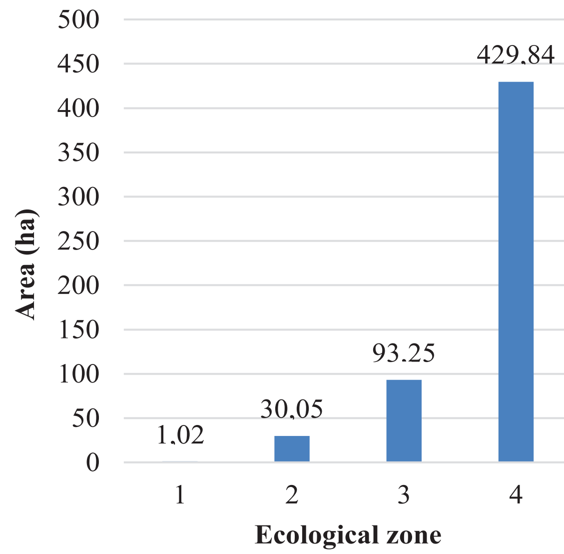

Fig. 8. Distribution of fallow aquaculture by ecological region.

Fallow aquaculture covered about 581.49 ha, and the area increased from ecological regions 1 to 4 (Fig. 7). The fallow shrimp pond area in region 1 merely accounted for 0.18%; on the contrary, the area of region 4 reached 429.84 ha and accounted for more than 70% of the total area of the fallow area (Fig. 8).

Discussion

Remote sensing in aquaculture classification

In terms of the satellite resolution and land use map scale for district level, a district with the total area larger than 12,000 ha should be mapped in the scale of 1:25,000 [15]. Hence, in theory, Landsat 8 imagery with a 30-metre spatial resolution merely achieves the map scale of 1:60,000 [16, 17], and it is merely suitable for provincial maps. However, the Thanh Phu district area is approximately 40,000 ha (i.e. nearly four times the size of the standard). Thus, the result map could be accepted in the context of freely high-resolution imagery is not available. The research period was from 2015 to 2016; hence, Sentinel-2 imagery with a 10-metre resolution was unavailable at the beginning of the research period. In further studies, the resolution of Landsat-8 imagery could be enhanced by combining multispectral bands and panchromatic band to obtain a higher spatial resolution of 15 metres (corresponding to the scale of 1:30,000).

The research identified the highly accurate aquaculture area including effective shrimp and fallow shrimp farms. The fallow shrimp pond (fallow pond) was objectively detected through the integration of spectral indices instead of visual classification [18]. However, the research was able to detect only the shrimp ponds where farmers had lost income, that is, fallow ponds in 2016. The other ineffective ponds that were still covered by water surface would not be recognized on the remotely sensed imagery. Similarly, the intensive and extensive aquaculture systems could not be distinguished through the imagery. The remote sensing technique could detect both the general aquaculture areas and the fallow ponds. However, some of LULC types mixed together-triple rice-orchard and rice shrimp rotation-mangrove forest-could not be classified in more detail using a single Landsat image. The use of a multi-series imagery could improve this limitation. High-resolution imagery and object-based image analysis via object texture are expected to distinguish extensive and intensive shrimp farming (i.e. industrial shrimp farming).

Ineffective shrimp in Thanh Phu district

According to the published references, the giant tiger prawn *(Penaeus monodon)* adapts to salinity from 5 to 31‰ [19], whereas the white leg shrimp *(Penaeus vannamei)* adapts to salinity from 7 to 34‰ [20]. Thus, brackish shrimp culture could be effectively cultivated in ecological regions 2, 3, and 4. However, the region with the highest salinity (i.e. region 4: 20 to 30‰) is the most vulnerable region. The prolonged sunny season (e.g. 2016) and lack of freshwater increased the water salinity in shrimp ponds and exceeded the highest level of salinity to which shrimps could effectively adapt. Therefore, high water salinity influenced the survival rate and productivity of shrimp and adversely affected the incomes of farmers. Finally, the area of the fallowed aquaculture ponds located in region 4 was rationally higher than the rest of the ecological regions.

Aquaculture cultivation in Thanh Phu district continues to encounter obstacles emanating from adverse weather conditions in the dry season, which increases temperatures and water salinity levels. Moreover, heavy rain, high salinity, pH and alkalinity change rapidly affect water quality, which consequently slows down shrimp growth. Market prices are the most serious problem in Thanh Phu district where selling prices are lower than product prices. The prices of aquatic fingerlings are relatively high. Thus, merely 50% of the farmers used quality aquatic fingerlings for their farming, whereas other farmers had no stocks of aquatic fingerlings on their farms. Hence, the randomly identified fallow shrimp pond was presented in the context of the farmers' decision to halt the cultivation.

Conclusions

This research examines the spatial distribution of aquaculture and fallow aquaculture ponds in Thanh Phu district, Ben Tre province by using the three indices of NDVI, MNDWI and NDBaI. The accuracy is assessed at 77%, which indicates the capacity of remote sensing in general aquaculture detection.

Moreover, fallow aquaculture ponds are commonly distributed in ecological region 4 (more than 70% of the total aquaculture area). High water salinity also affects this ecological region. The research reveals the aquaculture zones and fallow ponds, which correspond to water salinity by ecological region.

The suggestions for further research are related to the improvement of techniques and reduction in risk in the ineffective aquaculture region.

ACKNOWLEDGEMENTS

We would like to thank the intern-student from Suan Sunandha Rajabhat University for her assistance and performance. We are also grateful to the Ben Tre Department of Agriculture and Rural Development and Fisheries Department for providing the primary data and field survey. Our special thanks go to the staff of the Land Resources Department of the College of Environment and Natural Resources at Can Tho University, Vietnam, for their invaluable support during our research.

The authors declare that there is no conflict of interest regarding the publication of this article.

REFERENCES

[1] Trai. N. Van (2013), *Detailed plaining of Aquaculture on Binh Dai, Ba Tri and Thanh Phu district to 2020*.

[2] Ben Tre People's Committees (2011), *Impact assessment, detailed climate change scenarios in Ben Tre and recommend response solutions*.

[3] Ben Tre People's Committees (2010), *General report the overall planning of economic - social development in Ben Tre Province in 2020*.

[4] Prime Minister (2011), *Decision 83/QD-TTg: Approving the master plan of economic - social development in Ben Tre province in 2020*.

[5] Khoa. L. Van, N.T.C. Su, V.Q. Minh, P.T. Vu (2013), "Agro-ecological zoning according to hydrology, pedology and present land use for coastal districts in Ben Tre province", *Can Tho University Journal of Science*, **26**, pp.227-236.

[6] Thanh Phu People's Committees (2010), *Review Report about economy and society in Thanh Phu district in 2005, 2006, 2007, 2008, 2009, and 9 beginning months of 2010*.

[7] US. Geological Survey (2013), *Landsat Quality Assessment Band*, http://landsat.usgs.gov/qualityband.php.

[8] B. Kim, Y. Han, Y. Kim (2012), *Generation of cloud-free imagery using Landsat-8*.

[9] C.J. Tucker (1979), "Red and photographic infrared linear combinations for monitoring vegetation", *Remote Sensing of Environment*, **8(2)**, pp.127-150.

[10] S.K. McFeeters (1996), "The use of the Normalized Difference Water Index (NDWI) in the delineation of open water features", *International Journal of Remote Sensing*, **17(7)**, pp.1425-1432.

[11] H. Xu (2006), "Modification of normalised difference water index (NDWI) to enhance open water features in remotely sensed imagery", *International Journal of Remote Sensing*, **27(14)**, pp.3025-3033.

[12] R. Bouhennache, T. Bouden, A.A. Taleb, A. Chaddad (2015), *Extraction of urban land features from TM Landsat image using the land features index and Tasseled cap transformation*, http://www.inase.org/library/2015/barcelona/bypaper/ELECTR/ELECTR-22.pdf.

[13] A.R. As-Syakur, I.W.S. Adnyana, I.W. Arthana, I.WW. Nuarsa (2012), "Enhanced built-up and bareness index (EBBI) for mapping built-up and bare land in an urban area", *Remote Sensing*, **4(10)**, pp.2957-2970.

[14] N. Horning (2004), *Overview of accuracy assessment of land cover products Version 1.0*, American Museum of Natural History, Center for Biodiversity and Conservation.

[15] Ministry of Natural Resources and Environment (2007), *Decision 22/2007/QD-BTNMT: Issue regulations on establishment of land use map*.

[16] W.R. Tobler (1987), "Measuring spatial resolution", *Land Resources Information Systems Conference*, pp.12-16.

[17] W.R. Tobler (1988), "Resolution, resampling, and all that", *Building Data Bases for Global Science*, pp.129-137.

[18] N. Van Thao, N.D. Cu, and N.X. Thanh (2012), "Maping and detecting fallowed area of cultivated tiger shrimp ponds of coastal provinces by using remote sensing data", *J. Mar. Sci. Technol.*, **12(3)**, pp.34-45.

[19] The National Fisheries Promotion Center (2006), *Cultivation techniques for intensive giant tiger prawn (Penaeus monodon)*, Publishing house of Agriculture.

[20] Agricultural Extension Center Hochiminh city (2009), *Handbook: Whiteleg shrimp cultivation (Penaeus vannamei)*.

Doi: 10.31276/VJSTE.61(2).42-46

Attempting near-infrared transillumination imaging with simple instrumentation for studying dental lesions

Thi Hai Mien Pham*, Phu Duong Le, Thi Kim Tham Ta

University of Technology, Vietnam National University, Ho Chi Minh city

Received 13 November 2018; accepted 20 March 2019

***Abstract*:**

During the past decades, near-infrared (NIR) methods have been applied to many aspects of life, particularly in dentistry. X-ray methods involve reliable techniques that dentists use to evaluate tooth structure lesions. However, X-ray methods still have some limitations, such as affecting patient health and dentists. In addition, early demineralised enamel is barely detected by X-ray methods. Many studies have demonstrated the usefulness of NIR light for observing tooth structure due to the differences of the optical properties between sound and demineralised tooth tissues under NIR wavelengths. Early demineralisation located under the enamel layer can be observed by NIR imaging (780-1,300 nm). The areas suspected to be demineralised enamel are distinct from the stain and pigmentation because stain and pigmentation do not appear in NIR images. The demineralised areas are substantially darker than the surrounding sound tissues under NIR light. In this study, two optical systems with transillumination and scattering techniques using NIR light (940 nm) were built for capturing occlusal and approximal images of teeth. The systems fulfill some requirements, such as simple setup, safety, and affordable price for the purpose of the replacement of imported equipment.

Keywords: **approximal lesion, demineralisation, near-infrared, occlusal, teeth.**

Classification number: **2.3**

Introduction

Dental lesions are one of the most common diseases, affecting people of all ages across the world, and particularly children. Diagnoses of damaged structures of teeth in general and early dental present challenges for dentistry. Some available diagnostic methods for dental lesions include X-rays, clinical visual inspection, caries indicator dyes, fluorescent methods, electrical conductance measurements (ECM), etc.

The visual method is the most popular diagnostic method in dentistry because it can detect most occlusal lesions, cavitated enamel, and dentine lesions with high specificity. However, with low sensitivity, this method has trouble detecting early enamel lesions and proximal and hidden caries [1, 2].

In addition to the visual method, X-rays are commonly used as a diagnostic tool in dentistry. When X-rays pass through the oral cavity, much of the X-rays are absorbed by hard tissues such as teeth and bones [3]. The absorbed X-rays will pass through the film or a digital sensor, creating a radiographic image of the tooth. This method makes it possible to observe the structure of hard tissue and surrounding soft tissues that cannot be observed by clinical examination methods, such as proximal tooth surfaces or hidden caries. However, this method also produces many adverse effects, particularly for children and pregnant women, through the use of ionising radiation.

Today, in dentistry, near-infrared technology has been studied for decades and is being applied to the detection of early damages without use of ionising radiation [3, 4]. The NIR method yields tooth structure images detected by NIR camera. The images created are based on the optical properties of the tooth due to the transmission, absorption, and scattering of dental tissues in NIR wavelength. Because the absorption coefficients are exceptionally small in visible

*Corresponding author: Email: phamhaimien@hcmut.edu.vn

and NIR light, while scattering is strong in visible light and weak in NIR, enamel is translucent in the near infrared light. For dentin, the absorption coefficient depends upon the wavelength in the visible region with a value of $\mu_a \sim 4$ cm^{-1}, while the scattering is strong throughout the visible and NIR regions. Therefore, NIR light is the optimum wavelength for imaging dental lesions, particularly dentin caries [5].

The damaged tooth structure is mostly demineralised enamel, in which mineral density is reduced. As a result, demineralisation creates gaps in enamel and dentin tissues. Near-infrared light is scattered at the wall of these gaps and substantially attenuated by the absorption with the elongated pathlength due to multiple scattering [6]. For demineralisation, the scattering coefficient of demineralised enamel increases by one to two orders of magnitude at a wavelength of 1,300 nm [7]. According to the difference in optical properties between sound and demineralised enamel, their contrast in NIR images is rather pronounced. Notably, X-rays do not distinguish between sound enamel and demineralised enamel [4, 6].

NIR technology has been investigated for several decades around the world, and some NIR dental diagnostic devices have been commercialised. This study has aimed to build simple optical systems with reasonable prices. Many researchers have indicated that a wavelength of 1,300 nm is more effective than 940 nm due to the higher contrast of images at 1,300 nm, but performance is challenging because of the limited equipment (LED and camera). Therefore, the system used a 940-nm wavelength of which the extinction is lower than 40 cm^{-1} in enamel, and absorption of water is negligible [4]. 940-nm LED and NIR cameras are available at an affordable cost. This study has designed the transillumination and scattering NIR optical systems to record the approximal and occlusal images of teeth.

Materials and methods

The transillumination system illustrated in Fig. 1A consists of a light source, a tooth sample, and an NIR camera. An approximal image of tooth was observed clearly by this system. The transillumination method suits thin teeth such as incisors and canines. Samples were illuminated in visible light and 940-nm wavelengths and operated with an LED. An oral camera was used for capturing images. The camera was connected to a computer with a USB cable 2.0. The LED intensity and source-to-sample distance (about 1-1.5 cm) were adjusted for each sample to control image quality. Tooth samples were placed on a 360^0-rotating table to capture all sides of samples (Fig. 2A).

The optical scattering system is illustrated schematically in Figs. 1B and 2B. It consists of two 940-nm LEDs, a specimen, and an NIR camera. This system used two symmetrical light sources on two opposite sides of the sample. The scattering system was used to observe the occlusal surface. This method is an effective means of observing molar teeth because of their thickness. The camera was placed above the tooth and perpendicularly to the light path. The quality of the tooth structure image depends upon the position of the camera, the light sources, and tooth. The distance between the sample and the camera is about 1 to 1.5 cm, and the light sources were located below the gum line of the teeth. The power of the light sources is an important factor as well. If LED power is overly high, the recorded images will be overwhelmed by light, and no details of teeth can be seen. For this system, the power of each LED was 1.5 W.

Technical specifications of 940-nm LED: consumption power 1.5/3 W, input voltage 2.0 to 2.4 V, forward current 0.3-0.6 A, lumen efficiency 100 lm/W, and emitting angle 140^0.

Technical specifications of camera: sensor type CMOS, spectral range 350-1,000 nm, resolution 2Mpx, image rate 15 fps, focal length 1 to 2 cm, input voltage 5 V, temperature range $10-75^0$C, and outer dimensions of 17 cm (height) 2 cm (width) 1 cm (depth). With the purpose of designing a dental diagnostic device in the future, the size and the focal length of the selected camera are suitable for intraoral *in vivo* examination.

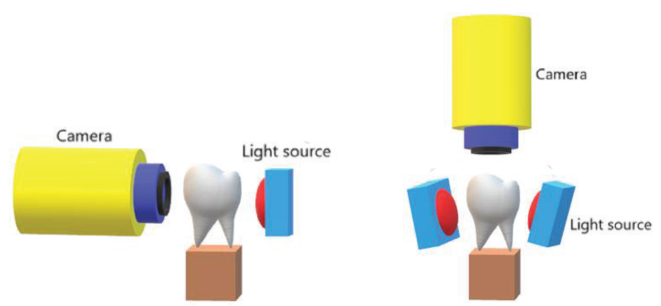

(A) (B)

Fig. 1. Schematic diagram of transillumination (A) and scattering systems (B).

(A) (B)

Fig. 2. Appearance of transillumination (A) and scattering systems (B).

Results and discussion

White-spot lesions

There are many causes of forming white spot lesions which are often overlooked in clinical observation, such as demineralisation, fluorosis, enamel hypoplasia, etc. Although X-rays are the gold standard in dentistry, but it is unable to detect white spot lesions at early stages [8]. Substantial research has demonstrated that the observation of early tooth lesions is more effective by NIR imaging. Under NIR light, many lesions appear with high contrast because the scattering coefficient of damaged tissue is lower than that of healthy enamel [5]. This is the sign of demineralisation appearing at the first stage of the progression of tooth lesion.

Figure 3 depicts a tooth sample with white-spot lesions. Under visible light (Fig. 3A), at the center of the chewing surface, relative to more translucent, healthy enamel, an opaque white area appeared. According to the doctor's conclusions based on clinical observations and X-ray (Fig. 3C), this sample has positive status. However, on the NIR image (Fig. 3B), the contrast of circled area is higher than the surrounding healthy enamel, which has demonstrated that the origin of this lesion is not fluorosis because fluorinated enamel is white in both NIR and visible images [4]. This is one of the advantages of the NIR method, which is useful to observe disease progression and improve diagnostic accuracy.

The similar results of white spot lesions are depicted in samples 2 and 3 (Figs. 4, 5).

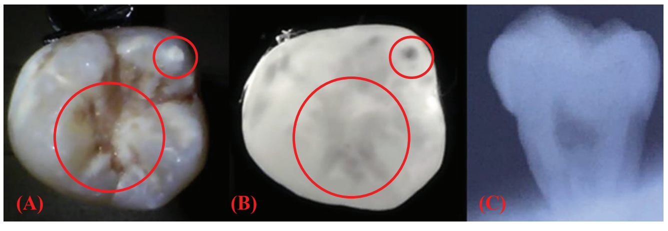

Fig. 3. Sample 1 under visible light (A), NIR light (B), and X-rays (C).

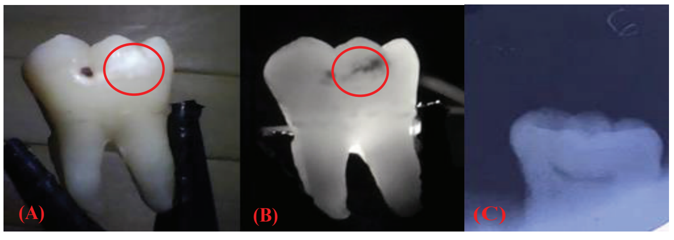

Fig. 4. Sample 2 under visible light (A), NIR light (B), and X-rays (C).

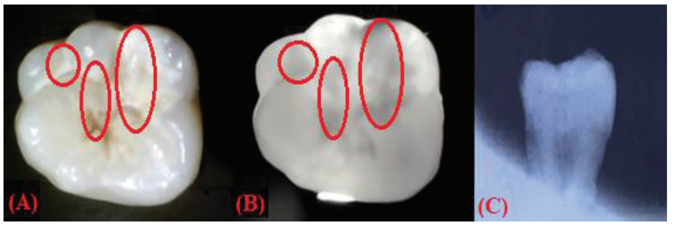

Fig. 5. Sample 3 under visible light (A), NIR light (B), and X-rays (C).

Occlusal lesions

Occlusal lesion is a type of injury that can easily be observed by infrared light scattering. It is formed by food debris inserted between occlusal pits and confused with dental plaque or fluorosis or enamel hypoplasia. In the NIR image, occlusal lesion is not mistaken for plaque or stains on the tooth.

Figure 6 demonstrates a tooth sample having a large area of demineralisation on the occlusal surface. However, this lesion is not clear on the X-ray film (Fig. 6C), but in the NIR image (Fig. 6B). The NIR image displays a high-contrast area, substantially darker than the surrounding area. For this sample, demineralisation occurred in a large area so that a deep hole was formed. Substantial research has indicated that the broken crystal structure of demineralised tissue can cause unkeeping of water in tissue and precipitates the creation of gaps in the enamel. In this area, the light is attenuated more by the absorption with the elongated pathlength due to multiple scattering [9, 10]. Therefore, the demineralised tissue is darker than surrounding healthy tissue under NIR light.

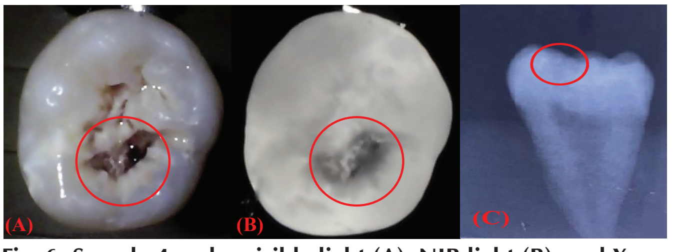

Fig. 6. Sample 4 under visible light (A), NIR light (B), and X-ray (C).

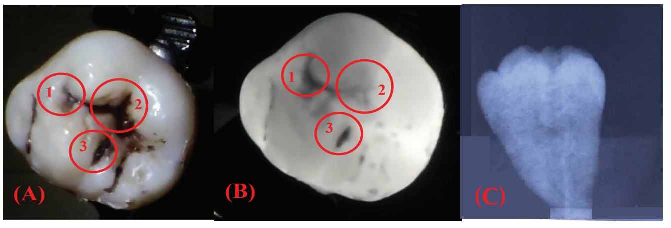

Fig. 7. Sample 5 under visible light (A), NIR light (B), and X-ray (C).

Figure 7 illustrates a sample with the appearance of an early cariuos lesion. Under visible light (Fig. 7A, circled area 2) on the occlusal surface, a large area regarded as a lesion appeared in the occlusal grooves. However, in the NIR image (Fig. 7B), this area does not exhibit a more severe lesion relative to other regions (circled area 1 and 3) because the concentrated dental plaque in the occlusal surface is easily confused with lesions under visible light. The disappearance of these plaques under infrared light demonstrates the effectiveness of the NIR method for the diagnosis of dental lesions. In addition, in the NIR image, the circled region 1 appears with a higher contrast than the surrounding enamel; however, it is regarded as a minor injury under visible light. The circled area 3 appears clearly under both visible and infrared light. In X-ray films (Fig. 7C), there is no recognition of the existence of these lesions.

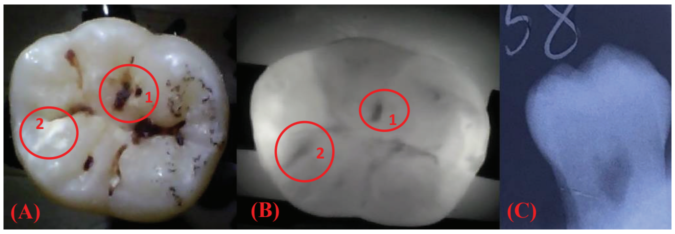

Fig. 8. Sample 6 under visible light (A), NIR light (B), and X-ray (C).

For teeth with many signs of injury on the occlusal surface, as illustrated in Fig. 8, the NIR method has exhibited high efficiency in determining the exact position of lesion. Under visible light (Fig. 8A), the brown regions are suspected of the demineralisation, which cannot be observed in the X-ray image (Fig. 8C). However, some brown stains, such as area 1, were apparent under NIR illumination. In addition, another region of injury (circled area number 2) could be observed clearly in the infrared image, while in visible light, it is difficult to be distinguished because of the similar color relative to healthy enamel.

Recurrent caries under fillings

Fillings are frequently used in the treatment of cavities at the stages of enamel or dentin decay. After fillings, the lesions can be relapsed, and they are referred to as 'recurrent caries under fillings'. The proportion of secondary caries is exceptionally high after filling in permanent teeth or primary teeth. Secondary caries primarily occur because of the formation of micro cracks after filling. When the micro crack width exceeds 50 micron, saliva enters the micro cracks between the filling and the tooth tissue. The cariogenic bacteria in the saliva grow when the environment of micro cracks is appropriate, thereby producing secondary caries [11].

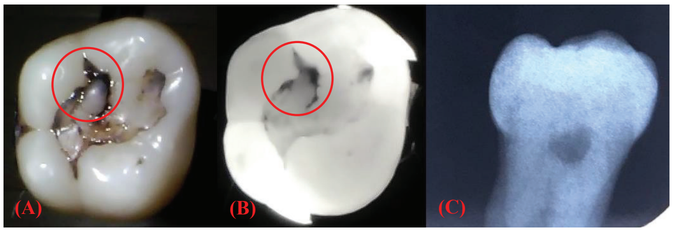

Fig. 9. Sample 7 under visible light (A), NIR light (B), and X-ray (C).

Figure 9 depicts a tooth sample with a filling on the occlusal surface. Under visible light (Fig. 9A, circled area), there were some dark areas around the filling, which rendered it difficult to distinguish between plaque and demineralisation, while the X-ray image (Fig. 9C) did not provide any information of the suspected lesion under filling because of the limitation of X-ray in scanning the occlusal surface. Because plaques do not absorb NIR light and disappear completely in NIR images [5], the darker area in Fig. 9B demonstrated the clear appearance of demineralised lesion.

Tooth discolorisation and plaque

Figure 10 illustrates a discolored sample with a cavity on the enamel surface and calculus. Under visible light, it is easy to recognise that the color of tooth changed to black. Fig. 10B displays a NIR image captured by the transmission method, in which calculus and discolored areas appeared as black. However, as mentioned above, infrared light cannot be absorbed by plaque and discolored area; therefore, they are not apparent in the NIR image. This means that in this sample, the demineralisation occurred under the calculus and discolored area. Notably, even the X-ray films (Fig. 10C) allow the definition of the presence of caries without the detection of early damages. This property of the tooth and NIR light interaction can be applied to distinguish demineralisation from discoloration and calculus.

The same results were recorded with other samples (Figs. 11, 12).

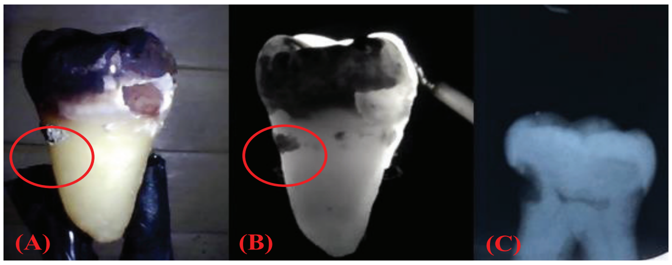

Fig. 10. Sample 8 under visible light (A), NIR light (B), and X-rays (C).

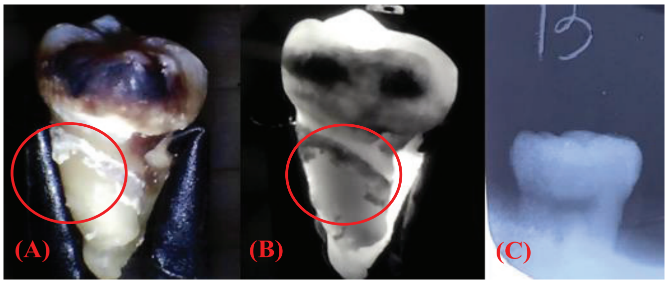

Fig. 11. Sample 9 under visible light (A), NIR light (B), and X-rays (C).

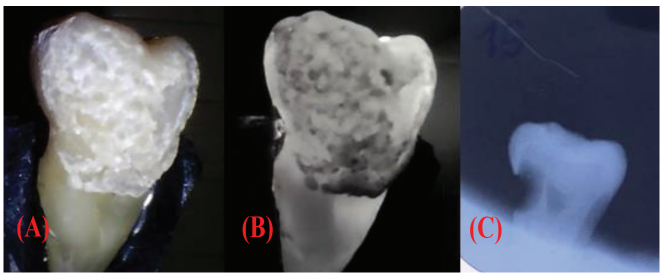

Fig. 12. Sample 10 under visible light (A), NIR light (B), and X-rays (C).

Conclusions

With the purpose of studying, designing, and manufacturing a dental diagnostic device with advantages such as simple setup, safety, and affordable price, in this study, two optical systems with transillumination and scattering techniques using 940 nm LED were designed and built. These systems were used to observe the approximal and occlusal of teeth, and they were able to discriminate between the demineralised and discolored teeth. The result indicates the possibility of applying the NIR technique in the development of a specificity and sensitivity dental screening tool without the use of ionising radiation. This method can support clinicians in detecting the early dental lesions. In the future, the hardware of the optical systems requires further improvement, and a photo processing software will be developed to increase the image quality.

ACKNOWLEDGEMENTS

This research is funded by Vietnam National University in Ho Chi Minh city (VNU-HCM) under grant number C2018-20-04.

The authors declare that there is no conflict of interest regarding the publication of this article.

REFERENCES

[1] Zangooei Booshehry (2010), "Dental caries diagnostic methods", *DJH*, **2(1)**, pp.1-12.

[2] Mirela Marinova-Takorova, et al. (2016), "Effectiveness of near-infrared transillumination in early caries diagnoisis", *Biotechnology & Biotechnological Equipment*, **30(6)**, pp.1207-1211.

[3] D.G. Bussaneli, et al. (2015), "Assessment of a new infrared laser transillumination technology (808 nm) for the detection of occlusal caries - an in vitro study", *Lasers Med. Sci.*, **30(7)**, pp.1873-1879.

[4] C.M. Buhler, Patara Ngaotheppitak, and Daniel Fried (2005), "Imaging of occlusal dental caries (decay) with near-IR light at 1310-nm", *Optics Express*, **13(2)**, pp.573-582.

[5] Daniel Fried, Michal Staninec, Cynthia L. Darling (2010), "Near-infrared imaging of dental decay at 1,310 nm", *J. Laser Dent.*, **18(1)**, pp.8-16.

[6] S.J. Robert, et al. (2003), "Near-infrared transillumination at 1,310-nm for the imaging of early dental decay", *Optics Express*, **11(18)**, pp.2258-2265.

[7] C.S. Jacob, et al. (2016), "Near-IR transillumination and reflectance imaging at 1,300 nm and 1,500-1,700 nm for *in vivo* caries detection", *Lasers in Surgery and Medicine*, **48(9)**, pp.828-836.

[8] Keith Angelino, David A. Edlund, and Pratik Shah (2017), "Near infrared imaging for detecting caries and structural deformities in teeth", *Journal of Translational Engineering in Health and Medicine*, **5**, p.e2300107.

[9] F. Daniel, et al. (1995), "Nature of light scattering in dental enamel and dentin at visible and near-infrared wavelengths", *Applied Optics*, **34(7)**, pp.1278-1285.

[10] Soojeong Chung, Daniel Fried, Michal Staninec, and Cynthia L. Darling (2011), "Multispectral near-IR reflectance and transillumination imaging of teeth", *Biomedical Optics Express*, **2(10)**, pp.2804-2814.

[11] X. Feng (2014), "Cause of secondary caries and prevention", *West China Journal of Stomatology*, **32(2)**, pp.107-116.

Doi: 10.31276/VJSTE.61(2).47-51

In vitro and field responses of various active ingredients to *Fusarium proliferatum* species which causes Fusarium root rot disease in Indian mulberry (*Morinda officinalis* How.) in Thai Nguyen

Duong Thi Nguyen*, **Nguyen Thi Nhu Hoa, Le Thi Kieu Oanh, Dang Kim Tuyen, Nguyen Chi Hieu, Duong Son Ha, To Thi Ngan**

Faculty of Agronomy, Thai Nguyen University of Agriculture and Forestry

Received 15 March 2019; accepted 30 May 2019

Abstract:

Fusarium proliferatum **has been identified as the causal pathogen of Fusarium root rot of Ba kich (*Morinda officinalis*) (FRRBK). No studies are available regarding the effectiveness of chemical treatments on the disease incidence of FRRBK. The efficacy of five active ingredients (metconazole, prochloraz, tebuconazole, kresoxim-methyl, and pyraclostrobin) from two chemical groups (demethylation inhibitors and quinone outside inhibitors) in reducing three isolates (BKVN, BKDT, and BKPL) of *F. proliferatum* mycelial growth was tested *in vitro*. The results indicate that only metconazole, prochloraz, and tebuconazole are highly effective in inhibiting the mycelial growth of *F. proliferatum*. These were selected for investigation of their efficacy with regard to the disease incidence of FRRBK in pot and in field conditions. Prochloraz and metconazole showed the highest efficacy and significantly suppressed the disease incidence of FRRBK in pot and in field conditions.**

Keywords: **Ba kich, demethylation inhibitors, *Fusarium proliferatum*, *Morinda officinalis*, quinone outside inhibitor.**

Classification number: **3.1**

Introduction

In Vietnam, Indian mulberry (*Morinda officinalis* How.) is locally known as ‘Ba kich’ and is widely grown in many mountainous provinces in the north of Vietnam. In Thai Nguyen province, Ba kich is mainly planted in Vo Nhai, Dai Tu, and Phu Luong districts for use in traditional medicine as it is rich in various medicinal compounds. Therefore, Ba kich is considered a cash crop, which brings substantial income for small households.

Fusarium root rot of Ba kich (FRRBK), caused by *Fusarium proliferatum*, is a widespread soilborne disease that causes serious damage and significant economic losses to Ba kich production in Vietnam in general and in Thai Nguyen in particular [1]. Several bio-products have been applied for the management of FRRBK in Thai Nguyen province. Tests of the efficacy of a new bio-product, MICROTECH-1(NL), were conducted in *in vitro*, pot, nursery, and field conditions. In *in vitro* antagonistic assay, MICROTECH-1(NL) significantly inhibited the mycelial growth of *F. proliferatum*. Double application of MICROTECH-1(NL) (applied both in the nursery and in the pot soil) significantly reduced disease incidence and markedly increased the number of plant-beneficial bacteria and actinomycota in rhizoplane Ba kich. In field conditions, double application of MICROTECH-1(NL) (both in nursery and in field soils) significantly decreased disease incidence compared to single application in either nursery or field.

However, bio-products usually act more slowly than chemical fungicides. Therefore, to immediately suppress the spread of the disease in nursery and field conditions and to maintain the plant’s yield, chemical fungicides are the better choice. In addition, no fungicides have been identified and registered specifically to control FRRBK in Vietnam; therefore, the effect of five active ingredients (a.i.) that are either demethylation inhibitor (DMI) (metconazole, prochloraz and tebuconazole) or quinone outside inhibitor (QoI) (kresoxim-methyl and pyraclostrobin) fungicides on the growth of the causal pathogen *in vitro*, and their efficacy on reducing the disease incidence of FRRBK in pot and in field conditions are assessed.

*Corresponding author: Email: duongthinguyen@tuaf.edu.vn

Materials and methods

Inoculum preparation

Three isolates of *F. proliferatum*, BKVN (Ba kich growing in Vo Nhai district), BKDT (Dai Tu district), and BKPL (Phu Luong district), which were previously identified as causal agents of FRRBK in Thai Nguyen province [1], were cultured on potato dextrose agar (PDA) plates for three days at 25^{0}C in dark conditions. A piece of PDA medium containing mycelium of each isolate was grown in potato dextrose broth at 25^{0}C with shaking at 120 rpm. After seven days of incubation, the harvested fungal suspensions were adjusted to 5×10^6 cfu/ml and used as inocula for further experiments.

Plants and a.i.

One-year old Ba kich plants that had previously been grown in small plastic pots (5×15×5 cm) were used. Five a.i. (Table 1) were applied in this study to evaluate their effects on the growth of *F. proliferatum* in *in vitro* condition; the highly effective a.i. were selected for their efficacy on the disease incidence of FRRBK in pot and in field conditions.

Table 1. Chemical active ingredients (a.i.) used in this study.

a.i.	Commercial name	a.i. tested (mg/l)	Group name	Mode of action
Metconazole	Workup 9 SL (Metconazole, min. 94%)	1-10-100	Demethylation inhibitors (DMI)	Sterol biosynthesis in membranes
Prochloraz	Agrivil 250EC (Prochloraz, min. 97%)	5-50-500	DMI	Sterol biosynthesis in membranes
Tebuconazole	Folicur 430SC (Tebuconazole, min. 95%)	3-30-300	DMI	Sterol biosynthesis in membranes
Kresoxim-methyl	1Sosim 300SC (Kresoxim-methyl, min. 95%)	10-100-1,000	Quinone outside inhibitor (QoI)	Inhibition of cell respiration (mitochondria). Inhibition of spore germination, germ tube elongation, mycelial growth and sporulation.
Pyraclostrobin	Headline 200FS (Pyraclostrobin)	10-100-1,000	QoI	Inhibition of cell respiration (mitochondria). Inhibition of spore germination, germ tube elongation, mycelial growth and sporulation.

Mycelial growth inhibition of F. proliferatum by different a.i.

The effect of different a.i. on the mycelial growth of *F. proliferatum* was determined by growing *F. proliferatum* on PDA plates (90 mm diameter). The experiment was replicated five times (one Pestri plate per replication) and the mean values were calculated. Each a.i. was separately applied to 100 ml of sterilised PDA medium at 60^{0}C before being divided equally into five Petri plates at the rates indicated in Table 1. Control plates were prepared by replacing a.i. with sterile distilled water. Mycelial discs of *F. proliferatum* of 5 mm diameter were transferred from the seven-day old growth colony to the PDA plates, tested, and incubated at 25±1^{0}C for seven days. Colony diameter growth was measured and recorded on the seventh day after treatment. The diameter of the *F. proliferatum* colony was measured in two directions at right angles to each other, and the average colony diameter was calculated. Measurement of the growth of *F. proliferatum* was undertaken at intervals of 24 hours for seven days. The inhibition percentage of each a.i. on the mycelial growth of *F. proliferatum* was determined on the seventh day of incubation following the formula (1-C_n/C_o) × 100, where C_n is the average diameter of the *F. proliferatum* colony on the treatment plates, and C_o is the average diameter of *F. proliferatum* colony on the control plates.

Effect of a.i. on disease incidence of FRRBK in pot conditions

Based on the inhibition percentage (%) of each a.i. on the mycelial growth of *F. proliferatum*, three a.i. were selected and subjected to analysis of their effects on the disease incidence of FRRBK in pot conditions (20×40×20 cm). An eight-leaf (about one-year old) seedling was grown in each pot containing *F. proliferatum*-infested soil. The preventive and curative effects of each a.i. were determined according to following experiments: (1) the a.i. was drenched in the soil one week before pathogen inoculation, (2) the a.i. and the pathogen spores were applied simultaneously, and (3) the a.i. was drenched in the soil one week after pathogen inoculation. Spore suspensions of BKVN, BKDT and BKPL isolates were applied separately as drenches. These experiments were replicated three times using a completely randomised block design and 30 pots (30 plants) per treatment.

Disease severity was recorded on 0 to 3 visual scales as previously described by Trabelsi, et al. (2017) [2]. All infected plants in each treatment were recorded for disease incidence (%) using the following formula:

$$\text{Disease incidence } (\%) = \frac{(\sum \text{scale} \times \text{number of plants infected})}{(\text{highest scale} \times \text{total number of plants})} \times 100$$

Efficacy of a.i. on FRRBK in field conditions

Three a.i. were applied in field experiments in Vo Nhai district to determine their efficacy on FRRBK. The experiments were replicated three times with a completely randomised block design and a plot size of 24×6 m planted with 100 Ba kich plants per treatment. The efficacy (E) of the a.i. was calculated as follows:

$$E = 1 - \frac{T_a \times C_b}{T_b \times C_a} \times 100$$

where: E: the efficacy of the active ingredient (%); T_a: disease incidence in the treatment after applying the a.i.; T_b: disease incidence in the treatment before applying the a.i.; C_a: disease incidence in the control after application; and C_b: disease incidence in the control before application.

Data analysis

The collected data were summarized as mean ± standard deviation and analysed using Statistix 10 software.

Results and discussion

Effect of different a.i. on the inhibition of the mycelial growth of F. proliferatum

In a dual-culture assay, the a.i. tested inhibited the growth of *F. proliferatum* BKVN, BKDT, and BKPL isolates by at least 48%; the highest values were obtained with prochloraz and metconazole. All DMI fungicides showed excellent activity in suppressing the mycelial growth of *F. proliferatum* up to seven days of incubation. In particular, metconazole and prochloraz completely suppressed colony growth of *F. proliferatum* at the concentrations of 10, 100 and 50, 500 mg/l, respectively. At 1 and 5 mg/l, the two a.i. inhibited up to more than 83-91% of the growth of *F. proliferatum* BKVN, BKDT, and BKPL isolates (Fig. 1). The application of another DMI fungicide, tebuconazole, also inhibited the mycelial growth of *F. proliferatum* BKVN, BKDT, and BKPL isolates by 70.38%, 71.80%, and 72.04%, respectively. The other two QoIs, kresoxim-methyl and pyraclotrobin, showed low inhibition (lower than 80% and 62%, respectively) (Fig. 1).

Effect of a.i. on the disease incidence of FRRBK in pot conditions

Treatment with a.i. one week before inoculation with *F. proliferatum* significantly reduced the disease incidence of FRRBK compared to the inoculated-untreated control. Of the a.i. tested, prochloraz and metconazole showed the highest suppression of disease incidence. The results indicated that with prochloraz treatments, disease incidence ranged from 2.59% for the BKDT isolate to 3.70% for the BKPL isolate. With metconazole treatments, disease incidence ranged from 4.07% for the BKVN isolate to 4.81% for the BKPL isolate. With the tebuconazole treatments, disease incidence ranged from 7.04% for the BKVN isolate to 9.26% for the BKDT isolate (Table 2).

Table 2. Disease incidence when Ba kich plants were treated with a.i. one week before the plants were inoculated with *F. proliferatum* spores.

a.i.	Disease incidence (%)		
	F. proliferatum BKVN	*F. proliferatum BKDT*	*F. proliferatum BKPL*
Metconazole	4.07^c	4.44^c	4.81^c
Prochloraz	3.33^c	2.59^c	3.70^c
Tebuconazole	7.04^b	9.26^b	8.15^b
Inoculated-untreated control	81.11^a	80.37^a	82.59^a
Non-inoculated-untreated control	0.00^d	0.00^d	0.00^d
p	<0.05	<0.05	<0.05
CV(%)	3.25	8.67	6.37
$LSD_{0.05}$	0.62	1.68	1.25

Note: values followed by a different letter(s) in the same column are significantly different (p<0.05).

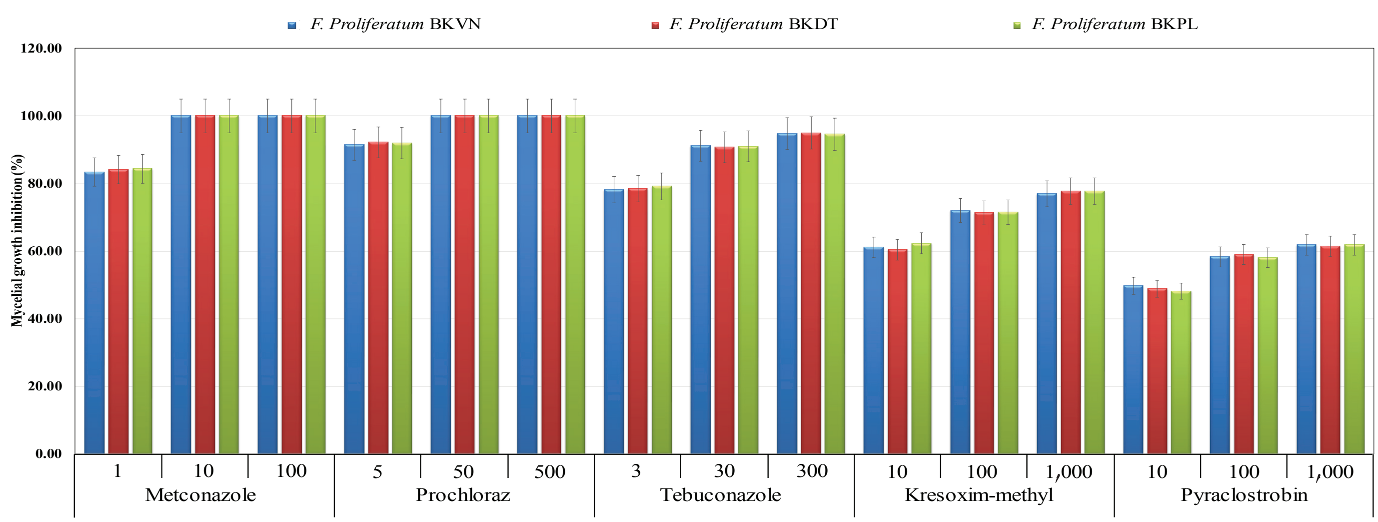

Fig. 1. The inhibition of the tested a.i. on mycelial growth of *F. prolifertum* isolates BKVN, BKDT, and BKPL. Three different concentrations of each a.i. (mg/l) were amended into PDA plates before the culturing of each isolate. Colony growth in diameter was measured and the inhibition values (%) were calculated.

The decrease of disease incidence when a.i. were applied simultaneously with inoculation by *F. proliferatum* spores showed similar trends, although the disease incidence was higher than when a.i. were applied one week before inoculation with *F. proliferatum*. Disease incidence in treatments with prochloraz or metconazole was statistically differentiated compared to treatments with tebuconazole and the inoculated-untreated control. Disease incidence with all a.i. ranged from 7.78% with prochloraz for the BKDT isolate to 13.70% with tebuconazole with BKVN isolate (Table 3).

Table 3. Disease incidence when Ba kich plants were treated with a.i. at the same time as the plants were inoculated with *F. proliferatum* spores.

a.i.	Disease incidence (%)		
	BKVN	*BKDT*	*BKPL*
Metconazole	9.26c	9.63c	10.74c
Prochloraz	8.15c	7.78c	8.52c
Tebuconazole	13.70b	15.56b	17.78b
Inoculated-untreated control	81.11a	80.37a	82.59a
Non-inoculated-untreated control	0.00d	0.00d	0.00d
p	<0.05	<0.05	<0.05
CV(%)	4.18	12.74	6.12
$LSD_{0.05}$	0.74	2.28	1.14

Note: values followed by a different letter(s) in the same column are significantly different (p<0.05).

Treatment with a.i. one week after inoculation with *F. proliferatum* also reduced disease incidence and showed similar trends. For the treatment with prochloraz, disease incidence was 13.70% for the BKDT isolate and 14.81% for the BKVN isolate. For the treatments with metconazole, disease incidence ranged from 18.52% for the BKDT isolate to 20.74% for the BKPL isolate. Disease incidence was more than 20% and reached 23.33% with tebuconazole (Table 4).

Table 4. Disease incidence when Ba kich plants were treated with a.i. one week after the inoculation with *F. proliferatum* spores.

Active ingredient	Disease incidence (%)		
	BKVN	*BKDT*	*BKPL*
Metconazole	18.89c	18.52bc	20.74b
Prochloraz	14.81d	13.70c	14.07c
Tebuconazole	22.22b	23.33b	20.37b
Inoculated-untreated control	81.11a	80.37a	82.59a
Non-inoculated-untreated control	0.00e	0.00d	0.00d
p	<0.05	<0.05	<0.05
CV(%)	2.52	10.89	5.41
$LSD_{0.05}$	0.55	2.35	1.24

Note: values followed by a different letter(s) in the same column are significantly different (p<0.05).

Efficacy of a.i. on FRRBK in field conditions

Double application of a.i. in the field significantly decreased disease incidence in comparison to the control. Among the three tested a.i., prochloraz showed the highest efficacy on FRRBK in the field condition. Its efficacy was 67.75% after one month of treatment, reached a maximum of more than 69% after 2-3 months after treatment, and started decreasing thereafter. Treatments with metconazole also significantly reduced the disease incidence of FRRBK, resulting in efficacy of 61.63% at one month after treatment; this reached a maximum of 65.66% at two months after treatment before gradually decreased thereafter. Tebuconazole also suppressed disease incidence of FRRBK in field conditions; however, its efficacy was lower than that of either prochloraz or metconazole (Table 5).

Table 5. Efficacy of different a.i. on FRRBK in field conditions.

Active ingredient	DI (%) before treatment	1 MAT		2 MAT		3 MAT		4 MAT		5 MAT	
		DI (%)	*Efficacy (%)*	*DI (%)*	*Efficacy (%)*	*DI (%)*	*Efficacy (%)*	*DI (%)*	*Efficacy (%)*	*DI (%)*	*Efficacy (%)*
Metconazole	6.56	10.33	61.63b	12.67	65.66a	16.33	61.88ab	23.00	57.98ab	33.89	53.87b
Prochloraz	6.22	8.33	67.75a	10.78	69.81a	12.56	69.87a	18.33	64.71a	27.78	60.43a
Tebuconazole	6.33	11.44	56.01c	15.00	58.38b	17.78	58.08b	23.56	53.90b	33.78	52.10b
Control	6.44	26.56	-	36.78	-	43.44	-	54.00	-	72.22	-
p			<0.05		<0.05		<0.05		<0.05		<0.05
CV(%)			4.95		6.10		9.91		10.64		7.81
$LSD_{0.05}$			1.87		2.41		3.84		3.83		2.65

Note: DI: disease incidence, MAT: month after treatment. Values followed by a different letter(s) in the same column are significantly different (p<0.05).

F. proliferatum has been reported as the causal pathogen of FRRBK in Vietnam [1]. To investigate the effects of different fungicides on *F. proliferatum*, DMI (metconazole, prochloraz, and tebuconazole) and QoI (kresoxim-methyl and pyraclostrobin) fungicides were evaluated in this study. Metconazole, prochloraz, and tebuconazole are sterol demethylation inhibitors that inhibit the C-14 α-demethylation of 24-methylenedihydrolanosterol, a precursor of the ergosterol of fungi [3]. Kresoxim-methyl and pyraclostrobin are QoIs that inhibit mitochondrial respiration by binding to cytochrome *c* oxidoreductase, leading to an energy deficiency due to a lack of Adenosine triphosphate (ATP) [4].

Our study reveals that DMI fungicides are more effective in inhibiting the mycelial growth of *F. proliferatum* than are QoI fungicides (Fig. 1). Among the tested a.i., prochloraz and metconazole were the most effective fungicides for inhibiting mycelial growth of *F. proliferatum*. Tebuconazole, another DMI fungicide, exhibited lower levels of inhibitory effects on the growth of *F. proliferatum*. The two QoI fungicides, kresoxim-methyl and pyraclostrobin, were the least effective (Fig. 1). Our results suggest that *F. proliferatum* is more sensitive to prochloraz and metconazole than to tubecunazole, kresoxim-methyl, and pyraclostrobin. The most effective fungicide was prochloraz, followed by metconazole and tebuconazole, among the a.i. tested for the inhibition of mycelial growth of *F. proliferatum*. In pot and field conditions, prochloraz had the highest efficacy in suppressing disease incidence in comparison with other fungicides and the control.

Previous studies indicate that DMI fungicides effectively control different diseases caused by *Fusarium*, such as *F. graminearum*, which causes Fusarium head blight in wheat [5], *F. oxysporum*, which causes Fusarium wilt in bananas [6], *F. subglutinans* and *F. temperatum*, which causes maize stalk rot [7], *F. proliferatum*, which causes Fusarium bulb rot in garlic [8], and *F. proliferatum*, which contaminates cereals [9]. Other studies have also revealed the greater efficacy of DMI fungicides on *Fusarium* species than the other groups of fungicides. Among those groups, prochloraz and tebuconazole have been proven to be more effective against *Fusarium* spp. than kresoxim-methyl [10, 11]. *Fusarium* species were more sensitive to fungicides belonging to the DMI group but were intrinsically resistant to complex III respiration inhibitors [12].

Our results show the high effectiveness of DMI fungicides (prochloraz, metconazole, and tebuconazole) in inhibiting mycelial growth of *F. proliferatum*, although tebuconazole failed to control FRRBK in field conditions (its efficacy was as low as 58%), suggesting that there were some factors might affect the efficacy of a.i. in field conditions. These are pathogen inocula in soil, fungicide application, soil temperature and relative humidity, and soil fertility [9, 13, 14].

Conclusions

Of the tested a.i., prochloraz and metconazole showed the highest efficacy in inhibiting the growth of *F. proliferatum* in *in vitro* conditions, and significantly suppressed disease incidence of FRRBK in pot and in field conditions.

The authors declare that there is no conflict of interest regarding the publication of this article.

REFERENCES

[1] D.T. Nguyen, N.C. Hieu, H.T.B Thao, T.X. Hoat (2019), "Molecular characterization of *Fusarium proliferatum* associated with root rot disease of Indian mulberry (*Morinda officinalis* How.) in Viet Nam", *Archives of Phytopathology and Plant Protection*, **52(1-2)**, pp.200-217.

[2] R. Trabelsi, H. Sellami, Y. Gharbi, A. Krid, M. Cheffi, S. Kammoun, M. Dammak, A. Mseddi, R. Gdoura, M.A. Triki (2017), "Morphological and molecular characterization of *Fusarium* spp. associated with olive trees dieback in Tunisia", *3 BioTech.*, **7(1)**, Doi: 10.1007/s13205-016-0587-3.

[3] Y. Yin, X. Liu, B. Li, Z. Ma (2009), "Characterization of sterol demethylation inhibitor-resistant isolates of *Fusarium asiaticum* and *F. graminearum* collected from wheat in China", *Phytopathol.*, **99(5)**, pp.487-497.

[4] B. Ma (2006), *Azoxystrobin sensitivity and resistance management strategies of Magnaporthe grisea causing gray leaf spot on perennial ryegrass (Lolium perenne) turf*, Ph.D. thesis, Pennsylvania State University, University Park, USA.

[5] D. Ivić, Z. Sever, B. Kuzmanovska (2011), "*In vitro* sensitivity of *Fusarium graminearum*, *F. avenaceum* and *F. verticillioides* to carbendazim, tebuconazole, flutriafol, metconazole and prochloraz", *Pestic. Phytomed.*, **26(1)**, pp.35-42.

[6] B. Nel, C. Steinber, N. Labuschagne, A. Viljoen (2007), "Evaluation of fungicides and sterilants for potential application in the management of Fusarium wilt of banana", *Crop. Prot.*, **26(4)**, pp.697-705.

[7] J.H. Shin, J.H. Han, J.K. Lee, K.S. Kim (2014), "Characterization of the maize stalk rot pathogens *Fusarium subglutinans* and *F. temperatum* and the effect of fungicides on their mycelial growth and colony formation", *Plant Pathol. J.*, **30(4),** pp.397-406.

[8] L.G. Paton, M.D.R. Marrero (2016), "*In vitro* and field efficacy of three fungicides against *Fusarium* bulb rot of garlic", *Eur. J. of Plant Pathol.*, **148(2)**, pp.321-328.

[9] P. Marin, A. de Ory, A. Cruz, N. Magan, M.T. González-Jaen (2013), "Potential effects of environmental conditions on the efficiency of the antifungal tebuconazole controlling *Fusarium verticillioides* and *Fusarium proliferatum* growth rate and fumonisin biosynthesis", *Int. J. Food Microbiol.*, **165(3)**, pp.251-258.

[10] C. Müllenborn, U. Steiner, M. Ludwig, E.C. Oerke (2008), "Effect of fungicides on the complex of Fusarium species and saprophytic fungi colonizing wheat kernels", *Eur. J. of Plant Pathol.*, **120(2)**, pp.157-166.

[11] J. Amini, D. Sidovich (2010), "The effects of fungicides on *Fusarium oxysporum* f. sp. *lycopersici* associated with fusarium wilt of tomato", *J. Plant Protect. Res.*, **50(2)**, pp.172-178.

[12] M. Pasquali, F. Spanu, B. Scherm, V. Balmas, L. Hoffmann, K.E. Hammond-Kosack, M. Beyer, Q. Migheli (2013), "FcStuA from *Fusarium culmorum* controls wheat foot and root rot in a toxin dispensable manner", *PLOS ONE*, **8(2)**, e57429, Doi: 10.1371/journal.pone.0057429.

[13] S.C. Vyas (1988), *Nontarget effects of agricultural fungicides*, London, UK: CRC Press.

[14] H.F. Schwartz, S.K. Mohan (2008), *Compendium of onion and garlic diseases and pests*, 127pp, Ed. APS Press.

Doi: 10.31276/VJSTE.61(2).52-59

The value of malnutrition-inflammation-atherosclerosis (MIA) syndrome for predicting mortality in patients with end-stage renal disease at Hue Central Hospital

Thi Khanh Trang Ngo, Bui Bao Hoang*, Tam Vo

University of Medicine and Pharmacy - Hue University

Received 20 October 2018; accepted 5 March 2019

Abstract:

Background: the role of malnutrition, inflammation, atherosclerosis, and particularly the combination of these three factors were closely related to cardiovascular events, hospitalisation frequency, and death in end-stage renal disease (ESRD) patients. This study examines the relationship between malnutrition-inflammation-atherosclerosis (MIA) syndrome and mortality among these patients during an 18-month period.

Subjects and methods: in this prospective observational cohort study, all cause-mortality was evaluated during an 18-month follow-up period. A total of 174 patients with ESRD (including 57 non-dialysis patients, 56 peritoneal dialysis patients, and 61 hemodialysis patients) were enrolled. M (malnutrition) was assessed by the seven-point subjective global assessment (SGA), serum albumin. I (inflammation) was assessed by serum hs-CRP, serum IL-6. A (atherosclerosis) was defined as IMT ≥0.9 mm or the presence of plaque in the carotid artery. The patients are classified into four groups by number of components (MIA0, MIA1, MIA2, MIA3).

Results: 73.6% of patients had at least one component of MIA syndrome. The proportion of patients with malnutrition, inflammation, and atherosclerosis accounted for 36.8%, 21.3%, and 50.6%, respectively. The proportion of patients with 3, 2, 1 component accounted for 4.0, 27.0, and 42.5%. There was no difference between MIA groups based on age, sex, percentage suffering from dyslipidemia, anemia, or Hb levels. Relative to patients experiencing no elements of MIA syndrome, patients with three components experienced a 13.16 times higher risk of mortality. Only malnutrition was a strong predictor of mortality with HR (95% CI): 5.90 (2.46-14.14).

Conclusion: clinical physicians should attend more closely to and provide early assessments of MIA syndrome in patients with ESRD. They should care for nutrition conditions and thereby provide early and effective treatments. This can contribute to enhancements in quality of life, and decrease mortality rates in patients.

Keywords: **end-stage renal disease, malnutrition-inflammation-atherosclerosis syndrome, MIA syndrome.**

Classification number: **3.2**

Introduction

Chronic kidney disease (CKD) is a global health problem which has received substantial attention in medicine because it has become increasingly common. This has increased treatment costs and decreased quality of life. Patients with CKD have received improved care by many measures, which has advanced patients' lifespans and considerably enhanced disease prognoses. However, the mortality rate among patients with end-stage renal disease (ESRD) remains high, and deaths associated with cardiovascular events are the most concerning. Many researchers have demonstrated the role of malnutrition, inflammation, and atherosclerosis in these outcomes, and particularly the combination of the three factors was closely associated with cardiovascular events, hospitalisation frequency, and death among these patients [1-3]. Nephrologists are currently concerned about the treatment, quality of life advancement, and minimisation of mortality rates among patients with CKD. In Vietnam, although a complete study has not determined the number of CKD patients yet, it was estimated that 20,000 ESRD patients were under treatment with the renal replacement therapy. The mortality of this population has not been

*Corresponding author: Email: bsbao@yahoo.com

investigated yet. Therefore, this study was designed to examine the prognostic value of malnutrition-inflammation-atherosclerosis (MIA) syndrome regarding mortality during an 18-month follow-up with ESRD patients.

Methods

Ethics statement

This study was approved by the Research and Ethical Committees for the use of human subjects at Hue University of Medicine and Pharmacy; informed consent from the patients is required.

Study design and patients

This is a prospective observational cohort study with no treatment interventions; all cause-mortality was recorded during the 18-month follow-up period. Convenience sampling was used for the research, and all subjects eligible were invited to participate.

This research was performed at the department of Nephrology and the Department of Dialysis at Hue Central Hospital in Hue city, Vietnam, from 1/2014 to 2/2017. A total of 174 patients with ESRD (including 57 non-dialysis patients, 56 peritoneal dialysis patients, and 61 hemodialysis patients) were enrolled.

In terms of patient selection criteria patients with ESRD who were at least 18 years old, agreed to participate in the study. Non-dialysis patients with glomerular filtration <15 ml/min/1.73 m^2 (eGFR based on formula of CKD-EPI 2009) were enrolled. Additionally, continuous ambulatory peritoneal dialysis patients had been stable for at least two months (when the postoperative catheter placement was stable and the patient had mastered the procedure). Hemodialysis patients were treated three times weekly for at least three months.

The exclusion criteria applied included fever (defined as axillary temperature >37.5^{0}C), acute or chronic infection, and patients accompanied by one of the following diseases or conditions: cerebrovascular disease, coronary artery disease, peripheral vascular disease, congenital heart disease, heart valve disease, arthritis, malignant disease, chronic lung disease, cirrhosis, autoimmune disease, trauma, acute exacerbation of chronic kidney failure, complications related to peritoneal dialysis patients such as catheter issues, herniae, and hydrothorax, fistula vein stenosis, or renal transplantation.

Definition of MIA factors and grouping

M (malnutrition) was measured with the seven-point SGA (if items SGA ≤5 points with no manifestations of normal nutrition) combined with serum albumin levels <40 g/l [4]. I (inflammation) was defined as serum hs-CRP level >5 mg/l (upper reference values) combined with serum IL-6 level >5.53 pg/ml (upper reference values). A (atherosclerosis) was defined as IMT ≥0.9 mm or the presence of plaque in the carotid artery [5].

The patients were classified into for groups based on the number of the components: MIA0, MIA1, MIA2, MIA3.

Techniques applied in this research

Venous blood samples were taken in the morning after an overnight fast, and prior to dialysis. A machine of Cobas e 501 was used for quantifying chemo-biological indices (albumin, total cholesterol, triglyceride, HDL-C, LDL-C, hs-CRP), of IMMULITE 2000 XPI for quantifying plasma IL-6 levels.

An Acuson X500 Ultrasound Machine was used for the diagnosis of atherosclerosis of the carotid artery. 7-5 MHz linear transducers were used for the assessment of the intima-media thickness and plaque morphology. This technique was performed by an experienced radiologist.

Collecting information regarding mortality during the 18-month follow-up period

Non-dialysis patients: made contact with the patients by phone. They received reexamination once every month. This enabled us to collect important information regarding disease progress (including events, death), treatment compliance, and patients' and their families' thoughts and desires regarding treatment choices for kidney failure.

After monitoring for 18 months, we discovered the following change in the quantity in the non-dialysis group:

Firstly, 28 patients who had received renal replacement therapy with peritoneal dialysis and hemodialysis were excluded from the analysis because our aim is solely to conduct observational research, as opposed to treatment intervention.

Secondly, among the other 29 patients, 19 patients and their families initially refused renal replacement therapy and asked for dialysis delay. 18 months later, they also received dialysis. The other 10 patients had glomerular filtration rates at 10-15 ml/minute. Because there were not yet symptoms associated with uremia and events (volume overload, metabolic abnormalities...), there were no indications of dialysis. This group was periodically treated and monitored. Therefore, for 18 months, there had still been 29 patients who received medical treatment and then dialysis. Therefore, for the analysis of the prognostic value of MIA syndrome, only 146 patients remained.

Patients with peritoneal dialysis and hemodialysis were monitored through appointments each month (patients with peritoneal dialysis) and through each dialysis session (patients with hemodialysis). Deaths were recorded based on outpatient medical records.

Our data only indicated the clinical value of MIA syndrome for predicting all-cause mortality in patients with ESRD.

Statistical analysis

All statistical analyses were performed using SPSS V22.0 (Statistical Package for Social Sciences). Quantitative variables were expressed as the mean ± standard deviation. Qualitative variables were expressed in terms of frequencies and percentages. Two ratios were compared using a Chi-squared test. An ANOVA test was used to compare means between groups. The COX model and the Kaplan-Meier method were used to investigate survival factors. The Kaplan-Meier method was used to analyse cumulative survival probability, and the COX model was applied to investigate the prognostic value of elements of MIA syndrome in relation to all-cause mortality. Differences with p<0.05 were considered statistically significant.

Results

Initially, the 174 patients (83 males and 91 females) included 57 non-dialysis patients, 56 peritoneal dialysis patients, and 61 hemodialysis patients. The average ages of these research subjects were 48.11±15.10, among whom non-dialysis patients were 50.83±16.67, peritoneal dialysis patients were 47.66±12.82; and hemodialysis patients were 45.98±15.36 (Tables 1, 2; Fig. 1).

Table 1. Percentage of patients who experienced at least one element of MIA.

Group	Experienced at least one factor of MIA		No factors of MIA	
	n	*%*	*n*	*%*
Non-dialysis (n=57)	42	73.7	15	26.3
Peritoneal dialysis (n=56)	41	73.2	15	26.8
Hemodialysis (n=61)	45	73.8	16	26.2
Total	128	73.6	46	26.4
p	>0.05			

Table 2. Percentage of patients by number of MIA elements.

Group	MIA3		MIA2		MIA1		MIA0	
	n	*%*	*n*	*%*	*n*	*%*	*n*	*%*
Non-dialysis (n=57)	3	5.3	18	31.6	21	36.8	15	26.3
Peritoneal dialysis (n=56)	2	3.6	14	25.0	25	44.6	15	26.8
Hemodialysis (n=61)	2	3.3	15	24.6	28	45.9	16	26.2
Total	7	4.0	47	27.0	74	42.5	46	26.5
p	>0.05*		>0.05		>0.05		>0.05	

* Fisher test.

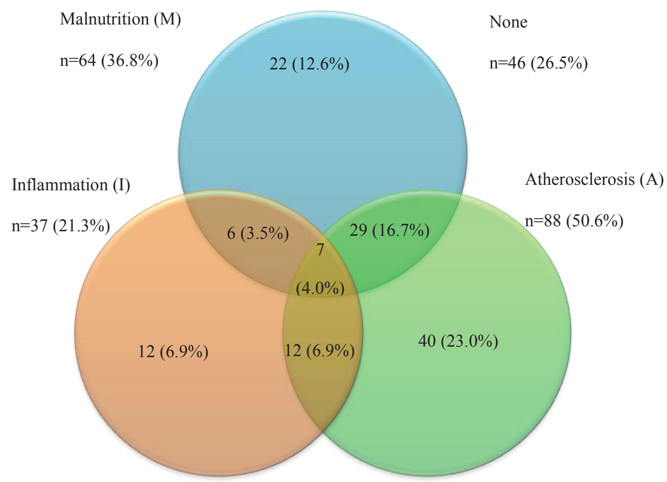

Fig. 1. Relationships between components of MIA syndrome among the patients.
Notably, 26.5% of the patients experienced no malnutrition, inflammation, or atherosclerosis.

During the 18-month follow-up period, 25 patients died from all causes. No differences were observed in terms of age, sex, percentage of patients with anemia, dyslipidemia, or treatment methods between the non-survival and survival groups (Table 3).

Table 3. Comparison between initial data among the non-survival group as opposed to the survival group.

Parameters		Non-survivals (n=25)		Survivals (n=121)		P-value
		n	*%*	*n*	*%*	
Age (years)	$\bar{X}$±SD	50.24±16.42		47.92±14.76		>0.05
Sex	Male	8	32.0	64	52.9	>0.05
	Female	17	68.0	57	47.1	
Patients with anemia	Yes	24	96.0	106	87.6	>0.05
	No	1	4.0	15	12.4	
Patients with dyslipidemia	Yes	19	76.0	87	71.9	>0.05
	No	6	24.0	34	28.1	
Treatment method	Non-dialysis	5	20.0	24	19.8	>0.05
	Peritoneal dialysis	10	40.0	46	38.0	
	Hemodialysis	10	40.0	51	42.2	

The probability of survival was diminished in malnourished patients (Table 4 and Fig. 2). Meanwhile, there was no significant difference in the probability of survival between patients with and without inflammation (Table 5 and Fig. 3). This was also noted between patients with and without atherosclerosis (Table 6 and Fig. 4).

Table 4. Probability of survival for patients with and without malnutrition.

Malnutrition	Group															
	Non-dialysis (n=29)				*Peritoneal dialysis (n=56)*				*Hemodialysis (n=61)*				*Total (n=146)*			
	Non-survivals (n=5)		*Survivals (n=24)*		*Non-survivals (n=10)*		*Survivals (n=46)*		*Non-survivals (n=10)*		*Survivals (n=51)*		*Non-survivals (n=25)*		*Survivals (n=121)*	
	n	%	n	%	n	%	n	%	n	%	n	%	n	%	n	%
Yes	5	41.7	7	58.3	7	35.0	13	65.0	6	33.3	12	66.7	18	36.0	32	64.0
No	0	0.0	17	100.0	3	8.3	33	91.7	4	9.3	39	90.7	7	7.3	89	92.7
p Log Rank	<0.05				<0.05				<0.05				<0.001			

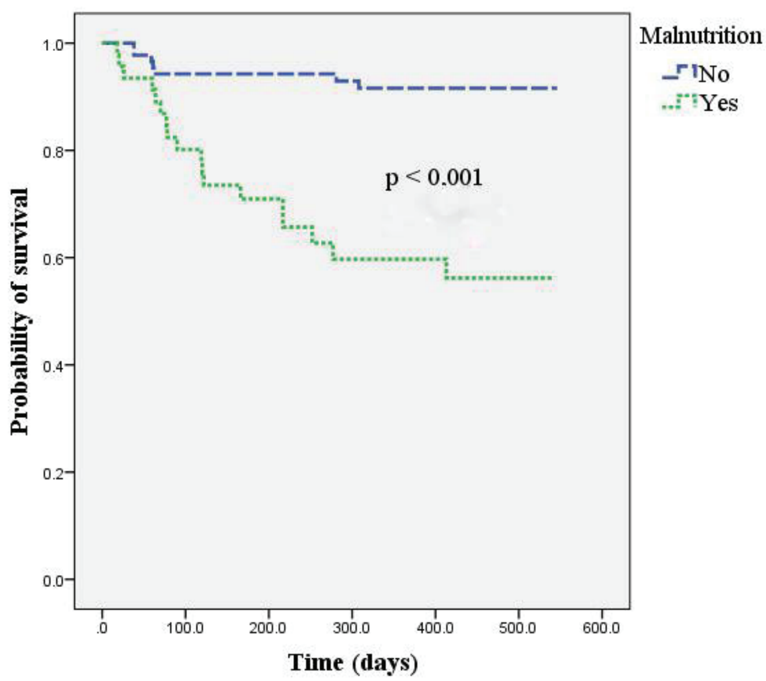

Fig. 2. Kaplan-Meier survival curves for patients with and without malnutrition.

Table 5. Probability of survival for patients with and without inflammation.

Inflammation	Group															
	Non-dialysis (n=29)				*Peritoneal dialysis (n=56)*				*Hemodialysis (n=61)*				*Total (n=146)*			
	Non-survivals (n=5)		*Survivals (n=24)*		*Non-survivals (n=10)*		*Survivals (n=46)*		*Non-survivals (n=10)*		*Survivals (n=51)*		*Non-survivals (n=25)*		*Survivals (n=121)*	
	n	%	n	%	n	%	n	%	n	%	n	%	n	%	n	%
Yes	3	42.9	4	57.1	2	15.4	11	84.6	1	7.1	13	92.9	6	17.6	28	82.4
No	2	9.1	20	90.9	8	18.6	35	81.4	9	19.1	38	80.9	19	17.0	93	83.0
p Log Rank	<0.05				>0.05				>0.05				>0.05			

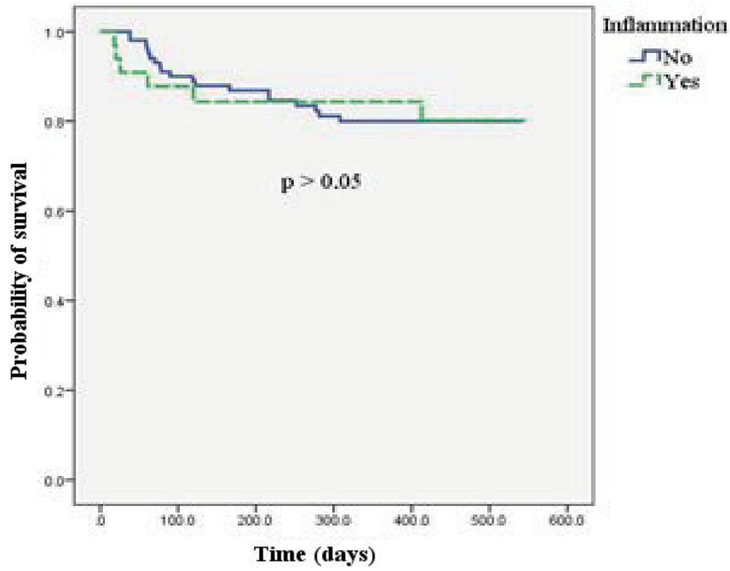

Fig. 3. Kaplan-Meier survival curves for patients with and without inflammation.

Table 6. Probability of survival for patients with and without atherosclerosis.

Atherosclerosis	**Group**															
	Non-dialysis (n=29)				***Peritoneal dialysis (n=56)***				***Hemodialysis (n=61)***				***Total (n=146)***			
	Non-survivals (n=5)		*Survivals (n=24)*		*Non-survivals (n=10)*		*Survivals (n=46)*		*Non-survivals (n=10)*		*Survivals (n=51)*		*Non-survivals (n=25)*		*Survivals (n=121)*	
	n	%	n	%	n	%	n	%	n	%	n	%	n	%	n	%
Yes	5	29.4	12	70.6	5	19.2	21	80.8	5	15.6	27	84.4	15	20.0	60	80.0
No	0	0.0	12	100.0	5	16.7	25	83.3	5	17.2	24	82.8	10	14.1	61	85.9
p Log Rank	>0.05				>0.05				>0.05				>0.05			

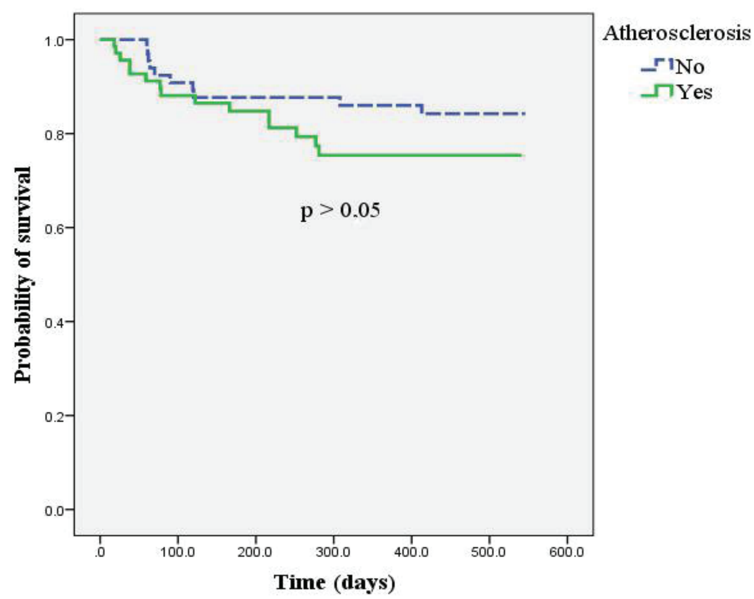

Fig. 4. Kaplan-Meier survival curves for patients with and without atherosclerosis.

Of all of the components of MIA, we discovered that only malnutrition was the independent predictor of mortality (Table 7).

Table 7. COX proportional hazards analysis for mortality in patients in relation to malnutrition.

Malnutrition	HR	95% CI	P-value
No	1	Reference	-
Yes	5.90	2.46-14.14	<0.001

The probability of mortality was significantly related to the presence and number of elements of MIA syndrome (Table 8 and Fig. 5). If the patient experienced all three components, the probability of mortality was 42.9%. Conversely, in patients without any components, this probably was 5.0%.

Table 9. COX proportional hazards analysis for mortality in relation to MIA groups.

MIA group	HR	95% CI	P-value
MIA0	1	Reference	-
MIA3	13.16	2.20-78.86	<0.05
MIA2	5.58	1.22-25.48	<0.05
MIA1	3.39	0.74-15.50	>0.05

Discussion

Malnutrition, inflammation, and atherosclerosis are all common causes of morbidity and mortality in ESRD patients. In addition, each component is predictive of cardiovascular events in these subjects [1, 6-8]. The strong association between inflammation, malnutrition, and atherosclerosis has been demonstrated in several studies and was summarised in a syndrome called MIA syndrome [9-11].

Table 8. Probability of survival for patients in relation to MIA groups.

MIA groups	Group															
	Non-dialysis (n=29)				*Peritoneal dialysis (n=56)*				*Hemodialysis (n=61)*				*Total (n=146)*			
	Non-survivals (n=5)		*Survivals (n=24)*		*Non-survivals (n=10)*		*Survivals (n=46)*		*Non-survivals (n=10)*		*Survivals (n=51)*		*Non-survivals (n=25)*		*Survivals (n=121)*	
	n	%	n	%	n	%	n	%	n	%	n	%	n	%	n	%
MIA3	3	100.0	0	0.0	0	0.0	2	100.0	0	0.0	2	100.0	3	42.9	4	57.1
MIA2	2	20.0	8	80.0	5	35.7	9	64.3	3	20.0	12	80.0	10	25.6	29	74.4
MIA1	0	0.0	7	100.0	4	16.0	21	84.0	6	21.4	22	78.6	10	16.7	50	83.3
MIA0	0	0.0	9	100.0	1	6.7	14	93.3	1	6.2	15	93.8	2	5.0	38	95.0
p Log Rank	<0.001				>0.05				>0.05				<0.05			

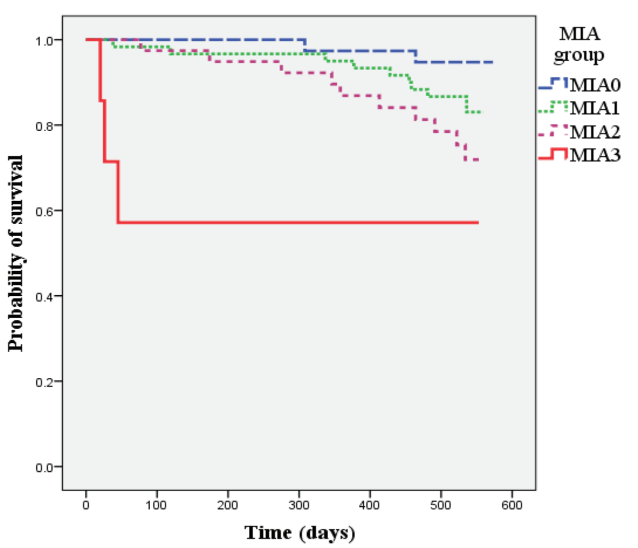

Fig. 5. Kaplan-Meier survival curves for patients in relation to MIA groups.

Relative to patients without any components of MIA, patients with all three components experienced an increased risk of death by a factor of 13.16 (Table 9).

Our results demonstrated that 73.6% of patients in the study group experienced at least one component of MIA syndrome; the proportion of these patients experiencing three components was 4.0%. This was 22.0% lower than that in a study by P. Stenvinkel, et al. (Sweden) which examined 109 predialysis patients [11]; 23.44% in A.R. Qureshi, et al. (Sweden) on over 128 patients with maintenance haemodialysis [6]; 11.0% in K. Turkmen, et al. (Turkey) on over 80 patients with maintenance haemodialysis and peritoneal dialysis [9]. In another study by A.Y. Wang, et al. (China) on 238 patients with peritoneal dialysis, the researchers identified MIA3 among 36 patients (15.1%), MIA2 among 62 patients (26.1%), MIA1 among 81 patients (34.0%), and MIA0 among 59 patients (24.8%) [8].

We discovered a difference in the distribution of the number of components between the results of our study and those of the researchers'. The causes of the difference may be related to the criteria for the diagnosis of MIA syndrome and the research subjects. In foreign countries, the causes of diabetes mellitus and hypertension accounted for a significant proportion while chronic glomerulonephritis and chronic pyelonephritis were the primary causes in our country. In addition, race is also related to inflammation and atherosclerosis rates.

H.Z. Tonbul, et al. (Turkey) conducted a study which examined 30 patients with peritoneal dialysis and 30 patients with maintenance haemodialysis. The results demonstrated that the MIA3 rate in the group with peritoneal dialysis was 3.33% and 0.0% in the group with maintenance haemodialysis [12].

Another study by Renée de Mutsert, et al. (Netherlands) which involved 815 patients with maintenance haemodialysis demonstrated that the MIA3 rate was 6% [2]. Therefore, our results are similar to those.

The association between malnutrition, inflammation and atherosclerosis was further confirmed by the overlap in the presence of these components in MIA syndrome (see Fig. 1). This result was identified by studies performed across the world:

A study by P. Stenvinkel, et al. examined the association between malnutrition, inflammation and atherosclerosis in 109 non-dialysis ESRD patients. It demonstrated that a significant proportion of patients with atherosclerosis also experienced malnutrition (24.0%), inflammation (13.0%) or both (30.0%). The majority of patients experienced inflammation (97.0%) and malnutrition (89.0%) with plaque in the carotid artery [11].

Similarly, the association between malnutrition, inflammation and atherosclerosis was also confirmed in diabetic patients with peritoneal dialysis [13] or ESRD patients (patients with maintenance haemodialysis and peritoneal dialysis) [7].

Our results and those of other researchers have identified the overlap between malnutrition, inflammation and atherosclerosis in ESRD patients. In addition, we discovered no difference in the number of components of MIA in all three groups (Tables 1, 2). This suggests that one, two, or all three components of MIA may be present among non-dialysis CKD patients as well as in patients who have received renal replacement therapy (with peritoneal dialysis and hemodialysis). This resulted in increased hospitalisations, morbidity and mortality from cardiovascular diseases, as well as quality of life decreases among those with many risks [14, 15].

In terms of the predictive value of MIA syndrome in ESRD patients, studies performed across the world have indicated that each component has an independent predictive value [1, 6-8]. However, we only demonstrated that malnutrition is an independent predictor of mortality in the study population. Our findings were consistent with other studies conducted around the world which illustrated that malnutrition is a risk factor for increases in morbidity and mortality in ESRD patients [16-18].

Therefore, it was an issue that we demonstrated that only malnutrition was an independent predictor of mortality in this study. This may be because serum hs-CRP and IL-6 levels were only assessed once. This could not be a representative of chronic inflammation; the follow-up duration in the study may not have been sufficiently lengthy (18 months); the cause of CKD of our subjects is chronic glomerulonephritis and chronic pyelonephritis. Meanwhile, research subjects in foreign countries are primarily patients with CKD due to diabetes and hypertension.

Although inflammation has been demonstrated to be an independent predictor of death from cardiovascular disease in many studies, the risk of cardiovascular events in inflammatory patients in our study did not depend significantly on serum hs-CRP and IL-6 levels. The current perception held that malnutrition is a risk factor for cardiovascular disease in uremic environments and that this is the cause of increased mortality in malnutrition patients. The exact mechanism of malnutrition that possibly increased the risk of cardiovascular disease remained unclear. It has recently been proven that malnutrition combined with an increase in oxidative stress can weaken the inner lining of the blood vessels, which may reduce the biological benefits of nitric oxide; this can precipitate immune system disorders which render the body susceptible to inflammation, infection and cardiovascular disease through the following hypothesis. This finding suggests that malnutrition exacerbated outcomes in CKD patient by contributing to present inflammation and atherosclerosis.

The strengths of this study, however, were that we investigated the role of compound elements believed to exert synergistic effects in relation to MIA syndrome. The results illustrated that the risk of mortality during the 18-month follow-up period would increase along with the number of components in MIA syndrome as follows: the risk of increased mortality in patients with two or more components. It was remarkable that the MIA3 group faced the risk of death increasing 13.16 times more relative to patients without component of MIA syndrome.

Studies performed around the world have also demonstrated an increased risk of mortality associated with MIA syndrome [2, 3, 6].

Therefore, it is necessary to proactively attend to and evaluate MIA syndrome; nutritional status should receive special attention for timely intervention to reduce the risk of death in these patients. However, this also presented a major challenge in clinical practice because many factors exerted effects on the assessment of nutritional status and inflammation in CKD patients. Malnutrition and inflammation tended to occur simultaneously and coexisted in ESRD patients. Some causes of malnutrition were also factors that promoted inflammation and vice versa. Therefore, MIA syndrome was proposed to emphasise the association of these two conditions in ESRD patients.

In summary, similarly to worldwide studies, we also discovered an interaction between malnutrition, inflammation, and atherosclerosis in ESRD patients. In the circle of this pathology, inflammation was mediated by inflammatory cytokines that caused malnutrition through the mechanism of energy consumption increases at rest, muscle protein breakdown increases, appetite suppression, and anorexia. Moreover, inflammation was also the cause of atherosclerosis; conversely, atherosclerosis caused inflammatory pathology. Finally, malnutrition contributed to developing chronic inflammation and atherosclerosis, which increased morbidity and mortality from cardiovascular disease in ESRD patients [11, 13].

Limitations of the study

The data only indicated the clinical value of MIA syndrome for predicting all-cause mortality in patients with ESRD. The study did not analyse the association between MIA syndrome and death from cardiovascular disease.

Conclusions

Studying 174 patients (including 57 non-dialysis patients, 56 peritoneal dialysis patients, and 61 hemodialysis patients) during the 18-month follow-up period has yielded the following conclusions:

- 73.6% of patients had at least one component of MIA syndrome. The proportion of patients with malnutrition, inflammation, and atherosclerosis accounted for 36.8%, 21.3%, and 50.6%, respectively. The proportion of patients with 3, 2, and 1 components accounted for 4.0%, 27.0%, and 42.5%, respectively.

- There is no difference between MIA groups in terms of age, sex, percentage of dyslipidemia, anemia, and Hb levels.

- Relative to patients experiencing no elements of MIA syndrome, patients with three components had an increased risk of mortality by a factor of 13.16. Only malnutrition was a strong predictor of mortality with HR (95% CI): 5.90 (2.46-14.14).

Recommendation

The findings of the research indicate the following recommendations: clinical physicians should attend more closely to and provide an early assessment of malnutrition-inflammation-atherosclerosis syndrome in patients with ESRD. They should care for nutrition conditions, based on which they can provide an early and positive treatment. This can advance quality of life and decrease mortality rates in ESRD patients.

The authors declare that there is no conflict of interest regarding the publication of this article.

REFERENCES

[1] I. Akdag, Y. Yilmaz, S. Kahvecioglu, et al. (2008), "Clinical value of the malnutrition-inflammation-atherosclerosis syndrome for long-term prediction of cardiovascular mortality in patients with end-stage renal disease: a 5-year prospective study", *Nephron Clinical Practice*, **108**, pp.99-105.

[2] Renée de Mutsert, D.C. Grootendorst, J. Axelsson, et al. (2008), "Excess mortality due to interaction between protein-energy wasting, inflammation and cardiovascular disease in chronic dialysis patients", *Nephrology Dialysis Transplantation*, **23**, pp.2957-2964.

[3] D. Sueta, S. Hokimoto, K. Sakamoto, et al. (2016), "Validation of the high mortality rate of malnutrition - inflammation - atherosclerosis syndrome - community - based observational study", *International Journal of Cardiology*, **30**, pp.1-6.

[4] National Kidney Foundation Kidney Disease Outcomes Quality Initiative (NKF KDOQI) (2000), "Clinical practice guidelines for nutrition in chronic renal failure", *American Journal of Kidney Diseases*, **35(6)**, pp.1-140.

[5] A. Zachetti (2003), "2003 European society of hypertension European society of cardiology guidelines for the management of arterial hypertension", *Jounal of Hypertension*, **21**, pp.1011-1053.

[6] A.R. Qureshi, A. Alvestrand, J.C. Divino-Filho, et al. (2002), "Inflammation, malnutrition, and cardiac disease as predictors of mortality in hemodialysis patients", *Journal of the American Society of Nephrology*, **13**, pp.28-36.

[7] K. Turkmen, H.Z. Tonbul, F.M. Erdur, et al. (2013), "Peri-aortic fat tissue and malnutrition-inflammation-atherosclerosis/calcification syndrome in end-stage renal disease patients", *International Urology and Nephrology*, **45**, pp.857-867.

[8] A.Y. Wang, J. Woo, C.W. Lam, et al. (2005), "Associations of serum fetuin-A with malnutrition, inflammation, atherosclerosis and valvular calcification syndrome and outcome in peritoneal dialysis patients", *Nephrology Dialysis Transplantation*, **20(8)**, pp.1676-1685.

[9] K. Turkmen, H. Kayikcioglu, O. Ozbek, et al. (2011), "The relationship between epicardial adipose tissue and Malnutrition, Inflammation, Atherosclerosis/Calcification syndrome in ESRD patients", *Clinical Journal of the American Society* of *Nephrology*, **6**, pp.1920-1925.

[10] Y.Y. Hyun, K.B. Lee, S.H. Hanson, et al. (2017), "Nutritional status in adults with predialysis chronic kidney disease: KNOW-CKD study", *Journal of Korean Medical Science*, **32**, pp.257-263.

[11] P. Stenvinkel, O. Heimburger, F. Paultre, et al. (1999), "Strong association between malnutrition, inflammation, and atherosclerosis in chronic renal failure", *Kidney International*, **55**, pp.1899-1911.

[12] H.Z. Tonbul, M. Demir, L. Altintepe, et al. (2006), "Malnutrition-inflammation-atherosclerosis (MIA) syndrome components in hemodialysis and peritoneal dialysis patients", *Renal Failure*, **28**, pp.287-294.

[13] R. Pecoits-Filho (2002), "The malnutrition, inflammation, and atherosclerosis (MIA) syndrome-the heart of the matter", *Nephrology Dialysis Transplantation*, **17(11)**, pp.28-31.

[14] I. Shahab, K.D. Nolph (2006), "MIA syndrome in peritoneal dialysis: prevention and treatment", *Peritoneal Dialysis: A Clinical Update*, **150**, pp.135-143.

[15] S. Zyga, G. Christopoulou, M. Malliarou, et al. (2011), "Malnutrition-inflammation-atherosclerosis syndrome in patients with end-stage renal disease", *Journal of Renal Care,* **37(1)**, pp.12-15.

[16] D. Churchill, D.W. Taylor, P.R. Keshaviah, et al. (1996), "Adequacy of dialysis and nutrition in continuous peritoneal dialysis; association with clinical outcomes", *Journal of the American Society of Nephrology*, **7**, pp.198-207.

[17] L. Foucan, H. Merault, F.L. Velayoudom-Cephise (2015), "Impact of protein energy wasting status on survival among Afro-Caribbean hemodialysis patients: a 3-year prospective study", *Springer Plus,* **4(452)**, pp.1-10.

[18] Renée de Mutsert, D.C. Grootendorst, E.W. Boeschoten, et al. (2009), "Subjective global assessment of nutritional status is strongly associated with mortality in chronic dialysis patients", *American Journal of Clinical Nutrition*, **89**, pp.787-793.

Doi: 10.31276/VJSTE.61(2).60-64

Clinical and paraclinical characteristics of metabolic syndrome in children with overweight and obesity in Dong Nai province, Vietnam

Ha Van Thieu*

Pham Ngoc Thach University of Medicine

Received 29 March 2019 ; accepted 28 May 2019

Abstract:

Background: childhood overweight is increasingly common worldwide as are its consequences, which include increased risk of later cardiovascular disease and diabetes. Although metabolic syndrome (MetS) has been extensively studied in adults, not much is known about the condition in children and adolescents. MetS and its individual components are detectable during childhood, and both commonly persist throughout adolescence and adulthood.

Objective: to determine the prevalence of MetS and cut-off values of waist circumference (WC) and body mass index (BMI) for predicting MetS in children with overweight and obesity.

Methods: we conducted cross-sectional analysis of 510 children with overweight and obesity aged 10 to 15 years in Bien Hoa city, Dong Nai province (2012-2014). MetS diagnosis was defined according to the 2007 International Diabetes Federation definition.

Results: a relationship existed between BMI and dyslipidaemia (p<0.05). Among all participants, 31.37% met the criteria for MetS (female>male, p>0.05). The most common manifestation of MetS in this study was WC-blood pressure-triglyceride (41.15%). The cut-off anthropometry values for predicting MetS were as follows: BMI of 25.00 in boys and 24.50 in girls, and WC of 82 cm in boys and 80 cm in girls.

Conclusions: the prevalence of MetS was 31.37% among children with overweight and obesity. The cut-off values of WC and BMI in this study could be the optimal threshold for predicting MetS in such children aged 10 to 15 years.

Keywords: **MetS in children, MetS in overweight, obesity, overweight, Vietnam.**

Classification number: **3.2**

Introduction

Metabolic syndrome (MetS) is one of the most concerning public health problems of the 21st century. According to the International Diabetes Federation (IDF), MetS is a cluster of risk factors for two major pandemics - cardiovascular disease (CVD) and type 2 diabetes - affecting quality of life and incurring significant costs to the health-care economy of multiple countries worldwide [1, 2].

Obesity is rapidly increasing with MetS in adults as well as in children. In Bolivia, M. Caceres, et al. studied 61 children aged 5-18 years with a body mass index (BMI)>95th percentile by age and gender (2006-2007); the results revealed that the proportion of children with MetS was 36% (40% in boys and 32.2% in girls). The prevalence of impaired glucose tolerance, elevated triglyceride (TG), low high-density lipoprotein cholesterol (HDL-C), high blood pressure (BP), and insulin resistance were 8.2, 42.6, 55.7, 24.5, and 39.4%, respectively [3]. Children at high risk of CVD could be identified from their waist circumference (WC) and waist-to-hip ratio [4].

A.P. Ferreira, et al. [5] studied 52 obese children aged 7-10 years, and found the prevalence of MetS was 17.3% with BMI>95th percentile, elevated TG, low HDL-C, high blood glucose, and hypertension. According to R. Weiss, et al.' 2004 study, the prevalence of MetS was also increasing in children. The figures were 38.7 and 49.7% in children with moderate and severe obesity, respectively [6].

MetS is closely related to overweight and obesity. This has prompted interest in terms of epidemiology and preventive approaches in the aspect of chronic noncommunicable diseases. CVDs in adults derive from metabolic disorders in childhood [6], and thus, early prevention of atherosclerosis would be conducive to enhanced results [7, 8]. CVD and its mortality are just the tip of the iceberg, of which series of metabolic abnormalities appeared silently before.

To construct an effective MetS monitoring and intervention system, having access to basic data on the nature of this problem is imperative. However, few studies

*Email: havanthieu67@gmail.com

have been conducted on MetS in children with overweight and obesity in Vietnam. Based on the abovementioned arguments, we conducted a study of MetS in such children aged 10 to 15 years. The aim was to contribute to the detection and prevention of the consequences caused by MetS, thereby contributing to reducing spending on treatment fees and improving patients' quality of life. This study had the following objectives:

1. To identify characteristics of dyslipidemia and blood glucose in children with overweight and obesity.

2. To determine clinical and subclinical characteristics of MetS as well as the cut-off values of WC and predictive BMI in children with overweight and obesity aged 10 to 15 years.

Material and methods

Study design

The study was conducted based on a cross-sectional study design.

Subjects: students aged 10-15 years who met an eligible diagnosis of overweight or obesity and were studying at secondary schools in Bien Hoa city, Dong Nai province.

Sampling

To determine the prevalence of MetS in overweight - obese children in the community, the sample size was calculated according to the formula of estimated sample size n=$\frac{Z^2}{d^2}.P.q$ (the testing sample size of prevalence of MetS in overweight - obesity children was approximately 15%); $n = \frac{1.96^2 x\,0.15x0.85}{0.04^2} = 306$.

Because of school sampling, adjusting to limit the design impact was done by multiplying by the design effect=1.5. Accordingly, the sample size was 306x1.5=459. The estimated participation rate was 95%; therefore, the necessary sample size was n=459/0.95=483. We chose approximately 500 overweight and obese students aged 10-15 years.

Sampling technique: multistage sampling.

Step 1: from a list of 32 secondary schools in Bien Hoa city, 16 were randomly chosen. Overweight and obese children were classified based on CDC classification 2000 by age and gender (2000 CDC BMI for ageing growth charts for girls and boys); 85^{th} percentile ≤BMI<95^{th} percentile was overweight and BMI≥95^{th} percentile was obese.

We divided the children into three levels: level 1=85^{th}≤ BMI<90^{th}; level 2=90^{th}≤BMI<95^{th}; and level 3: BMI≥95^{th} percentile.

Height was measured twice with subjects barefoot to an accuracy of ±0.1 cm. Furthermore, weight was measured twice with subjects lightly dressed to an accuracy of ±0.1 kg. BMI (kg/m^2) was calculated as weight (kg) divided by the square of height (m). WC was measured to an accuracy of ±0.1 cm with a nonelastic measuring tape. Moreover, it was measured at a point halfway between the lower border of the thorax and the iliac crest at the end of expiration.

Body fat ratio (BFP) measurements were based on bioelectrical impedance analysis and performed using an Omron device (Japan). Subjects were required to fast for 8 hours prior to taking a blood test.

Step 2: overweight and obese students were selected from the 16 secondary schools.

- The calculated sample size was 500. We selected an average of 32 overweight, obese students in each school, among which the number of boys and girls was nearly equal.

- All students of the selected classes were invited to join the study. A fact sheet explaining the purpose and procedure was provided to each student and their parents.

Step 3: diagnostic criteria of MetS.

- WC ≥90^{th} percentile based on the percentile of Y.T.S. Rita, et al. [4].

- TG≥150 mg/dL; HDL-C<40 mg/dL; systolic BP (SBP) ≥130 mmHg or diastolic BP (DBP) ≥85 mmHg; blood glucose ≥100 mg/dL [9].

- According to IDF (2007): WC≥90^{th} percentile and the presence of at least two standards listed by age and gender considering that children had MetS.

Step 4: data processing using the EPI.DATA software package.

Receiver operator characteristic (ROC) curve analysis was used to estimate risk cut-off points (WC and BMI by gender). Sensitivity, specificity, and positive and negative predictive values were calculated for each cut-off point. We used logistic regression odds ratios to determine the risk index of indicators according to the cut-off point of MetS. A p-value<0.05 was considered statistically significant.

Ethical issues

- These tests were conducted in agreement with families and schools prior to proceeding (with informed consent forms - ICF).

- The study was approved by the Science Council and Ethics Committee of Dong Nai Department of Health.

Results

The sample size included a total of 510 children with overweight and obesity. The proportions of boys and girls were 49.80 and 50.20%, respectively; 41.96% of participants were overweight and 58.04% were obese.

Characteristics of dyslipidemia and blood glucose (Tables 1, 2)

Table 1. Average values of blood lipid and blood glucose.

Criteria	General (X±SD) n=510	Male (X±SD) n=254	Female (X±SD) n=256	p-value
CT (mg/dL)	184.78±45.48	182.50±45.84	187.04±45.11	0.307
TG (mg/dL)	157.29±78.81	156.27±70.31	158.31±67.41	0.738
HDL-C (mg/dL)	51.58±7.86	52.14±7.39	51.03±8.28	0.111
LDL-C (mg/dL)	110.20±39.04	107.15±36.91	113.27±40.89	0.076
Glucose (mg/dL)	88.51±14.36	88.30±15.54	88.72±13.10	0.739

A t-test was used for the average data (all values are average±SD). Cholesterol (CT); triglyceride (TG); high-density lipoprotein cholesterol (HDL-C); low density lipoprotein cholesterol (LDL-C).

No differences existed in the average values of blood lipids, including CT, TG, HDL-C, LDL-C, and blood glucose between both genders (p>0.05).

Table 2. Blood lipid disorder according to BMI levels.

Blood lipid	BMI *Level 1* *n=34*	*Level 2* *n=180*	*Level 3* *n=296*	Total n=510	p-value
No disorder	14	49	49	112 (21.96%)	
Disorder	20	131	247	398 (78.04%)	
1 index	9 (3.77%)	91 (38.07%)	139 (58.16%)	239 (60.05%)	
2 indexes	6 (5.56%)	32 (29.63%)	70 (64.81%)	108 (27.14%)	0.001
≥3 indexes	5 (9.81%)	8 (15.68%)	38 (74.51%)	51 (12.81%)	

The percentages of the groups without and with blood lipid disorder were 21.96% and 78.04%, respectively. In the group with blood lipid disorder, the proportion of the disorder greater than or equal to three blood lipid indexes was a low percentage (12.81%), whereas the proportion of the disorder of one blood lipid index was a high percentage (60.05%). BMI at level 3 with a proportion of the disorder greater than or equal to three lipid indexes concurrently was higher than BMI at levels 1 and 2. This difference was statistically significant (p<0.05).

MetS

Clinical and subclinical characteristics of MetS (Tables 3-5):

Table 3. Proportion of MetS in total and by gender.

Gender	MetS	No MetS	Total	p-value
Male	71 (44.38%)	183 (52.29%)	254 (49.80%)	0.097
Female	89 (55.62%)	167 (47.21%)	256 (50.20%)	
Total	160 (31.37%)	350 (68.63%)	510 (100.00%)	

The proportion of MetS was 31.37%, with a higher percentage in females than males (p>0.05).

Table 4. Clinical and subclinical characteristics of MetS.

Criteria	No MetS (X±SD, n=350)	MetS (X±SD, n=160)	p-value
WC (cm)	84.07±6.12	87.44±7.11	0.001**
WC/HC	0.94±0.05	0.95±0.06	0.233
WC/Height	0.55±0.04	0.56±0.04	0.158
BMI	25.91±2.63	26.94±2.67	0.001**
SBP (mmHg)	117.30±11.31	130.91±13.53	0.001**
DBP (mmHg)	69.29±8.57	75.34±9.73	0.001**
TG (mg/dL)	139.17±57.57	196.94±74.67	0.001**
HDL-C(mg/dL)	53.01±6.76	48.45±9.41	0.001**
CT/HDL-C	3.63±1.17	3.79±1.08	0.144
Glucose (mg/dL)	86.04±12.59	93.92±16.39	0.001**

A t-test was used for the average data, p*<0.05 and p**<0.001. Waist circumference (WC); hip circumference (HC); Body Mass Index (BMI); systolic blood pressure (SBP); diastolic blood pressure (DBP); triglyceride (TG); high-density lipoprotein cholesterol (HDL-C); cholesterol (CT).

A statistically significant difference existed between the two groups with and without MetS with respect to WC, BMI, SBP, DBP, TG, HDL-C, and blood glucose (X±SD), p<0.05.

Table 5. Combined forms of MetS.

	WC-BP-TG	WC-TG-Glucose	WC-BP-Glucose	WC-BP-HDL-C	WC-TG-HDL-C	WC-Glucose-HDL-C
%	41.15%	21.05%	14.84%	9.57%	8.61%	4.78%

Blood pressure=BP.

The most common combination form was WC-BP-TG (41.15%).

Values of anthropometric cut-off points for predicting MetS (Figs. 1-4):

BMI cut-off point:

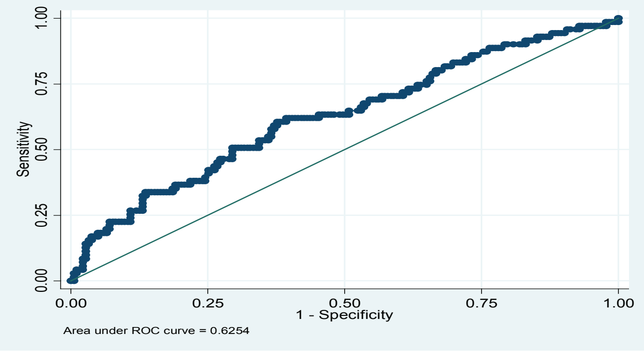

Fig. 1. ROC curve of the BMI to predict MetS in males.

For males: BMI=25.00; sensitivity (Se)=70.42%; specificity (Sp)=39.34%. Youden index=0.0976 was chosen as the value of the predictive cut-off point of MetS (95% confidence interval (CI): 54.68-70.39). Area under the curve ROC, AUC=0.6254.

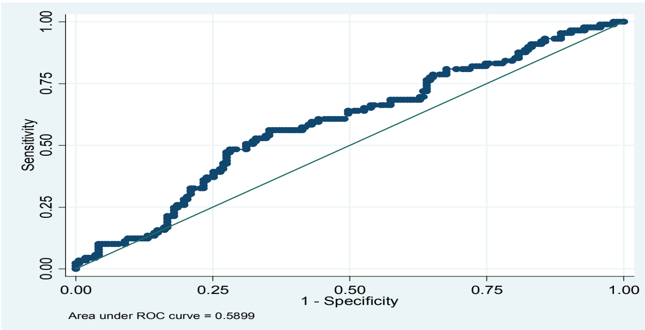

Fig. 2. ROC curve of the BMI for predicting MetS in females.

For females: BMI=24.50; Se=78.63%, Sp=33.93%. Youden index=0.1256 was chosen as the value of the predictive cut-off point of MetS (95% CI: 51.68-66.30). Area under curve ROC, AUC=0.5899.

WC cut-off point:

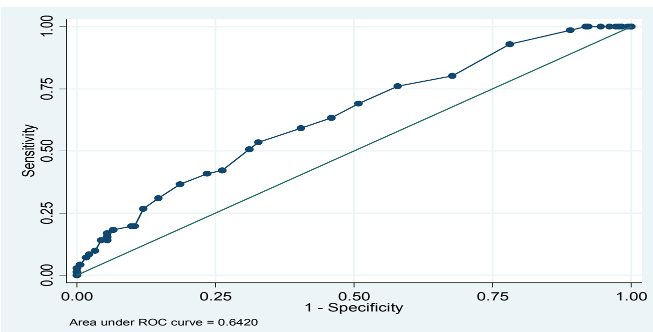

Fig. 3. ROC curve of the WC for predicting MetS in males.

For males: WC=82 cm; Se=76.06%, Sp=43.08%. Youden index=0.1914 was chosen as the value of the predictive cut-off point of MetS (95% CI: 56.73-71.66). Area under the curve ROC, AUC=0.6420.

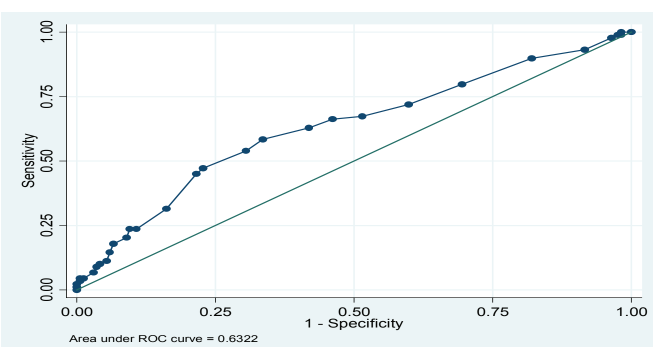

Fig. 4. ROC curve of WC for predicting MetS in females.

For females: WC=80 cm; Se=79.78%, Sp=31.54%. Youden index=0.1062 was chosen as the value of the predictive cut-off point of MetS (95% CI: 55.88-70.56). Area under the curve ROC, AUC=0.6322.

Discussion

Characteristics of dyslipidaemia and blood glucose

In South Korea, Kim studied 2,272 males and females aged 10-18 with overweight - obesity. Results revealed that variations existed in TG ($p<0.0001$), HDL-C ($p=0.001$), LDL-C ($p=0.001$), and CT ($p<0.0001$) in males, and in TG ($p<0.0001$), HDL-C ($p=0.003$), LDL-C ($p=0.004$), and CT ($p<0.002$) in women when compared with the results of a group with normal BMI [2].

In 2013, Khashayar conducted a study of 5,738 children in Iran aged 10-18 years (among whom 17.7% had overweight - obesity). Results showed that the proportion of the disorder of 1, 2, 3, and 4 blood lipid indexes were 34.7, 6.4, 1.2, and 0.4%, respectively [10].

Because Khashayar's study had only 17.7% overweight - obese children, the proportion of characteristics of dyslipidaemia might be lower than that in our study. The prevalence of MetS in our study was 2.5%, particularly for the overweight - obese group; according to IDF standards, this figure was found to be 15.4% [10]. Our research results were in relative agreement with other authors' findings.

MetS

Clinical and subclinical characteristics of MetS: Ferreira, et al. (2011) conducted a cross-sectional study of 958 children aged 7-11 years in Brazil, among whom the proportions of overweight and obesity were 10.8 and 7.7%, respectively. The prevalence of MetS was 23% in obese children (13.3% in males and 36% in females, $p<0.05$) [5]. In 2011, J. Olza, et al. [11] studied 478 obese children (213 females and 265 males) in Spain, and the results demonstrated a relatively high prevalence of MetS in prepubescence from 8.3 to 34.2% and in puberty from 9.7 to 41.2%. In the study of Caceres, the prevalence of MetS in obese children was 36% [3]. In the present study, the prevalence of MetS was 31.37% (female>male, $p>0.05$), which was similar to the abovementioned studies [3, 5].

Significant differences existed in the prevalence of TG, HDL-C, glucose, WC, SBP, and DBP between the groups with and without MetS [3]. Similar findings were found by D.A. Caranti, et al. [12]. In addition, we found that differences existed in each criterion between groups (Table 4).

W. Liu, et al. studied 1,844 children aged 7-14 years, the proportions of overweight and obesity were 11.1 and 7.2%, respectively. The proportion of the group with MetS was 6.6%, of which 33.1% were overweight children and 20.5% were obese; this figure was 2.3% in the group without MetS. Furthermore, 49.3% of children had at least one component of MetS [13]. The common combination forms were WC-BP-TG and WC-TG-glucose, which accounted for 41.15 and 21.05%, respectively.

Values of the anthropometric cut-off points for predicting MetS: in 2005, a study conducted in Italy showed that overweight - obese children with WC>90th percentile had more cardiovascular risk factors than did children with WC<90th percentile. The cut-off value of WC>70th percentile predicted an abnormal transformation based on the ROC (Se=76%, Sp=81%) [12].

In 2007, Hirschler studied BMI and WC for predicting MetS in children with a mean age of 8.7±2.4. A cut-off value of WC ≥75th percentile was the optimal threshold for predicting MetS in children. The optimal threshold for WC was 71.3 cm with Se=58.9% (95% CI: 48.4-68.9) and Sp=63.1% (95% CI: 58.4-67.7) to diagnose MetS [14].

A.P. Ferreira, et al. (2011) conducted a cross-sectional study on 958 children aged 7-11 years in Brazil, among which the proportion of children with overweight and obesity were 10.8 and 7.7%, respectively. The prevalence of MetS was 23% in obese children (13.3% in males and 36% in females, $p<0.05$) according to NCEP-ATP III criteria. The cut-off value of BMI was 24.5 kg/m^2, that of BFP was 41% based on dual energy X-ray absorptiometry, that of WC was 78 cm, and that of WC/HC was 0.92 to predict MetS in overweight and obese children [5].

In 2012, F. Saffari, et al. [15] conducted a study on more than 100 healthy children aged 6-16 years in Iran (58% were female) with BMI=26.02±4.38, of which overweight and obese children accounted for 20% and 80%, respectively. The frequency of insulin resistance was 81%; MetS accounted for 50% in the target group and 66.2% in the obese group (NCEP-ATP III standard). By contrast, in the study of Weiss, et al., MetS accounted for 25% in the overweight group and 42.5% in the obese group.

Our study focused on children aged 10-15 years with overweight - obese. The proportion of children with BMI>95th was 58.04%. The prevalence of MetS was 31.37% and the value of the predictive cut-off point of MetS was similar to foreign authors' findings. Moreover, we did not find many other studies for comparison; thus, the given value was used as a reference. Future studies should acquire more research data to determine the cut-off points of WC and BMI for predicting MetS.

Conclusions

In this study, the prevalence of dyslipidaemia among overweight - obese children aged 10-15 years old was 78.04%. A correlation existed between BMI levels and blood lipid disorders, $p<0.001$. Furthermore, the prevalence of MetS in this study was 31.37%, and the most common combined form of MetS among these subjects was WC-BP-TG, accounting for 41.15%.

The optimal values of the cut-off points for predicting MetS were as follows:

For males, BMI=5.00, AUC=0.6254; and for females, BMI=24.50, AUC=0.5899.

For males, WC=82 cm, AUC=0.6420; and for females, WC=80 cm, AUC=0.6322.

ACKNOWLEDGEMENTS

This research was supported by Dong Nai Department of Health and University of Medicine and Pharmacy, Ho Chi Minh city.

The author declares that there is no conflict of interest regarding the publication of this article.

REFERENCES

[1] M.S. Camhi, J. Kuo, R.D. Young (2008), "Identifying adolescent metabolic syndrome using body mass index and waist circumference", *Prev. Chronic. Dis.*, **5(4),** p.A115.

[2] H.V. Thieu (2008), "Study the harmful effects of overweight and obesity children", *The Ho Chi Minh city Journal of Medicine*, **12(4)**, pp.49-53.

[3] M. Caceres, C.G Teran, S. Rodriguez, et al. (2008), "Prevalence of insulin resistance and its association with metabolic syndrome criteria among Bolivian children and adolescents with obesity", *BMC Pediatrics*, **8**, p.31.

[4] Y.T.S. Rita, S. Hung-Kwan, C. Kai-Chow, et al. (2008), "Waist circumference and waist-to-height ratio of Hong Kong Chinese children", *BMC Public Health*, **8**, p.324.

[5] A.P. Ferreira, C.B. Ferreira, C.J. Brito, et al. (2011), "Prediction of metabolic syndrome in children through anthropometric indicators", *Arq. Bras. Cardiol.*, **96(2)**, pp.121-125.

[6] R. Weiss, J. Dziura, T. Burgert, et al. (2004), "Obesity and the metabolic syndrome in children and adolescent", *N. Engl. J. Med.*, **350**, pp.2362-2374.

[7] M. Fröhlich, A. Imhof, G. Berg, et al. (2000), "Association between CRP and features of the metabolic syndrome", *Diabetes Care*, **23**, pp.1835-1839.

[8] E. Simsek, H. Balta, Z. Balta, et al. (2010), "Childhood obesity-related cardiovascular risk factors and carotid intima-media thickness", *The Turkish Journal of Pediatrics*, **52**, pp.602-611.

[9] P. Zimmet, K.G.M.M. Alberti, F. Kaufman, et al. (2007), "The metabolic syndrome in children and adolescents - an IDF consensus report", *Pediatric Diabetes*, **8(5)**, pp.299-306.

[10] P. Khashayar, R. Heshmat (2013), "Metabolic syndrome and cardiovascular risk factors in a national sample of adolescent population in the Middle East and North Africa: the CASPIAN III study", *International Journal of Endocrinology*, **Vol.2013**, article ID 702095, Doi: 10.1155/2013/702095.

[11] J. Olza, M. Gil-Campos, R. Leis, et al. (2011), "Presence of the metabolic syndrome in obese children at prepubertal age", *Ann. Nutr. Metab.*, **58(4)**, pp.343-350.

[12] D.A. Caranti, S. Lazzer (2008), "Prevalence and risk factor of metabolic syndrome in Brazilian and Italian obese adolescents: a comparison study", *Int. J. Clin. Pract.*, **62(10)**, pp.1526-1532.

[13] W. Liu, R. Lin, AiLing Liu, et al. (2010), "Prevalence and association between obesity and metabolic syndrome among Chinese elementary school children: a school-based survey", *BMC Public Health*, **10**, pp.780.

[14] V. Hirschler (2007), "Waist circumference identifies primary school children with metabolic syndrome abnormalities", *Diabetes Technology and Therapeutics*, **9(2)**, pp.149-157.

[15] F. Saffari, S. Jalilolghadr, N. Esmailzadehha, et al. (2012), "Metabolic syndrome in a sample of the 6- to 16-year-old overweight or obese pediatric population: a comparison of two definitions", *Therapeutics and Clinical Risk Management*, **8**, pp.55-63.

Doi: 10.31276/VJSTE.61(2).65-70

Removal and bioaccumulation of copper by the freshwater green alga *Scenedesmus* sp.

Thanh Luu Pham[1, 2*]

[1]*Institute of Tropical Biology, Vietnam Academy of Science and Technology*
[2]*Graduate University of Science and Technology, Vietnam Academy of Science and Technology*

Received 15 August 2018; accepted 22 March 2019

Abstract:

Human activities generate vast amounts of wastewater, which contains various toxic metals. Microalgae are able to remove heavy metals from wastewater and accumulate lipid to produce biodiesel. In this study, the abilities to remove copper (Cu) and accumulate lipid of the green algal species *Scenedesmus* sp. were examined. The microalga *Scenedesmus* sp. was exposed to Cu concentrations of 0, 0.5, 1, 2, 5, and 10 mg/l under laboratory conditions. The results indicated that Cu inhibited the growth of *Scenedesmus* sp. at a 96h-EC_{50} of 7.54 mg/l. Furthermore, the highest removal rate was 89.5%. Lipid accumulation was increased significantly to 23.6% with the addition of Cu at 5 mg/l. The present study indicated that the green alga *Scenedesmus* sp. possesses the ability to remove Cu from aqueous media and accumulate lipid in its cells. Our results suggested that this species could be applied in wastewater treatment technology and biodiesel production.

Keywords: **bioremediation, green algae, heavy metal, lipid accumulation, water treatment.**

Classification number: **3.4**

Introduction

Agricultural and industrial activities generate vast amounts of wastewater that is frequently discharged into bodies of water without prior treatment. Wastewater contains high concentrations of toxic heavy metals, which might be persistent in nature. The presence of heavy metal ions-even at low concentrations-can be toxic to aquatic organisms [1]. Copper (Cu) is one of the most common metals in the world in terms of usage. Cu pollution has large adverse effects on the environment because of its persistency and bioaccumulation potential in living organisms. By transforming and being transported through the food web, heavy metals may result in severe and toxic effects on human health and aquatic life. Acute copper poisoning may cause intravascular haemolytic anaemia, acute liver and renal failure, shock, coma, and death, whereas symptoms of mild Cu poisoning include vomiting, nausea, and diarrhoea [1]. Chronic toxicity of Cu mainly occurs in the liver because it is the first site of deposition after Cu enters the blood [2]. Toxic effects may include the development of liver cirrhosis with episodes of haemolysis and damage to renal tubules, the brain, and other organs. Symptoms can progress to coma, hepatic necrosis, vascular collapse, and death [2]. Therefore, the treatment of wastewater to remove Cu is critical.

Many physical and chemical methods have been developed to remove heavy metals from contaminated water, such as reverse osmosis, electrophoresis, ultra-ion exchange, chemical precipitation, and phytoremediation [3]. However, all have exhibited disadvantages, such as requiring large amounts of reagents, high costs and energy requirements, and incomplete metal removal [3]. By contrast, biological methods such as using microalgae and aquatic plants are the most commonly used for heavy metal removal in wastewater because of their comparatively low construction and maintenance costs. Aquatic plants

*Email: thanhluupham@gmail.com

and microorganisms can remove heavy metals from water through the processes of uptake and metabolism-dependent bioaccumulation. Many studies have been performed on metal uptake by microalgae, using both living and nonliving biomass [1, 3, 4]. This method is a promising tool for the treatment of aqueous solutions polluted with heavy metals. It is characterised by its low cost, high metal binding capacity, and high removal efficiency of metals [5-7]. Although dry algae biomass has been successfully utilised in heavy metal adsorption experiments, living cells may be more advantageous because of their metabolic uptake and continuous growth.

Several algal species have been proven to be effective at adsorbing heavy metals from aqueous solutions. The ability of the green alga *Scenedesmus abundans*, both living and nonliving to remove cadmium (Cd) and Cu from water has been reported [4, 8]. These studies have suggested that the biological treatment of heavy metal-contaminated water based on *S. abundans* is possible. Furthermore, both Cu and Cd were sufficiently removed at high algal concentrations. In addition, Ouyang, et al. [8] reported that several green algae such as *Chlorella* spp. and *Scenedesmus* spp. are effective at removing zinc (Zn) and Cu from aqueous solutions, with the highest removal efficiency being near 100%. Other microalgae, including cyanobacteria such as *Spirulina* and *Phormidium* and diatoms such as *Phaeodactylum*, *Nitzschia,* and *Skeletonema* have also been reported as potential solutions for the phytoremediation of heavy metals from contaminated water and soil. Many unexplored algal species with the great ability to remove toxic metals from natural environment remain to be explored.

In Vietnam, heavy metal pollution is becoming a critical problem in environmental management. Studies have shown that in estuarine aquaculture, agricultural soil and surface water are contaminated with heavy metals [9-11]. Heavy metals in aquatic environments may threaten human health through food-web transformation. In cyanobacteria, very high levels of removal efficiency (up to 92%) for Cu and lead (Pb) by *Spirulina platensis* was reported [12]. Furthermore, the use of local green algae for heavy metal removal was studied [13]. Lam Ngoc Tuan (2008) [13] isolated more than 30 strains of *Chlorella* from Vietnamese waters and examined them for Cd removal ability, and reported Cd removal ability up to 95% by several strains. However, information about the removal of Cu by the green alga *Scenedesmus* is scant. In addition, the accumulation of lipid in tested algae remains unknown. Copper contamination in water, soil, and agriculture crops are considered serious problems [9-11]. Furthermore, the removal of copper from contaminated sources in Vietnam remains a challenge. Thus, the present study aimed to isolate *Scenedesmus* strains and use them to examine the effective removal of Cu ions and accumulation of lipid. The biosorption and bioaccumulation of Cu from aqueous solutions were investigated under laboratory conditions.

Materials and methods

Alga isolation and cultivation

The freshwater green alga *Scenedesmus* sp. (Fig. 1) was isolated from the Nhieu Loc-Thi Nghe canal, a polluted waterway in Ho Chi Minh City, and maintained as a pure unialgal culture in COMBO medium under laboratory conditions. All cultures were grown on a 12-h light/dark cycle at a temperature of 28 ± 1^0C under a light intensity of 50 μmol photons/m^{2}s provided by cool white fluorescent tubes.

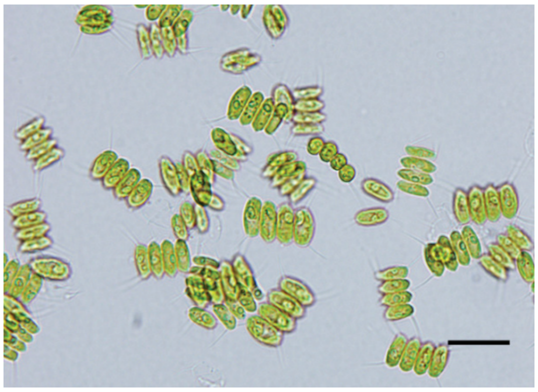

Fig. 1. Morphology of *Scenedesmus* sp. under a microscope. Scale bar: 20 μm.

Biosorption and bioaccumulation experiment

A stock solution of $Cu(NO_3)_2$ (Titrisol, Merck, Germany) with a concentration of 1,000 mg/l was diluted to concentrations of 0, 0.5, 1, 2, 5, and 10 mg/l, which were used in the biosorption and bioaccumulation experiments. Copper was spiked with design concentrations in Erlenmeyer flasks (500 ml) containing 300 ml of culture medium, and the living stock of *Scenedesmus* sp. was added to the initial concentration of 5×10^3 cell/ml. Samples were taken at 1 day intervals for a period of 7 days. Algal density was estimated directly using a Speirs-Levy eosinophil counting slide under an Olympus light microscope. Algal biomass was harvested at the end of the experiment by filtering onto GF/C glass fibre filters (Whatman, Kent, United Kingdom), dried at 80^0C overnight, and maintained at -20^0C for further processing. Erlenmeyer flasks with *Scenedesmus* sp. but without Cu were used as controls. All treatments were prepared in triplicate.

Growth inhibition test

The concentration of Cu that inhibited algal growth rate by 50% over 96 h (EC_{50}-96h) was determined based on the relative inhibition of growth rate as a function of $Cu(NO_3)_2$ concentration (mg/l). The average of the specific growth rate (ASGR) was obtained as the biomass increase after 96h using the following equation:

$$ASGR = \frac{\ln C_j - \ln C_i}{t_j - t_i}$$

where ASGR is the average specific growth rate from time *i* to time *j*; t_i is the initial time of the exposure period; t_j is the final time of exposure; C_i is the algal biomass at time *i*; and C_j is the algal biomass at time ***j***.

Percentage inhibition of growth was calculated as:

$$\%Ir = \frac{\mu_C - \mu_T}{\mu_C} \times 100$$

where %*Ir* is the percent inhibition in average specific growth rate; μ_C is the mean value for the average specific growth rate (µ) in the control group; and μ_T is the average specific growth rate for the treatment.

Total lipid analysis

The total lipid accumulated in the algal biomass was extracted according to the Bligh and Dyer method [14] and analysed using gravimetric quantification methods. In brief, a 50-ml centrifuge tube was washed and weighed after drying (W0), and approximately 50 mg dry weight (DW) of alga biomass (W1) was digested with 5 ml HCl 1 M at 80^0C for 30 min. The liquid supernatant was discarded after centrifugation. Lipid was then extracted with 5 ml of methanol:chloroform (2:1 v/v). After 3h, the chloroform layer was transferred to a culture dish that had been preweighed (W2). The dish was then dried completely and reweighed (W3). Lipid content (LC) was calculated according to the following formula:

LC (%) = (W3−W2)/(W1−W0)

Heavy metal analysis

The bioaccumulation of Cu in the dry biomass of *Scenedesmus* was homogenised in 5 ml of concentrated nitric acid (70%). After sonication for 3 min, the samples were completely digested for 12h at 80°C. All samples were then centrifuged at 4,000 rpm for 10 min at room temperature to remove cell debris. The supernatant was collected and maintained at 4°C prior to analysis. Cu content was detected using an inductively coupled plasma optical emission spectrometer (ICP OES). The ICP OES system with an axially viewed configuration (VISTA PRO; Varian, Mulgrave, Australia) equipped with a solid state detector, a cyclonic spray chamber, and a concentric nebuliser was used for metal detection. The ICP OES conditions were as follows: RF power: 1.3 kW; gas: argon; plasma flow: 15 l/min; auxiliary flow: 1.5 l/min; nebuliser flow: 0.75 l/min; instrument stabilisation delay: 15s; pump rate: 15 rpm; sample uptake delay: 70s; number of replicates: 3; read time: 5s; read: peak height; and rinse time: 30s. The data were presented in µg/g DW and all analyses were performed in triplicate.

Finally, the removal rate *Q* (%) and the adsorption capacity *q* (mg/g) were calculated using the following formula:

$$Q = \frac{C_0 - C}{C_0} \times 100\%$$

$$q = \frac{C_0 - C}{M} \times V$$

where C_0 and *C* are the initial and final concentrations of Cu (II) (mg/l). The *V* and *M* are the volume of solution (ml) and the mass of dry alga (g), respectively.

Statistical analyses

All data were presented as the mean ± standard deviation. The differences between exposure groups and control groups were tested for significance using a one-way analysis of variance (ANOVA). When the ANOVA was significant, pairwise comparison was applied using Tukey's HSD post-hoc test to detect significant differences between the treatment and control groups; *p*-values less than 0.05 were considered statistically significant.

Results

Algal growth under Cu exposure

The results showed that *Scenedesmus* sp. grew well in the controls and reached a maximal concentration after 6 or 7 days of incubation (Fig. 2A). All treatments reached the stationary growth phase at approximately the same time (after 6 days). Cell density in the control (CT) treatment increased from 5×10^3 to 3.2×10^6 after 1 week of culture. Cu resulted in differences in the algal growth. Cu at low concentrations (up to 2 mg/l) did not influence the growth of *Scenedesmus* sp., but at 5 mg/l or higher Cu caused a significant decrease in its growth. In addition, a further increase of Cu^{2+} concentration up to 10 mg/l or higher resulted in a sharp decrease in biomass concentration (Fig. 2A).

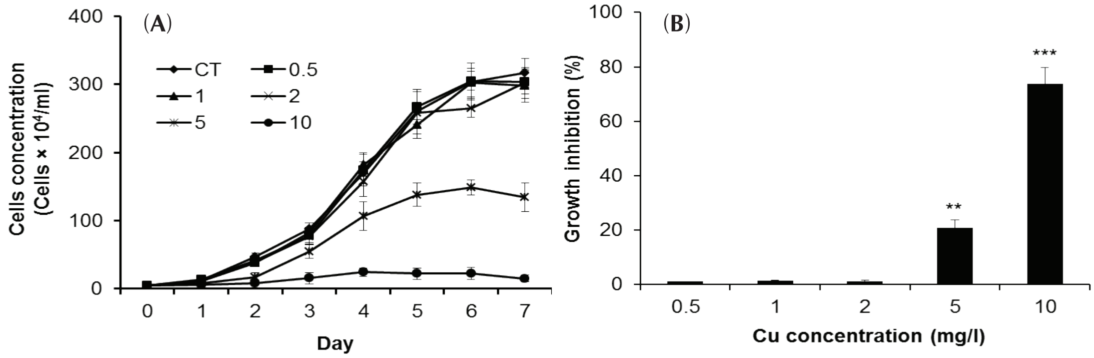

Fig. 2. Growth curves (A) and growth inhibition (B) of *Scenedesmus* sp. exposed to different Cu concentrations. Asterisks indicate significant differences. ANOVA test (*, $p<0.05$; **, $p<0.01$; ***, $p<0.001$). CT: control treatment.

The 96h-EC_{50} value of Cu for the growth inhibition of *Scenedesmus* sp. was 7.54 mg/l. Growth inhibition increased as Cu concentration increased to 1 mg/l or higher. Cu caused significant effects and dose-dependent increases on the growth of *Scenedesmus* sp. Significant differences from the control growth rates were detected at a concentration of 1 mg/l or higher in *Scenedesmus* sp. Cu at a concentration of 10 mg/l almost completely inhibited the growth of *Scenedesmus* sp. (Fig. 2B).

Total LC

Cu metal ion had a small positive influence on the total lipid production in *Scenedesmus* sp. Cu at 1 mg/l did not influence lipid production, but a further increase to 2 mg/l led to a significant increase in total lipid production (Fig. 3). Total LC ranged from 15.1 to 19.4%. The maximum total LC of 19.4% was obtained at a Cu concentration of 5 mg/l. Different concentrations of Cu increased total lipid production by 20.3-23.9% in *Scenedesmus* sp.

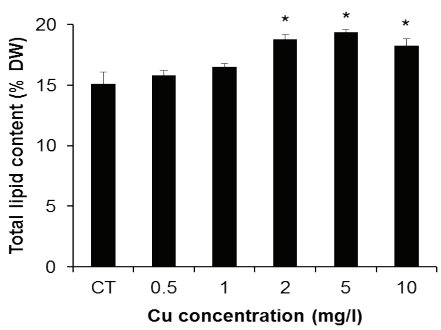

Fig. 3. Total LC of *Scenedesmus* sp. under exposure to different Cu concentrations. CT: control treatment; DW: dry weight.

Removal efficiency and Cu accumulation

The Cu removal efficiency and bioaccumulation of Cu in *Scenedesmus* sp. were investigated at different initial metal concentrations for 7 days (Fig. 4). Results showed that the metal removal rate became higher as metal concentrations increased to 2 mg/l. A further increase in Cu concentration did not result in higher removal rates. The highest removal rate of Cu was 89.5% at 2 mg/l. The highest concentration of Cu (10 mg/l) resulted in a reduction in Cu removal capacity (Fig. 4A).

Figure 4B shows the accumulation of Cu by *Scenedesmus* sp. The Cu concentration in *Scenedesmus* sp. ranged from 0.2 to 4.59 mg/g DW. Furthermore, the accumulation of Cu was dose-dependent. Higher initial Cu concentrations resulted in a larger amount of Cu being accumulated in dry *Scenedesmus* sp. biomass. The accumulation was 0.2 mg/g DW (40%) and 5.59 mg/g DW for 0.5 mg/l and 10 mg/l of Cu, respectively.

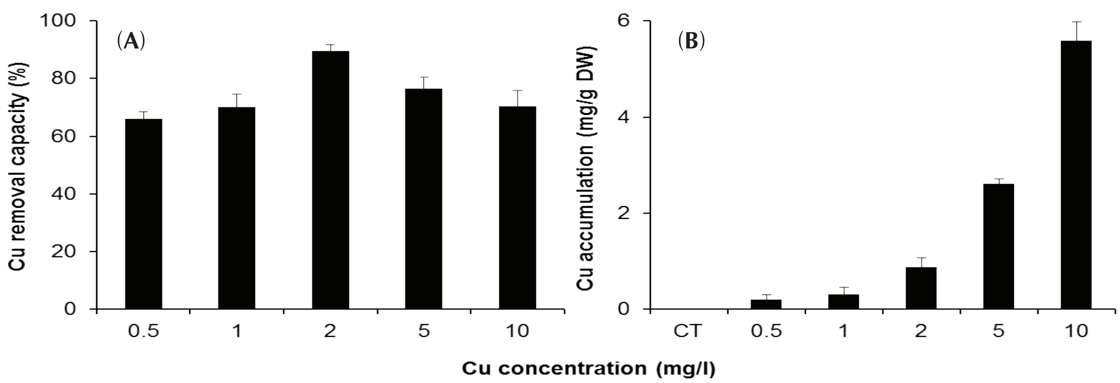

Fig. 4. Removal rate (A) and bioaccumulation of Cu by *Scenedesmus* sp. (B). CT: control treatment.

Discussion

In this study, experiments were performed to characterise the adverse effects and biosorption of Cu from water using the freshwater green algae *Scenedesmus* sp.. Cell density was monitored to determine the effect of Cu on algal growth. Studies have demonstrated that Cu is necessary for algal growth or respiration [15, 16]; however, excessive concentrations have caused adverse effects on the growth of green algae [15, 16]. In addition, Schamphelaere, et al. [17] found that the toxicity of heavy metals toward green algae may depend on the algal species and exposure time. When the green alga *S. abundans* was exposed to different concentrations of Cu, Terry and Stone [18] reported that its growth was inhibited at Cu concentrations up to 15 mg/l. Photosystems of algae can be damaged by excessive amounts of heavy metals, resulting in a reduction in photosynthetic pigments such as chlorophyll-*a*. In addition, high Cd concentrations reduced cells' size and caused a decrease in growth rate [18]. The results of the present study are in agreement with the observations of Ouyang, et al. [8], who reported that some heavy metals, including Cu, Cr, Zn, Cd, and Pb, significantly inhibited the growth of green algae. The effects of these five metals on the growth of green algae were dependent on both concentration and exposure time. The results of the present study indicated that the green algae *Scenedesmus* sp. is sensitive to Cu; hence, contaminated water entering a treatment pond would have to be diluted to maintain algal growth.

In addition, studies have demonstrated that lipid production from algae increased significantly under heavy metal stress conditions. The lipid productivity of the green alga *Scenedesmus* sp. increased in the presence of iron, magnesium, and calcium with the addition of EDTA during cultivation [19, 20]. Che, et al. [21] reported that the effect of iron on the green alga *Monoraphidium* sp. and the biomass and lipid productivity of microalgae exhibited an increasing tendency with the concentration of iron ions being augmented. An appropriate concentration of iron ions in an aqueous solution might result in benefits for biomass production and lipid accumulation [21]. Liu, et al. [22] also reported that the total LC in *C. vulgaris* increased by 3-7-fold when the alga was reinoculated into new media supplemented with an iron concentration of 1.2×10^{-5} mol/l $FeCl_3$. Heavy metals such as Cu and Zn are known to increase the total LC of the flagellate eukaryote *Euglena gracilis* and green alga *Chlorella* sp. [23]. The total LC of the microalga *C. minutissima* significantly increased by 21% and 94% with the addition of Cd and Cu, respectively [23]. In the present study, the lipid production of *Scenedesmus* sp. was enhanced under Cu exposure. Algae use lipid production as a means of energy storage when their growth is depressed by environmental stresses, such as the presence of heavy metals. Under stress conditions, the photosynthetically fixed carbon supply possibly exceeds the ability of the cells to multiply, causing the build-up of carbon in storage molecules [24]. The mechanism formation, pathways, and composition of different lipid types within algae have been well-documented [25, 26]. The main reason for increased lipid production under stress conditions in green algae is the production of major chloroplast fatty acid in cells, which are favourable for triacylglycerol (TAG) production, and thus, appear to be advantageous for higher neutral lipid production [27].

Algae have the ability to remove heavy metals from aqueous solutions; however, the diverse results in terms of toxicity and metal removal ability reported in the literature have indicated that various forms of aquatic organisms possess different responses to heavy metal exposure [1, 6, 18, 28]. Therefore, it is necessary to characterise the effects of metal concentrations on each species considered. Many species of green algae (e.g., *Chlorella* spp. and *Scenedesmus* spp.) have been investigated for their for heavy metal and nutrient removal as well as lipid production in wastewater [29-32]. Moreover, studies have shown that *Scenedesmus* spp. and *Chlorella* spp. possess the ability to remove Pb up to 89% from aqueous solution [6, 33]. Terry and Stone [18] reported that living *S. abundans* had the ability to remove Cu up to 99% from aqueous solution. Chen, et al. [33] invoked a feedback mechanism involving multiple transporters in the presence of hardness cations or other metal ions such as Cu and Ni to explain the increasing Pb bioaccumulation they observed in the green alga *C. reinhardtii*. In the present study, the isolated *Scenedesmus* sp. removed up to 89% of Cu from the solution. However, excessively high concentrations of Cu in water may inhibit the growth of algae. Inhibition of the growth of *Scenedesmus* sp. resulted in a reduction in Cu removal capacity at high concentrations. The results of the present study were in line with relevant studies that have reported *Scenedesmus* sp. as being able to remove and accumulate Cu to some extent depending on the concentration of the metal and duration of contact between the phytoplankton and metal [18, 34]. Further studies are required to better understand the removal and bioaccumulation mechanisms of Cu in tropical microalgae.

Conclusions

The present study indicated that the microalgae *Scenedesmus* sp. exhibited Cu biosorption and bioaccumulation abilities. High concentrations of Cu caused growth inhibition of the green algae. The removal efficiency and accumulation of Cu were most dependent on the initial metal concentrations. The total lipid production in *Scenedesmus* sp. was enhanced under exposure to Cu in concentration range of 2-10 mg/l. The results indicated the potential of *Scenedesmus* sp. in wastewater treatment and biofuel production.

ACKNOWLEDGEMENTS

This research was funded by the Vietnam National Foundation for Science and Technology Development (NAFOSTED) under grant number 106.04-2018.314.

The author declares that there is no conflict of interest regarding the publication of this article.

REFERENCES

[1] A.A. Al-Homaidan, H.J. Al-Houri, A.A. Al-Hazzani, G. Elgaaly, N.M.S. Moubayed (2014), "Biosorption of copper ions from aqueous solutions by *Spirulina platensis* biomass", *Arab. J. Chem.*, **7(1)**, pp.57-62.

[2] A. Jan, M. Azam, K. Siddiqui, A. Ali, I. Choi, Q. Haq (2015), "Heavy metals and human health: mechanistic insight into toxicity and counter defense system of antioxidants", *Int. J. Mol. Sci.*, **16(12)**, p.26183.

[3] A.K. Zeraatkar, H. Ahmadzadeh, A.F. Talebi, N.R. Moheimani, M.P. McHenry (2016), "Potential use of algae for heavy metal bioremediation, a critical review", *J. Environ. Manage.*, **181**, pp.817-831.

[4] L. Xin, H. Hong-ying, Y. Jia (2010), "Lipid accumulation and nutrient removal properties of a newly isolated freshwater microalga, *Scenedesmus* sp. LX1, growing in secondary effluent", *New Biotechnol.*, **27(1)**, pp.59-63.

[5] M. Kesaano, R.C. Sims (2014), "Algal biofilm based technology for wastewater treatment", *Algal Research*, **5**, pp.231-240.

[6] S.K. Kumar, H.-U. Dahms, E.-J. Won, J.-S. Lee, K.-H. Shin (2015), "Microalgae: A promising tool for heavy metal remediation", *Ecotoxicol. Environ. Saf.*, **113**, pp.329-352.

[7] X. Zhang, X. Zhao, C. Wan, B. Chen, F. Bai (2016), "Efficient biosorption of cadmium by the self-flocculating microalga *Scenedesmus obliquus* AS-6-1", *Algal Research*, **16**, pp.427-433.

[8] H. Ouyang, X. Kong, W. He, N. Qin, Q. He, Y. Wang, R. Wang, F. Xu (2012), "Effects of five heavy metals at sub-lethal concentrations on the growth and photosynthesis of *Chlorella vulgaris*", *Chin. Sci. Bull.*, **57(25)**, pp.3363-3370.

[9] C.N. Kien, N.V. Noi, L.T. Son, H.M. Ngoc, S. Tanaka, T. Nishina, K. Iwasaki (2010), "Heavy metal contamination of agricultural soils around a chromite mine in Vietnam", *Soil Sci. Plant Nutr.*, **56(2)**, pp.344-356.

[10] V.T. Nguyen, A. Ozaki, T.H. Nguyen, D.A. Nguyen, T.Y. Tran, K. Kurosawa (2016), "Arsenic and heavy metal contamination in soils under different land use in an estuary in Northern Vietnam", *Int. J. Environ. Res. Public Health*, **13(11)**, pp.1091.

[11] T.T.H. Nguyen, W. Zhang, Z. Li, J. Li, C. Ge, J. Liu, X. Bai, H. Feng, L. Yu (2016), "Assessment of heavy metal pollution in Red river surface sediments, Vietnam", *Mar. Pollut. Bull.*, **113(1)**, pp.513-519.

[12] Minh Thi Thao, Bui Dinh Nhi, Dam Thi Thanh Huong (2017), "Study on biosorption of copper and lead ions by *Spirulina platensis*", *Journal of Analytical Sciences*, **22(1)**, pp.126-133 (in Vietnamese).

[13] Lam Ngoc Tuan (2008), *Study on using several Chlorella strains to biosorption of cadimi from wastewater*, PhD thesis, Hanoi University of Science and Technology (in Vietnamese).

[14] E.G. Bligh, W.J. Dyer (1959), "A rapid method of total lipid extraction and purification", *Can. J. Biochem. Physiol.*, **37**, pp.911-917.

[15] A. Juneja, R. Ceballos, G. Murthy (2013), "Effects of environmental factors and nutrient availability on the biochemical composition of algae for biofuels production: a review", *Energies*, **6(9)**, p.4607.

[16] N.F. Mykhaylenko, E.K. Zolotareva (2017), "The effect of copper and selenium nanocarboxylates on biomass accumulation and photosynthetic energy transduction efficiency of the green algae *Chlorella vulgaris*", *Nanoscale Research Letters*, **12**, p.147.

[17] D.K.A.C. Schamphelaere, C. Nys, C.R. Janssen (2014), "Toxicity of lead (Pb) to freshwater green algae: development and validation of a bioavailability model and inter-species sensitivity comparison", *Aquat. Toxicol.*, **155**, pp.348-359.

[18] P.A. Terry, W. Stone (2002), "Biosorption of cadmium and copper contaminated water by *Scenedesmus abundans*", *Chemosphere*, **47(3)**, pp.249-255.

[19] G. Mujtaba, W. Choi, C.-G. Lee, K. Lee (2012), "Lipid production by *Chlorella vulgaris* after a shift from nutrient-rich to nitrogen starvation conditions", *Bioresour. Technol.*, **123**, pp.279-283.

[20] H.-Y. Ren, B.-F. Liu, F. Kong, L. Zhao, G.-J. Xie, N.-Q. Ren (2014), "Enhanced lipid accumulation of green microalga *Scenedesmus* sp. by metal ions and EDTA addition", *Bioresour. Technol.*, **169**, pp.763-767.

[21] R. Che, L. Huang, X. Yu (2015), "Enhanced biomass production, lipid yield and sedimentation efficiency by iron ion", *Bioresour. Technol.*, **192**, pp.795-798.

[22] Z.-Y. Liu, G.-C. Wang, B.-C. Zhou (2008), "Effect of iron on growth and lipid accumulation in *Chlorella vulgaris*", *Bioresour. Technol.*, **99(11)**, pp.4717-4722.

[23] J. Yang, J. Cao, G. Xing, H. Yuan (2015), "Lipid production combined with biosorption and bioaccumulation of cadmium, copper, manganese and zinc by oleaginous microalgae *Chlorella minutissima* UTEX2341", *Bioresour. Technol.*, **175**, pp.537-544.

[24] E. Hounslow, R.V. Kapoore, S. Vaidyanathan, D.J. Gilmour, P.C. Wright (2016), "The search for a lipid trigger: the effect of salt stress on the lipid profile of the model microalgal species *Chlamydomonas reinhardtii* for biofuels production", *Curr. Biotechnol.*, **5(4)**, pp.305-313.

[25] I.A. Guschina, J.L. Harwood (2006), "Lipids and lipid metabolism in eukaryotic algae", *Prog. Lipid Res.*, **45**, pp.160-186.

[26] J.L. Harwood, I.A. Guschina (2009), "The versatility of algae and their lipid metabolism", *Biochimie*, **91**, pp.679-684.

[27] D. Pal, I. Khozin-Goldberg, Z. Cohen, S. Boussiba (2011), "The effect of light, salinity, and nitrogen availability on lipid production by *Nannochloropsis* sp.", *Appl. Microbiol. Biotechnol.*, **90(4)**, pp.1429-1441.

[28] N. Abdel-Raouf, A.A. Al-Homaidan, I.B.M. Ibraheem (2012), "Microalgae and wastewater treatment", *Saudi. J. Biol. Sci.*, **19(3)**, pp.257-275.

[29] Y. Feng, C. Li, D. Zhang (2011), "Lipid production of *Chlorella vulgaris* cultured in artificial wastewater medium", *Bioresour. Technol.*, **102(1)**, pp.101-105.

[30] C.M. Monteiro, P.M.L. Castro, F.X. Malcata (2009), "Use of the microalga *Scenedesmus obliquus* to remove cadmium cations from aqueous solutions", *World J. Microbiol. Biotechnol.*, **25(9)**, pp.1573-1578.

[31] Y.K. Wong, K.K. Yung, Y.F. Tsang, Y. Xia, L. Wang, K.C. Ho (2015), "*Scenedesmus quadricauda* for nutrient removal and lipid production in wastewater", *Water Environ. Res.*, **87(12)**, pp.2037-2044.

[32] M. Sacristán de Alva, V.M. Luna-Pabello, E. Cadena, E. Ortíz (2013), "Green microalga *Scenedesmus acutus* grown on municipal wastewater to couple nutrient removal with lipid accumulation for biodiesel production", *Bioresour. Technol.*, **146**, pp.744-748.

[33] J. Chen, J. Li, W. Dong, X. Zhang, R.D. Tyagi, P. Drogui, R.Y. Surampalli (2018), "The potential of microalgae in biodiesel production", *Renew Sust. Energ. Rev.*, **90**, pp.336-346.

[34] B.N. Tripathi, J.P. Gaur (2004), "Relationship between copper- and zinc-induced oxidative stress and proline accumulation in *Scenedesmus* sp.", *Planta*, **219(3)**, pp.397-404.

Doi: 10.31276/VJSTE.61(2).71-78

Studying the characteristics of heavy rainfall in the central coastal provinces of Vietnam (Quang Binh case study)

Nguyen Van Thang[1], Vu Van Thang[1], Tran Dinh Trong[1*], Jerome Faucet[2]

[1]*Vietnam Institute of Meteorology, Hydrology and Climate Change*
[2]*German Red Cross in Hanoi, Vietnam*

Received 14 September 2018; accepted 3 May 2019

Abstract:

This paper explores the maximum amount of rainfall in the Central coastal provinces of Vietnam (Quang Binh case study) for return periods of 5 years, 10 years, 20 years, 50 years, and 100 years, which correspond to frequencies of 20%, 10%, 5%, 2%, and 1%, respectively. The results show that at a frequency of 20%, the maximum intensity of rain during a heavy rain spell can range from 636.6 to 696.0 mm, while the maximum one-day amount received was over 300 mm, which can occur many times in 5 years. At a frequency of 1%, the intensity of rain during a heavy rain spell can range from 1,197.9 to 1,268.3 mm, while the maximum one-day amount ranged from 487.4 to 521.9 mm. However, such values are very rare over the course of 100 years. In addition, in terms of annual rainfall, the spatial distribution of heavy rainfall in coastal areas was significantly smaller than that in mountainous areas. The highest one-day and five-day rainfall have the same pattern of spatial distribution as annual rainfall.

Keywords: **frequency of extreme rainfall, heavy rain, temporal and spatial distribution.**

Classification number: **5.2**

Introduction

Quang Binh, one of the central coastal provinces of Vietnam, has a very complex climate and terrain. The province is the one most affected by natural disasters: tropical cyclones, floods, and flash floods occur with high frequency and severity [1-3]. Typhoons and floods usually occur from September to December, and are concentrated in October and November. Tropical cyclones lead to heavy rain and high tides, resulting in floods in the lowland and flash floods in mountainous areas. Other forms of natural disasters, such as early floods ('Lũ tiểu mãn' or 'Lũ đầu mùa' in Vietnamese), often occur from April to June each year. On average, two or three floods occur in Quang Binh every year [4, 5].

Natural disasters severely affect socio-economic development and human life. In Vietnam, prevention of natural disasters and warnings preceding them are still limited, especially in the provinces, such as Quang Binh, that are frequently and directly affected by them. With this in mind, the Vietnam Red Cross (VNRC) and the German Red Cross (GRC) aim to pilot a new approach called forecast-based financing that uses forecast-based thresholds to automatically release money to pay for pre-planned short-term emergency preparedness action in the critical time period after a forecast but before a disaster [6].

To support that goal, the GRC and the Center for Meteorology and Climatology under the Vietnam Institute of Meteorology, Hydrology and Climate change jointly signed a research contract entitled "Disasters Profile of Quang Binh Province and Review and assessment of the availability and usage of early warning system and Weather forecasts". One of the objectives of this contract was to analyse the disaster profile of Quang Binh, focusing on heavy rains and floods.

This paper is extracted from the contract's outcomes,

*Corresponding author: Email: trantrong209@gmail.com.

and aims to analyse the characteristics of rain and heavy rain in the research area, including an analysis of frequency of extreme rainfalls, and of the temporal and spatial distribution characteristics of heavy rainfall.

Data and methodology

The data used in this paper are: i) The daily precipitation observed for the period of 1961-2014 at the three meteorological stations of Tuyen Hoa, Dong Hoi, and Ba Don, which is used to calculate the temporal characteristics of the distribution of rainfall (total precipitation, one-day maximum precipitation (RX1day), five-day maximum precipitation (RX5day)); ii) The data set of annual maximum precipitation and one-day maximum precipitation at these three meteorological stations, which is used to calculate the frequency of heavy rain events/one-day maximum intensity; and iii) Data set from 10 gauge stations (with at least 30 years of data) in Quang Binh province and six gauge stations in the neighbouring provinces of Ha Tinh and Quang Tri, which are used to calculate and map the spatial distribution of heavy rainfall [7, 8]. Fig. 1 shows the geographical location and the network of hydro-meteorological observation stations used.

Fig. 1. Geographical location and network of hydro-meteorological observation stations.

The methodologies used are the Gumbel Generalized Extreme Value distribution [9-12] for calculating the maximum amount of rainfall in Quang Binh for return periods of 5 years, 10 years, 20 years, 50 years and 100 years, which correspond to frequencies of 20%, 10%, 5%, 2% and 1%, respectively; and climate statistics and Geographic Information System (GIS) for the temporal and spatial distribution characteristics of heavy rainfall [13-18].

Results and discussion

Analysis and evaluation the frequency of heavy rainfall in Quang Binh province

Frequency of heavy rain events:

Table 1 shows the results calculated for the maximum amount of rainfall in a heavy rain event based on observations from 1961 to 2014 at three stations (Ba Don, Dong Hoi, Tuyen Hoa) in Quang Binh for return periods of 5 years, 10 years, 20 years, 50 years and 100 years (corresponding to frequencies of 20%, 10%, 5%, 2% and 1%, respectively). Table 2 shows the number of events in the 1961-2014 period in which the total rainfall was equal to or greater than average maximum rainfall in a heavy rain spell for the same return periods shown in Table 1.

Table 1. Calculated maximum rainfall in a heavy rain event for the given return periods at three meteorological stations in Quang Binh province (mm).

Stations	Return periods (years)				
	5	*10*	*20*	*50*	*100*
Ba Don	636.6	775.4	908.5	1,080.8	1,210.0
Dong Hoi	675.9	802.2	923.4	1,080.3	1,197.9
Tuyen Hoa	696.0	834.5	967.4	1,139.4	1,268.3

Table 2. The number of events during the 1961-2014 period in which the total rainfall was equal to or greater than the value calculated for the given return periods at the three meteorological stations.

Stations	Return periods (years)				
	5	*10*	*20*	*50*	*100*
Ba Don	9	5	2	2	1
Dong Hoi	13	6	2	0	0
Tuyen Hoa	13	5	3	1	0

For 100-year return period (frequency of 1%), this is very rare occurrence: the calculated maximum rainfall in an event at each of the three stations in Quang Binh ranged from 1,197.9 mm to 1,268.3 mm. In fact, in the 54 years' worth of observed data used in this study, there was only one event, at Ba Don station, in which the total rainfall was greater than the calculated value of the 100-year return period shown in Table 1 (1,350.5 mm in September, 1967). In addition, in September 1978, a heavy rain event at Ba Don station reached 1,169.1 mm, which approximates the calculated rainfall in Table 1. For Dong Hoi and Tuyen Hoa stations, during the 1961-2014 period, there were no extreme rainfall events in which the rainfall was equal to or greater than the calculated threshold of 100-year return period. At Dong Hoi station, the maximum precipitation in a heavy rain event was 1,021.7 mm, which occurred in September, 1979. At Tuyen Hoa station, the total rainfall of rain events in October 1995 reached approximately 1,236.3 mm, which approximates the calculated rainfall of 100-year return period.

For 50-year return period (frequency of 2%), the calculated maximum rainfall in an event at the three stations in Quang Binh was more than 1,000 mm, with the highest value, at Tuyen Hoa station, reaching 1,139.4 mm. For this frequency, in 1961-2014 period, Ba Don station had two events that exceeded the threshold of 1,000 mm, in 1967 and 1978. Tuyen Hoa station had one occurrence that exceeded this threshold, in 1995 (1,236.3 mm), and two events in which the total rainfall was greater than 1,000 mm (though still under the threshold), in 2009 (1,008.1 mm) and 2010 (1,037.9 mm). At Ba Don station, there were no events in which the total rainfall was equal to or greater than the calculated value, and there was only one event, in 1979, in which the total rainfall was greater than 1,000 mm.

For 20-year return period (frequency of 5%), the calculated maximum rainfall in events at the three stations in Quang Binh were 908.5 mm (Ba Don), 923.4 mm (Dong Hoi), and 967.4 mm (Tuyen Hoa). According to the observations during the 1961-2014 period, there were two events each at Ba Don and Dong Hoi stations and three events at Tuyen Hoa in which the total rainfall was equal to or greater than the calculated value of 20-year return period.

For 10-year return period (frequency of 10%), the calculated maximum rainfall in an event at stations in Quang Binh ranged from 775.4 mm (Ba Don station) to 834.5 mm (Tuyen Hoa station). In 1961-2014, these events occurred five times each at Ba Don and Tuyen Hoa stations, and six times at Dong Hoi station.

For 5-year return period (frequency of 20%), this is more frequent occurrence: the calculated maximum rainfall in an event at each of the three stations in Quang Binh was 636.6 mm, 675.9 mm, and 696.0 mm, at Ba Don, Dong Hoi, and Tuyen Hoa stations, respectively. According to observations from the 1961-2014 period, these events occurred nine times at Ba Don station and thirteen times each at Dong Hoi and Tuyen Hoa stations. In general, the average maximum rainfall in an event in the corresponding return period is in practice comparable to the statistics.

Frequency of one-day maximum precipitation intensity:

Table 3 shows the results calculated for the one-day maximum precipitation intensity based on observed data from the three stations for 1961 to 2014 for the given return periods of 5 years, 10 years, 20 years, 50 years and 100 years (corresponding to frequencies of 20%, 10%, 5%, 2%, and 1%, respectively). Table 4 shows the number of days in the 1961-2014 period on which the rainfall was equal to or greater than the maximum precipitation intensity for the different return periods presented in Table 3.

Table 3. One-day maximum rainfall intensity for given return periods at the three stations in Quang Binh province (mm).

Stations	Return periods (years)				
	5	*10*	*20*	*50*	*100*
Ba Don	301.2	354.6	405.9	472.2	521.9
Dong Hoi	292.3	339.5	384.8	443.5	487.4
Tuyen Hoa	329.6	391.6	451.0	528.0	585.7

Table 4. The number of days in the 1961-2014 period on which the rainfall was equal to or greater than calculated intensity for given return period at the three stations in Quang Binh province.

Stations	Return periods (years)				
	5	*10*	*20*	*50*	*100*
Ba Don	10	6	3	1	1
Dong Hoi	9	3	2	1	1
Tuyen Hoa	11	7	3	1	0

For 100 years return period (frequency of 1%), the calculated one-day maximum rainfall intensity at the three stations was 521.9 mm, 487.4 mm, and 585.7 mm at Ba Don, Dong Hoi and Tuyen Hoa, respectively. However, this is a very rare event with only one occurrence at each of Ba Don and Dong Hoi, and no occurrence at Tuyen Hoa during the 1961-2014 period. In particular, in 54 years' worth of observed data used in this study, the maximum one-day intensity of rainfall was 526.7 mm at Ba Don station (5th October 2010) and 554.6 mm at Dong Hoi station (9th October 1995); these are the two days on which the rainfall intensity at meteorological stations in Quang Binh reached the calculated threshold value of the 100-year return period.

For the 50-year return period (frequency of 2%), the calculated one-day maximum rainfall intensity was 472.2 mm at Ba Don station, 443.5 mm at Dong Hoi station, and 528.0 mm at Tuyen Hoa station. According to the 1961-2014 observations used in this study, such an event has occurred once at each station in Quang Binh. At Ba Don and Dong Hoi stations, such events were mentioned in the 100-year return period, and at Tuyen Hoa station, the maximum rainfall intensity reaches 548.4 mm on 18th Octorber 1993.

For the 20-year return period (frequency of 5%), at Ba Don station, the one-day maximum precipitation intensity reached 405.9 mm - such an event occurred three times in the 1961-2014 period. At Dong Hoi station, the one-day maximum rainfall intensity for the 20-year return period was

384.8 mm, and in the 1961-2014 period there were two days on which rainfall was equal to or greater than the calculated value. At Tuyen Hoa station, the one-day maximum rainfall intensity and the number of days on which it occurred were 451 mm and three days, respectively.

For 10-year return period, at the three stations in Quang Binh, the one-day maximum rainfall intensity ranged from 339.5 mm at Dong Hoi station to 391.6 mm at Tuyen Hoa station. The number of days on which rainfall was equal to or greater than the calculated value for 10-year return period were six, three, and seven days at Ba Don, Dong Hoi, and Tuyen Hoa stations, respectively.

For 5-year return period, the number of days on which rainfall was equal to or greater than the calculated value for 5-year return period was a more frequent occurrence. There were 10 days on which rainfall was equal to or greater than 301.2 mm at Ba Don (one-day rainfall intensity for the 5-year return period), nine days on which rainfall was equal to or greater than 292.3 mm at Dong Hoi, and 11 days on which rainfall was equal to or greater than 329.6 mm at Tuyen Hoa. According to the observation data for the period 1961-2014, the frequency of occurrence of the one-day maximum rainfall intensity in Quang Binh correlates well with the frequency of the calculated result of the Gumbel function.

(the time of 'Tieu Man' or early floods, when the gradually strengthening southwest monsoon gradually meets the weak intrusion of cold air). The three months with the highest rainfall occur in autumn (September, October, and November), with the monthly rainfall reaching 400 mm in September and 600 mm in October. The dry season in Quang Binh province occurs from January to April, with monthly rainfall of less than 50 mm at most of the stations (Fig. 2 and Table 5).

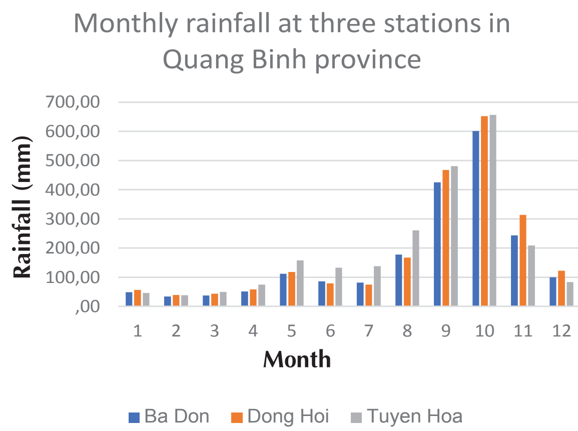

Fig. 2. Annual cycle of rainfall for the period 1961-2014.

Table 5. Rainfall characteristics for the 1961-2014 period.

	Jan	Feb	Mar	Apr	May	Jun	Jul	Aug	Sep	Oct	Nov	Dec	Yearly
One-day maximum rainfall (Rx1day) (A)													
Ba Don	21.8	14.8	16.6	25.5	51.7	42.6	39.2	83.0	141.1	176.7	80.8	38.6	235.6
Dong Hoi	22.8	17.9	21.8	29.0	51.1	40.5	34.6	74.2	146.7	179.4	94.3	44.8	234.2
Tuyen Hoa	15.5	15.1	21.4	31.8	59.7	54.5	57.3	104.1	150.5	192.7	66.4	25.9	253.4
Five-day maximum rainfall (Rx5day) (B)													
Ba Don	31.7	22.4	22.4	33.2	68.4	63.6	58.5	125.8	247.1	331.6	136.8	61.3	418.2
Dong Hoi	34.5	26.7	28.2	38.1	66.8	58.5	53.4	114.8	268.7	360.6	169.0	74.7	450.7
Tuyen Hoa	25.8	24.5	30.0	41.8	91.4	91.1	87.4	166.1	268.0	366.6	112.4	43.7	462.4
Number of days with rainfall greater than 50 mm (R50) (C)													
Ba Don	0.0	0.0	0.0	0.2	0.5	0.4	0.5	0.9	2.3	3.6	1.2	0.3	9.7
Dong Hoi	0.1	0.1	0.1	0.3	0.7	0.3	0.3	0.9	2.6	4.0	1.8	0.4	11.5
Tuyen Hoa	0.0	0.0	0.0	0.2	0.6	0.5	0.7	1.1	2.8	3.8	0.9	0.1	10.7

Temporal distribution of heavy rainfall in Quang Binh province

Annual evolution:

The rainy season in Quang Binh occurs from August to December [16, 17]. The temporal distribution of rainfall in Quang Binh is a double-peaked annual cycle, with the highest peak in October and an extra peak occurring in May

Over a year, the one-day maximum rainfall at the three stations in Quang Binh ranged from 234.2 mm to 253.4 mm (Table 5A). The one-day maximum rainfall is often observed during the rainy season and is concentrated in September and October. On average, for the 1961-2014 period, the one-day maximum rainfall at the three stations in Quang Binh ranged from 141.1 mm to 150.5 mm in September, and from 176.7 mm to 192.7 mm in October (Fig. 3).

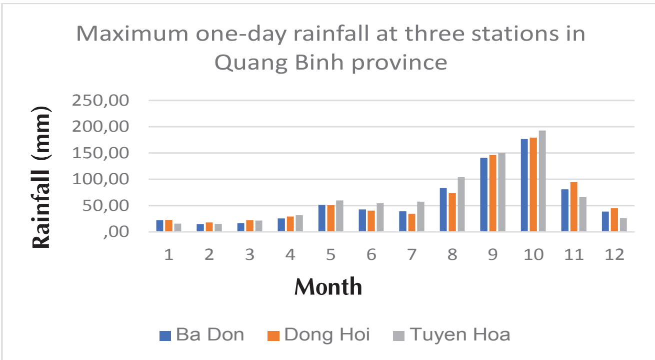

Fig. 3. Annual cycle of the maximum one-day rainfall for the period 1961-2014.

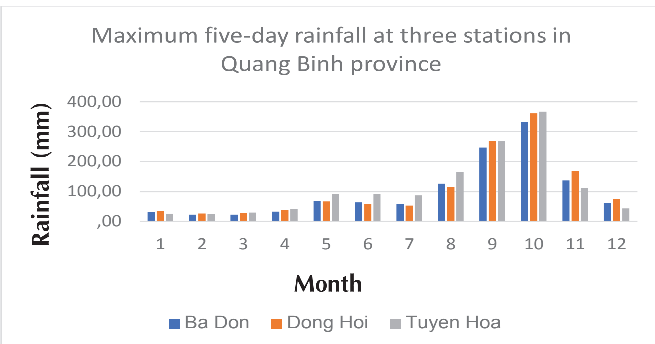

Fig. 4. Annual cycle of the maximum five-day rainfall for the period 1961-2014.

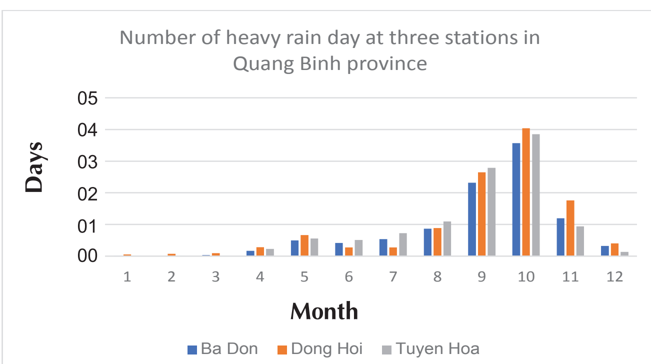

Fig. 5. Annual cycle of the number of rainy days over 50 mm for the period 1961-2014.

On average, for the 1961-2014 period, the annual maximum five-day rainfall at the three stations in Quang Binh province ranged from 418.2 mm to 462.4 mm (Table 5B). The maximum five-day rainfall also occurs in September and October, with values from 247.1 mm to 268.7 mm in September and from 331.6 mm to 366.6 mm in October (Fig. 4).

In terms of the annual occurrence of heavy rainfall, the three stations in Quang Binh province witness approximately 10-11 days of heavy rain (Table 5C). Similar to the maximum daily rainfall, the heavy rain days often occur in the rainy season, especially in September and October. At the three stations, on average for the 1961-2014 period, there were approximately 2-3 heavy rain days in September, and 3-4 in October. From January to April, heavy rain days rarely occur in Quang Binh (Fig. 5).

Analysis of rainfall trends in Quang Binh:

Figure 6 shows the trends in annual rainfall at the three stations for the period of 1961-2014. In general, the trends in annual rainfall vary greatly between stations. Annual rainfall increased by 37.6 mm and 58.9 mm per decade at Ba Don and Tuyen Hoa stations, respectively, while it decreased by approximately 46.2 mm per decade at Dong Hoi station.

Figure 7 shows the trends in annual maximum one-day rainfall at the three stations in Quang Binh province. For the period 1961-2014, the annual Rx1day experienced positive trends at rate of 4-16 mm per decade. The annual Rx1day rate of decrease at Ba Don station was the fastest in the province, approximately 15.98 mm per decade.

Figure 8 shows the trends in annual maximum five-day rainfall (Rx5day) at the three stations in Quang Binh for the period of 1961-2014. It can be seen that, similarly to the annual rainfall, the trend in Rx5day change at the three stations was not uniform but alternated between an

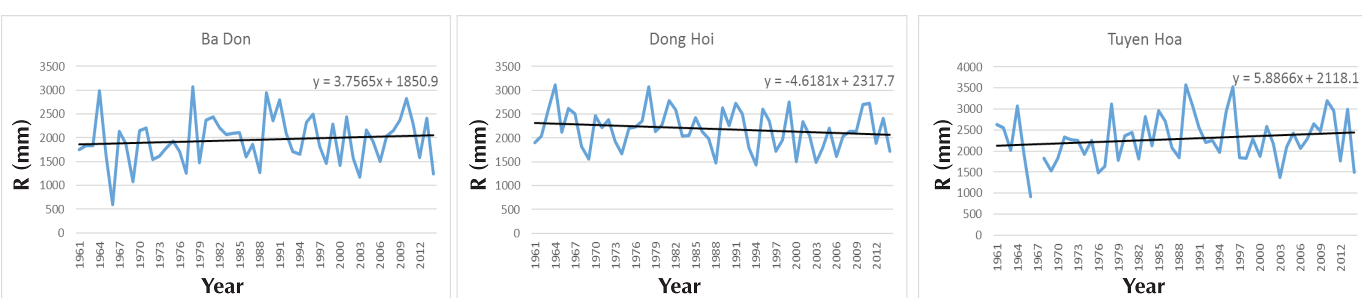

Fig. 6. Trends in rainfall at the three stations in Quang Binh, 1961-2014.

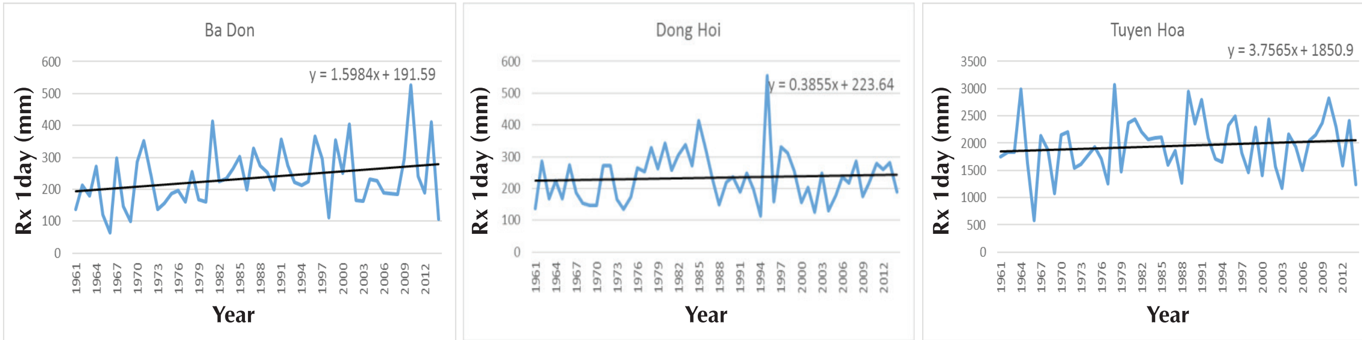

Fig. 7. Trends in Rx1day at the three stations in Quang Binh, 1961-2014.

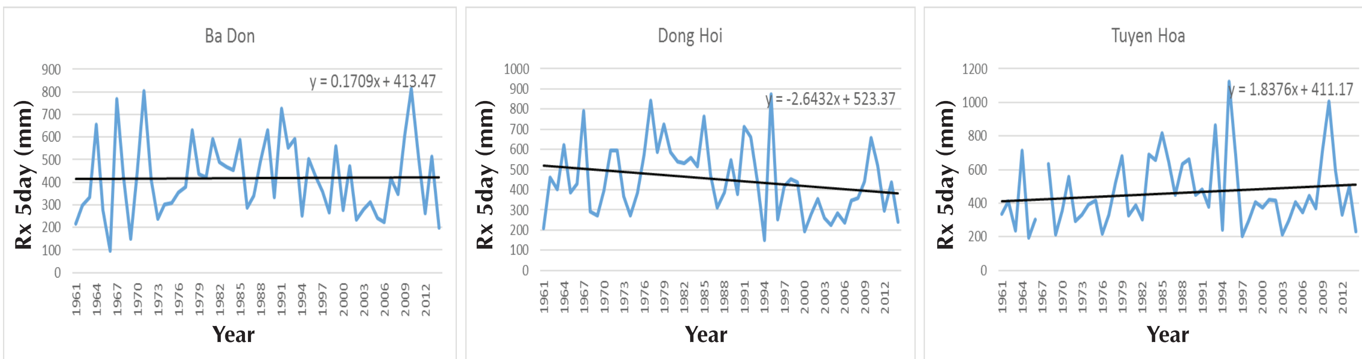

Fig. 8. Trends in Rx5day at the three stations in Quang Binh, 1961-2014.

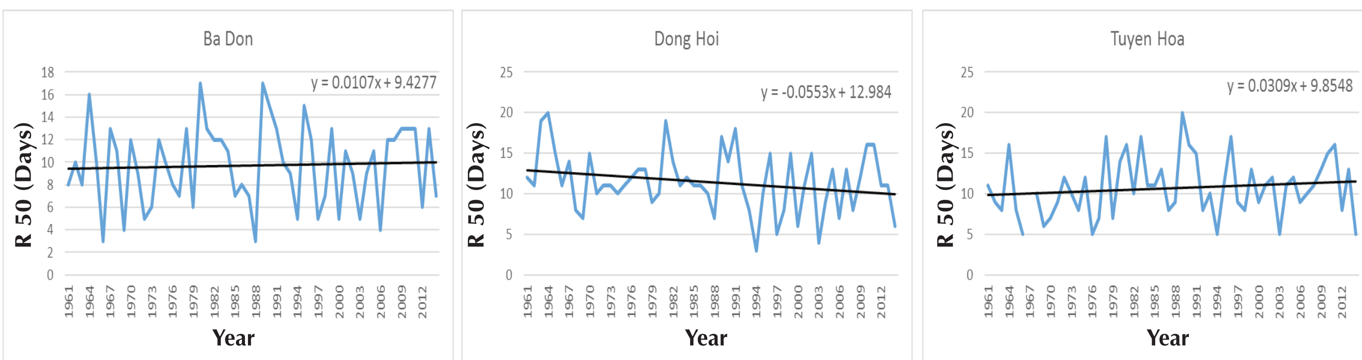

Fig. 9. Trends in R50 at the three stations, 1961-2014.

upward trend and a decline over the 54 years. Specifically, the Rx5day tended to increase at Ba Don and Tuyen Hoa stations, with increases of 1.7 mm/decade and 18.4 mm/decade, respectively, while a downward trend occurred at Dong Hoi station, at 26.4 mm/decade.

Figure 9 shows the trends in number of heavy rain days (R50) at the three stations for the period of 1961-2014. Similar to the annual rainfall, R50 showed increasing trends at Ba Don and Tuyen Hoa stations, at a rate of 0.1 and 0.3 days per decade, respectively, and a decreasing trend at Dong Hoi station, at a rate of approximately 0.55 days per decade.

Spatial distribution of heavy rain in Quang Binh province

Distribution of the annual average total rainfall:

The average total rainfall is in the 2,000 to 2,400 mm range in Quang Binh province. Rainfall in coastal areas is significantly lower than in mountainous areas. For instance, the lowest annual average rainfall is in the coastal district of Quang Trach, with a value of about 1,900 mm. The highest rainfall is concentrated in two regions: the mountainous areas along the border with Laos and the northern border abutting the Ky Anh heavy rain centre (one of the highest rainfall centres in Vietnam is located in Ky Anh province), with rainfall from 2,200 to over 2,800 mm (Fig. 10).

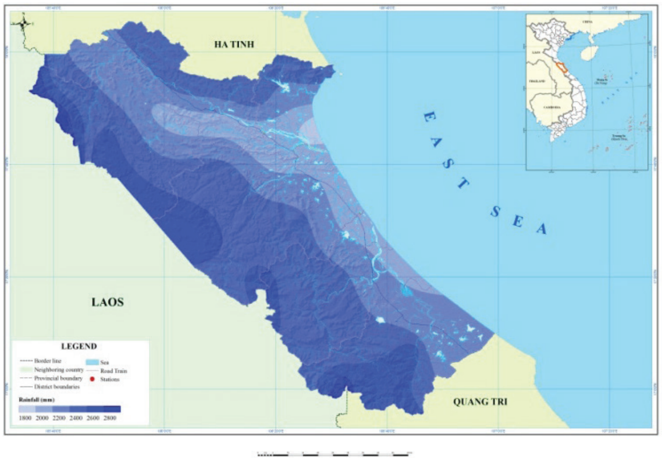

Fig. 10. Spatial distribution of the average total rainfall in Quang Binh province.

Distribution of the maximum one-day rainfall:

The maximum one-day rainfall in Quang Binh province ranges from 230 and 280 mm (Fig. 11). The RX1day shows obvious differentiation, with the highest values in the north and west of Quang Binh, and the lowest values in the east. The largest value for RX1day was found at Dong Tam station (Tuyen Hoa district), while the lowest value was found at Dong Hoi station (Dong Hoi city).

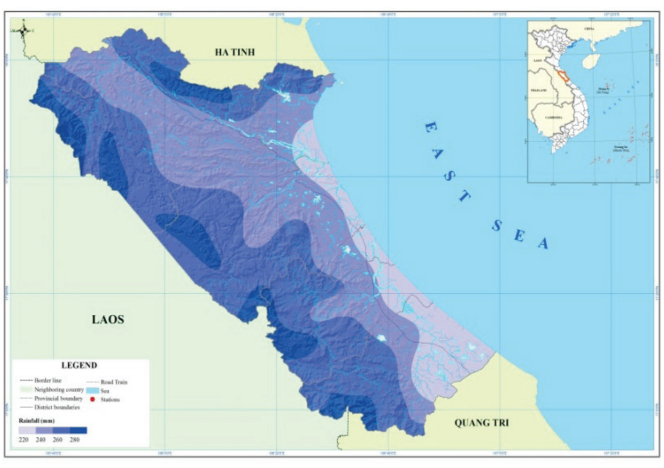

Fig. 11. Spatial distribution of the maximum one-day rainfall in Quang Binh province.

Distribution of the maximum five-day rainfall (RX5day):

The maximum consecutive five-day rainfall (RX5day) in Quang Binh ranges from 400 to 500 mm (Fig. 12). The distribution of RX5day is quite similar to that of the RX1day - the largest values are in the north and west and the lowest values in the east. The largest value for RX5day was found at Dong Tam station (Tuyen Hoa district), while the lowest value was found at Ba Don station (Quang Trach district).

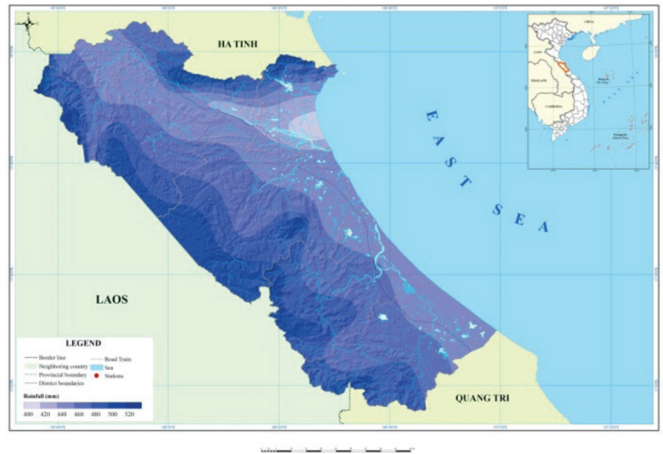

Fig. 12. Spatial distribution of the maximum consecutive five-day rainfall in Quang Binh province.

Distribution of the number of days with rainfall greater than 50 mm (R50):

Figure 13 shows the spatial distribution of the number of days with rainfall greater than 50 mm in Quang Binh. The values for R50 range from about 10 to 13 days per year for the whole of Quang Binh province. The lowest value was found at Minh Hoa and Ba Don stations with 9.7 days, while the highest is 13.4 days at Kien Giang station.

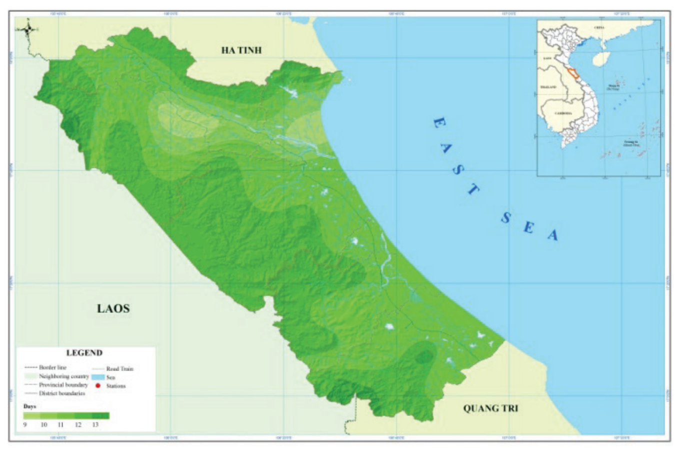

Fig. 13. Spatial distribution of the number of days with rainfall greater than 50 mm in Quang Binh province.

Conclusions

Quang Binh province is greatly affected by natural disasters, with tropical cyclones, floods, and flash floods occurring at high frequency and severity. In-depth study of heavy rainfall is highly relevant for supporting socio-economic development and human life in Vietnam in general and in Quang Binh in particular.

The maximum rainfall during one heavy spell of rainfall and the one-day heavy rainfall were calculated according to the frequency of occurrence of 20%, 10%, 5%, 2%, and 1% (i.e., the 5-year, 10-year, 20-year, 50-year, and 100-year return periods). The results show that at the frequency of occurrence of 20%, the maximum intensity of a heavy rain spell can reach from 636.6 to 696.0 mm, and this can occur many times in five years. Conversely, at a frequency of 1%, the intensity of a heavy rain spell can reach 1,197.9 to 1,268.3 mm; however, this value is very rare in 100 years.

In terms of the maximum one-day rainfall, at the frequency of occurrence of 20%, the maximum one-day reached over 300 mm, and this can occur many times in five years. Conversely, at a frequency of 1%, the maximum one-day can reach from 487.4 to 521.9 mm; however, this value is very rare in 100 years.

For the period 1961-2014, the average annual rainfall in Quang Binh ranged from 2,000 to over 2,400 mm, with the rainy season lasting from August to December and peaking in October. In terms of spatial distribution, rainfall in coastal areas was significant lower than in mountainous areas. The highest rainfall was concentrated in two regions: the mountainous areas along the border with Laos and the northern area bordering on the Ky Anh heavy rain centre, where rainfall from over 2,200 mm to over 2,800 mm was recorded. The highest one-day and five-day rainfall has the same pattern of distribution as the annual rainfall.

ACKNOWLEDGEMENTS

This paper is part of a research contract entitled ‘Disasters Profile of Quang Binh Province and Review and Assessment of the Availability and Usage of Early Warning System and Weather Forecasts’, jointly signed by the GRC and the Center for Meteorology and Climatology, with financial support from the Boll Foundation (Boll Stiftung). The authors acknowledge the support and contribution of the VNRC and the GRC. In addition, special thanks are given to the research team at the Center for Meteorology and Climatology for participating in the research, and supporting and contributing to the completion of this paper.

The authors declare that there is no conflict of interest regarding the publication of this article.

REFERENCES

[1] https://www.quangbinh.gov.vn/3cms/dieu-kien-tu-nhien.htm.

[2] Duc Ngu Nguyen, Hieu Trong Nguyen (2013), *Climate and climate resources in Vietnam,* Hanoi Science and Technology Publishing House.

[3] Duc Ly Nguyen, Hai Duong Ngo, Dai Nguyen (2013), *Quang Binh climate and hydrology*, Hanoi Science and Technology Publishing House.

[4] Xuan Hau Nguyen (2015), *Assessment of the impact of climate change on the flooding of Nhat Le basin, Quang Binh province*, Vietnam Academy of Science and Technology.

[5] Long Duc Vu (2014), *Research on developing technology for flood warning, forecasting and flooding warning for main rivers in Quang Binh, Quang Tri provinces*, Synthesis report of the ministerial level project.

[6] GRC, VNRC (2017), *Community-based disaster management in rural and urban areas in Quang Binh (2015-2018)*, Boll Foundation sponsed project.

[7] Dai Nguyen (2007), *Collecting and adjusting hydro-meteorological data of Quang Binh province from 1956 to 2005*, Synthesis report of the provincial level project.

[8] Vietnam Meteorological and Hydrological Administration (2017), *Observation data set of meteorology and hydrology, updated to 2017.*

[9] Francesco De Paola, Maurizio Giugni, Maria Elena Topa, and Edoardo Bucchignani (2014), “Intensity-Duration-Frequency (IDF) rainfall curves, for data series and climate projection in African cities”, *Springerplus*, **3**, p.133, Doi: 10.1186/2193-1801-3-133.

[10] S.C. Liew, S.V. Raghavan and S.-Y. Liong (2014), “How to construct future IDF curves, under changing climate, for sites with scarce rainfall records?”, *Hydrol. Process*, **28**, pp. 3276-3287, Doi: 10.1002/hyp.9839.

[11] L.M Nhat, Y.Tachikawa, K. Takara (2006), “Establishment of intensity-duration-frequency curves for precipitation in the monsoon area of Vietnam”, *Annuals of Disas. Prev. Res. Inst.*, **49B**, Kyoto University.

[12] X. Wang, G. Huang and J. Liu (2014), “Projected increases in intensity and frequency of rainfall extremes through a regional climate modeling approach”, *J. Geophys. Res. Atmos.*, **13**, pp.271-13,286, Doi: 10.1002/2014JD022564.

[13] Binh Thai Hoang (2009), *Developing flood maps at downstream area of Nhat Le river system (My Trung - Tam Lu - Dong Hoi)*, Graduate thesis, VNU University of Science.

[14] Cam Vinh Lai, Hau Xuan Nguyen (2007), *Study and implementation on online forecasting technology on the area and level of flooding in river basins of Central Vietnam*, Synthesis report of the project, Vietnam Institute of Science and Technology.

[15] K. Dairaku, K. Kuraji, M. Suzuki, N. Tang Tham, W. Jirasuktaveekul, and K. Punyatrong (2000), “The effect of rainfall duration and intensity on orographic rainfall enhancement in a mountainous area: a case study in the Mae Chaem watershed, Thailand”, *J. Japan Soc. Hydrol. Water Resour*, **13**, pp.57-68.

[16] T. Oki and K. Musiake (1994), “Seasonal change of the diurnal cycle of precipitation over Japan and Malaysia”, *J. Appl. Meteor.*, **33**, pp.1445-1463.

[17] Oyebande (1982), “Deriving rainfall intensity-duration-frequency relationships and estimates for regions with inadequate data”, *Hydrological Science Journal*, **27(3)**, pp.353-367.

[18] A.K. Weisse and P. Bois (2001), “Topographic effects on statistical characteristics of heavy rainfall and mapping in the French”, *J. Appl. Meteor.*, **40**, pp.720-740.

Doi: 10.31276/VJSTE.61(2).79-83

A comparison of $PM_{2.5}$ and PAHs in ambient air between an urban background site and a background site in Ho Chi Minh city

Thi Hien To*, Doan Thien Chi Nguyen, Xuan Vinh Le, Huu Huy Duong

Faculty of Environment, University of Science, Vietnam National University Ho Chi Minh city

Received 23 October 2018; accepted 25 February 2019

Abstract:

This study aims to evaluate the differences between $PM_{2.5}$, PAHs concentration, PAHs species, and their gas/particle partitioning in an urban background site as opposed to another background site. Saigon zoo was selected as a representative of the urban background site (UBS), and the Can Gio mangrove reserve was selected as the other background site (BS). $PM_{2.5}$ and gas and particle-phase PAHs samples were collected at the UBS between March 2017 and February 2018, while the samples were collected at the BS for one week in the dry season (April) and in the rainy season (October). The results demonstrated that both $PM_{2.5}$ and PAHs concentrations at the UBS were significantly higher than those at the BS. The $PM_{2.5}$ concentration at the UBS and BS ranged from 13.3 to 67.6 µg/m^3 and from 5.1 to 22.7 µg/m^3, respectively. The total concentration of 14 PAHs at the UBS was 2.6 times greater than that at BS. Phenanthrene (Phe) was the dominant PAH in ambient air at both sites. Benzo[g,h,i]perylene (BghiP) and Indeno[1, 2, 3-cd]pyrene (InP), which indicate the traffic source, accounted for 3.6 and 3.3% of total PAHs at the UBS, while that at the BS accounted for 1.5 and 1.3%, respectively. This result suggested that vehicular emission strongly affected the UBS site.

Keywords: **Can Gio mangrove, gas/particle partitioning, $PM_{2.5}$, polycyclic aromatic hydrocarbons (PAHs), Saigon zoo.**

Classification number: **5.2**

Introduction

Particulate matter (PM) is a critical measure of atmospheric pollution due to its effect onthe environment. Particles are defined by their aerodynamic diameters; for example, $PM_{2.5}$ has aerodynamic diameters of less than 2.5 µm. $PM_{2.5}$ causes detrimental health effects because when they are inhaled, they can penetrate deep into the alveoli of the lungs and become deposited there. The size of $PM_{2.5}$ particulate matter is not the only notable factor for health effects; the chemical composition is also important [1]. Polycyclic aromatic hydrocarbons (PAHs) are products of incomplete combustion of organic matter, and they are ubiquitous in our environment. Anthropogenic emission sources of PAHs in the atmosphere include traffic, domestic heating, oil refining, and other industrial processes [2, 3]. PAHs are well-known because of their carcinogenic and mutagenic properties. PAHs associated with fine particles, which can deeply infiltrate the human respiratory system, may cause severe problems to human health. Research regarding air quality of background sites has provided information concerning the contributions of local sources, whether they are from regional backgrounds or from long-range transport [4]. In Ho Chi Minh city, studies of background air quality are limited. This study aims to evaluate the differences in $PM_{2.5,}$ PAHs concentration, PAHs species, and their gas/particle partitioning between UBS and BS. Fourteen PAHs analysed in both gas and particle phases included acenaphthene (Ace), fluorene (Flu), phenanthrene (Phe), anthracene (Ant), fluoranthene (Flt), pyrene (Pyr), benz[a]anthrancene (BaA), chrysene (Chr), benzo[b]fluoranthene (BbF), benzo[k]fluoranthene (BkF), benzo[a]pyrene (BaP), dibenz[a,h]anthracene (DahA), benzo[g,h,i]perylene (BghiP), and indeno[1,2,3-cd]pyrene (InP).

Materials and methods

Sampling

Saigon zoo in Ho Chi Minh city (10.787°N,106.707°E) was selected as are presentative for the UBS because it is not

*Corresponding author: Email: tohien@hcmus.edu.vn.

heavily influenced by either traffic or industrial emissions. Can Gio (10.615°N,106.816°E), located in southeastern Ho Chi Minh city, was selected as the BS of the city. The distance between the two sampling sites is about 20 kilometers. A map of the sampling sites is illustrated in Fig. 1. $PM_{2.5}$, and gas and particle-phase PAH samples were collected at the UBS between March 2017 and February 2018, while the samples were collected at the BS for one week in the dry season (April) and in the rainy season (October). $PM_{2.5}$ was collected on quartz fiber filters, and an impactor was used at a flow rate of 10 l/min in 24 hours [5]. A high-volume sampler was used to collect gas phase and particle phase PAHs simultaneously running at a flow rate of 200 l/min in 24 hours. Particle-phase PAHs were collected on glass fiber filters, and gas-phase PAHs were adsorbed on polyurethane foams (PUFs) [6]. The samplers were set up at 1.5 meters above the ground. A total of 90 $PM_{2.5}$ samples and 24 gas and particle-phase PAHs samples and 14 $PM_{2.5}$ samples and 14 gas and particle-phase PAHs samples were collected at the UBS and BS, respectively.

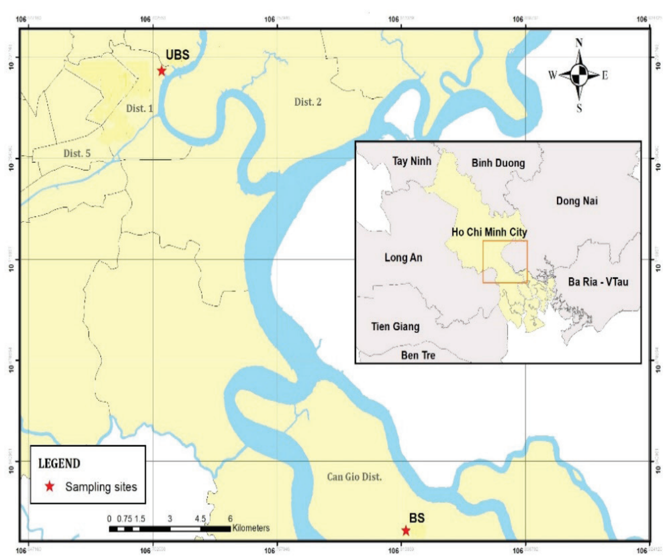

Fig. 1. Map of the sampling sites.

Sampling preparation

Glass and quartz filters were wrapped in aluminum foil, heated for 8 hours at 400^{0}C, and placed in a desiccator at least 2 days. The particle mass of samples was determined by weighing the filters before and after sampling using a RADWAG6 Digit Micro Balance. PUFs were extracted from as oxhlet system with 5% diethyl ether in hexane left for 16 hours; they were then wrapped in aluminum foil. The PUFs were brought to the sampling sites in glass jars sealed with teflon lids.

Chemical analysis

Particle-phase PAHs were extracted through sonication three times in the toluene and ethanol (3/1, v/v) solvent; the solution was then filtered to remove solid substances. The filtrate was cleaned up with NaOH, followed by H_2SO_4 and Millipore water. The extract was concentrated by a rotary evaporator and was evaporated to near dryness using a gentle stream of nitrogen. The residue was completely dissolved in methanol. The extract was stored after passing through a 0.45 µm syringe filter until it was injected into the High-Performance Liquid Chromatography with Fluorescence Detection (HPLC-FLD) system for analysis [7].

Compendium Method TO-13A, USEPA was used for gas phase PAHs [6]. PAHs in PUFs were extracted from a soxhlet system with 5% diethyl ether in hexane left for 16 hours. The extract was concentrated further by a rotary evaporator to near dryness under a stream of pure nitrogen. The PAHs were then dissolved in methano land stored at -4^{0}C until analysis by a HPLC-FLD machine.

All measurements were performed using a Shimadzu HPLC-FLD machine (including an LC - 20AD pump, a CTO - 20A column oven, a SIL - 20A auto sampler, and aInersil ODS - P 5 µm (4.0 × 250 mm) column). The recovery test was determined by spiking known amounts of a mixture of PAHs standards on to a filter or PUF; the spiked sample was then treated in the same manner as the field samples. Six measurements of the spiked samples were replicated for calculating the recovery of PAHs. The recovery results for particle-phase PAHs were 57.6-104.8%, with the relative standard deviations of 2.4-15.4%; for gas-phase PAHs, they were 95.2-182.5%, with the relative standard deviations of 5.42-56.6%. The method detection limit (MDL) of the PAH compounds in particle-phase varied from 0.1 pg/m^3 for Ant and BkF to 20 pg/m^3 for Ace. While in the gas-phase, MDL varied from 0.2 pg/m^3 for BaP to 2.95 pg/m^3 for Phe [8]. Laboratory blanks and field blanks for correcting the potential contamination from the experiment were prepared and analysed as samples. Microsoft Excel was used for statistical analysis.

Results and discussion

Atmospheric concentration of $PM_{2.5}$

$PM_{2.5}$ samples were collected at the UBS between March 2017 and February 2018, while the samples were collected at the BS for one week in the dry season (April) and in the rainy season (October). A summary of average concentrations of $PM_{2.5}$ at the BS and UBS during the sampling period is illustrated in Fig. 2. The $PM_{2.5}$ concentration at the UBS was significantly higher than level at the BS. The $PM_{2.5}$ concentration ranged from 13.3 to 67.6 µg/m^3, with a mean of 35.4±12.9 µg/m^3 and from 5.1 to 22.7 µg/m^3 with a mean of 13±5.8 µg/m^3 at the UBS and BS, respectively. The $PM_{2.5}$ concentration at UBS in the dry season was higher than in the rainy season (t-test, $p<0.05$), while there was no difference at the BS. Relative to other background sites in the world, the

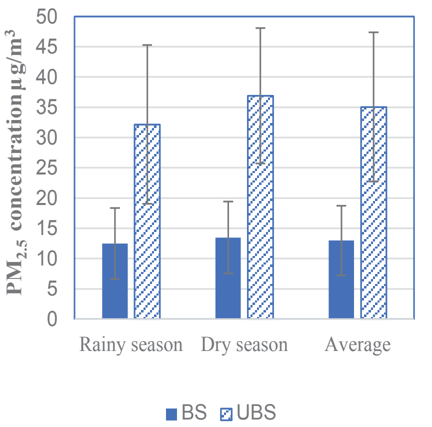

Fig. 2. Summary of $PM_{2.5}$ concentration at the BS and UBS during the sampling period.

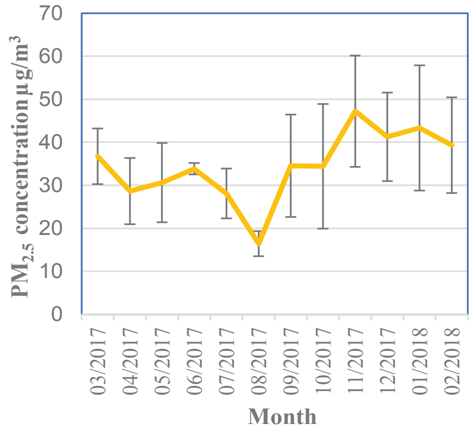

Fig. 3. Monthly average concentration of $PM_{2.5}$ at the UBS from 3/2017 to 2/2018.

Total PAH concentration in the particle-phase varied from 1.4 to 9.1 ng/m^3 (with an annual mean of 4.28 ng/m^3) and from 0.3 to 1.6 ng/m^3 (with an annual mean of 0.84 ng/m^3) at the UBS and BS, respectively. There was also a seasonal trend; the particle-phase PAHs were higher in the rainy season, while the gas-phase PAHs were higher in the dry season at the UBS. $PM_{2.5}$-bound PAHs accounted for 91.8% of total PAHs in the particle-phase, particularly high molecular weight PAHs such as BaP, BghiP, and InP. This result is similar to the study of Céline Liaud [10]. Significant correlations were obtained for the following PAHs (DahA, BbF, BkF, BghiP, InP) in the $PM_{2.5}$, indicating that these high-molecular weight PAHs and $PM_{2.5}$ presented common pollution sources. Gas-phase PAHs ranged from 13.4 to 47.7 ng/m^3 (with an annual mean of 29.46 ng/m^3) and from 5.7 to 20.7 ng/m^3 (with an annual mean of 11.91 ng/m^3) at the UBS and BS, respectively. The gas-phase PAHs at both sites were larger than those in the particle-phase and tended to increase in the dry season when the temperature rose. Phe was the dominant PAH at both sampling sites. BghiP and InP which indicates traffic source accounted for 3.6 and 3.3% of total PAHs at the UBS, while those at the BS accounted for 1.5 and 1.3%, respectively. This result suggested that vehicular emission heavily affected the UBS site. Indeed, Sai Gon zoo (UBS) is located in the center

$PM_{2.5}$ concentration at the UBS was significantly higher than at an urban background in Southeastern Italy 5.5-31.6 µg/m^3 [4] and a rural background area in Spain 12-17 µg/m^3 [9].

Figure 3 indicated the monthly average concentration of $PM_{2.5}$ at the UBS between March 2017 and February 2018. The $PM_{2.5}$ concentration tended to decrease in the rainy season and increase in the dry season. Wet deposit was pivotal in removing particles in the rainy season. There were 10 days (which accounted for 11% of entire data) when the $PM_{2.5}$ concentration at UBS exceeded the Vietnam National Technical Regulation on Ambient Air Quality QCVN 05:2013/BTNMT. The annual $PM_{2.5}$ concentration of 35.1±5.8 µg/m^3 also exceeded the regulation, demonstrating a high risk of long-term exposure to human health.

This study has found that the $PM_{2.5}$ concentration was exceptionally high on the 18th of January 2018, with the value of 67.6 µg/m^3 higher than the others in this month. However, the $PM_{2.5}$ concentration at Ho Chi Minh city US Consulate air monitoring station was also high, with a value of 69.3 µg/m^3. To understand this event, the Hypslit model provided by NOAA was used. The backward trajectory result on the 18th of January 2018 is illustrated in Fig. 4. The result of a 72-hour trajectory demonstrates that the air mass came from the East-North-East direction, from the Philippines to Ho Chi Minh city. At 6 pm on the 15th of January 2018, the height of air mass was about 2500 m, which was the same as the Mayon volcano that erupted on this day. It was clear that the $PM_{2.5}$ from the Mayon volcanic eruption was transported to Ho Chi Minh city. Based on this result, it is important to recognize this special event and investigate how it affects air quality and human health.

Atmospheric concentration of PAHs

Table 1 displays a summary of average concentrations of 14 PAHs as well as the total PAH concentrations measured in gas and particle-phases during the sampling period.

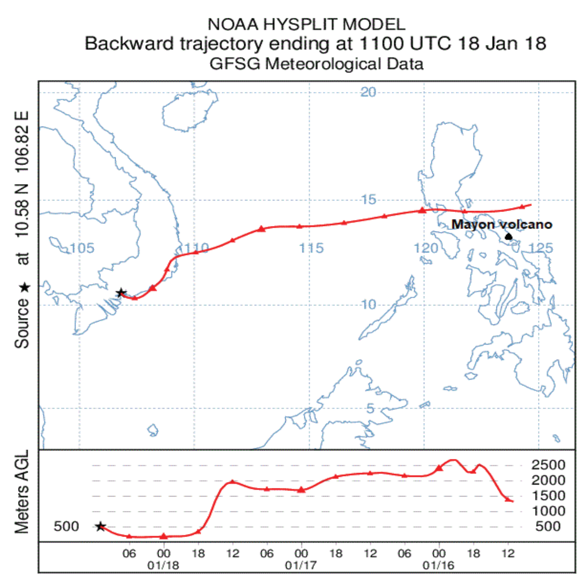

Fig. 4. 72-hour air trajectory ending on the 18th of January 2018 at the UBS (backward trajectory result using Hysplit model).

Table 1. Summary of annual and seasonal mean concentrations of 14 PAHs and the total PAH concentrations (ng/m³) measured in gas-phase and particle-phases at the UBS and BS during the sampling period.

Sampling sites	UBS			BS		
PAHs ng/m³	*Average (Gas and particle phase)*	*Rainy season (Gas and particle phase)*	*Dry season (Gas and particle phase)*	*Average (Gas and particle phase)*	*Rainy season (Gas and particle phase)*	*Dry season (Gas and particle phase)*
Ace	0.04/0.01	0.06/0.01	0.02/BDL	0.01/BDL	BDL/BDL	0.04/BDL
Flu	3.02/0.05	2.65/0.07	3.47/0.02	1.19/0.03	1.12/0.02	1.34/0.07
Phe	16.84/0.29	15.90/0.39	17.99/0.17	6.56/0.16	5.01/0.07	10.18/0.35
Ant	1.06/0.02	1.11/0.02	0.99/0.01	0.38/0.01	0.20/BDL	0.79/0.02
Flt	3.95/0.17	3.69/0.18	4.27/0.16	1.84/0.06	1.55/0.05	2.52/0.09
Pyr	3.87/0.18	3.74/0.18	4.03/0.17	1.59/0.05	1.35/0.04	2.13/0.06
BaA	0.15/0.08	0.12/0.08	0.19/0.07	0.06/0.02	0.04/0.01	0.10/0.02
Chr	0.27/0.14	0.21/0.14	0.35/0.13	0.12/0.03	0.10/0.03	0.18/0.05
BbF	0.01 /0.03	0.01/0.03	0.02/0.03	0.01/0.01	0.01/0.01	BDL/BDL
BkF	0.09/0.23	0.09/0.26	0.09/0.20	0.06/0.03	0.06/0.03	0.05/0.02
BaP	0.09 /0.38	0.12/0.39	0.05/0.36	0.03/0.05	0.02/0.05	0.04/0.06
DahA	0.01/0.29	0.02/0.33	BDL/0.26	BDL/0.08	BDL/0.08	BDL/0.06
BghiP	0.04/1.24	0.04/1.43	0.04/0.10	0.06/0.15	0.06/0.16	0.07/0.13
InP	0.01/1.17	0.02/1.41	BDL/0.88	BDL/0.17	BDL/0.17	BDL/0.19
Total	**29.46/4.28**	**27.78/4.94**	**31.51/3.47**	**11.91/0.84**	**9.53/0.71**	**17.45/1.12**

BDL: below detection limit.

of Ho Chi Minh city and surrounded by streets with high traffic density. There are few sources emitting $PM_{2.5}$ and PAHs at Can Gio (BS); additionally, those sources are stable throughout the year. This is why $PM_{2.5}$ and particle-phase PAHs were low, with a non-seasonal trend.

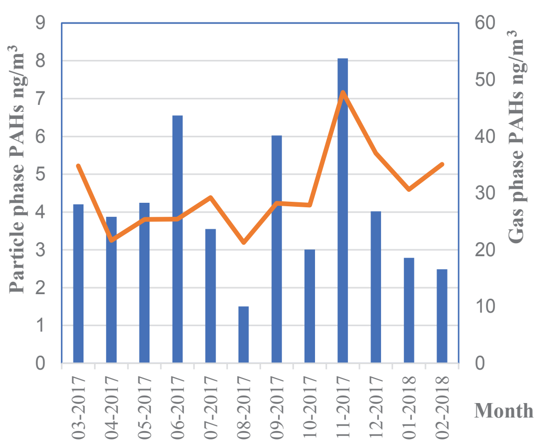

Fig. 5. Monthly mean concentration of gas-particle phase PAHs at the UBS during sampling period.

Monthly concentrations of total PAHs in gas and particle-phases at the UBS are illustrated in Fig. 5. Total PAHs had the lowest value in August and had the highest value in both gas and particle-phases in November. PAHs are well-known because of their carcinogenic and mutagenic potency for humans. BaP is a representative PAH because it is one of the most potent carcinogens known. The health risk assessment of PAHs can be determined based on its BaP equivalent concentration (BaP_{eq}). For each PAH, BaP_{eq} is calculated by multiplying its concentration with the corresponding toxic equivalent factor (TEF). The European Commission has recommended a limit value for BaP of 1 ng/m³ (Table 2).

Table 2. The BaPeq concentration (ng/m³) at the UBS and BS.

BaP_{eq}	Gas-phase Average±SD (Min-Max)	Particle-phase Average±SD (Min-Max)
UBS	0.14±0.045 (0.058-0.24)	0.77±0.47 (0.18-1.89)
BS	0.055±0.034 (0.014-0.14)	0.15±0.098 (0.029-0.30)

The average BaP_{eq} at UBS was 0.91 ng/m³. In three months (September, November and December), the BaP_{eq} concentration were 1.3, 2 and 1.1 ng/m³ exceeding the European Commission. The BaP_{eq} in the particle-phase accounted for 84%; notably, high-molecular weight PAHs, which is the strongest toxicity PAHs, displayed a dominant concentration. The average BaP_{eq} at the BS was 0.2 ng/m^3, which was 4.5 times lower than at the UBS.

Gas/particle partitioning of PAHs

High-molecular weight PAHs were dominant and accounted for 77.5% of the particle-phase PAHs. In contrast, low-molecular weight PAHs were also dominant and accounted for 71.2% of the gas-phase PAHs. Ace was below the detection limit in both phases, because Ace is easily decomposed by photochemical reaction in atmosphere. The particle-phase fraction Φ - $C_p/(C_p+C_g)$ was calculated to understand the PAHs' gas/particle partitioning, where C_p is the concentration of particle-phase PAH, and C_g is the concentration of gas-phase PAH (Table 3).

Table 3. The particle-phase fraction Φ of individual PAHs at the UBS and BS.

	Flu	Phe	Ant	Flt	Chr	BbF	BkF	BaP	DahA	BghiP
UBS	0.017	0.018	0.016	0.049	0.329	0.846	0.686	0.829	1.000	0.963
BS	0.027	0.021	0.009	0.033	0.199	0.565	0.242	0.779	1.000	0.750

The Φ of three-and four-ringPAHs at both sites were similar. The Φ of three-and four-ring PAHs (from Flu to Chr) were lower than 0.5, indicating that these PAHs are primarily distributed during the gas-phase. The Φ of five- and six-ringPAHs (BbF, BaP, DahA, BghiP) were larger than 0.5 and close to 1, which indicated that these PAHs are dominant in the particle-phase. However, there is a different Φ of BkF between the UBS and the BS. The Φ value at the BS was below 0.5, which did not align with other previous studies [3, 8]. Therefore, further research should be conducted to understand this situation.

Conclusions

This study has aimed to compare the $PM_{2.5}$, PAHs concentrations at two background sites and to provide more information about regional air quality in Ho Chi Minh city. The $PM_{2.5}$ and PAH concentrations at the UBS were substantially higher than those at the BS. The $PM_{2.5}$ concentration decreased in the rainy season and increased in the dry season. The Mayon volcanic eruption affected Ho Chi Minh city's atmosphere. Further evaluation is necessary to understand the effects of this event on human health. The BaP_{eq} in September, November, and December of 2017 exceeded the European Commission for PAHs, indicating a high risk of exposure. This study suggests that when investigating urban air pollution, it is necessary to assess not only the urban background but also the regional background, which will provide more information to understand local and long-range transport sources.

ACKNOWLEDGEMENTS

The authors are grateful to the Ho Chi Minh Department of Science and Technology for supporting this research under Grant No. 120/2017/HD-SKHCN.

The authors declare that there is no conflict of interest regarding the publication of this article.

REFERENCES

[1] María Soledad Callén, Amaia Iturmendi, José Manuel Lopez (2014),"Source apportionment of atmospheric $PM_{2.5}$-bound polycyclic aromatic hydrocarbons by a PMF receptor model: Assessment of potential risk for human health", *Environmental Pollution*, **195**, pp.167-177.

[2] Yamasaki Hiroyasu, Kazuhiro Kuwata, and Hiroko Miyamoto (1982), "Effects of ambient temperature on aspects of airborne polycyclic aromatic hydrocarbons", *Environmental Science & Technology*, **16**, pp.189-194.

[3] Masao Kishida, Ayako Nishikawac, Keiichi Fujimori, Yasuhiko Shibutani (2011), "Gas-particle concentrations of atmospheric polycyclic aromatic hydrocarbons at an urban and a residential site in Osaka, Japan: effect of the formation of atmospherically stable layer on their temporal change", *Journal of Hazardous Materials*, **192**, pp.1340-1349.

[4] Cesari Daniela, Donateo Antonio, Conte Marianna, Merico Eva, et al. (2016), "An inter-comparison of $PM_{2.5}$ at urban and urban background sites: chemical characterization and source apportionment", *Atmospheric Research*, **174-175**, pp.106-119.

[5] U.S. Environmental Protection Agency (1998), *Guideline on Speciated Particulate Monitoring.*

[6] U.S. Environmental Protection Agency (1999), *Compendium Method TO-13A Determination of Polycyclic Aromatic Hydrocarbons (PAHs) in Ambient Air Using Gas Chromatography/Mass Spectrometry (GC/MS).*

[7] Thi Hien To, Phuong Nam Pham, Sadanaga Yasuhiro, Kameda Takayuki, Takenaka Norimichi, Bandow Hiroshi (2007), "Comparison of particle-phase polycyclic aromatic hydrocarbons and their variability causes in the ambient air in Ho Chi Minh city, Vietnam and in Osaka, Japan, during 2005-2006", *Science of the Total Environment*, **382,** pp.70-80.

[8] Doan Thien Chi Nguyen, Xuan Vinh Le, Huu Huy Duong, Norimichi Takenaka, Thi Hien To (2017), "Gas-particlepartitioning of polycyclic aromatic hydrocarbons - PAHs in ambient air in Ho Chi Minh city", *Vietnam Journal of Science and Technology*, **55**, pp.97-102.

[9] Querol Xavier, Alastueya Andres, et al. (2008), "Spatial and temporal variations in airborne particulate matter (PM_{10} and $PM_{2.5}$) across Spain 1999-2005", *Atmospheric Environment*, **42**, pp.3964-3979.

[10] Céline Liaud, Thierry Dintzer, Valérie Tschamber, Gwénaelle Trouve, Stéphane Le Calvé (2014), "Particle-bound PAHs quantification using a 3-stages cascade impactor in French indoor environments", *Environmental Pollution*, **195**, pp.64-72.

Doi: 10.31276/VJSTE.61(2).84-89

Calculating the carbon footprint of rice production in Vietnam and formulating a proposal for mitigation options

Dao Minh Trang[1], Huynh Thi Lan Huong[1*], Mai Van Trinh[2]

[1]*Vietnam Institute of Meteorology, Hydrology and Climate Change*

[2]*Institute for Agricultural Environment, Vietnam Academy of Agricultural Sciences*

Received 15 March 2019; accepted 28 May 2019

Abstract:

This study aims to develop a method for calculating the carbon footprint of rice during its life cycle by combining Life Cycle Assessment (LCA) and the 2006 Guideline of the Intergovernmental Panel on Climate Change (IPCC) for National Greenhouse Gas Inventories (GL 2006) for paddy rice grown in Phu Luong commune, Dong Hung district, Thai Binh province, Vietnam. In the course of the study, a LCA survey that included activities in the upstream processes, the agricultural process, and the post-farm stage was conducted based on interviews with three groups of 30 farmer households that apply the conventional practice of rice production, the system of rice intensification (SRI), or the wide-narrow row method. These cultivation practices are applied for both the winter-spring crop and summer-autumn crop seasons. The emissions were calculated by multiplying the activity data by the default emission factors in GL 2006 or in other relevant studies. The emission factors of methane (CH_4) from rice cultivation and nitrous oxide (N_2O) from agricultural soil were adjusted using actual measurement results from the Institute of Agricultural Environment (IAE) in 2016. The results of the calculations show that the main sources of the emissions that constitute the carbon footprint of rice include: (i) CH_4 emissions from rice cultivation; (ii) electricity generation for irrigation; (iii) diesel combustion for the operation of agricultural machinery, and (iv) fertiliser production. Emissions from other activities were negligible. The carbon footprint of spring rice is 2.69 kgCO_2e/kg of rice grown using the conventional paddy cultivation method, 2.35 kgCO_2e/kg for rice grown using the SRI method, and 2.29 kgCO_2e/kg for rice grown using the wide-narrow row method. In summer, the carbon footprint for rice grown using the conventional method is 3.72 kgCO_2e/kg of rice, 3.56 kgCO_2e/kg of rice using SRI, and 3.3 kgCO_2e/kg of rice using the wide-narrow row method. Three mitigation options are proposed: integrated crop management for rice; alternate wetting and drying; and the substitution of urea fertiliser ($CO(NH_2)_2$) with ammonium sulphate ($(NH_4)_2SO_4$).

Keywords: **carbon footprint, greenhouse gas, LCA, mitigation, rice.**

Classification number: **5.2**

Introduction

The term *carbon footprint* is defined as "the quantity of GHGs (greenhouse gases) expressed in terms of CO_2e, emitted into the atmosphere by an individual, organization, process, product, or event from within a specified boundary" [1]. The scope of a carbon footprint depends on the range of activities to be taken into account, including Tier 1 (on-site emissions), Tier 2 (emissions embodied in purchased energy), and Tier 3 (all other indirect emissions not covered under Tier 2) [2, 3]. The choice of direct or indirect emissions is incompatible across the different studies. In most cases, including all indirect emissions in the calculation is very complex; therefore, many studies of carbon footprints calculate only direct emissions or indirect emissions at Tier 2 but not include indirect emissions at Tier 3. However, indirect emissions may account for the majority of the carbon footprints of many activities and products.

Carbon-footprint calculations can be undertaken based on a product-based approach or an activity-based approach, that is, GHG emissions from the activities of individuals, groups, or organisations. The carbon footprints of activities are the annual GHG emission inventories of individuals,

* Corresponding author: Email: huynhlanhuong@gmail.com.

groups, organisations, companies, and governments. National GHG inventories are based on emissions from activities within the territories of countries. This means that production, transport, and other activities occurring in countries, such as international transport and emissions from imported products, are excluded. However, the product carbon footprint (PCF) refers to the LCA of the whole or part of the product or the service life cycle; this means that all GHG emissions from every activity involved in providing a product or service to consumers should be included. This is the more comprehensive and fairer approach, since consumers would be made "responsible" for emissions. For example, in this study, the GHG emissions from imported fertiliser or pesticides that are used in rice cultivation must become part of the life-cycle analysis, though such emissions should not be included in the national inventory.

One of the guidelines for calculating GHG emissions using the activity-based approach is the GL 2006 of the Intergovernmental Panel on Climate Change (IPCC). Since 2009, government agencies and international organisations have made significant strides in developing standards and guidelines for calculating PCFs [4]. At present, three PCF calculation guidelines are universally accepted: PAS 2050 of the British Standards Institute [2], the GHG Protocol of the World Resources Institute and the World Business Council for Sustainable Development [1], and ISO 14067 [5]. All these standards are based on the LCA method specified in ISO 14040 and ISO 14044. Apart from those of the IPCC, most publications on LCA in Vietnam are also based on the Vietnamese Standard TCVN ISO 14040:2009 on environmental management, life-cycle assessment, and principles and framework. In 2017, the Food and Agriculture Organization (FAO) developed guidelines for calculating GHG emissions from major agricultural products such as corn, wheat, barley, cassava, and soybeans [6].

Study area

Phu Luong commune is located in the northwest of Dong Hung district in Thai Binh province (Fig. 1). It comprises 4.77 km^2. Most rural households in Phu Luong commune depend on agriculture. It includes five villages: Duyen Tuc, Duyen Giang, Duyen Phu, Duyen Trang Dong, and Duyen Trang Tay. In 2017, Phu Luong commune had 2,608 households with 8,202 inhabitants [7].

According to IAE (2016) [7], Phu Luong has a total planted paddy rice area of 299.04 ha; the winter crop covers 137.9 ha; the spring, summer, and autumn cereals cover 23.25 ha. The spring rice yield reaches 7.3 tons/ha, and the summer yield reaches 6.3 tons/ha.

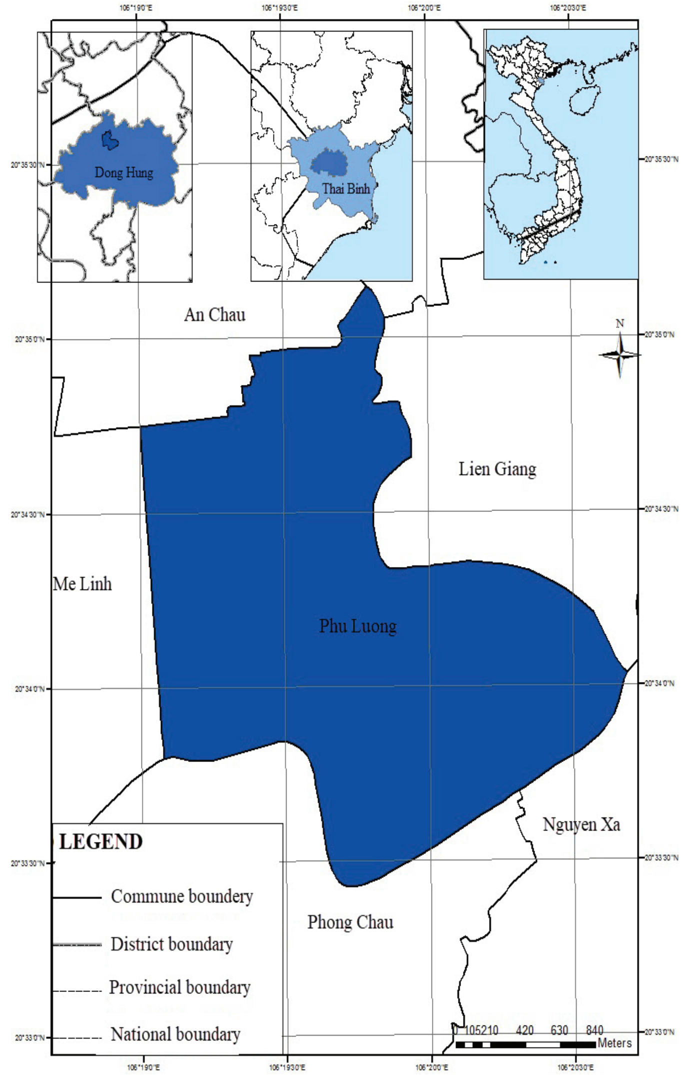

Fig. 1. Geographical location of Phu Luong commune.

Material and methodology

Data collection

Activity data such as cultivated land area, crop variety, the growth duration of rice, the capacity and frequency of the use of agricultural machinery, the amount of fertiliser and pesticide used, crop productivity, and the method used to treat straw (burying or burning) are taken from the results of interviews with 90 farmer households in Phu Luong commune. Three types of cultivation are used: the conventional one, the wide-narrow row method, and the system of rice intensification (SRI) for the spring and season crops. Emission factors are taken from GL 2006 [8], FAO [6], and other relevant studies.

Methodology

The methodology of this study is based on combining LCA and GL 2006 [8] and other studies (Fig. 2).

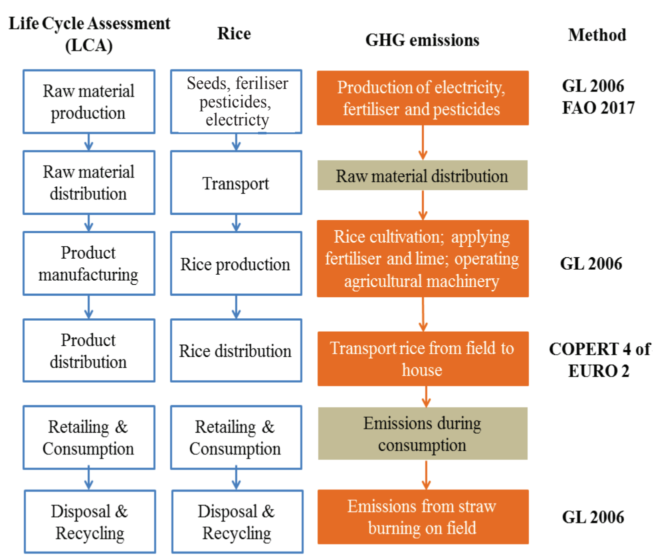

Fig. 2. Methodology for the calculation of the carbon footprint for rice.

The procedure for calculating the carbon footprint for rice involves five steps:

Step 1: select the GHGs in terms of the regulations of the Kyoto Protocol, including CO_2, nitrous oxide (N_2O), and methane (CH_4).

Step 2: determine the scope of the calculation: GHG emissions from upstream processes (electricity generation and the production of fertiliser, lime, and pesticides); rice production (rice cultivation, diesel combustion for the operation of agricultural machinery, and the application of fertiliser and lime), and the post-production of rice (transporting rice from farms to households and on-site straw burning).

Step 3: collect activity data.

Activity data were collected by means of questionnaires provided to 90 farmer households in Phu Luong commune. The households interviewed were selected based on stratified random sampling.

Step 4: calculate the carbon footprint.

Calculation of GHG emissions/removals:

Table 1 presents the formulas used for the calculation in the study.

Table 1. Summary of formulas used to compute the carbon footprint of rice.

Stage	Activity	Source	Tier
Upstream processes	1. Electricity generation for the operation of agricultural machinery	Formula 2.1, Vol. 2, GL 2006 [8], p.2.11	Tier 2
	2. Fertiliser production	FAO [6], p.13	Tier 1
	3. Lime production	Formula 2.8, Vol. 3, GL2006 [8] p.2.22	Tier 1
	4. Pesticide production	FAO [6], p.13	Tier 1
Rice production	5. Methane emissions from rice cultivation	Formula 5.1, Vol. 4, GL 2006 [8], p.5.45	Tier 2
	6. Diesel combustion for the operation of agricultural machinery	Formula 2.1, Vol. 2, GL 2006 [8], p.2.11	Tier 1
		FAO [6], Nemecek and Kagi [9]	
	7. Lime application	Formula 11.12, GL 2006 [8], p. 11.27	Tier 1
	8. CO_2 emissions from urea application	Formula 11.12, GL 2006 [8], p.11.27	Tier 1
	9.1. Direct N_2O emissions from agricultural soil	Formula 11.1, Vol. 4, GL 2006 [8]	Tier 2
	9.2 N_2O indirect emission from agricultural soil	Formula 11.9, Vol. 4, GL 2006 [8]	Tier 1
Post-farm	10. Transport rice from farms to houses	Computer programme to calculate emissions from road transport (COPERT 4) of the European	Tier 1
	11. On-site straw burning	Formula 2.27, GL 2006 [8], p.2.42	Tier 1
		Gadde, et al. 2009 [10]	

Calculating the carbon footprint:

The global warming potential (GWP) of all tiers is calculated individually using the IPCC's conversion factor. According to the IPCC's Fifth Assessment Report (AR5) [11], the GWP value of CH_4 is 28 and that of N_2O is 265. The formula for calculating the GWP of tier$_i$ (i = 1, 2, or 3) is as follows:

GWP (tier$_i$) = emission/removal of CH_4 x 28 + emission/removal of N_2O x 265 + emission/removal of CO_2

where GWP is measured in kg CO_2e/ha.

The carbon footprint is calculated by summing the GWP of all tiers; its value can be presented as spatial or yield-scaled carbon footprints, which are calculated as follows:

$$CF_s = \sum_{i=1}^{3}[GWP(tier_i)]$$

$$CF_y = \frac{CF_s}{Grain\ yield}$$

where CF_s is the spatial carbon footprint (kg CO_2e/ha) and CF_y is the yield-scaled carbon footprint (kg CO_2e/yield).

This study uses the carbon footprint by both yield and spatial unit, that is, kg CO_2e/kg rice and kg CO_2e/ha.

Step 5: analysis of uncertainty (optional).

Uncertainty regarding the results of the calculation usually stems from uncertainty regarding the model and of the data. The results of GHG-emission calculations cannot avoid uncertainty.

Results and discussion

The GHG emissions for each activity in life cycle of rice in the spring and summer seasons are presented in Table 2.

It can be seen from Table 2 that the carbon footprint of spring rice is 2.69 kg CO_2e/kg of rice for the conventional practice, 2.35 kg CO_2e/kg of rice for the SRI method, and 2.29 kg CO_2e/kg of rice for the wide-narrow row method. In the summer season, the carbon footprint of rice is 3.72 kg CO_2e/kg of rice for thee conventional practice, 3.56 kg

Table 2. Carbon footprint of rice in Phu Luong commune.

No.	Sources of GHG emissions	GHG	GHG emissions (kg CO_2e/ha)					
			Spring rice			*Summer rice*		
			Conventional	*SRI*	*Wide-narrow row*	*Conventional*	*SRI*	*Wide-narrow row*
1	Electricity generation for the operation of agricultural machinery		3,143.10	3,143.09	3,143.09	2,619.25	2,619.25	2,619.25
2	Fertiliser production	CO_2	1,842.77	1,718.23	1,735.17	1,777.48	1,709.03	1,674.15
2.1	N-fertiliser	CO_2	*526.35*	*457.68*	*655.14*	*513.77*	*450.21*	*640.20*
2.2	P-fertiliser	CO_2	*8.08*	*13.27*	*14.10*	*7.94*	*13.27*	*13.52*
2.3	K-fertiliser	CO_2	*57.66*	*63.57*	*63.50*	*54.14*	*61.84*	*63.13*
2.4	NPK	CO_2	*1,250.68*	*1,183.70*	*1,002.44*	*1,201.64*	*1,183.70*	*957.30*
3	Lime production	CO_2	23.15	0.00	12.76	23.15	0.00	12.76
4	Pesticide production	CO_2	3.83	3.83	3.83	3.83	3.83	3.83
5	Methane emissions from rice cultivation	CH_4	7,870.93	5,765.76	5,556.19	10,646.16	10,110.0	8,990.94
6	Fertiliser application		506.58	414.20	497.65	548.42	431.31	538.53
6.1	CO_2 emissions from urea application	CO_2	*81.55*	*63.39*	*78.44*	*81.55*	*88.31*	*85.75*
6.2	Direct N_2O emissions from agricultural soil	N_2O	*425.04*	*350.81*	*419.21*	*466.87*	*343.00*	*452.77*
7	Lime application	CO_2	3.70	0.00	2.04	3.70	0.00	2.04
8	Diesel combustion for the operation of agricultural machinery		2,642.20	2,816.43	2,717.66	2,688.90	2,816.43	2,662.07
8.1	Tractor	CO_2	*1,940.87*	*1,940.87*	*1,940.87*	*1,940.87*	*1,940.87*	*1,940.87*
		N_2O	*4.68*	*4.97*	*8.42*	*4.79*	*4.97*	*8.32*
8.2	Combine harvester	CO_2	*694.97*	*852.44*	*750.46*	*694.97*	*852.44*	*694.97*
		N_2O	*1.68*	*2.06*	*1.81*	*1.68*	*2.06*	*1.81*
9	Transporting rice from farm to house	CO_2	3.46	5.37	3.72	3.46	5.85	3.67
10	On-site straw burning	CH_4	49.59	0.00	106.69	689.47	516.09	602.22
		N_2O	3.43	0.00	7.37	47.63	35.65	41.60
	Total (kg CO_2e/ha)		**16,092.74**	**13,866.90**	**13,786.17**	**19,051.44**	**18,247.45**	**17,151.04**
	Carbon footprint of rice (kg CO_2e/kg of rice)		**2.69**	**2.35**	**2.29**	**3.72**	**3.56**	**3.3**

CO_2e/kg of rice for the SRI method, and 3.3 kg CO_2e/kg of rice for the wide-narrow row method.

Proposal for mitigation options

Selection criteria

Vietnam submitted its Nationally Determined Contribution (NDC) to the United Nations Framework Convention on Climate Change (UNFCCC) on 29 September in 2015. In its NDC, Vietnam committed that with domestic resources, by 2030 Vietnam will reduce its GHG emissions by 8% compared to the Business-As-Usual (BAU scenario). The above-mentioned 8% contribution could be increased to 25% given receiving international support. The implementation of NDC will contribute to the global efforts to achieve the Paris Agreement, reaching the goal of limiting the average temperature increase less than 2^0C in 2100.

Based on the criteria for selecting the preferred GHG-emission mitigation options in Vietnam's NDC [12], the criteria that are developed include:

- Harmony with strategies and planning for agricultural and rural development.

- Mitigation cost (USD/ton CO_2e).

- Mitigation potential.

- Mitigation potential according to the results of the calculation of the carbon footprint of rice.

- Availability of technology.

- And co-benefits: bringing benefits to the economy, society, and environment and climate-change adaptation.

Selection of prioritised mitigation options

Based on the results of the calculations, it can be observed that the largest source of GHG emissions is from methane from rice cultivation in both the spring and summer seasons and in all three forms of cultivation; followed by electricity production for operating agricultural machinery; burning diesel for operating farm machinery; and fertiliser production.

According to Vietnam's NDC [12], 15 mitigation options in the agricultural sector have been developed based on agriculture and land use software. Of the 15 mitigation options for agriculture, five are selected in this study for rice production (Table 3). The option of 'biogas development' was not selected as farmers in Phu Luong commune mostly apply chemical fertilisers and very little farmyard manure.

Table 3. Mitigation costs and co-benefits of mitigation options for rice production in Phu Luong commune.

Option	Mitigation cost ($/t.$CO_2$e)	Co-benefit
A1. Reuse of agricultural residues	63.0	- Increase organic content in soil
A2. Alternate wetting and drying	88.0	- Reduce water volume for irrigation
A3. Introduction of biochar	75.0	- Reduce GHG emissions
A4. Integrated crop management (ICM) for rice	20.0	- Reduce cost of seeds and fertiliser
A5. Substitution of urea ($CO(NH_2)_2$) fertiliser by ammonium sulphate ($(NH_4)_2SO_4$)	30.0	- Reduce costs of seeds and fertiliser

Source: MONRE [12].

Mitigation options were assessed based on the criteria by scoring them from 1 to 5 (1 being the lowest, 5 being the highest). For farmers, mitigation costs and co-benefits are two most important factors and hence these two criteria have greater weight than the others. The results of the evaluation are presented in Table 4.

Table 4. Prioritised mitigation options for rice production.

Option	Criteria: *Mitigation potential based on rice carbon footprint (x1)*	*Harmony with policies (x1)*	*Mitigation cost (x2)*	*Technology availability (x1)*	*Co-benefits (x2)*	Total	Rank of priority
A1	1	4	3	3	3	20	5
A2	5	5	1	3	5	25	2
A3	4	4	2	2	4	22	4
A4	5	4	5	3	3	28	1
A5	3	3	5	2	3	24	3

Based on the evaluation results, the study proposes that ICM receive the highest priority for GHG-emission reduction for rice production. The second priority options are alternate wetting and drying and the substitution of urea fertiliser by $(NH_4)_2SO_4$.

Conclusions

This study developed a methodological framework and conducted a pilot calculation of carbon footprints in the life cycle of rice for Phu Luong commune. The results are quite similar to those reported in earlier studies around the world, such as 2.9 kgCO_2e/kg of rice in Italy [13], 2.92 kg CO_2e/kg of rice in Thailand [14], and ranging from 1.5

to 2.5 kg CO_2e/kg of rice in China [15]. According to the results of the calculations, GHG emissions from operating agricultural machinery account for a large proportion of emissions; however, thus far, there has not been much research on mitigation potential as this concerns the use of agricultural machinery. Therefore, this research direction should be considered in future.

The authors declare that there is no conflict of interest regarding the publication of this article.

REFERENCES

[1] D. Pandey, M. Agrawal, J.S. Pandey (2011), "Carbon footprints: Current methods of estimation", *Environmental Monitoring and Assessment*, **178**, pp.135-160.

[2] BSI (2008), *PAS 2050:2008: Specification for the assessment of the life cycle greenhouse gas emissions of goods and services*, United Kingdom.

[3] Carbon Trust (2007), *Carbon footprint measurement methodology*, **V1.1**, The Carbon Trust, London, UK.

[4] Cong Khanh Doan, Thi Thanh Huyen Truong, Huy Hoan Tran, Thi Kim Tuyen Vo, Van Thang Tran, Hong Thom Nguyen, Trung Thanh Ho, Ngoc Thinh Tran and Huu Lam Son Nguyen (2014), *Assessment of the current status and development trends of the market for low-carbon commodities in Vietnam and on the world and propose solutions to promote*, Summary report 04.14/CC, Ministry of Industry and Trade.

[5] ISO (2013), *ISO/TS 14067: Greenhouse gases - Carbon footprint of products-Requirements and guidelines for quantification and communication.*

[6] FAO (2017), *Global database of GHG emissions related to feed crops: Methodology*, **V1**, Livestock Environmental Assessment and Performance Partnership. FAO, Rome, Italy.

[7] Institute of Agricultural Environment (2016), *Developing a comprehensive pilot Measurement-Reporting-Verification (MRV) framework for NAMAs on a selected agricultural sub-system comprised of rice cultivation and improved cookstoves.*

[8] IPCC (2006), *IPPC Guidelines for National Greenhouse Gas Inventories*, IGES, Japan.

[9] T. Nemecek and T. Kagi (2007), *Life cycle inventories of agricultural systems*, 46pp.

[10] B. Gadde, S. Bonnet, C. Menke and S. Garivate (2009), "Air pollutant emissions from rice straw open field burning in India, Thailand and the Philippines", *Journal of Environmental Pollution,* **157**, pp.1554-1558.

[11] IPCC (2014), *Climate Change 2014: Synthesis Report: Contribution of Working Group I, II and III to the Fifth Assessment Report of the Intergovernmental Panel of Climate Change*, Geneva, Switzerland, 151pp.

[12] Ministry of Natural Resources and Environment (2015), *Technical report: Vietnam's Intended Nationally Determined Contribution.*

[13] S. Kasmaprapruet, W. Paengjuntuek, P. Saikhwan, H. Phungrassami (2009), "Life Cycle Assessment of Milled Rice Production: Case Study in Thailand", *European Journal of Scientific Research*, **30(2)**, pp.95-203.

[14] G.A. Blengini and M. Busto (2009), "The life cycle of rice: Life Cycle Assessment of alternative agri-food chain management systems in Vercelli (Italy)", *Journal of Environmental Management*, **90**, pp.1512-1522.

[15] X. Xu, B. Zhang, Y. Liu, Y. Xue, B. Di (2013), "Carbon footprints of rice production in five typical rice districts in China", *Acta Ecologica Sinica*, **33**, pp.227-232.

Doi: 10.31276/VJSTE.61(2).90-96

Assessment of hydro-climatological drought conditions for Hong-Thai Binh river watershed in Vietnam using high-resolution model simulation

Ho Viet Cuong[1], Do Hoai Nam[1*], Trinh Quang Toan[2]

[1]Vietnam Academy for Water Resources

[2]Hydrologic Research Laboratory, Department of Civil and Environmental Engineering, University of California, USA

Received 20 March 2019; accepted 5 June 2019

Abstract:

Understating hydro-climatological conditions in a transboundary is always challenging because of issues in sharing available data among riparian countries. The present study has explored the hydro-climatological drought conditions over Hong-Thai Binh river watershed (H-TBRW) based on the downscaled rainfall and reproduced streamflow by the state-of-the-art coupled regional hydroclimate model. The standardized precipitation index (*SPI)* and streamflow drought index (*SDI)* indicators are used to define the climatological and hydrological drought conditions, respectively. Both *SPI* and *SDI* are derived from the precipitation and streamflow data reproducibility for the H-TBRW during 1950-2015. The results demonstrate a slight increasing trend in both climatological and hydrological conditions. Over the H-TBRW, results reveal that the Da and Thao rivers strongly expect drought conditions; meanwhile, the remaining rivers are very likely to experience similar drought conditions as in the past.

Keywords: **coupled WEHY-HCM model, drought, Standardized Precipitation Index, Streamflow Drought Index.**

Classification number: **5.2**

Introduction

In the monsoon regions, though annual mean rainfall is high, the rainfall distribution is quite distinct between the seasons. The rainy season often accounts for 70-90% of the annual mean rainfall [1]. Under a changing climate, increases in surface temperature tend to accelerate evapotranspiration processes, causing greater water vapour in the air that subsequently results in more precipitable water. However, increased precipitation is mostly distributed in the wet season; meanwhile, the dry season is very likely to be drier (e.g., [2, 3]). In other words, droughts are intensifying and are causing adverse impacts on lives, water resources, agriculture, and food security.

Conventional assessments of trend and variability of droughts were mostly conducted using ground hydro-meteorological observation (e.g., [4, 5]) or combined observation and model simulations [6]. It is known that the existing ground observation networks in developing countries are quite scattered and are extremely short on record length. This situation diminishes studies of drought conditions, especially the investigation of spatial variation of droughts across transboundary river basins where data are inaccessible or are not shared among the riparian countries. As an extension of the previous work regarding the reconstruction and evaluation of changes in hydrologic conditions over a transboundary region [7], this study will further capture the trend and variability of droughts in the past climate (1950-2015). The work will be based on the simulations derived from a regional climate model coupled with a physically based hydrology model for the H-TBRW, the portion lying in the territory of Vietnam of the Red river. Some well-known drought indices are employed to detect the trend and variability of both meteorological and hydrological drought conditions. These indices are calculated for a range of time scales as addressed in the literature (e.g., [3, 5]) in order to provide a choice of index appropriate for different meteorological, agricultural and hydrological applications.

Methodology, study area, and data

Hydro-meteorological drought indicators

Droughts often cause impacts over a widespread area

*Corresponding author: Email: namdh@vawr.org.vn

during a long period of time; these are commonly referred to as social, economic, and social impacts. It is widely accepted that droughts are defined in terms of meteorological, hydrological, agricultural, and socioeconomic conditions. However, this study considers only the first two terms, and drought indices are calculated solely based on precipitation and streamflow data as described in the following paragraphs.

Standardized Precipitation Index (SPI): precipitation and evapotranspiration are primary variables controlling the formation and persistence of drought conditions. However, it is quite difficult to estimate evapotranspiration rates, so drought climatology studies have used mostly data on precipitation. Among the available indices in the literature used to identify meteorological drought condition - for example, Palmer drought severity index [8], crop moisture index [9], and surface water supply index [10] - the standardized precipitation index (*SPI*) has been widely accepted for drought assessment studies (e.g., [11-14]). The SPI is formulated to estimate the precipitation deficit for multiple time scales, *i*, which indicate drought conditions throughout the watershed.

SPI is simply defined as the ratio of the difference of precipitation from the mean for a specified time period over the corresponding standard deviation determined from past records as expressed in equation 1 below:

$$SPI_i = \frac{P_i - \overline{P_i}}{\sigma_i} \qquad (1)$$

where *SPI* is standardized precipitation index for time scale *i* (e.g., 1-, 3-, 6-, 12-, 24-, and 48-month time scales); P_i is precipitation for time scale *i*; $\overline{P}_i$ is climatological mean precipitation for time scale *i*; σ_i is standard deviation precipitation for time scale *i*.

The *SPI* is computed by fitting a probability density function to the frequency distribution of precipitation summed over the time scale of interest. *SPI* values can be greater (positive) or less (negative) than the climatological mean precipitation. Table 1 below depicts categorical *SPI* values reflecting drought classifications from extremely wet to dry conditions.

Table 1. Drought classification by *SPI* value (modified after [5]).

State	*SPI* value	Category	*SPI* value	Category
	Positive		*Negative*	
1	2.00 or more	Extreme wet	0 to -0.99	Mild drought
2	1.50 to 1.99	Severe wet	-1.00 to -1.49	Moderate drought
3	1.00 to 1.49	Moderate wet	-1.50 to -1.99	Severe drought
4	0 to 0.99	Mild wet	-2.00 or less	Extreme drought

Streamflow Drought Index (SDI): similar to *SPI*, the *SDI* was developed to explore the water resources conditions of the watershed based on the information of cumulative streamflow volumes for reference periods, as expressed in equation 2 [15]:

$$V_{i,k} = \sum_{j=1}^{3k} Q_{i,j} \quad i = 1, 2, \ldots; j = 1, 2, \ldots 12; k = 1, 2, 3, 4 \qquad (2)$$

where $V_{i,k}$ denotes the cumulative streamflow volume for the i-th hydrological year and the k-th reference period, k = 1 for October-December, k = 2 for October-March, k = 3 for October-June, and k = 4 for October-September.

Based on cumulative streamflow volumes $V_{i,k}$, the *SDI* is defined for each reference period k of the i-th hydrological year as follows:

$$SDI_{i,k} = \frac{V_{i,k} - \overline{V_k}}{\sigma_k} \quad i = 1, 2, \ldots; k = 1, 2, 3, 4 \qquad (3)$$

where V_k and σ_k are the mean and the standard deviation of cumulative streamflow volumes of reference period k as these are estimated over a long period of time, respectively. By this definition, *SDI* values are also categorized into five states of hydrological conditions of the watershed as presented in Table 2.

Table 2. Drought classification by *SDI* value (modified after [15]).

State	*SPI* value	Category	*SPI* value	Category
	Positive		*Negative*	
1	Greater than zero	Non-drought	0 to -0.99	Mild drought
2			-1.00 to -1.49	Moderate drought
3			-1.50 to -1.99	Severe drought
4			-2.00 or less	Extreme drought

Study area

The Red river is categorized among the five major transboundary river systems in Southeast Asia and flows from Yunnan province in Southwest China through northern Vietnam to the Gulf of Tonkin (Fig. 1). The Red river covers a drainage area of 169,020 km^2, of which 48% is in China's territory, 51% is in Vietnam's territory, and only 1% is in Laos' territory. The H-TBRW is named for the downstream portion of the Red river basin in Vietnam. The H-TBRW covers 26 provinces and cities (including Hanoi and Hai Phong), with a total population of 30 million.

As it is located in a tropical region, the H-TBRW is strongly influenced by the tropical monsoon climate. Average annual precipitation is spatially distributed in a wide range over the river basin (from 700-2,100 mm in China to 1,200-4,800 mm in Vietnam). The rainy season is from April through October, representing 85-90% of the total annual rainfall, and the dry season is from November to April representing only 10-15% of the total annual rainfall. With regard to water availability, the river basin produces 136 km^3/year, of which 83 km^3 (61%) is generated in Vietnam's territory.

Fig. 1. Map of the Red river basin (left) and the H-TBRW comprising five main tributaries in Vietnam (right).

Precipitation and streamflow data reproducibility

Due to transboundary issues, information about precipitation and streamflow in the portions beyond the border of Vietnam is not available to the public. Attempts have been made to cover this problem through the provision of reanalysis products. One of the recent precipitation products is APHRODITE - Asian Precipitation Highly Resolved Observational Data Integration Towards the Evaluation - providing gridded daily precipitation over the Asia monsoon region from 1951 to 2015. APHRODITE has advantages for studies of water resources. However, it is worth noting that APHRODITE is a reanalysis product based on historical measurement of precipitation, so it is not able to offer some type of quantitative projection in the future. In addition, featured with 0.25-degree grid cells, APHRODITE is considered a coarse spatial resolution product that diminishes water resources studies at local scales.

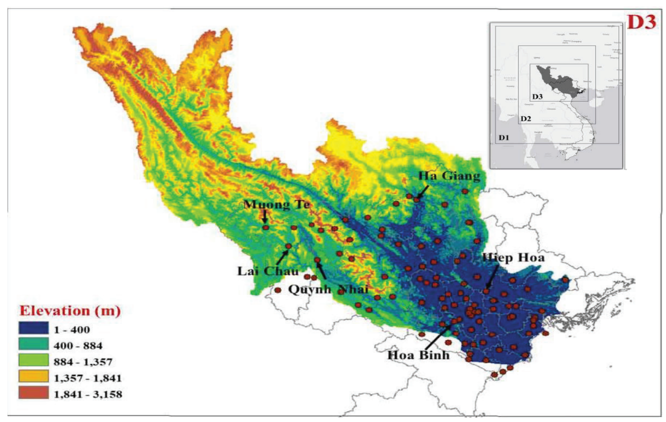

Fig. 2. Cascading computational domains of the downscaling model and location of observation sites in the H-TBRW (modified after [7]).

As a result, high spatial and temporal resolution atmospheric and streamflow data - which were already reconstructed and verified for the entire Red river basin for period 1950-2015 [7, 16] - are employed in this study to derive hydro-meteorological drought indices.

The high-resolution atmospheric and streamflow data are a dynamic downscaling product reproduced using a coupled regional hydroclimate model, or simply referred to as the WEHY-HCM [7, 16]. Atmospheric conditions were reproduced using weather research forecast (WRF) simulations. The WRF simulations were originally nested in the coarse resolution (1.25-degree) reanalysis data, ERA-20C, which were developed by the European Centre for Medium Range Weather Forecasts. These simulations were performed for a domain (D1) with a spatial resolution of 81 km. The WRF simulations were then further refined through cascading domains of 27 km (D2) and 9 km (D3), respectively, as illustrated in Fig. 2. The WRF provided simulation outputs every three hours. The simulated rainfall was then aggregated into larger temporal scales (e.g., daily or monthly time series) for model verification. Results illustrated that the simulated rainfall for the historical period 1975-2006 over the H-TBRW is comparable to the observed precipitation datasets either derived from direct point measurement or the APHRODITE product. Detailed model verification can be seen in the literature [7].

With regard to streamflow data reproducibility, the downscaled precipitation is used to drive the Watershed Environmental Hydrology Model (WEHY) for hydrologic simulations in the H-TBRW. The WEHY is a physically based hydrologic model that is developed based on actual physical processes and information from the model computational unit areas throughout the watershed domain [16]. The model was also designed for coupling regional climate models (e.g., the WRF model) through its land surface component. In addition, the model parameters are nearly calibration-free because they are estimated based on actual physical information of the catchment such as topography, soil, and land use/cover. Therefore, it illustrates advantages for the assessment of water resources in scattered observation catchments.

The WEHY model setup for the H-TBRW was realized in the literature [16]. For a short description, the entire H-TBRW was divided into computational units (or sub-basins) based on similarity in topography and land surface information. Runoff is generated from the dynamic interaction of hillslope flow and channel routing. The monthly discharges at Yen Bai station were employed for model calibration and validation. Model performance statistics exhibited agreement between the monthly simulated and observed discharges. Nash Sutcliffe Efficiency Coefficients of 0.87 and 0.86 were obtained for the model calibration and validation, respectively. Relative errors in runoff volume were less than 5%. These indicate a reasonable reproduction of the monthly discharges for the H-TBRW and useful application for further assessment of hydrologic conditions over the Red river basin.

Results and discussion

Climatological drought conditions over H-TBRW

In general, droughts last from a couple of months to a few years. This study attempts to understand climatological drought conditions corresponding to the time scales of one, three, six, nine, 12, and 24 months. The previous study [7] revealed a reasonable agreement of the reproduced monthly precipitation over the H-TBRW with the APHRODITE product. However, this study again performs the verification of *SPI* derived from the reproduced precipitation data against those determined using rain-gauge measurements. The verification is conducted on a sub-basin average basis. As illustrated in Fig. 1, the H-TBRW is delineated into five sub-catchments, namely, Da, Thao, Lo-Gam, and Upper Thai Binh sub-catchments, and the Red river delta. Available observed precipitation data during the period from 1975 to 2006 are employed for the *SPI* verification.

This study first attempted to test the *SPI* derived from the reproduced precipitation using the Nash Sutcliffe Efficiency Coefficient, which can suggest the agreement in time and severity level of drought conditions of the *SPI*. A test was conducted for the Da river sub-catchment over a period of five years (1990-1994). Results reveal that the simulated *SPI* and that obtained using observation data are quite similar, as seen in Fig. 3. Performance statistics are presented in Table 3 and reveal encouraging results. However, it is noted that similar *SPI* verification is quite challenging for the remaining sub-catchments because rainfall remains an unpredictable variable among the others simulated by the WRF model. It is understood as the uncertainties of the model structure, parameterization schemes, boundary, and initial conditions. In general, most model simulations tend to provide information about a climatological trend rather than a precise simulation of an event magnitude and the time it occurs. In addition, ground observation sites are quite scattered, leading to substantial errors for area rainfall estimates. It is noted that the calculated *SPIs* considering rainfall as a gamma distribution variable outperform those calculated considering rainfall as a normal distribution variable that tends to underestimate the drought conditions [17].

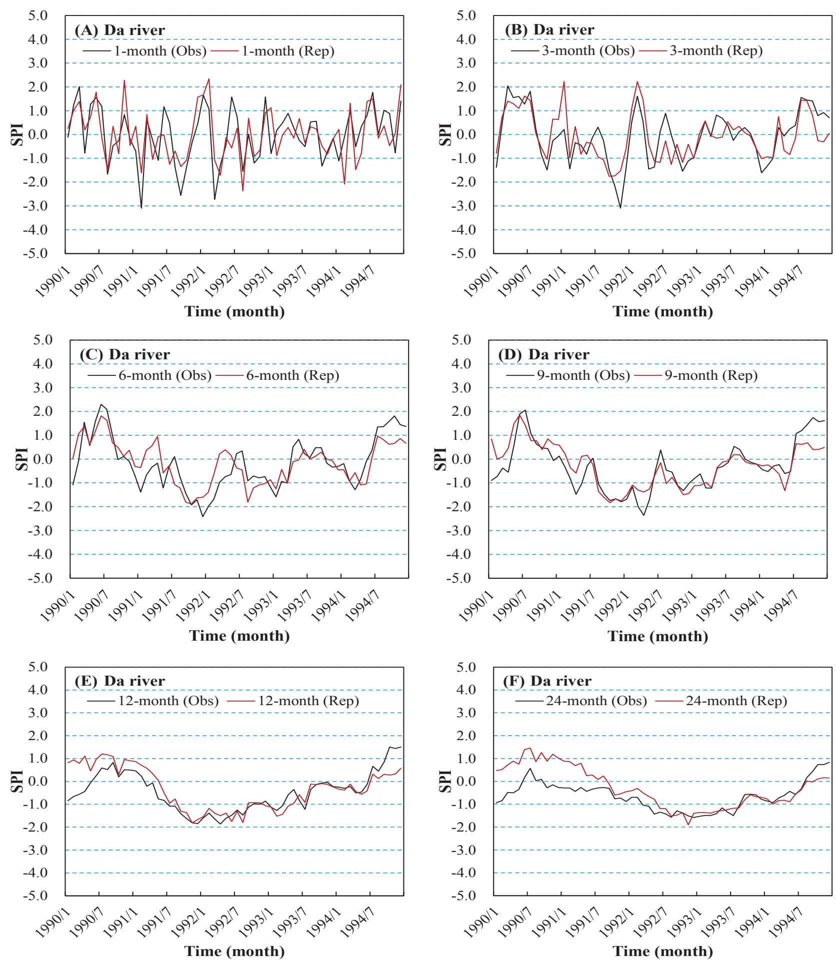

Fig. 3. Verification of SPIs for the Da river sub-catchment with different time scales: (A) 1-month; (B) 3-month; (C) 6-month; (D) 9-month; (E) 12-month; and (F) 24-month.

Table 3. Statistics of *SPI* verification for Da sub-catchment.

Sub-catchment	Nash Sutcliffe Efficiency Coefficient					
	1-month	*3-month*	*6-month*	*9-month*	*12-month*	*24-month*
Da river	0.37	0.58	0.65	0.69	0.56	NA

NA: not applicable.

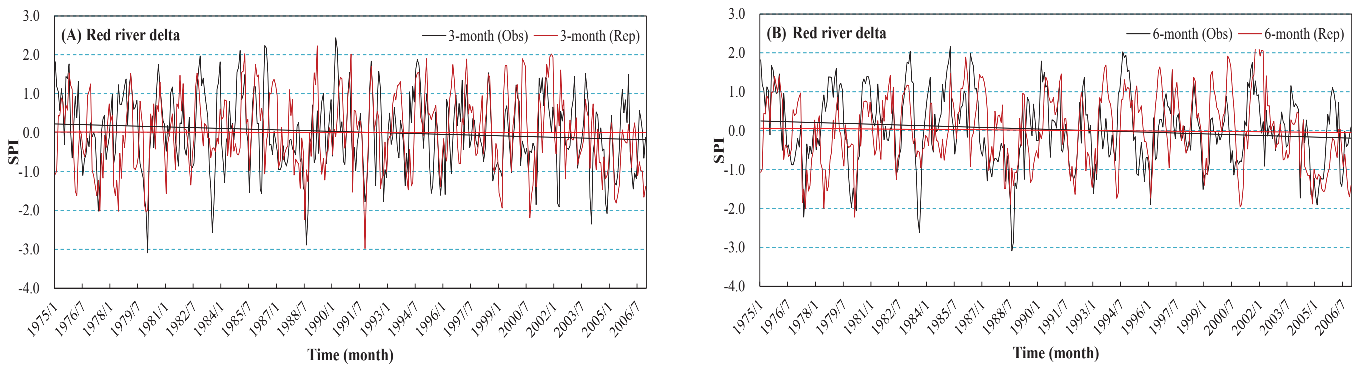

Fig. 4. Verification of *SPI* trend for the Red river delta with time scales: (A) 3-month; (B) 6-month.

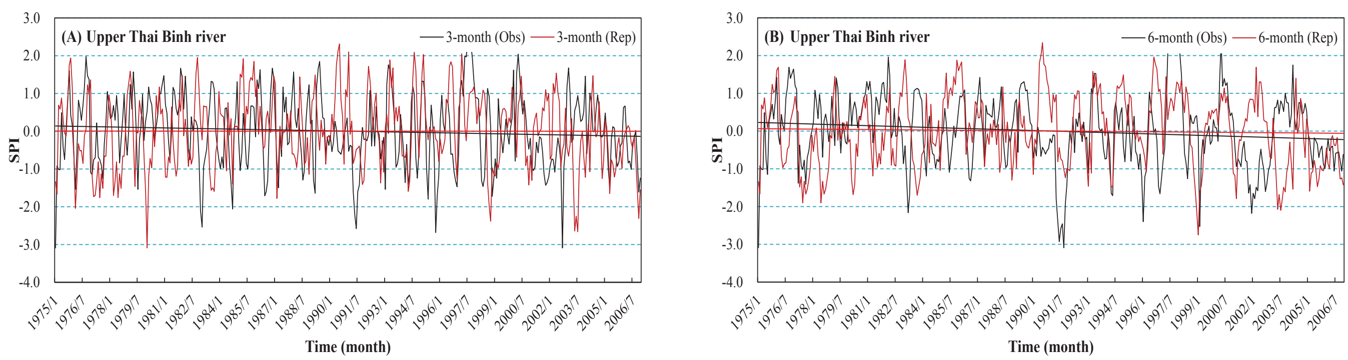

Fig. 5. Verification of *SPI* trend for the Upper Thai Binh river sub-catchment with time scales: (A) 3-month; (B) 6-month.

Table 4. Number of severe drought events simulated by model versus actual observation during 1975-2006 in Red river delta and Upper Thai Binh river sub-catchment.

Sub-catchment	1-month	3-month	6-month	9-month	12-month	24-month	Average
Red river delta							
Observation	27	20	21	19	26	14	21
Model	35	23	21	16	14	17	21
Absolute relative error (%)	30%	15%	0%	16%	46%	21%	21%
Upper Thai Binh river							
Observation	27	20	21	19	26	14	21
Model	35	23	21	16	14	17	21
Absolute relative error (%)	30%	15%	0%	16%	46%	21%	21%

Thus, the next attempts are focusing on model verification in terms of climatological drought trend and risk. For example, Figs. 4 and 5 illustrate the drought trends (time scales of three and six months) obtained from model simulation versus actual observation during 1975-2006 in the Red river delta and Upper Thai Binh sub-catchment. Results demonstrate that both modelled and observed drought trends are comparable and indicate a slight decrease in droughts. Similar results (not shown) are found for the remaining time scales. Table 4 demonstrates the risk of severe drought conditions (represented by a number of drought events that *SPI* is less than minus-1.5) in the Red river delta and Upper Thai Binh sub-catchment. These results indicate a reasonable performance of the model simulation against observation. On average, the number of severe drought events are well reproduced by the WRF model. However, the model still provides the average absolute relative errors of about 20%.

As a result, climatological drought conditions of various time scales in the H-TBRW are reproduced based on the simulated rainfall for the period 1950-2015, a sufficiently long time scale that is able to reflect the most accurate climatological condition in comparison with such studies as [18, 19], which assessed the drought conditions using shorter periods of time. Fig. 6 illustrates an example of climatological drought conditions with the time scale of six months in the H-TBRW. Results show there has been a slight increase of drought conditions in the Red river delta, Lo-Gam, and Thai Binh sub-watersheds; meanwhile, an intensified implication of drought has been observed for Da and Thao sub-watersheds. It is not revealed in this text; however, in terms of time scales, the drought conditions have been more severe with increased time scales. Table 5 presents the number of climatological severe and extreme droughts in the H-TBRW during 1950-2015. Among the five sub-watersheds, the Red river delta and Upper Thai Binh sub-watershed experienced more severe drought events; however, the Da sub-watershed has observed more extreme drought events.

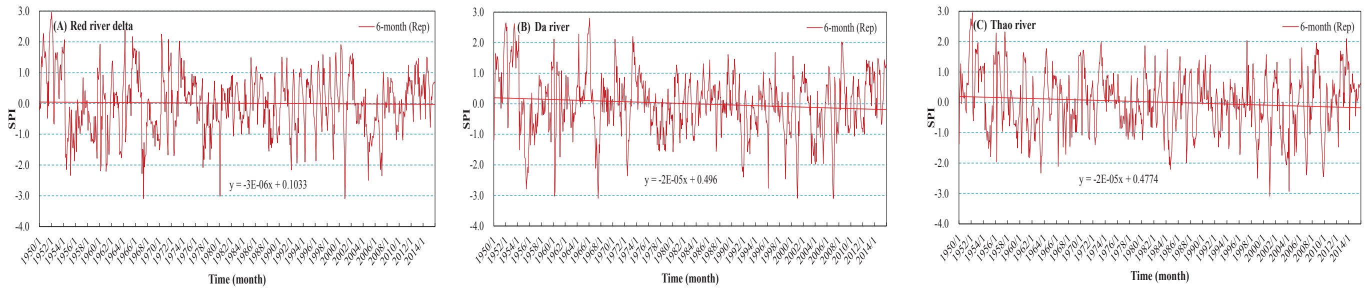

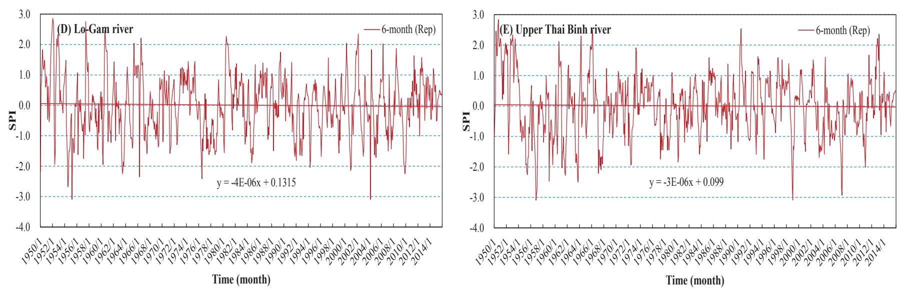

Fig. 6. Climatological drought conditions simulated by model during 1950-2015 for the H-TBRW sub-catchment: (A) Red river delta, (B) Da river, (C) Thao river, (D) Lo-Gam river, and (E) Upper Thai Binh river with the straight lines representing the trend of the drought conditions.

Table 5. Climatological severe and extreme drought events simulated by model during 1950-2015 in Red river delta and Upper Thai Binh river sub-catchment.

Sub-catchment	1-month	3-month	6-month	9-month	12-month	24-month	Average
Red river delta							
Severe drought	65	55	53	50	45	54	54
Extreme drought	30	21	15	10	8	27	19
Da river							
Severe drought	54	53	56	48	44	49	51
Extreme drought	20	29	26	25	21	19	23
Thao river							
Severe drought	57	51	50	49	48	37	49
Extreme drought	22	12	15	23	23	14	18
Lo-Gam river							
Severe drought	45	50	57	59	59	45	53
Extreme drought	18	16	13	12	9	12	13
Upper Thai Binh river							
Severe drought	74	58	56	48	47	38	54
Extreme drought	22	21	19	23	20	20	21

Hydrological drought conditions over the H-TBRW

The present study examines hydrological drought conditions based on the reproduced streamflow at various sites in the H-TBRW. The hydrological drought conditions are explored for different time periods. Within this text, Fig. 7 illustrates the hydrological drought trends over the past 65 years at the Da and Thao rivers (Hoa Binh and Yen Bai, respectively). It appears that the hydrological drought in the Da river is becoming slightly severe; meanwhile, the drought situation in the Thao river is rather stable. The drought situations (not shown) in other rivers are also found to be similar. These trends indicate minor stress on water availability for the water-use sectors in the downstream areas. However, it is noted that the influence of reservoir operation is excluded from the streamflow simulations. Thus, the next effort of this research series will further elaborate this trend of drought as both reservoir operation and projection data are analyzed.

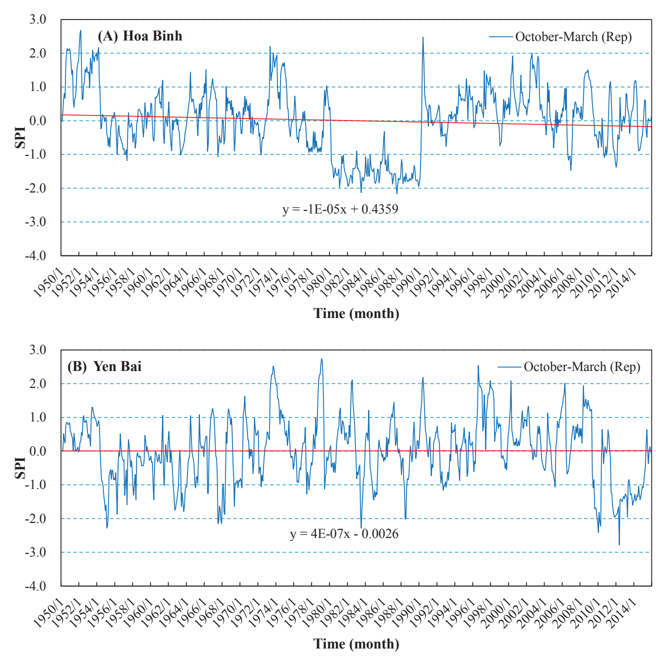

Fig. 7. Hydrological drought conditions (October-March) simulated by model during 1950-2015 for the H-TBRW sub-catchment: (A) Da river (at Hoa Binh), and (B) Thao river (at Yen Bai) representing the trend of the drought conditions.

Conclusions and remarks

Understating hydro-climatological conditions in a transboundary is always challenging because of the insufficient data availability. The present study has explored the hydro-climatological drought conditions over the H-TBRW based on the downscaled rainfall and reproduced streamflow by the state-of-the-art WEHY-HCM model. The results demonstrate a slight increase in trends of both climatological and hydrological conditions (*SPI* and *SDI*). Over the H-TBRW, the Da and Thao rivers are expecting a stronger implication of drought; meanwhile, the remaining rivers are quite likely to experience similar drought conditions as in the past.

It is also noted that there exist model intrinsic uncertainties because of imperfect model structure, parameterization schemes, boundary, and initial conditions. In general, model simulations provide reasonable climatological trends rather than a precise simulation of an event magnitude and the time it occurs. As a result, model bias correction will be still needed for further interpretation of the hydro-climatological drought conditions in such sub-catchments of the H-TBRW.

ACKNOWLEDGEMENTS

This study was financially supported by the National Science and Technology Program for 2016-2020 (KC.08.05/16-20), Ministry of Science and Technology in Vietnam. The study was implemented at the Key Laboratory of River and Coastal Engineering (KOLRCE-Vietnam).

The authors declare that there is no conflict of interest regarding the publication of this article.

REFERENCES

[1] K.N. Kumar, et al. (2013), "On the observed variability of monsoon droughts over India", *Weather Clim. Extrem.*, **1**, pp.42-50.

[2] IPCC (2018), *Climate Change 2013: The Physical Science Basis. Contribution of Working Group I to the Fifth Assessment Report of the Intergovernmental Panel on Climate Change*, Cambridge University Press, Cambridge, UK and New York, NY, USA, 1585pp.

[3] K. Takara, et al. (2009), "Assessing climate change impact on water resources in the Tone river basin, Japan, using super-high resolution atmospheric model output", *J. Disaster. Res.*, **4(1)**, pp.12-22.

[4] D.H. Burn, M.A.H. Elnur (2002), "Detection of hydrologic trends and variability", *J. Hydrol.*, **255**, pp.107-122, http://dx.doi.org/10.1016/S0022-1694(01)00514-5.

[5] L.H. Benjamin, M.A. Saunders (2002), "A drought climatology for Europe", *International Journal of Climatology*, **22**, pp.1571-1592.

[6] A. Dai (2013), "Increasing drought under global warming in observations and models", *Nat. Clim. Change*, **3**, pp.52-58, http://dx.doi.org/10.1038/nclimate1633.

[7] C. Ho, A. Nguyen, A. Ercan, M.L. Kavvas, V. Nguyen, T. Nguyen (2018), "Assessment of atmospheric conditions over the Hong-Thai Binh river watershed by means of dynamically downscaled ERA-20C reanalysis data", *Journal of Water and Climate Change*, jwc2018291, Doi: 10.2166/wcc.2018.291.

[8] W.C. Palmer (1965), *Research Paper No. 45 - Meteorological drought*, U.S. Department of Commerce, Weather Bureau, Washington D.C.

[9] W.C. Palmer (1968), "Keeping track of crop moisture conditions, nationwide: the new Crop Moisture Index", *Weatherwise*, **21(4)**, pp.156-161.

[10] B.A. Shafer, L.E. Dezman (1982), "Development of a Surface Water Supply Index (SWSI) to assess the severity of drought conditions in snowpack runoff areas", *Proceedings of the Western Snow Conference*, pp.164-175, Colorado State University, Fort Collins, Colorado.

[11] R.A. Seiler, M. Hayes, L. Bressan (2002), "Using the standardized precipitation index for flood risk monitoring", *International Journal of Climatology*, **22(11)**, pp.1365-1376.

[12] S.K. Min, W.T. Kwon, E.H. Park, Y.G. Choi (2003), "Spatial and temporal comparisons of droughts over Korea with East Asia", *International Journal of Climatology*, **23**, pp.223-233.

[13] S. Morid, V. Smakhtin, M. Moghaddasi (2006), "Comparison of seven meteorological indices for drought monitoring in Iran", *International Journal of Climatology*, **26(7)**, pp.971-985.

[14] National Centers for Environmental Information, https://www.ncdc.noaa.gov/sotc/drought/201904#det-spi.

[15] I. Nalbantis, G. Tsakiris (2009), "Assessment of hydrological drought revisited", *Water Resour Manag.*, **23(5)**, pp.881-897.

[16] C. Ho, T. Trinh, A. Nguyen, Q. Nguyen, A. Ercan, M.L. Kavvas (2019), "Reconstruction and evaluation of changes in hydrologic conditions over a transboundary region by a regional climate model coupled with a physically-based hydrology model: application to Thao river watershed", *Science of The Total Environment.*, **668**, pp.768-779.

[17] H.V. Cuong, N.T.N. Nhan, T.V. Bach, T.Q. Toan (2019), "Research on drought conditions in the Red - Thai Binh basin with meteorological and hydrological data recovered from the combined model WEHY-WRF", *Journal of Water Resources Science and Technology*, **52**, pp.48-64 (in Vietnamese).

[18] N.V. Thang, et al. (2015), *National Science and Technology Program, code KC.08.17/11-15. Study and establish a drought forecast and warning system for Vietnam with a duration of up to 3 months* (in Vietnamese).

[19] V.T. Hang, T.T. Ha (2013), "Comparison of drought indices for climatological regions of Vietnam", *VNU Journal of Science: Natural Sciences and Technology*, **2S(29)**, pp.51-57 (in Vietnamese).

Vietnam Journal of Science, Technology and Engineering (VJSTE): Manuscript Template

General Instructions on using this template and submitting a manuscript to VJSTE: Thank you for preparing a manuscript for submission to VJSTE. Using this template, or following the guidelines below, will help us in processing your paper. Our goal is to be able to identify each section of your manuscript so that we can accurately record the title, authors, abstract, etc. and also be able to enrich it by including reference links and an accurate layout.

You can submit your paper at http://vietnamscience.vn

So that we can identify the parts of your paper, and even if you do not use our template, please begin each section with the specific key words listed below. Please do not use paragraph breaks in the title, author list, or abstract.

Title

Authors

Affiliations

Abstract

One Sentence Summary

Main Text

Acknowledgements

References

Several of these headings are optional, for example, not all papers will include a one-sentence summary, figures or tables.

Please use the .docx format (all version after Word 2007).

More specific formatting instructions are provided in the actual template, which follows.

Title: How to Format a Science Paper (replace with your real title)

Authors: The author list should be one single paragraph (no breaks). Authors should be listed by first name or initial followed by last name and separated by commas. Use superscript numbers to link affiliations, and symbols *†‡ for author notes. For example, X. Jones[1]*, P. Smith[1,2]

Affiliations:

[1]Affiliations should be preceded by superscript numbers corresponding to the author list, and each affiliation should end with a period.

[2]Each affiliation should be a separate paragraph.

*Correspondence to: include the email addresses or telephone number of the corresponding author(s). Please use the asterisk (*) symbol for the corresponding author information.

Abstract: The abstract should be about 100-150 words, and organized in this structure: An opening sentence that sets the question that you address and is comprehensible to the general reader, background content specific to this study, results, and a concluding sentence. It should be one paragraph only.

One Sentence Summary: A brief summary of the main result of your paper, without excessive jargon and less than 150 characters.

Main Text: In general, this should include a brief (1-2 paragraph) introduction, followed by a statement of the specific scope of the study, followed by results and then interpretations. Please avoid statements of future work or claims of priority, and avoid repeating the conclusions at the end.

All of the Figures and Tables should be cited in order (which should be cited as, for example, figure S1, and table S1). You can include page breaks if you would like to place the figures within the text.

Subheads: These can be included in Research Articles or Reviews and should be brief.

Equations can be included. We do not recommend using the native Word 2007, 2008, 2010 or 2011 equation editor. This can in some cases produce less reliable MathML, the online markup language we use, which may result in display errors. Instead, use the legacy equation editor in word (Insert menu; select insert object; select word equation) or use Mathtype (recommended). If you enter equations in simple LaTeX, check that they will convert accurately (Word 2007 and higher can convert simple LaTeX equations).

Fig. #: (Begin each figure caption with a label, "**Fig. 1.**" for example, as a new paragraph.).

Fig. 1. The figure caption should begin with an overall descriptive statement of the figure followed by additional text. They should be immediately after each figure. Figure parts are indicated with capital letters (**A**). If you prefer, you can place both the actual figures and captions logically through the text near where they are cited rather than at the end of the file (but not both). If a paragraph in the main text begins with the name of a figure, write out "Figure" in full (e.g., <para>"Figure 1 shows….").

Fig. 2. You can place graphics above each equation as part of this file.

Table #: (Begin each table caption with a label "**Table 1.**", etc.) as a new paragraph.

Table 1. Start this caption with a short description of your table. Format tables using the Word Table commands and structures. Do not create tables using spaces or tabs characters.

Acknowledgments: The acknowledgments should include a statement about where the data reported in the paper are presented, archived, or available. If in an archive, include the accession number or a placeholder for it. Please also include relevant funding information such as grant numbers and funding agencies. You can also include a statement of author contributions here. The acknowledgements can be multiple paragraphs.

References:

References should be cited in bracket with a number [1]. Multiple reference citations are separated by commas [2, 3] or if a series, dashes [4-6].

References are listed in numerical order, and in the same order in which they are cited in text. The reference list should include all and only those references you have cited in the text. The reference list appears at the end of the paper.

Please include the above heading "References".

Please do not mix in references with explanatory notes.

The reference consist of: Family name(s) and initials of all authors (year of publication), "Titles of journal articles" (optional), *Title of journal, book or other publication*, **volume(number)**, page numbers.

Example of a reference list:

[1] T. Binzoni, T.S. Leung, D. Boggett, D.T. Delpy (2002), "A new near infrared laser-Doppler flowmeter for deep tissue perfusion monitoring", *MAGMA*, **14,** pp.74-75.

[2] T. Binzoni, T.S. Leung, D. Boggett, D.T. Delpy (2003), "Non-invasive laser Doppler perfusion measurements of large tissue volumes and human skeletal muscle blood RMS velocity", *Phys. Med. Biol.*, **48(1)**, pp.2527-2549.

ISSN 2525-2461

Vietnam Journal of Science, Technology and Engineering

JUNE 2019 • VOL.61 NUMBER 2

EDITORIAL OFFICE

113 Tran Duy Hung Str., Cau Giay Dist., Hanoi

Tel: (84.24) 39436793; Fax: (84.24) 39436794

Email: khcnvn@most.gov.vn

Website: vietnamscience.vn

PUBLICATION LICENCE

No.1153/GP-BTTTT 26th July 2011

No.2528/GP-BTTTT 26th December 2012

No.592/GP-BTTTT 28th December 2016